University of Illinois at Urbana-Champaign
ACRC
Air Conditioning and Refrigeration Center A National Science Foundation/University Cooperative Research Center

Probabilistic Flow Regime Map Modeling of Two-Phase Flow

E. W. Jassim, T. A. Newell, and J. C. Chato

ACRC TR-248 August 2006

For additional information:

Air Conditioning and Refrigeration Center
University of Illinois
Department of Mechanical Science & Engineering
1206 West Green Street
Urbana, IL 61801

(217) 333-3115

Prepared as part of ACRC Project #184
Experimental Measurement and Modeling of Oil Holdup
during Refrigerant Condensation and Evaporation
T. A. Newell, and J. C. Chato, Principal Investigators

The Air Conditioning and Refrigeration Center was founded in 1988 with a grant from the estate of Richard W. Kritzer, the founder of Peerless of America Inc. A State of Illinois Technology Challenge Grant helped build the laboratory facilities. The ACRC receives continuing support from the Richard W. Kritzer Endowment and the National Science Foundation. The following organizations have also become sponsors of the Center.

Arçelik A. S.
Behr GmbH and Co.
Carrier Corporation
Cerro Flow Products, Inc.
Daikin Industries, Ltd.
Danfoss A/S
Delphi Thermal and Interior
Embraco S. A.
Emerson Climate Technologies, Inc.
General Motors Corporation
Hill PHOENIX
Honeywell, Inc.
Hydro Aluminum Precision Tubing
Ingersoll-Rand/Climate Control
Lennox International, Inc.
LG Electronics, Inc.
Manitowoc Ice, Inc.
Matsushita Electric Industrial Co., Ltd.
Modine Manufacturing Co.
Novelis Global Technology Centre
Parker Hannifin Corporation
Peerless of America, Inc.
Samsung Electronics Co., Ltd.
Sanden Corporation
Sanyo Electric Co., Ltd.
Tecumseh Products Company
Trane
Visteon Automotive Systems
Wieland-Werke, AG

For additional information:

Air Conditioning & Refrigeration Center
Mechanical & Industrial Engineering Dept.
University of Illinois
1206 West Green Street
Urbana, IL 61801

217 333 3115

Abstract

The purpose of this investigation is to develop models for two-phase heat transfer, void fraction, and pressure drop, three key design parameters, in single, smooth, horizontal tubes using a common probabilistic two-phase flow regime basis. Probabilistic two-phase flow maps are experimentally developed for R134a at 25 ºC, 35 ºC, and 50 ºC, R410A at 25 ºC, mass fluxes from 100 to 600 kg/m^2-s, qualities from 0 to 1 in 8.00 mm, 5.43 mm, 3.90 mm, and 1.74 mm I.D. horizontal, smooth, adiabatic tubes in order to extend probabilistic two-phase flow map modeling to single tubes. An automated flow visualization technique, utilizing image recognition software and a new optical method, is developed to classify the flow regimes present in approximately one million captured images. The probabilistic two-phase flow maps developed are represented as continuous functions and generalized based on physical parameters. Condensation heat transfer, void fraction, and pressure drop models are developed for single tubes utilizing the generalized flow regime map developed. The condensation heat transfer model is compared to experimentally obtained condensation data of R134a at 25 ºC in 8.915 mm diameter smooth copper tube with mass fluxes ranging from 100 to 300 kg/m^2-s and a full quality range. The condensation heat transfer, void fraction, and pressure drop models developed are also compared to data found in the literature for a wide range of tube sizes, refrigerants, and flow conditions.

Table of Contents

Page

Abstract iii

List of Figures vii

List of Tables xiv

Chapter 1: Introduction 1

1.1 Nomenclature 1

1.2 Introduction 1

1.3 Status of two-phase flow regime maps 1

1.4 Status of flow regime map based two-phase flow models 3

1.4.1 Condensation heat transfer models 3

1.4.2 Void fraction models 3

1.4.3 Pressure drop models 4

1.5 Simplified flow regimes of the present study 4

1.6 Overview of the thesis 5

References 6

Chapter 2: Probabilistic Determination of Two-Phase Flow Regimes Utilizing an Automated Image Recognition Technique 8

2.1 Abstract 8

2.2 Nomenclature 8

2.3 Introduction 8

2.4 Experimental setup and methods 10

2.4.1 Two-phase flow loop and test section design 10

2.4.2 Flow visualization technique 12

2.4.3 Flow visualization test matrix 13

2.4.4 Image recognition software development 13

2.5 Results 18

2.6 Conclusion and discussion 20

References 20

Chapter 3: Probabilistic Two-Phase Flow Regime Maps in Tubes and Their Generalization to Physical Parameters 22

3.1 Abstract 22

3.2 Nomenclature 22

3.3 Introduction 22

3.4 Literature review 23

3.5 Probabilistic two-phase flow regime maps 25

3.6 Parametric modeling of time fraction data 37

3.7 Generalization of time fraction exponents 38

3.8 Evaluation of generalized flow map for 1.74 mm tube 40

3.9 Conclusion 41

References 41

Chapter 4: Prediction of Two-Phase Condensation in Single Tubes Using Probabilistic Flow Regime Maps 43

- **4.1 Abstract 43**
- **4.2 Nomenclature 43**
- **4.3 Introduction 44**
- **4.4 Literature review 45**
- **4.5 Heat transfer data 49**
- **4.6 Probabilistic two-phase flow map condensation model 52**
  - 4.6.1 Intermittent/liquid flow regime condensation model 52
  - 4.6.2 Stratified flow regime condensation model 53
  - 4.6.3 Annular flow regime condensation model 53
- **4.7 Probabilistic two-phase flow map condensation model evaluation 54**
- **4.8 Conclusion 59**
- **References 59**

Chapter 5: Prediction of Refrigerant Void Fraction in Horizontal Tubes Using Probabilistic Flow Regime Maps 61

- **5.1 Abstract 61**
- **5.2 Nomenclature 61**
- **5.3 Introduction 62**
- **5.4 Literature review 63**
  - 5.4.1 Lockhart-Martinelli parameter based void fraction models 63
  - 5.4.2 Slip ratio based void fraction models 63
  - 5.4.3 Mass flux based void fraction models 64
  - 5.4.4 Other void fraction models 65
- **5.5 Present void fraction model development 68**
  - 5.5.1 Generalized two phase flow map 68
  - 5.5.2 Probabilistic two-phase flow regime map void fraction model 71
  - 5.5.3 Evaluation of the present void fraction model 71
- **5.6 Conclusion 80**
- **References 81**

Chapter 6. Probabilistic Two-Phase Flow Regime Map Modeling Of Refrigerant Pressure Drop In Horizontal Tubes 83

- **6.1 Abstract 83**
- **6.2 Nomenclature 83**
- **6.3 Introduction 84**
- **6.4 Literature review 85**
  - 6.4.1 Two-phase multiplier pressure drop models 85
  - 6.4.2 Other pressure drop models 90
- **6.5 Present pressure drop model development 92**
  - 6.5.1 Generalized two phase flow map 93
  - 6.5.2 Probabilistic two-phase flow regime map pressure drop model 94
  - 6.5.3 Evaluation of the present pressure drop model 95

6.6 Conclusion 106
References 106
Chapter 7: Concluding Remarks 109
7.1 Nomenclature 109
7.2 Conclusion 109
7.3 Future work 111
References 112
Appendix A: Additional Probabilistic Two-Phase Flow Maps 113

List of Figures

Page

Figure 1.1. Steiner (1993) type flow map depiction 2
Figure 1.2. Probabilistic flow map with time fraction curve fits for R410A, 10 ºC, 300 kg/m^2-s in a 6-port 1.54 mm hydraulic diameter microchannel taken from Jassim and Newell (2006) 3
Figure 1.3. Simplified depiction of intermittent, stratified and annular flow 5
Figure 2.1. Depiction of a typical Steiner (1993) type flow map 9
Figure 2.2. Probabilistic flow map with time fraction curve fits for R410A, 10 ºC, 300 kg/m^2-s in a 6-port 1.54 mm hydraulic diameter microchannel taken from Jassim and Newell (2006) 10
Figure 2.3. Two-phase flow loop schematic 11
Figure 2.4. Flow visualization schematic 12
Figure 2.5. Flow visualization pictures of R410A, 3.9 mm I.D. tube, 200 kg/m^2-s, 0.99 quality, and 25 degrees C with a plane diffuse background (left) and with a striped diffuse background (right) 12
Figures 2.6a-c. R134a liquid in 5.43 mm I.D. Glass tube without thresholding, with thresholding, and with a directional Sobel filter applied, respectively 14
Figures 2.7a-d. R410A vapor in 5.43 mm I.D. glass tube without thresholding, with thresholding, with a directional Sobel filter applied, and a magnified view, respectively 14
Figures 2.8a-c. R134a at 200 kg/m^2-s, 2.2% quality, and 25 ºC in 5.43 mm I.D. glass tube without thresholding, with thresholding, and with a directional Sobel filter applied, respectively 14
Figures 2.9a-c. R134a at 100 kg/m^2-s, 44.1% quality, and 25 ºC in 5.43 mm I.D. glass tube without thresholding, with thresholding, and with a directional Sobel filter applied, respectively 15
Figures 2.10a-d. R410A at 300 kg/m^2-s, 79.3% quality, and 25 ºC in 5.43 mm I.D. glass tube without thresholding, with thresholding, with a directional Sobel filter applied, and a magnified view, respectively 15
Figure 2.11. Pixel brightness distribution of the pixel lines in Figure 2.7d of R410A vapor in 5.43 mm I.D. glass tube with a directional Sobel filter applied 16
Figure 2.12. pixel brightness distribution of the pixel lines in Figure 2.10d of R410A at 300 kg/m^2-s, 79.3% quality, and 25 ºC in 5.43 mm I.D. glass tube with a directional Sobel filter applied 17
Figure 2.13. Probabilistic two-phase flow regime map for R410A, 100 kg/m^2-s, 25 ºC, adiabatic 3.90 mm I.D. tube 19
Figure 2.14. Probabilistic two-phase flow regime map for R410A, 200 kg/m^2-s, 25 ºC, adiabatic 3.90 mm I.D. tube 19
Figure 2.15. Probabilistic two-phase flow regime map for R410A, 300 kg/m^2-s, 25 ºC, adiabatic 3.90 mm I.D. tube 19
Figure 2.16. Probabilistic two-phase flow regime map for R410A, 400 kg/m^2-s, 25 ºC, adiabatic 3.90 mm I.D. tube 20
Figure 3.1. Probabilistic flow map with time fraction curve fits for R410A, 10 ºC, 300 kg/m^2-s in a 6-port 1.54 mm hydraulic dia. microchannel taken from Jassim and Newell (2006) 24
Figure 3.2. Flow visualization schematic from Jassim et al. (2006a) 25
Figure 3.3 Two-phase flow loop schematic from Jassim et al. (2006a) 25

Figure 3.4. Probabilistic flow map with generalized time fraction curve fits for 8.00 mm diameter tube, R134a, 25 ºC, 100 kg/m^2-s 26
Figure 3.5. Probabilistic flow map with generalized time fraction curve fits for 8.00 mm diameter tube, R134a, 25 ºC, 200 kg/m^2-s 26
Figure 3.6. Probabilistic flow map with generalized time fraction curve fits for 8.00 mm diameter tube, R134a, 25 ºC, 300 kg/m^2-s 27
Figure 3.7. Probabilistic flow map with generalized time fraction curve fits for 8.00 mm diameter tube, R410A, 25 ºC, 100 kg/m^2-s 27
Figure 3.8. Probabilistic flow map with generalized time fraction curve fits for 8.00 mm diameter tube, R410A, 25 ºC, 200 kg/m^2-s 27
Figure 3.9. Probabilistic flow map with generalized time fraction curve fits for 8.00 mm diameter tube, R410Aa, 25 ºC, 300 kg/m^2-s 28
Figure 3.10. Probabilistic flow map with generalized time fraction curve fits for 8.00 mm diameter tube, R410Aa, 25 ºC, 400 kg/m^2-s 28
Figure 3.11. Probabilistic flow map with generalized time fraction curve fits for 5.43 mm diameter tube, R134a, 25 ºC, 100 kg/m^2-s 28
Figure 3.12. Probabilistic flow map with generalized time fraction curve fits for 5.43 mm diameter tube, R134a, 25 ºC, 200 kg/m^2-s 29
Figure 3.13. Probabilistic flow map with generalized time fraction curve fits for 5.43 mm diameter tube, R134a, 25 ºC, 300 kg/m^2-s 29
Figure 3.14. Probabilistic flow map with generalized time fraction curve fits for 5.43 mm diameter tube, R134a, 25 ºC, 400 kg/m^2-s 29
Figure 3.15. Probabilistic flow map with generalized time fraction curve fits for 5.43 mm diameter tube, R410A, 25 ºC, 100 kg/m^2-s 30
Figure 3.16. Probabilistic flow map with generalized time fraction curve fits for 5.43 mm diameter tube, R410A, 25 ºC, 200 kg/m^2-s 30
Figure 3.17. Probabilistic flow map with generalized time fraction curve fits for 5.43 mm diameter tube, R410A, 25 ºC, 300 kg/m^2-s 30
Figure 3.18. Probabilistic flow map with generalized time fraction curve fits for 5.43 mm diameter tube, R410A, 25 ºC, 400 kg/m^2-s 31
Figure 3.19. Probabilistic flow map with generalized time fraction curve fits for 3.90 mm diameter tube, R134a, 25 ºC, 100 kg/m^2-s 31
Figure 3.20. Probabilistic flow map with generalized time fraction curve fits for 3.90 mm diameter tube, R134a, 25 ºC, 200 kg/m^2-s 31
Figure 3.21. Probabilistic flow map with generalized time fraction curve fits for 3.90 mm diameter tube, R134a, 25 ºC, 300 kg/m^2-s 32
Figure 3.22. Probabilistic flow map with generalized time fraction curve fits for 3.90 mm diameter tube, R134a, 25 ºC, 400 kg/m^2-s 32
Figure 3.23. Probabilistic flow map with generalized time fraction curve fits for 3.90 mm diameter tube, R410A, 25 ºC, 100 kg/m^2-s 32

Figure 3.24. Probabilistic flow map with generalized time fraction curve fits for 3.90 mm diameter tube, R410A, 25 ºC, 200 kg/m^2-s 33
Figure 3.25. Probabilistic flow map with generalized time fraction curve fits for 3.90 mm diameter tube, R410A, 25 ºC, 300 kg/m^2-s 33
Figure 3.26. Probabilistic flow map with generalized time fraction curve fits for 3.90 mm diameter tube, R410A, 25 ºC, 400 kg/m^2-s 33
Figure 3.27. Probabilistic flow map with generalized time fraction curve fits for 1.74 mm diameter tube, R134a, 25 ºC, 400 kg/m^2-s..........34
Figure 3.28. Probabilistic flow map with generalized time fraction curve fits for 1.74 mm diameter tube, R134a, 25 ºC, 500 kg/m^2-s..........34
Figure 3.29. Probabilistic flow map with generalized time fraction curve fits for 1.74 mm diameter tube, R134a, 25 ºC, 600 kg/m^2-s..........34
Figure 3.30. Probabilistic flow map with generalized time fraction curve fits for 1.74 mm diameter tube, R410A, 25 ºC, 400 kg/m^2-s 35
Figure 3.31. Probabilistic flow map with generalized time fraction curve fits for 1.74 mm diameter tube, R410A, 25 ºC, 500 kg/m^2-s 35
Figure 3.32. Probabilistic flow map with generalized time fraction curve fits for 1.74 mm diameter tube, R410A, 25 ºC, 600 kg/m^2-s 35
Figure 3.33. Qualitative trend observed as the intermittent/liquid flow regime time fraction curve increases (moves from dashed line to solid line)..........36
Figure 3.34. Qualitative trend observed as the stratified flow regime time fraction curve increases (moves from dashed line to solid line)..........36
Figure 3.35. Qualitative trend observed as the annular flow regime time fraction curve increases (moves from dashed line to solid line)..........36
Figure 3.36. Probabilistic flow map with time fraction curve fits for 8.00 mm diameter tube, R134a, 25 ºC, 300 kg/m^2-s..........37
Figure 3.37. The intermittent/liquid time fraction curve fit constants “i” vs. the dimensionless group *Xi*. 39
Figure 3.38. The stratified time fraction curve fit constants “s” vs. the dimensionless group *Xs*...........40
Figure 4.1. Steiner (1993) type flow map depiction 46
Figure 4.2. Probabilistic flow map with time fraction curve fits for R410A, 10 ºC, 300 kg/m^2-s in a 6-port 1.54 mm hydraulic dia. microchannel taken from Jassim and Newell (2006)...........48
Figure 4.3. Two-phase flow loop schematic..........48
Figure 4.4. Probabilistic flow map with generalized time fraction curve fits for 8.00 mm diameter tube, R134a, 25 ºC, 300 kg/m^2-s. 48
Figure 4.5. Heat transfer test section design..........50
Figure 4.6. Sub-cooled liquid R134a heat transfer in 8.915 mm diameter smooth tube with heat addition varying from 2,600 to 5,600 W/m^2-K..........50
Figure 4.7. Average quality vs. condensation heat transfer coefficients for R134a, 25 ºC, 100 kg/m^2-s, in 8.915 mm I.D. smooth tube, 4600-5400 W/m^2..........51

Figure 4.8. Average quality vs. condensation heat transfer coefficients for R134a, 25 ºC, 200 kg/m^2-s, in 8.915 mm I.D. smooth tube, 4700-5600 W/m^2 51
Figure 4.9. Average quality vs. condensation heat transfer coefficients for R134a, 25 ºC, 300 kg/m^2-s, in 8.915 mm I.D. smooth tube, 4700-5500 W/m^2 52
Figure 4.10. Experimental vs. predicted condensation heat transfer for R11 data outlined in Table 4.1 55
Figure 4.11. Experimental vs. predicted condensation heat transfer for R12 data outlined in Table 4.1 55
Figure 4.12. Experimental vs. predicted condensation heat transfer for R134a data outlined in Table 4.1 56
Figure 4.13. Experimental vs. predicted condensation heat transfer for R22 data outlined in Table 4.1 56
Figure 4.15. Experimental vs. predicted condensation heat transfer for R32/R125 (60/40% by weight) data outlined in Table 4.1 57
Figure 4.16. Experimental vs. predicted condensation heat transfer for all data outlined in Table 4.1 58
Figure 5.1. Probabilistic flow map with time fraction curve fits for R410A, 10 ºC, 300 kg/m^2-s in a 6-port 1.54 mm hydraulic dia. microchannel taken from Jassim and Newell (2006). 67
Figure 5.2. Steiner (1993) type flow map depiction 68
Figure 5.3. Two-phase flow loop schematic 70
Figure 5.4. Probabilistic flow map with generalized time fraction curve fits for 8.00 mm diameter tube, R134a, 25 ºC, 300 kg/m^2-s. 70
Figure 5.5. Void fraction data summarized in Table 5.1 vs. void fraction predicted by present model and separated by refrigerant 72
Figure 5.6. Void fraction data summarized in Table 5.1 vs. void fraction predicted by Wallis (1969) and Domanski (1983) and separated by refrigerant 73
Figure 5.7. Void fraction data summarized in Table 5.1 vs. void fraction predicted by Zivi (1964) and separated by refrigerant 73
Figure 5.8. Void fraction data summarized in Table 5.1 vs. void fraction predicted by Smith (1969) and separated by refrigerant 74
Figure 5.9. Void fraction data summarized in Table 5.1 vs. void fraction predicted by Rigot (1973) and separated by refrigerant 74
Figure 5.10. Void fraction data summarized in Table 5.1 vs. void fraction predicted by present model Rouhani and Axelsson (1970) and separated by refrigerant 75
Figure 5.11. Void fraction data summarized in Table 5.1 vs. void fraction predicted by El Hajal et al. (2003) and separated by refrigerant 75
Figure 5.12. Void fraction data summarized in Table 5.1 vs. void fraction predicted by Taitel and Barnea (1990) and separated by refrigerant 76
Figure 5.13. Void fraction data summarized in Table 5.1 vs. void fraction predicted by Graham (1998) and separated by refrigerant 76
Figure 5.14. Void fraction data summarized in Table 5.1 vs. void fraction predicted by Armand (1946) and separated by refrigerant 77
Figure 5.15. Void fraction data summarized in Table 5.1 vs. void fraction predicted by Premoli (1971) and separated by refrigerant 77

Figure 5.16. Void fraction data summarized in Table 5.1 vs. void fraction predicted by Tandon (1985) and separated by refrigerant 78
Figure 5.17. Void fraction data summarized in Table 5.1 vs. void fraction predicted by Yashar et al. (2001) and separated by refrigerant........ 78
Figure 5.18. Void fraction data summarized in Table 5.1 vs. void fraction predicted by the homogeneous model and separated by refrigerant........ 79
Figure 5.19. Void fraction data summarized in Table 5.1 vs. void fraction predicted by present model and separated by heat transfer type 80
Figure 6.1. Probabilistic flow map with time fraction curve fits for R410A, 10 ºC, 300 kg/m^2-s in a 6-port 1.54 mm hydraulic dia. microchannel taken from Jassim and Newell (2006)......... 92
Figure 6.2. Steiner (1993) type flow map depiction 92
Figure 6.3. Two-phase flow loop schematic from Jassim et al. (2006c)........ 94
Figure 6.4. Probabilistic flow map with generalized time fraction curve fits for 8.00 mm diameter tube, R134a, 25 ºC, 300 kg/m^2-s from Jassim et al. (2006b) 94
Figure 6.5. Frictional pressure drop data summarized in Table 6.1 vs. pressure drop predicted by present model and separated by refrigerant........ 97
Figure 6.6. Frictional pressure drop data summarized in Table 6.1 vs. pressure drop predicted by Friedel (1979) and separated by refrigerant........ 97
Figure 6.7. Frictional pressure drop data summarized in Table 6.1 vs. pressure drop predicted by Souza et al. (1993) and separated by refrigerant........ 98
Figure 6.8. Frictional pressure drop data summarized in Table 6.1 vs. pressure drop predicted by modified Souza et al. (1993) and separated by refrigerant........ 98
Figure 6.9. Frictional pressure drop data summarized in Table 6.1 vs. pressure drop predicted by Souza and Pimenta (1995) and separated by refrigerant........ 99
Figure 6.10. Frictional pressure drop data summarized in Table 6.1 vs. pressure drop predicted by modified Souza and Pimenta (1995) and separated by refrigerant........ 99
Figure 6.11. Frictional pressure drop data summarized in Table 6.1 vs. pressure drop predicted by Jung and Radermacher (1989) and separated by refrigerant........ 100
Figure 6.12. Frictional pressure drop data summarized in Table 6.1 vs. pressure drop predicted by Chisholm (1973) and separated by refrigerant........ 100
Figure 6.13. Frictional pressure drop data summarized in Table 6.1 vs. pressure drop predicted by Grönnerud (1979) and separated by refrigerant........ 101
Figure 6.14. Frictional pressure drop data summarized in Table 6.1 vs. pressure drop predicted by Niño’s (2002) annular flow model and separated by refrigerant........ 101
Figure 6.15. Frictional pressure drop data summarized in Table 6.1 vs. pressure drop predicted by Zhang and Kwon (1999) and separated by refrigerant 102
Figure 6.16. Frictional pressure drop data summarized in Table 6.1 vs. pressure drop predicted by Tran et al. (2000) and separated by refrigerant........ 102
Figure 6.17. Frictional pressure drop data summarized in Table 6.1 vs. pressure drop predicted by McAdams (1954) and separated by refrigerant........ 103

Figure 6.18. Frictional pressure drop data summarized in Table 6.1 vs. pressure drop predicted by Niño's (2002) intermittent flow model and separated by refrigerant 103
Figure 6.19. Frictional pressure drop data summarized in Table 6.1 vs. pressure drop predicted by Adams (2003) and separated by refrigerant 104
Figure 6.20. Frictional pressure drop data summarized in Table 6.1 vs. pressure drop predicted by Müller-Steinhager and Heck (1986) and separated by refrigerant 104
Figure 6.21. Frictional pressure drop data summarized in Table 6.1 vs. pressure drop predicted by present model and separated by heat transfer conditions 106
Figure A.1. Probabilistic flow map with generalized time fraction curve fits for 8.00 mm diameter tube, R134a, 35 ºC, 100 kg/m^2-s....113
Figure A.2. Probabilistic flow map with generalized time fraction curve fits for 8.00 mm diameter tube, R134a, 35 ºC, 200 kg/m^2-s....113
Figure A.3. Probabilistic flow map with generalized time fraction curve fits for 8.00 mm diameter tube, R134a, 35 ºC, 300 kg/m^2-s....114
Figure A.4. Probabilistic flow map with generalized time fraction curve fits for 8.00 mm diameter tube, R134a, 49.7 ºC, 100 kg/m^2-s....114
Figure A.5. Probabilistic flow map with generalized time fraction curve fits for 8.00 mm diameter tube, R134a, 49.7 ºC, 200 kg/m^2-s....115
Figure A.6. Probabilistic flow map with generalized time fraction curve fits for 8.00 mm diameter tube, R134a, 49.7 ºC, 300 kg/m^2-s....115
Figure A.7. Probabilistic flow map with generalized time fraction curve fits for 5.43 mm diameter tube, R134a, 35 ºC, 100 kg/m^2-s 116
Figure A.8. Probabilistic flow map with generalized time fraction curve fits for 5.43 mm diameter tube, R134a, 35 ºC, 200 kg/m^2-s 116
Figure A.9. Probabilistic flow map with generalized time fraction curve fits for 5.43 mm diameter tube, R134a, 35 ºC, 300 kg/m^2-s 117
Figure A.10. Probabilistic flow map with generalized time fraction curve fits for 5.43 mm diameter tube, R134a, 35 ºC, 400 kg/m^2-s....117
Figure A.11. Probabilistic flow map with generalized time fraction curve fits for 5.43 mm diameter tube, R134a, 49.7 ºC, 100 kg/m^2-s....118
Figure A.12. Probabilistic flow map with generalized time fraction curve fits for 5.43 mm diameter tube, R134a, 49.7 ºC, 200 kg/m^2-s....118
Figure A.13. Probabilistic flow map with generalized time fraction curve fits for 5.43 mm diameter tube, R134a, 49.7 ºC, 300 kg/m^2-s....119
Figure A.14. Probabilistic flow map with generalized time fraction curve fits for 3.90 mm diameter tube, R134a, 35 ºC, 100 kg/m^2-s....119
Figure A.15. Probabilistic flow map with generalized time fraction curve fits for 3.90 mm diameter tube, R134a, 35 ºC, 200 kg/m^2-s....120
Figure A.16. Probabilistic flow map with generalized time fraction curve fits for 3.90 mm diameter tube, R134a, 35 ºC, 300 kg/m^2-s....120

Figure A.17. Probabilistic flow map with generalized time fraction curve fits for 3.90 mm diameter tube, R134a, 35 ºC, 400 kg/m^2-s....121

Figure A.18. Probabilistic flow map with generalized time fraction curve fits for 3.90 mm diameter tube, R134a, 49.7 ºC, 100 kg/m^2-s....121

Figure A.19. Probabilistic flow map with generalized time fraction curve fits for 3.90 mm diameter tube, R134a, 49.7 ºC, 200 kg/m^2-s....122

Figure A.20. Probabilistic flow map with generalized time fraction curve fits for 3.90 mm diameter tube, R134a, 49.7 ºC, 300 kg/m^2-s....122

Figure A.21. Probabilistic flow map with generalized time fraction curve fits for 3.90 mm diameter tube, R134a, 49.7 ºC, 400 kg/m^2-s....123

Figure A.22. Probabilistic flow map with generalized time fraction curve fits for 1.74 mm diameter tube, R134a, 35 ºC, 400 kg/m^2-s....123

Figure A.23. Probabilistic flow map with generalized time fraction curve fits for 1.74 mm diameter tube, R134a, 35 ºC, 500 kg/m^2-s....124

Figure A.24. Probabilistic flow map with generalized time fraction curve fits for 1.74 mm diameter tube, R134a, 35 ºC, 600 kg/m^2-s....124

List of Tables

Page

Table 2.1. Test section and stripe dimensions 11
Table 4.1. Condensation data pool used to compare the present models with other models in the literature 55
Table 4.2. Statistical comparison of condensation models with experimental data using different refrigerants (in %) 58
Table 5.1. Void fraction data used to compare the present models with other models in the literature....................... 71
Table 5.2. Statistical comparison of void fraction models with experimental data separated by refrigerants (in %) 79
Table 6.1. Pressure drop data used to compare the present models with other models in the literature 95
Table 6.2. Statistical comparison of pressure drop models with experimental data separated by refrigerants (in %) 105

Chapter 1: Introduction

1.1 Nomenclature

dP	pressure drop (kPa)
dz	unit length (m)
F	observed time fraction (-)

Greek symbols

α	void fraction (-)

Subscripts

liq	pertaining to the liquid flow regime
int	pertaining to the intermittent flow regime
vap	pertaining to the vapor flow regime
ann	pertaining to the annular flow regime

1.2 Introduction

Two-phase vapor-liquid flow in tubes is found in numerous residential, commercial, and industrial applications. These applications include refrigeration, air conditioning, power generation, and chemical processing. The prediction of two-phase heat transfer, void fraction, and pressure drop is important in the design and optimization of these systems. Prediction of heat transfer is used to determine the total length of tube required which is important in optimizing the size and cost of heat exchangers. Prediction of void fraction, the fraction of the heat exchanger volume occupied by vapor, is used to predict the required charge of a system. Void fraction is also often used in heat transfer and pressure drop models. Prediction of pressure drop is required for determining pumping power and component stresses.

The present study will focus on the development of probabilistic two-phase flow regime map modeling of condensation heat transfer, void fraction and pressure drop in single, smooth, horizontal tubes on a consistent flow regime basis.

1.3 Status of two-phase flow regime maps

The physics involved in two-phase flow is very complicated because often the liquid and vapor phases are turbulent with both interphase and tube interface interactions. Consequently, many investigators, such as Garimella (2004), Garimella et al. (2003), Coleman and Garimella (2003), El Hajal et al. (2003), Thome et al. (2003), Didi et al. (2002), Zurcher et al. (2002a&b), Mandhane et al. (1974), and Baker (1954) have described the importance of using experimentally obtained flow regime information with physically relevant characteristic models for predicting of flow field parameters. As a result, much attention has been directed towards developing two-phase flow regime maps. There are three main types of two-phase flow maps in the literature: Baker/Mandhane type, Taitel-Dukler type, and Steiner (1993) type. Baker (1954) developed one of the first two-phase flow regime maps with air-water and air-oil data in large tubes. Baker (1954) used superficial vapor mass flux times a fluid property scaling factor on the vertical axes and superficial liquid mass flux times a different fluid property scaling factor on the horizontal axis. Mandhane et al. (1974) later developed a similar map with air water data, but used superficial gas and liquid velocities on the horizontal and vertical axes, respectively. Dobson and Chato (1998) then made modifications to the flow map of Mandhane et al. (1974) by multiplying the axis by the square root of the vapor to air density ratio.

Taitel-Dukler (1976) developed a mechanistic type flow map with the Lockhart-Martinelli parameter on the horizontal axis and a modified Froude rate times a transition criteria on the vertical axis. Most of the recent two-phase flow regime maps found in the literature are Steiner (1993) type flow maps of the form found in Figure 1.1. Garimella (2004), Garimella et al. (2003), El Hajal et al. (2003), Thome et al. (2003), and Didi et al. (2002) all use similar Steiner style flow maps with quality on the horizontal axis and mass flux on the vertical axis. All three types of flow maps indicate a particular flow regime at any given flow condition with lines dividing the transitions. This seems to lack a physical basis as Coleman and Garimella (2003) and El Hajal et al. (2003) indicate that more than one flow regime seems to exist near the boundaries. This poses a problem when attempting to develop pressure drop, void fraction, and heat transfer models that incorporate all flow regimes without having discontinuities at the boundaries. In addition, it is difficult to implement this type of flow map into a model because the flow maps cannot readily be represented by continuous functions for all quality ranges. The presence of more than one flow regime at the flow map boundaries seems to indicate that a probabilistic representation of the flow regimes may be better suited in describing the flow.

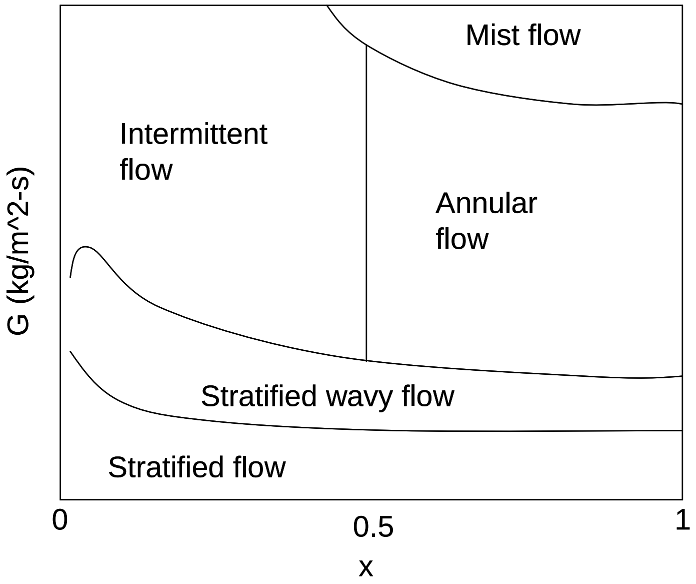

Figure 1.1. Steiner (1993) type flow map depiction

Niño (2002) presented two-phase flow mapping in horizontal microchannels in a distinctly different manner than found in the rest of the literature indicated above. Instead of definitively categorizing the flow regime at a given mass flux and quality, they recorded the time fraction in which each flow regime was observed in each channel at a given mass flux and quality. This was accomplished by obtaining numerous pictures of a given mass flux and quality at evenly spaced time intervals. Jassim and Newell (2006) curve fit the time fraction data obtained by Niño (2002) with continuous functions over the entire quality range that have physically correct limits. A probabilistic two-phase flow regime map for a multi-port microchannel tube from Jassim and Newell (2006) with time fraction data and curve fits can be seen in Figure 1.2.

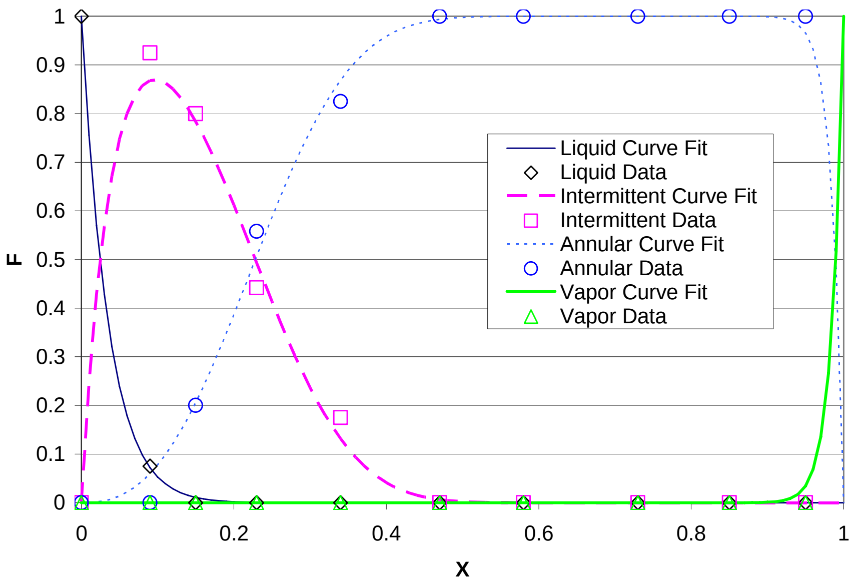

Figure 1.2. Probabilistic flow map with time fraction curve fits for R410A, 10 ºC, 300 kg/m^2-s in a 6-port 1.54 mm hydraulic diameter microchannel taken from Jassim and Newell (2006)

1.4 Status of flow regime map based two-phase flow models

The majority of the two-phase flow models in the literature before 1990 were developed for particular flow regimes or flow conditions. After 1990, however, we find the incorporation of flow regime maps into two-phase flow models in order to provide accurate predictions for multiple flow regimes for a wide range of fluid properties and flow conditions.

1.4.1 Condensation heat transfer models

Numerous flow regime map based two-phase flow heat transfer models were recently developed in tubes in order to predict condensation heat transfer in multiple flow regimes. Haraguchi et al. (1994), Dobson and Chato (1998) were some of the first to present flow regime map based condensation heat transfer models to predict heat transfer in multiple flow regimes. Cavallini et al. (2002) developed a similar flow regime map based condensation model but based it on a large database consisting of over 2000 refrigerant condensation data points with 9 different refrigerants in 3.1 to 21.4 mm diameter tubes. Thome et al. (2003) then accounted for more flow regimes and verified their model with a database of 15 different fluids that includes 1850 refrigerant data points and 2771 hydrocarbon data points. Cavallini et al. (2003) then modified the Cavallini et al. (2002) model to eliminate discontinuities at flow regime boundaries. All of these models use traditional style flow maps which can lead to discontinuities at flow regime boundaries. Cavallini et al. (2002), Thome et al. (2003), Cavallini et al. (2003) models use interpolations at the flow regime boundaries to eliminate the discontinuities, but these models are seen to be very complicated due to the nature of the flow regime maps used, which are not readily represented by continuous functions.

1.4.2 Void fraction models

Recently, Jassim and Newell (2006) developed a probabilistic two-phase flow map void fraction model for R410A, R134a, and air water in 1.54 mm 6-port microchannels and is given in Equation 1.1.

$$\alpha_{total} = F_{liq}\alpha_{liq} + F_{\text{int}}\alpha_{\text{int}} + F_{vap}\alpha_{vap} + F_{ann}\alpha_{ann} \tag{1.1}$$

The void fraction is simply predicted as the sum of the products of the time fractions and void fraction models representative of the respective flow regimes. This model does not contain discontinuities because of the nature of the probabilistic flow regime maps used, and it allows for easy replacement of the flow regime models as more accurate models are identified for each flow regime. No other flow regime map based void fraction models could be found in the literature.

1.4.3 Pressure drop models

Jassim and Newell (2006) developed a probabilistic two-phase flow map pressure drop model for R410A, R134a, and air water in 1.54 mm 6-port microchannels on the same time fraction basis as their void fraction model and is given in Equation 1.2.

$$\left(\frac{dP}{dz}\right)_{total} = F_{liq}\left(\frac{dP}{dz}\right)_{liq} + F_{\text{int}}\left(\frac{dP}{dz}\right)_{\text{int}} + F_{vap}\left(\frac{dP}{dz}\right)_{vap} + F_{ann}\left(\frac{dP}{dz}\right)_{ann} \tag{1.2}$$

Like Jassim and Newell's (2006) void fraction model, their pressure drop model does not have discontinuities and it allows for easy replacement of the flow regime models as more accurate models are identified for each flow regime. No other flow regime map based pressure drop models could be found in the literature, however some developments were made in this direction. Didi et al. (2002) sought to determine which existing pressure drop model is most accurate for a given flow regime in large tubes. Garimella (2004), Garimella et al. (2003), and Chung and Kawaji (2004) developed flow regime based pressure drop models of the intermittent two-phase flow regime in microchannels, which attempt to incorporate the physics of the flow into the model. These models require the use of a flow regime map to determine the flow regime that exists and require flow visualization data on the slug rate.

1.5 Simplified flow regimes of the present study

Single tubes of approximately 3 mm in diameter and larger are found to contain a stratified flow regime which is absent in the 1.54 mm hydraulic diameter microchannels of Nino (2002). Damianides and Westwater (1988) support this observation because they indicate that the transition from "microchannel" behavior to "large tube" behavior occurs in the 3 mm tube diameter range. Furthermore, vapor only flow is not present below a quality of 100% in single tubes. Consequently, the flow regime maps and two-phase flow models developed by Jassim and Newell (2006) are not applicable to large tubes with hydraulic diameters above 3 mm.

Many flow regimes have been identified in the literature for single horizontal large tubes, however three main flow regimes are evident: intermittent, stratified, and annular flow as depicted in Figure 1.3. The intermittent flow regime is characteristic of broken vapor sections or bubbles where the vapor does not have a clear path to flow. The stratified flow regime has liquid at the bottom of the tube and mostly vapor at the top of the tube. The annular flow regime has a relatively uniform rough turbulent liquid film around the entire tube wall with an unobstructed path for the vapor to flow. The present study will focus on these three flow regimes with their given definitions.

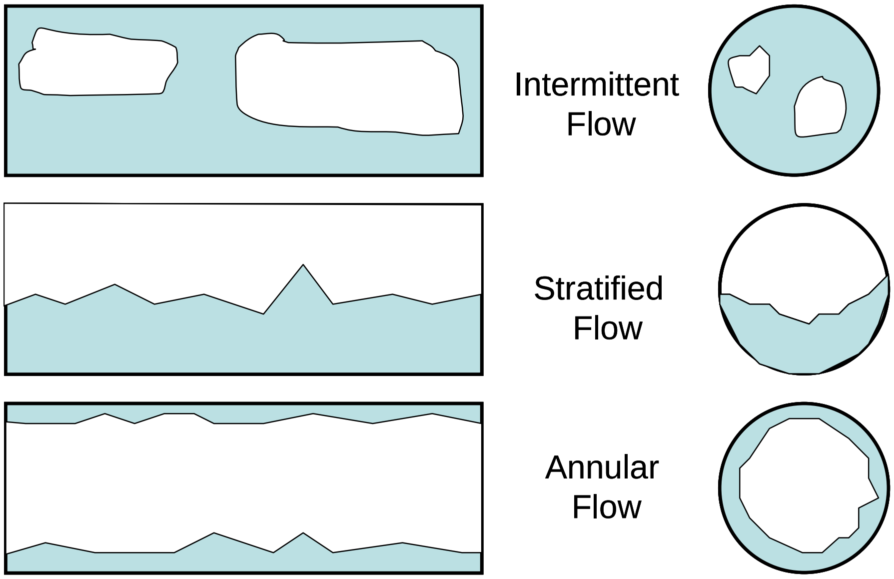

Figure 1.3. Simplified depiction of intermittent, stratified and annular flow

1.6 Overview of the thesis

Probabilistic two-phase flow regime map modeling is developed for large tubes in the present study as a common means of predicting condensation heat transfer, void fraction, and pressure drop. Chapters 2 through 6 of this thesis are written as self-contained documents covering the primary research activities of this investigation.

Chapter 2, referred to as Jassim et al. (2006a), describes the experimental facilities used to obtain time fraction data necessary to create probabilistic flow regime maps for a range of tube sizes, fluid properties, and flow conditions. New methods for automated flow regime detection have been developed and are discussed. The new automated flow regime detection system and software algorithms are based on relatively inexpensive “board camera” technology, providing other researchers with a means for characterizing complex flow fields.

Chapter 3, referred to as Jassim et al. (2006b), describes the techniques developed for representing the flow regime data as continuous functions. Additionally, the development of physically based parameters that generalizes the flow regime model for several refrigerants, tube diameters, mass fluxes, saturation conditions, and qualities are presented.

A probabilistic two-phase flow regime map condensation heat transfer model is developed in Chapter 4, referred to as Jassim et al. (2006c), using the generalized flow regime map developed in Chapter 3. The present model and other condensation heat transfer models found in the literature are compared to experimentally obtained R134a condensation data in 8.915 mm diameter smooth tube and a database of refrigerant condensation heat transfer results from independent sources.

Chapter 5, referred to as Jassim et al. (2006d), describes the development of a probabilistic two-phase flow regime map void fraction model using the same generalized flow regime map developed in Chapter 3. The new flow regime void fraction prediction model is compared to a database of refrigerant void fraction under condensation, adiabatic, and evaporation conditions along with models found in the literature.

A probabilistic two-phase flow regime map pressure drop model is developed in Chapter 6, referred to as Jassim et al. (2006e), also using the generalized flow regime map developed in Chapter 3. The new pressure drop model is compared to a database of refrigerant pressure drop under condensation, adiabatic, and evaporation conditions along with pressure drop models found in the literature.

Chapter 7 contains concluding remarks with perspectives related to improvement of the modeling approach developed in this research.

References

Baker, O., “Simultaneous Flow of Oil and Gas,” *Oil and Gas Journal* 53 (1954) 185-195.

Cavallini, A., G. Censi, D. Del Col, L. Doretti, G.A. Longo, and L. Rossetto, “In-Tube Condensation of Halogenated Refrigerants,” *ASHRAE Transactions*, 108:1 (2002) 146-161.

Cavallini, A., G. Censi, D. Del Col, L. Doretti, G.A. Longo, L. Rossetto, and C. Zilio, “Condensation Inside and Outside Smooth and Enhanced Tubes - A Review of Recent Research,” *International Journal of Refrigeration*, Vol. 26:1, 373-392, 2003.

Chung, P.M.-Y. and M. Kawaji, “The Effect of Channel Diameter on Adiabatic Two-Phase Flow Characteristics in Microchannels,” *International Journal of Multiphase Flow* 30 (2004) 735-761.

Coleman, J.W., S.Garimella, “Two-Phase Flow Regimes in Round, Square and Rectangular Tubes during Condensation of Refrigerant R134a,” *International Journal of Refrigeration* 26 (2003) 117-128.

Diamanides, C. and J.W. Westwater, “Two-phase Flow Patterns in a Compact Heat Exchanger and in Small Tubes,” *Proceedings of the 2nd. U.K. National Conference on Heat Transfer*, Glasgow, Scotland, (2) (1988) 1257-1268.

Didi, M.B. and N. Kattan, J.R. Thome, “Prediction of Two-Phase Pressure Gradients of Refrigerants in Horizontal Tubes,” *International Journal of Refrigeration* 25 (2002) 935-947.

Dobson, M. K. and J.C. Chato, “Condensation in Smooth Horizontal Tubes,” *Journal of Heat Transfer* 120 (1998) 245-252.

El Hajal, J., J.R. Thome, and A. Cavalini, “Condensation in Horizontal Tubes, Part 1: Two-Phase Flow Pattern Map,” *International Journal of Heat and Mass Transfer* 46 (2003) 3349-3363.

Garimella, S., “Condensation Flow Mechanisms in Microchannels: Basis for Pressure Drop and Heat Transfer Models,” *Heat Transfer Engineering* 25:3 (2004) 104-116.

Garimella, S., J.D. Killion, and J.W. Coleman, “An Experimentally Validated Model for Two-Phase Pressure Drop in the Intermitent Flow Regime for Noncircular Microchannels,” *Journal of Fluids Engineering* 125 (2003) 887-894.

Haraguchi, H., S. Koyama, and T. Fujii, “Condensation of Refrigerants HCFC 22, HFC 134a, and HCFC 123 in a Horizontal Smooth Tube (2nd report, Proposal of Empirical Expressions for Local Heat Transfer Coefficient),” *Trans. JSME* 60(574) (1994) 245-252.

Jassim, E. W., T. A. Newell, and J. C. Chato, “Probabilistic Two-Phase Flow Regime Maps in Tubes and Their Generalization to Physical Parameters,” to be submitted to the International Journal of Heat and Mass Transfer (2006b).

Jassim, E. W., T. A. Newell, and J. C. Chato, “Prediction of Refrigerant Void Fraction in Horizontal Tubes using Probabilistic Flow Regime Maps,” to be submitted to the International Journal of Heat and Mass Transfer (2006d).

Jassim, E. W., T. A. Newell, and J. C. Chato, “Prediction of Two-Phase Condensation in Single Tubes using Probabilistic Flow Regime Maps,” to be submitted to the International Journal of Heat and Mass Transfer (2006c).

Jassim, E. W., T. A. Newell, and J. C. Chato, “Probabilistic Determination of Two-Phase Flow Regimes Utilizing an Automated Image Recognition Technique,” to be submitted to Experiments In Fluids (2006a)

Jassim, E.W. and T. A. Newell. “Prediction of Two-Phase Pressure Drop and Void Fraction in Microchannels using Probabilistic Flow Regime Mapping,” *International Journal of Heat and Mass Transfer* 49 (2006) 2446-2457.

Mandhane, J.M., G.A. Gregory, and K. Aziz, “A Flow Pattern Map for Gas-Liquid Flow in Horizontal and Inclined Pipes,” *International Journal of Multiphase Flow* 1 (1974) 537-553.

Niño, V.G. “Characterization of Two-phase Flow in Microchannels,” Ph.D. Thesis, University of Illinois, Urbana-Champaign, IL, 2002.

Steiner, D., “Heat Transfer to Boiling Saturated Liquids,” VDI-Wārmeatlas (VDI Heat Atlas), Verein Deutscher Ingenieure, VDI-Gesellschaft Verfahrenstechnik und Chemieingenieurwesen (GCV), Dū sseldorf, Chapter Hbb (1993).

Taitel, Y. and A.E. Dukler, “A Model for Predicting Flow Regime Transitions in Horizontal and Near Horizontal Gas-Liquid Flow,” *American Institute of Chemical Engineering Journal*, 22 (1976) 47-55.

Thome, J.R., J. El Hajal, and A. Cavalini, “Condensation in Horizontal Tubes, Part 2: New Heat Transfer Model Based on Flow Regimes,” *International Journal of Heat and Mass Transfer* 46 (2003) 3365-3387.

Zurcher, O., D. Farvat, and J.R Thome, “Evaporation of Refrigerants in a Horizontal Tube: And Improved Flow Pattern Dependent Heat Transfer Model Compared to Ammonia Data,” *International Journal of Heat and Mass Transfer* 45 (2002) 303-317.

Zurcher, O., D. Farvat, and J.R. Thome, “Development of a Diabatic Two-Phase Flow Pattern Map for Horizontal Flow Boiling,” *International Journal of Heat and Mass Transfer* 45 (2002) 291-301.

Chapter 2: Probabilistic Determination of Two-Phase Flow Regimes Utilizing an Automated Image Recognition Technique

2.1 Abstract

Probabilistic two-phase flow maps are experimentally developed for R134a at 25, 35, and 50 ºC, R410A at 25 ºC, mass fluxes from 100 to 600 kg/m^2-s, qualities from 0 to 1 in 8.00 mm, 5.43 mm, 3.90 mm, and 1.74 mm I.D. single, smooth, adiabatic, horizontal tubes in order to extend the probabilistic two-phase flow map modeling techniques developed in the literature for multi-port microchannels to single tubes. A new web camera based flow visualization technique utilizing an illuminated diffuse striped background was utilized to enhance images, detect fine films, and aid in the automated image recognition process developed in the present study. The average time fraction classification error is less than 0.6%.

2.2 Nomenclature

dP	pressure drop (Pa)
dz	unit length (m)
F	observed time fraction (-)
x	flow quality (-)

Subscripts

ann	pertaining to the annular flow regime
liq	pertaining to the liquid flow regime
int	pertaining to the intermittent flow regime
vap	pertaining to the vapor flow regime

Greek symbols

α	void fraction (-)

2.3 Introduction

Flow regime maps developed from flow visualization observations are commonly used or developed in the literature such as Wojtan et al. (2005a&b), Garimella (2004), Garimella et al. (2003), Coleman and Garimella et al. (2003), El Hajal et al. (2003), Thome et al. (2003), Didi et al. (2002), Zurcher et al. (2002a&b), Dobson and Chato (1998), Mandhane et al. (1974), and Baker (1954) to aid in the modeling of two-phase flow. The three main types of two-phase flow regime maps in the literature Baker/Mandhane, Taitel-Dukler, and the most commonly used Steiner (1993) type depict boundaries between flow regimes that are not easily represented by continuous functions. This is evident from Figure 2.1, which contains a depiction of a typical Steiner (1993) type flow map. Two phase flow models that incorporate these traditional flow maps are complicated in order to eliminate discontinuities at flow regime boundaries and incorporate the flow regime information as functions. Furthermore Coleman and Garimella (2003) and El Hajal et al. (2003) indicate that more than one flow regime can exist near the boundaries or within a given flow regime on a Steiner (1993) type flow map for single tubes.

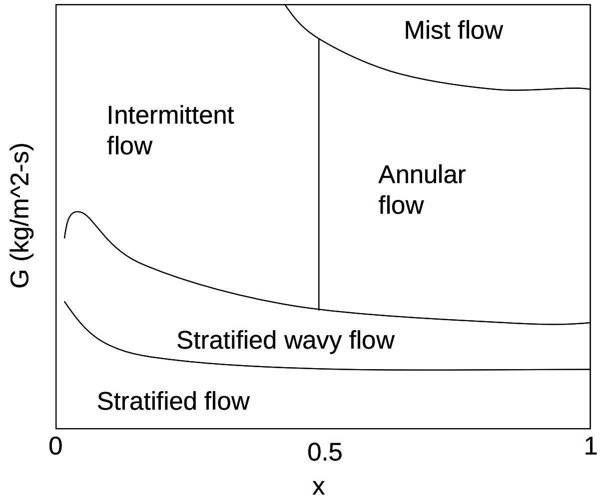

Figure 2.1. Depiction of a typical Steiner (1993) type flow map

Probabilistic two-phase flow regime maps first developed by Niño (2002) for refrigerant and air-water flow in multi-port microchannels are found by Jassim and Newell (2006) to eliminate the discontinuities created by traditional flow maps. Probabilistic two phase flow regime maps have quality on the horizontal axis and the fraction of time in which a particular flow regime is observed in a series of pictures taken at given flow condition (*F*) on the y axis as seen in Figure 2.2. Jassim and Newell (2006) developed curve fit functions to represent the data that are continuous for the entire quality range with correct physical limits for the time fraction data obtained for 6-port microchannels by Niño (2002). Jassim and Newell (2006) then utilized the probabilistic flow regime map time fraction curve fits to predict pressure drop and void fraction as shown in Equations 2.1 and 2.2, respectively.

$$\left(\frac{dP}{dz}\right)_{total} = F_{liq}\left(\frac{dP}{dz}\right)_{liq} + F_{\text{int}}\left(\frac{dP}{dz}\right)_{\text{int}} + F_{vap}\left(\frac{dP}{dz}\right)_{vap} + F_{ann}\left(\frac{dP}{dz}\right)_{ann} \tag{2.1}$$

$$\alpha_{total} = F_{liq}\alpha_{liq} + F_{\text{int}}\alpha_{\text{int}} + F_{vap}\alpha_{vap} + F_{ann}\alpha_{ann} \tag{2.2}$$

In this way pressure drop and void fraction models developed for a particular flow regime are easily and properly weighted for the entire quality range on a consistent time fraction basis.

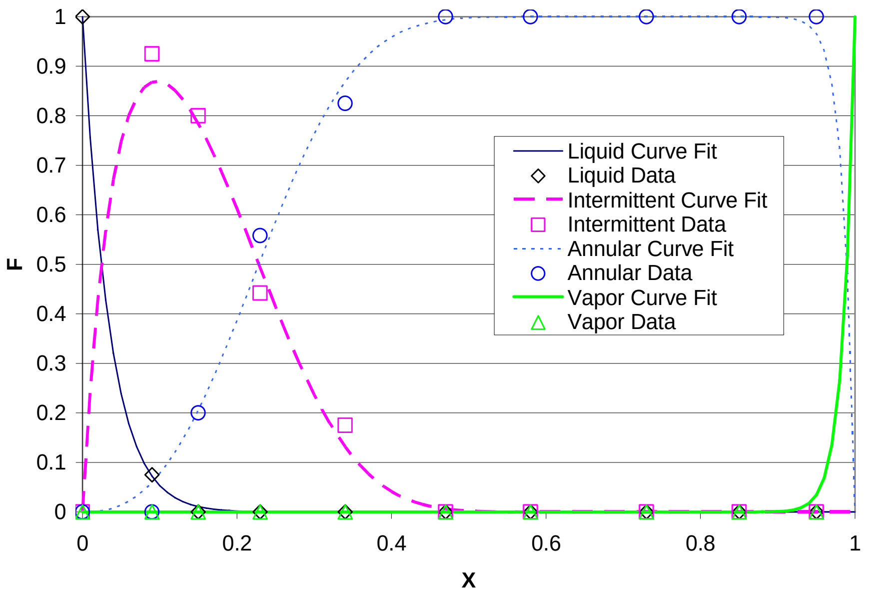

Figure 2.2. Probabilistic flow map with time fraction curve fits for R410A, 10 ºC, 300 kg/m^2-s in a 6-port 1.54 mm hydraulic diameter microchannel taken from Jassim and Newell (2006)

The difficulty with this probabilistic flow map based modeling technique is that large numbers of pictures must be classified for each flow condition in order to create a large number of flow maps necessary to generalize the time fraction functions with respect to refrigerant properties and flow conditions. Plzak and Shedd (2003) developed an automated image recognition software to automatically detect the flow regime present from a series of images at a given flow condition. Consequently, this software is suitable for the formulation of traditional Steiner (1993), Baker/Mandhane, and Taitel-Dukler type flow maps. The present study develops image recognition software that determines the flow regime present in each image for a series of images at each given flow condition in order to formulate the time fraction of each flow regime to create probabilistic flow regime maps.

In the present study probabilistic two-phase flow maps are experimentally developed for 8.00 mm, 5.43 mm, 3.90 mm, and 1.74 mm diameter single, smooth, adiabatic, horizontal tubes for R134a at 25, 35 and 50 ºC and R410A at 25 ºC saturation temperatures and for a range of mass fluxes and qualities in order to aid in the future modeling of two-phase pressure drop, void fraction, and heat transfer. A new optical method is utilized to enhance the images and aid in the image recognition process. Nearly one million flow visualization pictures were utilized in the formulation of the probabilistic two-phase flow regime maps.

2.4 Experimental setup and methods

2.4.1 Two-phase flow loop and test section design

Flow visualization data was obtained from the two-phase flow loop depicted in Figure 2.3. The liquid refrigerant is pumped with a gear pump that is driven by a variable frequency drive from the bottom of a 2 liter receiver tank through a water cooled shell and tube style subcooler in order to avoid pump cavitation. The liquid refrigerant then travels through a Coriolis style mass flow meter with an uncertainty of ±0.1% followed by a preheater used to reach the desired quality. The preheater consists of a finned tube heat exchanger with opposing electric resistance heater plates bolted on either side of the heat exchanger. The electric heaters are controlled with on/off switches and a variable auto transformer to provide fine adjustment of quality. This preheater design has enough thermal mass so that the heaters do not burn out at a quality of 100% and has a small enough thermal mass so that steady state conditions can be rapidly attained. The refrigerant is then directed through 90 degree bends to remove effects of heat flux from the preheater such as dryout before it reaches the test section. Finally, the refrigerant is condensed in a water cooled brazed plate heat exchanger and is directed back into the receiver tank. The pressure before the inlet of the preheater is measured by a pressure transducer with accuracy of ±1.9 kPa. The temperatures before the inlet of the preheater and the test section are measured with type T thermocouples with an uncertainty of ±0.1 ºC. These pressures and temperatures are used to determine the thermodynamic states necessary to compute the test section inlet quality.

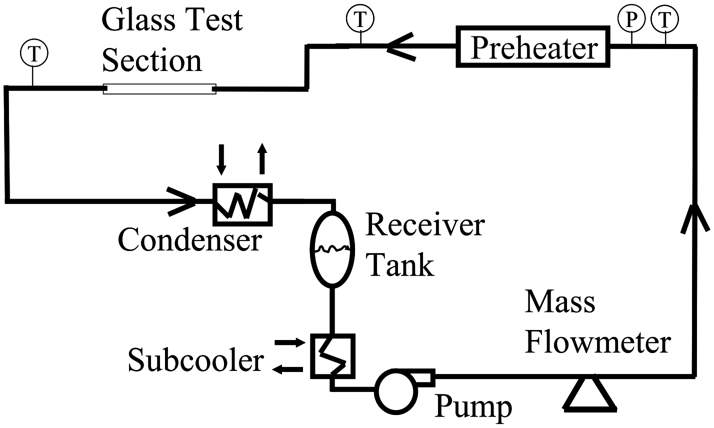

Figure 2.3. Two-phase flow loop schematic

The test sections consist of glass tubes with dimensions as listed in Table 2.1. The 8.00 mm I.D. test section is 0.254m long since the inner diameter of the incoming copper pipe was also 8 mm. The 5.4 mm and 3.9 mm test sections are 1.2m long and were transitioned gradually in order to avoid transition effects. The 1.7 mm I.D. tube is 0.254m long to avoid fracture and excessive pressure drop and was gradually reduced into from the 8 mm ID tube to avoid entrance effects. Brass compression fittings with nylon ferrules were used to join the copper pipe of the flow loop to the glass test section in order to avoid leakage or fracture of the test section. The refrigerant is condensed after the test section in a flat plate heat exchanger with cold water at 5 ºC. The loop temperature is controlled by varying the flow rate of the cold water entering the condenser.

Table 2.1. Test section and stripe dimensions

test section I.D. (mm)	test section O.D. (mm)	test section length (m)	stripe width (mm)	center to center stripe distance (mm)	distance of striped film from centerline of tube (mm)
8.00	12.70	0.25	2.1	5.1	48
5.43	9.53	1.20	1.1	3.5	36
3.90	6.35	1.20	0.8	2.1	20
1.74	3.00	0.25	0.3	1.0	3

2.4.2 Flow visualization technique

A web camera (an inexpensive digital "board camera" used to communicate over the World Wide Web) based flow visualization technique was developed and used in this study as depicted in the schematic in Figure 2.4. A CCD type web camera with 640x480 pixel resolution, 30 frame per second shutter speed, and adjustable focal length is used to capture the images. A diffuse white film pigmented with evenly spaced black stripes are placed in the background (behind the glass tube) and illuminated with a stroboscope directed towards the camera. The stroboscope is also cycled at 30 frames per second in order to create clear images. The stripe width, spacing, and distance from the centerline of the test sections are indicated in Table 2.1. These dimensions were determined to best enhance the detection of fine films, and are varied according to pipe diameter to maintain approximately the same stripes per pipe diameter length and the same stripe width and spacing per pipe diameter length.

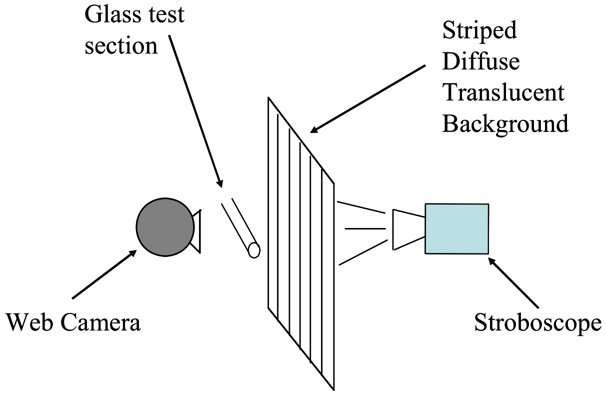

Figure 2.4. Flow visualization schematic

The striped background serves to enhance the image as seen in Figure 2.5. Both images in Figure 2.5 were taken for R410A in 3.9 mm I.D. tube, a mass flux of 200 kg/m^2-s, a 0.99 quality, and at a 25 ºC saturation temperature with the same diffuse paper background. However, the image on right has evenly spaced black stripes on the background. The black stripes provide contrast that enhances the image and allows for the detection of fine liquid films. Furthermore, these stripes aid in the image recognition process. The stripes appear to be out of focus in Figure 2.5 because the camera focal length is adjusted to the center of the tube instead of the stripes in the background.

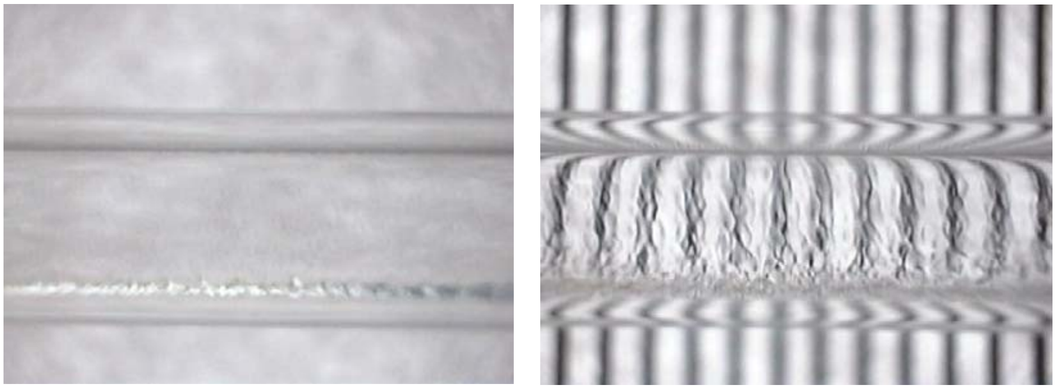

Figure 2.5. Flow visualization pictures of R410A, 3.9 mm I.D. tube, 200 kg/m^2-s, 0.99 quality, and 25 degrees C with a plane diffuse background (left) and with a striped diffuse background (right)

2.4.3 Flow visualization test matrix

Flow visualization pictures were taken for the following test matrix:

- R134a at 25 ºC, 35 ºC, and 49.7 ºC and R410A at 25 ºC
- 8.00 mm, 5.43 mm, 3.90 mm, and 1.74 mm I.D. glass test sections
- mass fluxes of 400, 500, 600 kg/m^2-s for the 1.74 mm ID test sections
- mass fluxes of 100, 200, 300, 400 kg/m^2-s for other tube sizes
- qualities from 0 to 100%

Approximately 30 seconds of flow visualization video (900 images) were taken for each flow condition.

2.4.4 Image recognition software development

Image recognition software was developed in order to automatically classify the flow regimes of the obtained images. The original image is first converted into black and white as seen in Figures 2.6a, 2.7a, 2.8a, 2.9a, 2.10a for different flow conditions and refrigerants. Next, the pixels are thresholded (pixel values above a threshold value are turned white and below that value are turned black) to a percentage of the brightness of the white background as seen in Figures 2.6b, 2.7b, 2.8b, 2.9b, 2.10b. This percentage varied based upon tube type since the light intensity changed as the distance of the background from the centerline of the tube varied with tube size. It should be noted that thin vertical black lines are drawn between the vertical stripes in Figures 2.6b, 2.7b, 2.8b, 2.9b, and 2.10b for illustration purposes and will be discussed later. If the threshold value is set correctly, the vapor to liquid interface will appear black. The black stripes which normally appear through the tube from the background during liquid flow as seen in Figure 2.6b are bent/scattered horizontally when vapor is present in the tube as seen in Figures 2.7b, 2.8b, 2.9b, and 2.10b for vapor only, intermittent, stratified, and annular flows, respectively. Consequently, black regions are found in the normally white space of the thresholded images. This phenomenon is utilized in the image recognition process to detect the presence of vapor at a given tube location. The vertical pixel lines that lie directly between the black stripes seen through the tube when all liquid is present are always white with the maximum pixel value of 255 as seen in Figure 2.6b. Vertical black lines were drawn in the thresholded images in 6b, 7b, 8b, 9b, and 10b to indicate the location of the pixel lines that were scanned. If all of the pixel values in all of the vertical pixel lines scanned are equal to 255, i.e. unbroken as in Figure 2.6b, then the flow is classified in the liquid flow regime. If the flow has one or more broken lines, indicating the presence of vapor, and one or more of the lines are unbroken, indicating the presence of liquid, the flow is classified as intermittent flow. A three pipe diameter length of tube is used to determine whether the flow is liquid only or intermittent.

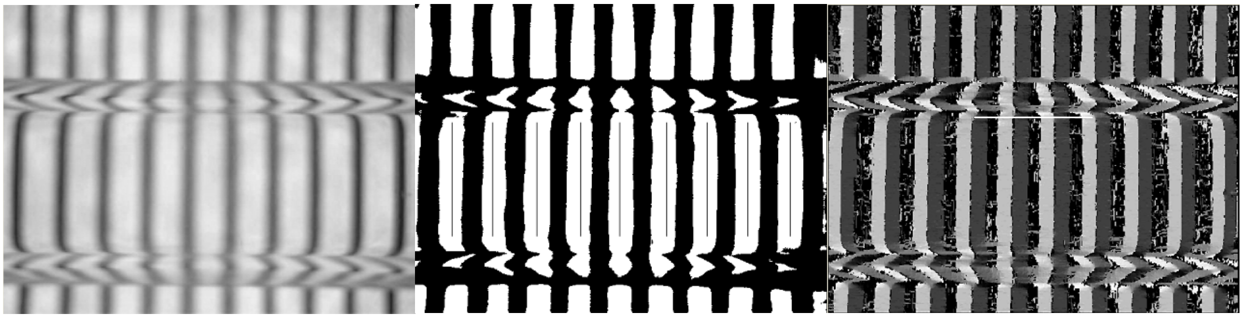

Figure 2.6a. Figure 2.6b. Figure 2.6c.

Figures 2.6a-c. R134a liquid in 5.43 mm I.D. Glass tube without thresholding, with thresholding, and with a directional Sobel filter applied, respectively

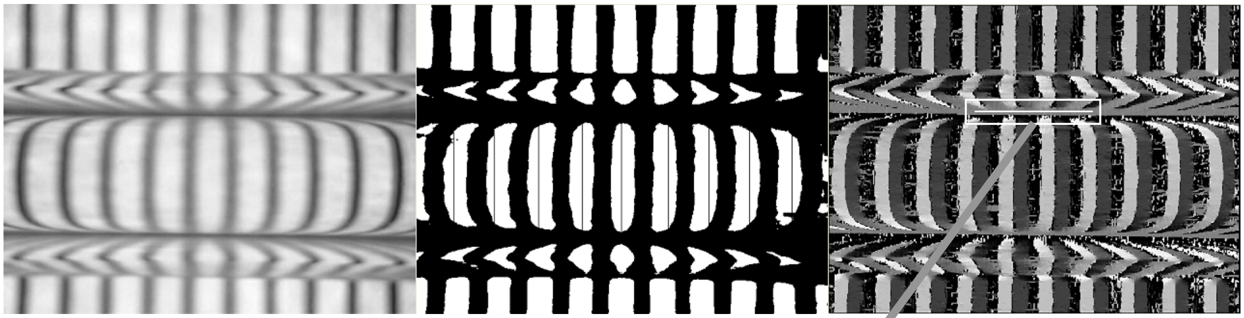

Figure 2.7a. Figure 2.7b. Figure 2.7c.

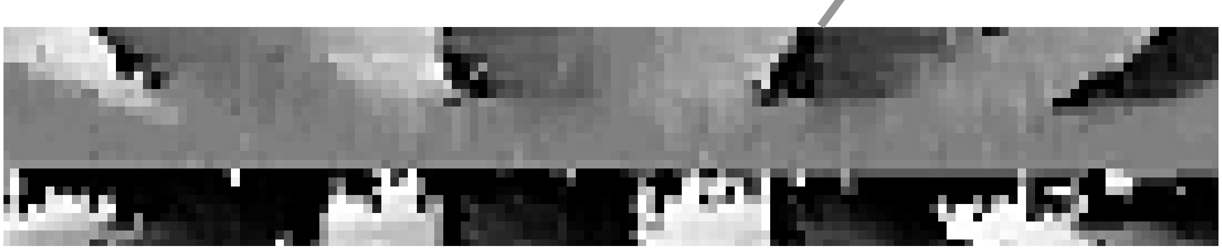

Figure 2.7d.

Figures 2.7a-d. R410A vapor in 5.43 mm I.D. glass tube without thresholding, with thresholding, with a directional Sobel filter applied, and a magnified view, respectively

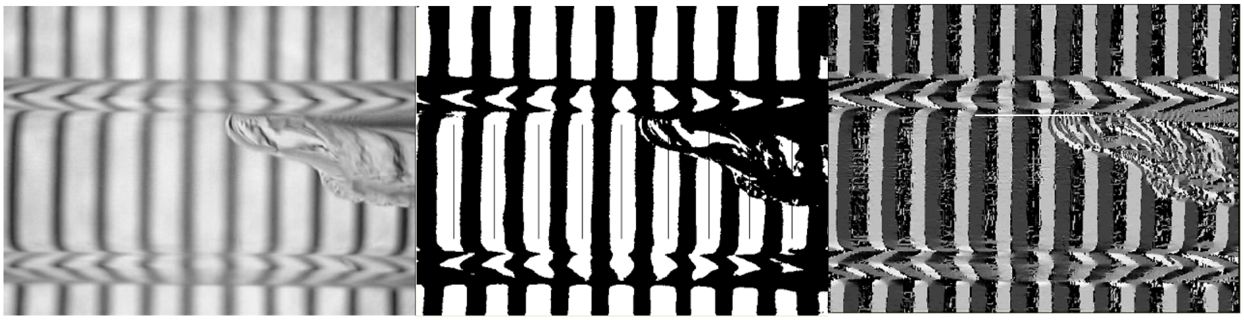

Figure 2.8a. Figure 2.8b. Figure 2.8c.

Figures 2.8a-c. R134a at 200 kg/m^2-s, 2.2% quality, and 25 ºC in 5.43 mm I.D. glass tube without thresholding, with thresholding, and with a directional Sobel filter applied, respectively

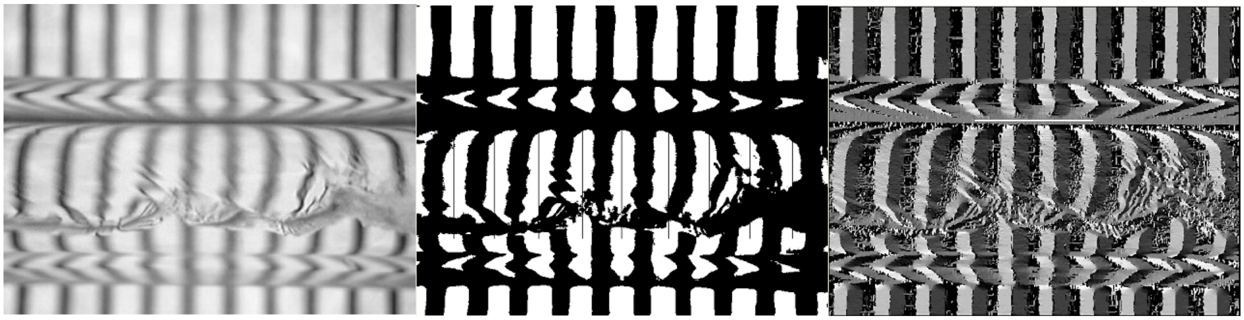

Figure 2.9a Figure 2.9b Figure 2.9c

Figures 2.9a-c. R134a at 100 kg/m^2-s, 44.1% quality, and 25 ºC in 5.43 mm I.D. glass tube without thresholding, with thresholding, and with a directional Sobel filter applied, respectively

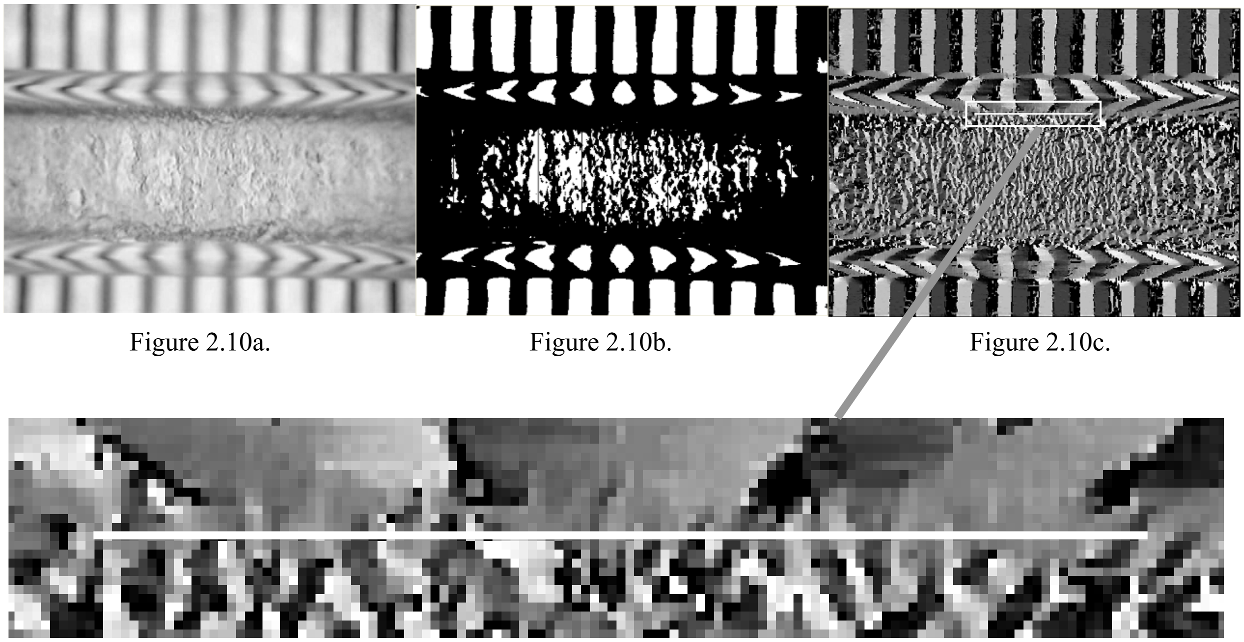

Figure 2.10a. Figure 2.10b. Figure 2.10c.

Figure 2.10d.

Figures 2.10a-d. R410A at 300 kg/m^2-s, 79.3% quality, and 25 ºC in 5.43 mm I.D. glass tube without thresholding, with thresholding, with a directional Sobel filter applied, and a magnified view, respectively

If all of the scanned lines are broken a directional Sobel filter algorithm is utilized as seen in Figures 2.6c, 2.7c, 2.8c, 2.9c, and 2.10c in order to determine whether the flow is stratified or annular (Figures 2.6c and 2.8c are shown for illustration purposes). The directional Sobel filter computes the direction of each pixel gradient vector and assigns a pixel intensity between 0 and 255 corresponding to 0 through 360º (counterclockwise) with 0 pointing directly down on the page. Two horizontal pixel lines one diameter long are scanned on the directional Sobel filtered image at the top of the tube in the center of the solid gray region when vapor is present (this region is absent when liquid is present). The location of these scanned horizontal pixel lines are indicated by a white line drawn on each image and can be seen in Figures 2.6c, 2.7c, 2.8c, 2.9c, and 2.10c for different flow conditions. Figures 2.7d and 2.10d depict magnified views of the scanned regions in Figures 2.7c and 2.10c for vapor only flow and annular flow, respectively. When only vapor is present, as in Figure 2.7, the scanned region depicted in Figure 2.7d is relatively homogeneous with the majority of the pixel values at or near 128 which indicates a pixel brightness gradient pointing in the upward direction. Figure 2.11 supports this observation as it depicts the scanned pixel brightness values from Figure 2.7d that are sorted in descending order. The pixel brightness distribution for a fully stratified flow where only vapor is present at the top of the tube is similar to the distribution in Figure 2.11. However, as annular flow is approached a liquid film appears at the top of the tube and it increases in waviness. This increase in waviness causes the distribution of the scanned pixel brightness to change as the waves scatter light in multiple directions as can be seen in Figure 2.10d for a fully annular flow. The once homogeneous gray region when vapor was present with most of the pixel brightness values at 128 becomes inhomogeneous. The pixel values of the scanned pixel lines of Figure 2.10d are depicted in Figure 2.12. Figure 2.12 shows a greater number of pixels that have deviated from the baseline of 128 and also has a greater magnitude of deviation of pixel brightness values. This phenomenon is utilized in order to detect annular flow. The difference between each scanned pixel value above 128 and the baseline of 128 are summed and divided by the total number of pixels scanned in order to obtain the average positive deviation from the baseline. The average positive deviation from the baseline was used instead of the mean absolute deviation or the standard deviation because it was found to have the least scatter when vapor is present at the top of the tube. A one pipe diameter length of tube is used to determine whether the image is stratified or annular in order to provide a sufficiently large number of pixels for reasonable resolution.

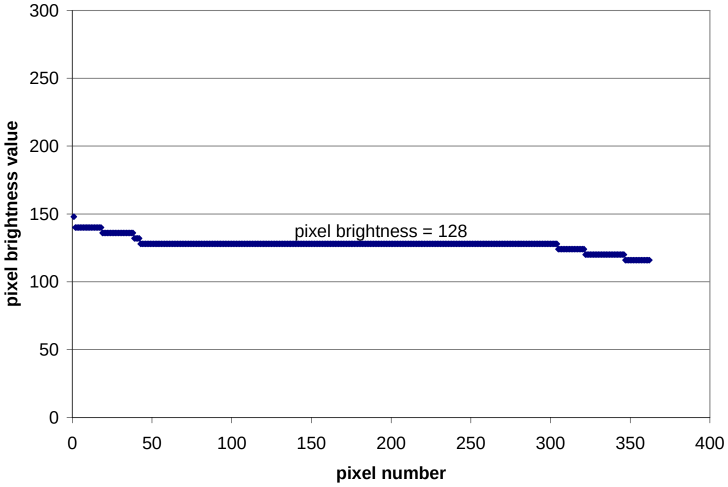

Figure 2.11. Pixel brightness distribution of the pixel lines in Figure 2.7d of R410A vapor in 5.43 mm I.D. glass tube with a directional Sobel filter applied

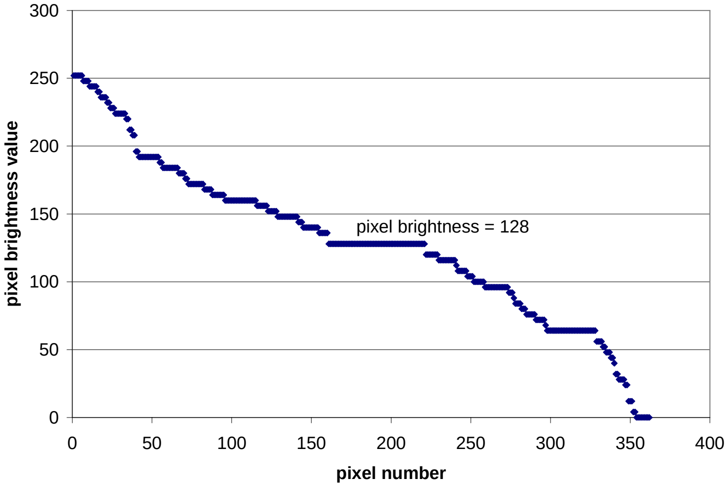

Figure 2.12. pixel brightness distribution of the pixel lines in Figure 2.10d of R410A at 300 kg/m^2-s, 79.3% quality, and 25 ºC in 5.43 mm I.D. glass tube with a directional Sobel filter applied

Vapor or fully stratified flow (with no liquid at the top of the tube), is found to have an average positive deviation of 1.61, a maximum average positive deviation of 2.07 and a minimum average positive deviation of 0.916. The average positive deviation of the vapor only condition appears to have no dependence on tube size or refrigerant. The flow is classified as annular if the average positive deviation is greater than 9, and classified as stratified if the average positive deviation is 9 or less. This threshold value was selected through comparison with annular flow heat transfer data. Observations indicated that the presence of a liquid film is not sufficient for defining an "annular" flow. Instead, some level of film activity, related to an agitation in a film that results in the characteristics ascribed to annular film heat transfer, is used to determine the threshold level.

The automated flow visualization software loops through each image in an AVI video file and classifies the flow regime present and keeps a running total of the number of images in each flow regime. Furthermore, a batch file system was utilized that sequentially reads filenames from a text file and outputs time fraction information to another text file.

The accuracy of the image recognition software in the liquid and intermittent flow regime was determined by manually classifying 4800 images of different tube size, mass fluxes, fluids, and qualities. The software is found to have a maximum time fraction error of $\pm$0.04 and an average error of $\pm$0.01 for the liquid and intermittent flow regimes. The error in the stratified and annular flow regimes is estimated by changing the average positive deviation threshold by 0.58 in either direction, half of the difference between the maximum and minimum average positive deviation observed when vapor exists at the top of the tube, and then computing the error associated with this change. Using this method the average error in the annular and stratified flow regime time fraction is found to be $\pm$0.01 with a maximum of $\pm$0.152 and a minimum of 0.

An alternate algorithm for automated image detection was also used with similar results. In this method the image is thresholded at a lower value than for the first method so that the black stripes from the background appear to be thin but solid. In this case the presence of a liquid vapor interface will bend/scatter the light so that white pixels will appear, i.e. the black stripe is broken, where the solid black stripe exists during liquid only flow. After the image is thresholded, the pixel lines located inside the black stripes which appear on the tube from the background during liquid flow are scanned. If all of the pixels in a line are black, pixel intensity of 0, it would indicate that the flow is liquid at that location. If some of the pixels are white, i.e. the black stripe is broken with a pixel intensity of 255, it would indicate that a vapor-liquid interface exists at that location. Consequently, if all of the pixels in the scanned vertical pixel lines are black, the black stripe is unbroken with a value of 0, the image would be classified as liquid flow. If it is not classified as liquid flow (at least one of the scanned pixel lines contains white pixels) and at least one of the pixel lines contains only black pixels, indicating liquid bridging, then the image is classified as intermittent flow. If all of scanned lines contain white pixels then the same algorithm is utilized as described in the first method to classify the image as either stratified or annular flow.

2.5 Results

Probabilistic two phase flow regime maps were created from the time fraction data collected for the test matrix described above. Figures 2.13 through 2.16 depict probabilistic two-phase flow regime maps for R410A at 25^{o} in the 3.90 mm test section with a mass fluxes varying from 100 to 400 kg/m^{2}-s, respectively. The solid points in the figures represent the time fraction output from the image recognition code developed. The liquid flow regime is considered to be part of the intermittent flow regime hence they are summed together. The annular flow regime time fraction drops off drastically as quality is decreased below 0.4, however there is a minimum at approximately 0.1 quality and the time fraction is seen to increase at lower qualities. This seems to lack a physical basis since the annular flow time fraction should disappear as quality approaches zero. The intermittent and liquid flow regime should approach 1 as quality approaches 0 since all the flow should become liquid. Therefore, we postulate that that the classified low quality annular flow is intermittent flow with bubbles longer than the field of view. Further investigation with a high speed camera would be required to verify this postulate. The time fraction data at qualities below the minimum in the annular flow time fraction was subtracted from the annular flow regime and added to the intermittent flow regime. The resulting extrapolated intermittent and liquid, and annular flow regimes are plotted in Figures 2.13 through 2.16 as “hollow” points. The uncertainty in quality in Figure 2.13 is the highest where it is less than ± 0.033 at x=0.99, ± .018 at x=.5, and ±.003 at x=.02 and the uncertainty in quality is the lowest in Figure 2.16 where it is less than ± 0.018 at x=0.99, ± .01 at x=.5, and ±.002 at x=.02. The uncertainty in mass flux is maximum of ±4% with the majority of the uncertainty below ±2%.

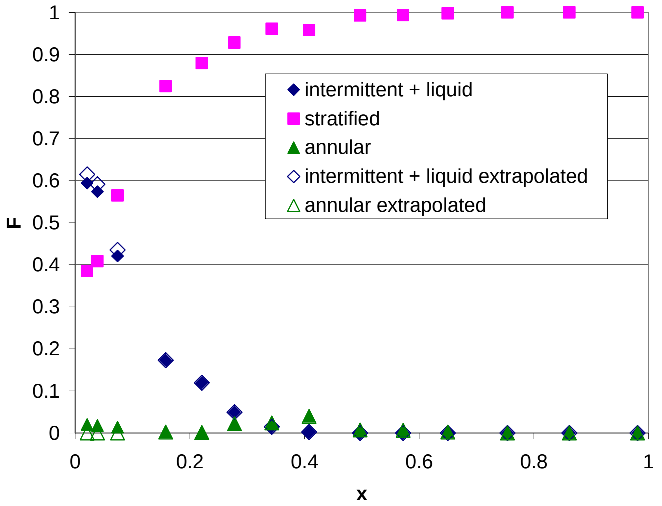

Figure 2.13. Probabilistic two-phase flow regime map for R410A, 100 kg/m^2-s, 25 ºC, adiabatic 3.90 mm I.D. tube

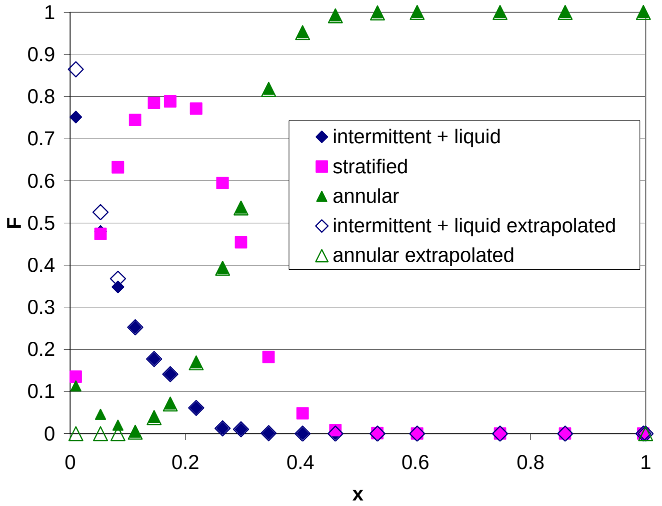

Figure 2.14. Probabilistic two-phase flow regime map for R410A, 200 kg/m^2-s, 25 ºC, adiabatic 3.90 mm I.D. tube

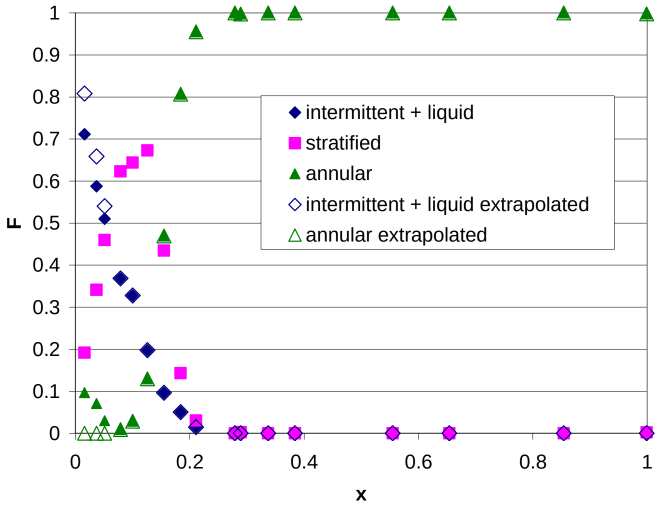

Figure 2.15. Probabilistic two-phase flow regime map for R410A, 300 kg/m^2-s, 25 ºC, adiabatic 3.90 mm I.D. tube

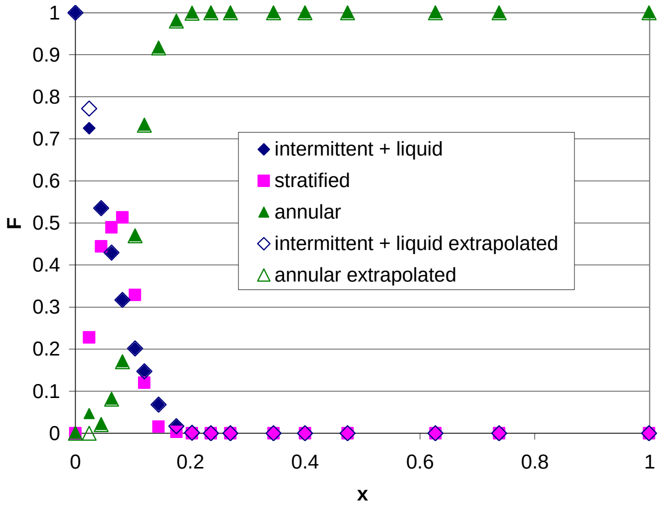

Figure 2.16. Probabilistic two-phase flow regime map for R410A, 400 kg/m^2-s, 25 ºC, adiabatic 3.90 mm I.D. tube

2.6 Conclusion and discussion

In summary, probabilistic two-phase flow maps have been found in the literature to be useful in the modeling of two-phase flow in multi-port microchannels. A two-phase flow loop was constructed and a new web camera based image recognition technique was developed in order to obtain the flow visualization images necessary to develop probabilistic two phase flow maps for smooth, horizontal, adiabatic, single channel tubes. The flow visualization technique utilizes an illuminated striped diffuse background to enhance the images and aid in the image recognition process. Nearly one million flow visualization images were obtained for R134a at 25, 35, and 50 ^{o}C, R410A at 25 ºC, mass fluxes from 100 to 600 kg/m^2-s, qualities from 0 to 1 in 8.00 mm, 5.43 mm, 3.90 mm, and 1.74 mm I.D. smooth adiabatic tubes in order to provide the flow visualization data necessary to generalize probabilistic flow regime maps. Image recognition software was developed in order to classify the flow regime present in each image and formulate the time fraction of each flow regime for a give flow condition. The error in image recognition software in detecting time fraction was found to be a maximum of $\pm$0.04 and an average of $\pm$0.01 for the intermittent and liquid flow regimes and an average of $\pm$0.01 with a maximum of $\pm$0.152 for the stratified and annular flow regimes. Curve fits can be made of the probabilistic two-phase flow maps in order to generalize the time fraction information using physically meaningful parameters. The time fraction information represented as continuous functions can be utilized to model single tube pressure drop, void fraction, and heat transfer with a common two-phase flow map basis in a similar manner as Jassim and Newell (2006) had demonstrated for multi-port microchannels.

References

Baker, O., “Simultaneous Flow of Oil and Gas,” *Oil and Gas Journal* 53 (1954) 185-195.

Coleman, J.W., S.Garimella, “Two-Phase Flow Regimes in Round, Square and Rectangular Tubes during Condensation of Refrigerant R134a,” *International Journal of Refrigeration* 26 (2003) 117-128.

Didi, M.B. and N. Kattan, J.R. Thome, “Prediction of Two-Phase Pressure Gradients of Refrigerants in Horizontal Tubes,” *International Journal of Refrigeration* 25 (2002) 935-947.

Dobson, M. K. and J.C. Chato, “Condensation in Smooth Horizontal Tubes,” *Journal of Heat Transfer* 120 (1998) 245-252.

El Hajal, J., J.R. Thome, and A. Cavalini, “Condensation in Horizontal Tubes, Part 1: Two-Phase Flow Pattern Map,” *International Journal of Heat and Mass Transfer* 46 (2003) 3349-3363.

Garimella, S., “Condensation Flow Mechanisms in Microchannels: Basis for Pressure Drop and Heat Transfer Models,” *Heat Transfer Engineering* 25:3 (2004) 104-116.

Garimella, S., J.D. Killion, and J.W. Coleman, “An Experimentally Validated Model for Two-Phase Pressure Drop in the Intermitent Flow Regime for Noncircular Microchannels,” *Journal of Fluids Engineering* 125 (2003) 887-894.

Jassim, E.W. and T. A. Newell. “Prediction of Two-Phase Pressure Drop and Void Fraction in Microchannels using Probabilistic Flow Regime Mapping,” *International Journal of Heat and Mass Transfer* 49 (2006) 2446-2457.

Mandhane, J.M., G.A. Gregory, and K. Aziz, “A Flow Pattern Map for Gas-Liquid Flow in Horizontal and Inclined Pipes,” *International Journal of Multiphase Flow* 1 (1974) 537-553.

Niño, V.G. “Characterization of Two-phase Flow in Microchannels,” Ph.D. Thesis, University of Illinois, Urbana-Champaign, IL, 2002.

Plzak, K. M., and T.A. Shedd, 2003, “A Machine Vision-Based Horizontal Two-Phase Flow Regime Detector,” *Sixth ASME-JSME Thermal Engineering Joint Conference*, Paper 385.

Steiner, D., “Heat Transfer to Boiling Saturated Liquids,” VDI-Wārmeatlas (VDI Heat Atlas), Verein Deutscher Ingenieure, VDI-Gesellschaft Verfahrenstechnik und Chemieingenieurwesen (GCV), Dū sseldorf, Chapter Hbb (1993).

Thome, J.R., J. El Hajal, and A. Cavalini, “Condensation in Horizontal Tubes, Part 2: New Heat Transfer Model Based on Flow Regimes,” *International Journal of Heat and Mass Transfer* 46 (2003) 3365-3387.

Wojtan, L., Ursenbacher, T. and Thome, J.R., 2005, Investigation of Flow Boiling in Horizontal Tubes: Part I – A New Diabatic Two-Phase Flow Pattern Map, *Int. J. Heat Mass Transfer*, Vol. 48: p. 2955-2969.

Wojtan, L., Ursenbacker, T. and Thome, J.R., 2005, Investigation of Flow Boiling in Horizontal Tubes: Part II – Development of a New Heat Transfer Model for Stratified-Wavy, Dryout and Mist Flow Regimes, *Int. J. Heat Mass Transfer*, Vol. 48: p. 2970-2985.

Zurcher, O., D. Farvat, and J.R Thome, “Evaporation of Refrigerants in a Horizontal Tube: And Improved Flow Pattern Dependent Heat Transfer Model Compared to Ammonia Data,” *International Journal of Heat and Mass Transfer* 45 (2002) 303-317.

Zurcher, O., D. Farvat, and J.R. Thome, “Development of a Diabatic Two-Phase Flow Pattern Map for Horizontal Flow Boiling,” *International Journal of Heat and Mass Transfer* 45 (2002) 291-301.

Chapter 3: Probabilistic Two-Phase Flow Regime Maps in Tubes and Their Generalization to Physical Parameters

3.1 Abstract

Probabilistic two-phase flow maps are investigated for R134a at 25 ºC, 35 ºC, and 49.7 ºC, and R410A at 25 ºC with quality ranging from 0 to 1 and mass fluxes varying from 100 to 600 kg/m^2-s in single, smooth, horizontal, adiabatic 8.00 mm, 5.43 mm, 3.90 mm, and 1.74 mm diameter tubes. Nonlinear curve fits are developed for the intermittent, stratified, and annular flow regimes. The flow map variations with physical parameters are described and the time fraction curve fit constants are generalized based on physical parameters in order to facilitate the incorporation of flow regime information in heat transfer, pressure drop, and void fraction models.

3.2 Nomenclature

a	curve fit constant (-)
b	curve fit constant (-)
c	curve fit constant (-)
d	curve fit constant (-)
D	hydraulic diameter (m)
F	observed time fraction (-)
Fr_{vo}	vapor only Froude number (-)
G	mass flux (kg/m^2-s)
g	curve fit constant (-)
g_a	gravitational acceleration (9.81m/s^2)
i	intermittent flow regime curve fit constant (-)
s	stratified flow regime curve fit constant (-)
We_{vo}	vapor only Weber number for vapor (-)
Xi	dimensionless group correlating the intermittent/liquid flow regime (-)
Xs	dimensionless group correlating the stratified flow regime (-)
x	flow quality (-)

Greek symbols

ρ	density (kg/m^3)
σ	surface tension (N/m)

Subscripts

ann	pertaining to the annular flow regime
int	pertaining to the intermittent flow regime
l	liquid
liq	pertaining to the liquid flow regime
strat	pertaining to the stratified flow regime
v	vapor
vap	pertaining to the vapor flow regime

3.3 Introduction

It is evident from the works by Wojtan et al. (2005a&b)), Garimella (2004), Garimella et al. (2003), Coleman and Garimella et al. (2003), El Hajal et al. (2003), Thome et al. (2003), Didi et al. (2002), Zurcher et al. (2002a&b), Cavallini et al. (2002) Dobson and Chato (1998) that it is important to use flow regime information in order to accurately model two-phase flow. Probabilistic two-phase flow regime maps are found in the literature (Niño (2002) to provide a quantitative representation of the flow regimes present in multi-port microchannels. These flow maps can be represented by continuous functions for qualities from 0 to 1, and eliminate discontinuities created by distinct boundaries present in traditional flow maps. These attributes allow the flow regime information from probabilistic two-phase flow regime maps to be easily incorporated into pressure drop, void fraction and heat transfer models on a consistent basis. Probabilistic flow regime maps have recently been developed in the literature for single tubes by Jassim et al. (2006a) but the appropriate time fraction functions have yet to be identified. Furthermore, the curve fit constants must be linked to physical parameters in order to facilitate the incorporation of these flow maps into two-phase flow models.

In the present study probabilistic two-phase flow maps obtained by the method detailed in Jassim et al. (2006a) are presented for R134a at 25 ºC, 35 ºC, and 49.7 ºC, and R410A at 25 ºC with quality ranging from 0 to 1 and mass fluxes varying from 100 to 600 kg/m^2-s in single, smooth, horizontal, adiabatic 8.00 mm, 5.43 mm, 3.90 mm, and 1.74 mm diameter tubes. The variation in characteristics of these flow maps are described in terms of physical parameters. Nonlinear continuous curve fit functions are developed for the intermittent, stratified, and annular flow regimes. The curve fit constants are generalized to physical parameters in order to facilitate the incorporation of flow regime information in heat transfer, pressure drop, and void fraction models for single tubes.

3.4 Literature review

Probabilistic two-phase flow regime maps were first developed by Niño (2002) in order to more precisely describe the two-phase flow regimes present in multi-port microchannels using R134a, R410A, and air-water. Niño (2002) found that multiple flow regimes can exist in different ports at the same instant in time. Moreover, multiple flow regimes can exist at a given flow condition if a single channel is observed over a length of time. Coleman and Garimella (2003) and El Hajal et al. (2003) seem to support this in that they indicate that more than one flow regime seem to exist near the boundaries of traditional flow maps that indicate a particular flow regime at a given flow condition for single tubes. Niño (2002) recorded the fraction of time that each flow regime was observed for each given flow condition in order to form probabilistic two-phase flow regime maps.

Jassim and Newell (2006) developed curve fits to represent the time fraction data of Niño (2002) which have correct physical limits and are continuous from a quality of 0 to 1 as seen in Figure 3.1. The time fraction functions used for the liquid, intermittent, vapor, and annular flow regimes are given in Equations 3.1 through 3.4.

$$F_{liq} = (1-x)^a \tag{3.1}$$

$$F_{\text{int}} = (1-x)^{(bx^c)} - (1-x)^{(d)} \tag{3.2}$$

$$F_{vap} = x^g \tag{3.3}$$

$$F_{ann} = 1 - F_{liq} - F_{\text{int}} - F_{vap} \tag{3.4}$$

Jassim and Newell (2006) then incorporated the time fraction curve fits into a pressure drop and a void fraction model on a consistent basis. They found that the flow regime information was easy to implement since the probabilistic two-phase flow maps can be represented as continuous functions for the entire quality range, and since it eliminates discontinuities associated with the use of traditional Baker (1954)/Mandhane (1974) type, Taitel-Dukler

(1976) type, and Steiner (1993) type flow maps. The models developed agreed well with the pressure drop and void fraction data obtained by Niño (2002) with the same test section geometry as their flow visualization experiments.

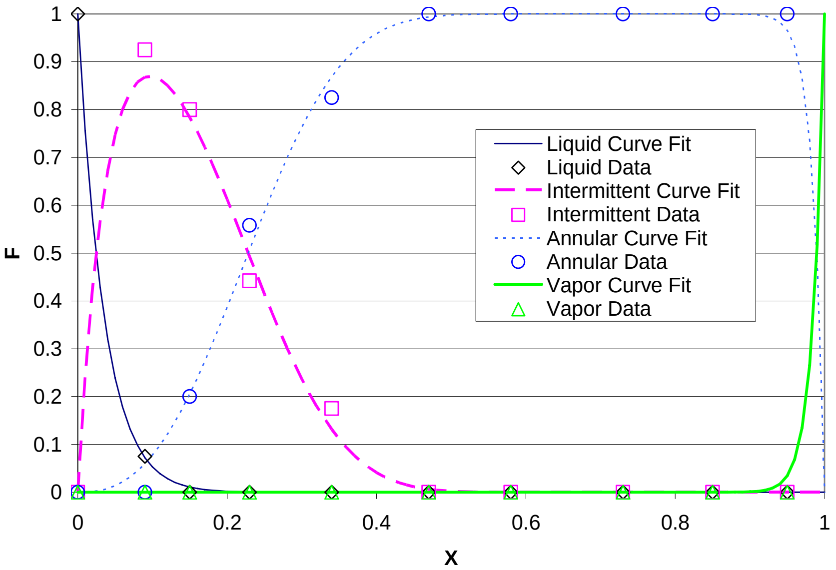

Figure 3.1. Probabilistic flow map with time fraction curve fits for R410A, 10 ºC, 300 kg/m^2-s in a 6-port 1.54 mm hydraulic dia. microchannel taken from Jassim and Newell (2006)

In order to extend probabilistic two-phase flow map modeling to tubes Jassim et al. (2006a) developed an automated flow visualization technique to classify the large numbers of images required to develop probabilistic two-phase flow maps. The technique utilizes a web camera to capture digital images of glass tube test sections with a striped diffuse background that is illuminated with a stroboscope cycling at the same frequency as the camera as seen in Figure 3.2. They developed a Visual Basic based image recognition software which classifies approximately 900 images per flow condition into either liquid, intermittent, stratified, or annular flow. The average error in the image recognition process was reported to be below 0.01 and a maximum error of 0.04 for the intermittent/liquid flow regime, and 0.152 for the stratified and annular flow regimes. The maximum uncertainty in quality and mass flux was found to be $\pm$0.033% and $\pm$4.0%, respectively, for the 3.9 mm and greater tube diameters, and $\pm$0.04 and $\pm$4.0%, respectively, for the 1.74 mm diameter tube. The uncertainty in quality and mass flux was largely below 1% and 2%, respectively. The two-phase flow loop design of Jassim et al. (2006a) can be seen in Figure 3.3. In Figure 3.3 the refrigerant is seen to flow through 90^o bends after the preheater to remove any heat transfer effects of evaporation such as dryout. Time fraction data was collected for R134a at 25 ºC, 35 ºC, and 49.7 ºC, and R410A at 25 ºC, qualities from 0 to 1, and mass fluxes varying from 100 to 600 kg/m^2-s in horizontal adiabatic 8 mm, 5.43 mm, 3.90 mm, and 1.74 mm diameter tubes. The intermittent and liquid flow were considered to be a single flow regime since the liquid time fraction was found to be relatively small.

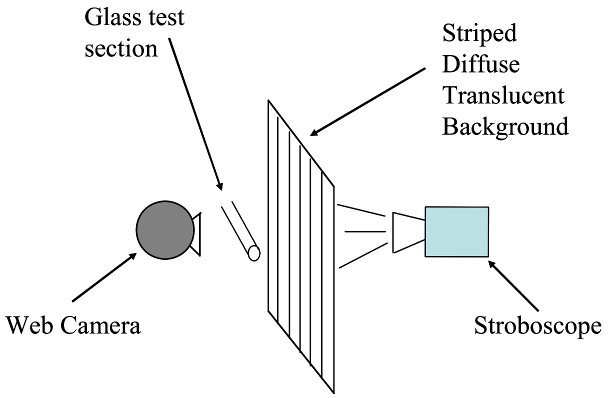

Figure 3.2. Flow visualization schematic from Jassim et al. (2006a)

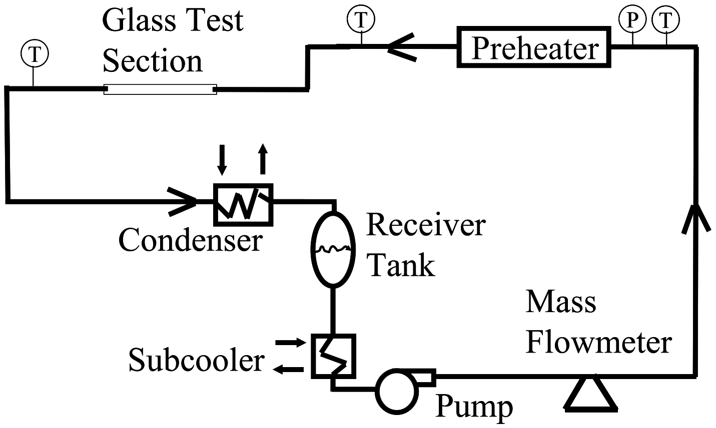

Figure 3.3 Two-phase flow loop schematic from Jassim et al. (2006a)

3.5 Probabilistic two-phase flow regime maps

Probabilistic two-phase flow regime maps generated from the time fraction data collected by Jassim et al. (2006a) can be seen for the 8.00 mm diameter tube with R134a at 25 ºC and 100 through 300 kg/m^2-s in Figures 3.4-3.6, respectively, for the 8.00 mm diameter tube with R410A at 25 ºC and 100 through 400 kg/m^2-s in Figures 3.7-3.10, respectively, for the 5.43 mm diameter tube with R134a at 25 ºC and 100 through 400 kg/m^2-s in Figures 3.11-3.14, respectively, for the 5.43 mm diameter tube with R410A at 25 ºC and 100 through 400 kg/m^2-s in Figures 3.15-3.18, respectively, for the 3.90 mm diameter tube with R134a at 25 ºC and 100 through 400 kg/m^2-s in Figures 3.19-3.22, respectively, for the 3.90 mm diameter tube with R410A at 25 ºC and 100 through 400 kg/m^2-s in Figures 3.23-3.26, respectively, for 1.74 mm diameter tube with R134a at 25 ºC and 400 through 600 kg/m^2-s in Figures 3.27-3.29, respectively, and for the 1.74 mm diameter tube with R410A at 25 ºC and 400 through 600 kg/m^2-s in Figures 3.30-3.32, respectively. Additional probabilistic two-phase flow maps for R134a at elevated temperatures can be seen in Figures A1-A24 in Appendix A. Figures 3.4-3.32 and A1-A24 contain experimental data (solid pints) and extrapolated data (hollow points) where the low quality annular flow was considered by Jassim et al. (2006a) to be intermittent flow with long bubbles just as Jassim and Newell (2006) considered low quality vapor flow to be intermittent flow. Figures 3.4-3.32 and A1-A24 (Appendix A contains flow maps of R134a at 35 and 49.7 ºC) also contain generalized curve fits developed in the subsequent analysis.

From these graphs it can be seen that the intermittent/liquid flow regime time fraction increases with decreasing mass flux, decreasing diameter, and increasing vapor density as summarized in Figure 3.33. The stratified flow regime time fraction is seen to increase with decreasing mass flux, increasing diameter, and increasing vapor density as depicted in Figure 3.34. The annular flow regime experiences the opposite trends as the stratified flow regime: it increases with increasing mass flux, decreasing diameter, and decreasing vapor density as depicted in Figure 3.35.

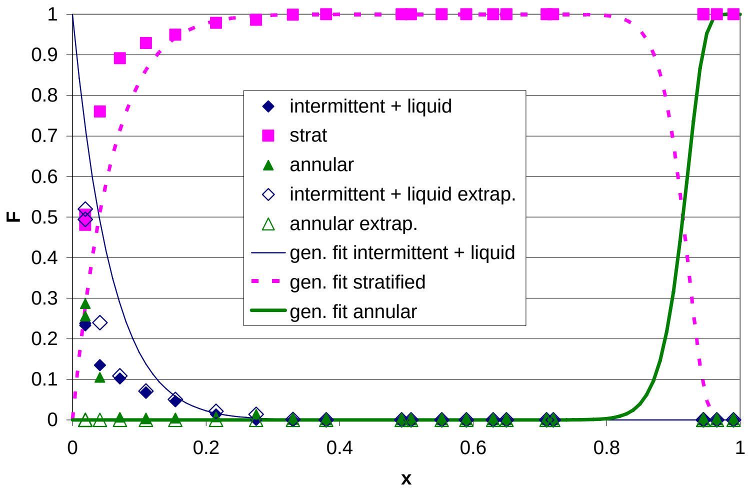

Figure 3.4. Probabilistic flow map with generalized time fraction curve fits for 8.00 mm diameter tube, R134a, 25 ºC, 100 kg/m^2-s

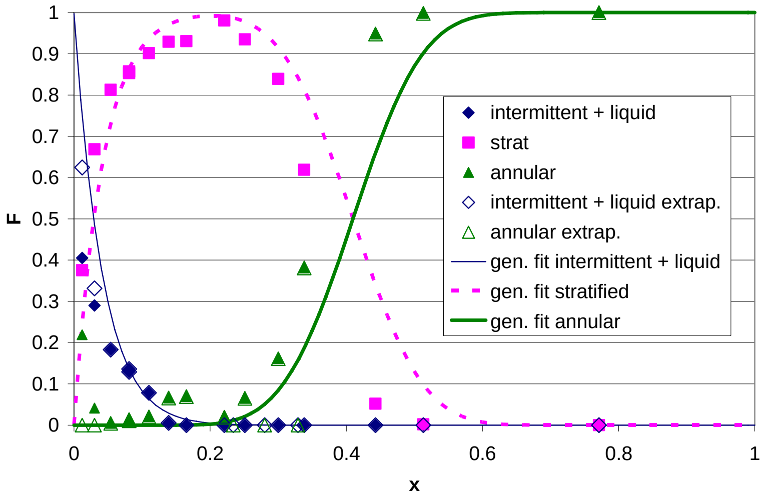

Figure 3.5. Probabilistic flow map with generalized time fraction curve fits for 8.00 mm diameter tube, R134a, 25 ºC, 200 kg/m^2-s

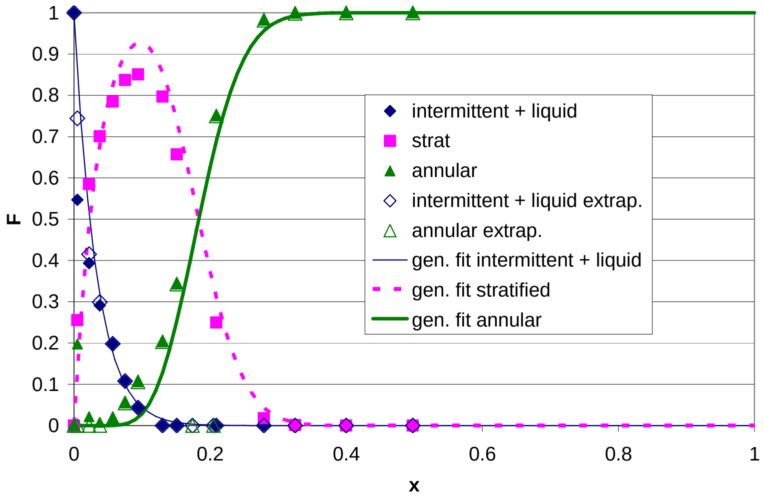

Figure 3.6. Probabilistic flow map with generalized time fraction curve fits for 8.00 mm diameter tube, R134a, 25 ºC, 300 kg/m^2-s

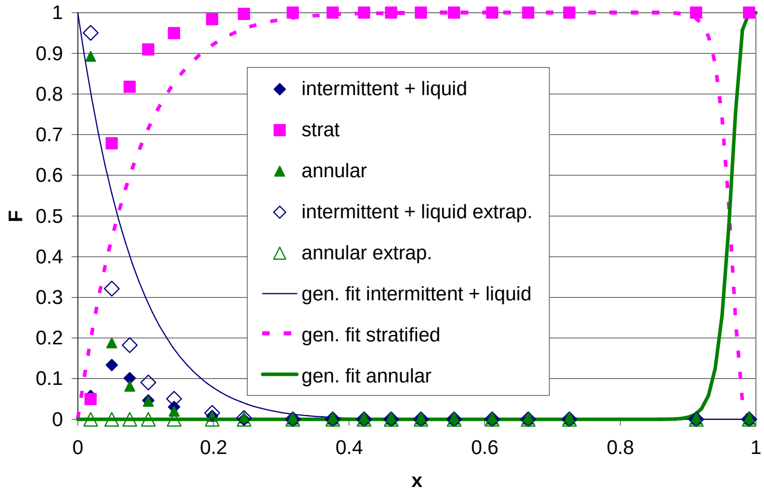

Figure 3.7. Probabilistic flow map with generalized time fraction curve fits for 8.00 mm diameter tube, R410A, 25 ºC, 100 kg/m^2-s

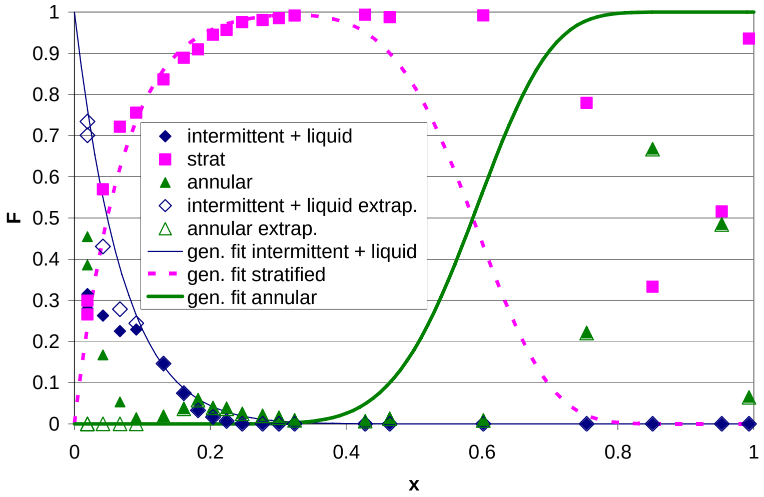

Figure 3.8. Probabilistic flow map with generalized time fraction curve fits for 8.00 mm diameter tube, R410A, 25 ºC, 200 kg/m^2-s

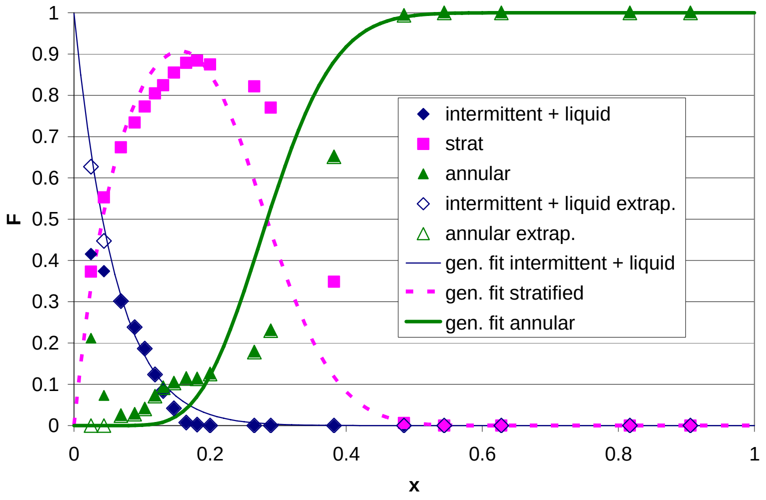

Figure 3.9. Probabilistic flow map with generalized time fraction curve fits for 8.00 mm diameter tube, R410Aa, 25 ºC, 300 kg/m^2-s

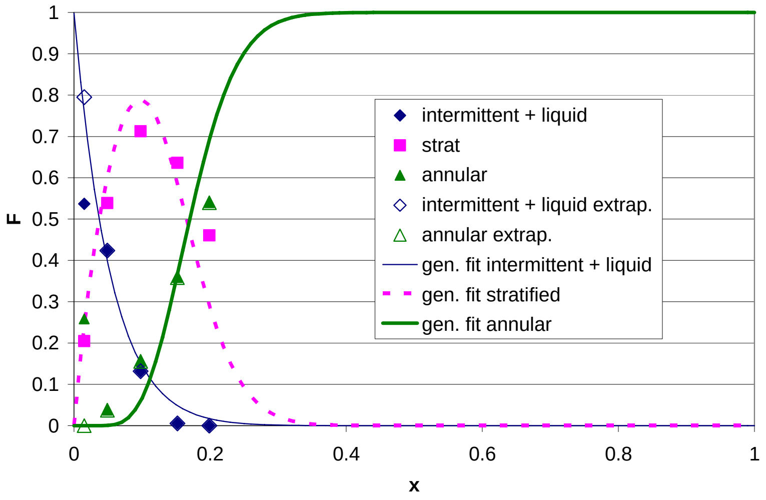

Figure 3.10. Probabilistic flow map with generalized time fraction curve fits for 8.00 mm diameter tube, R410Aa, 25 ºC, 400 kg/m^2-s

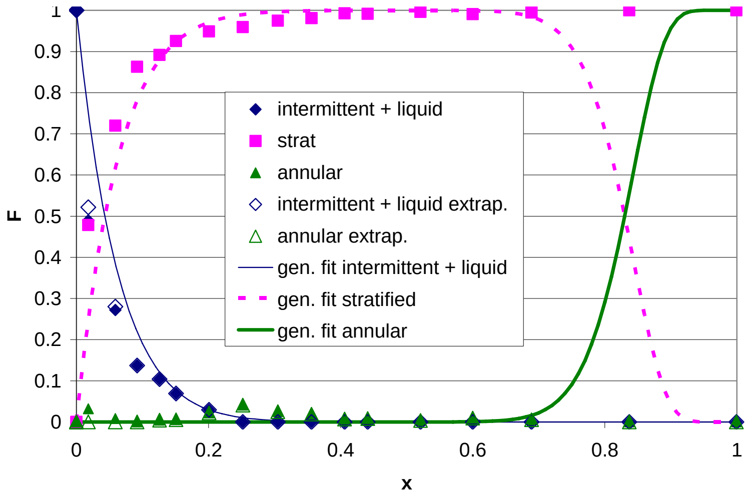

Figure 3.11. Probabilistic flow map with generalized time fraction curve fits for 5.43 mm diameter tube, R134a, 25 ºC, 100 kg/m^2-s

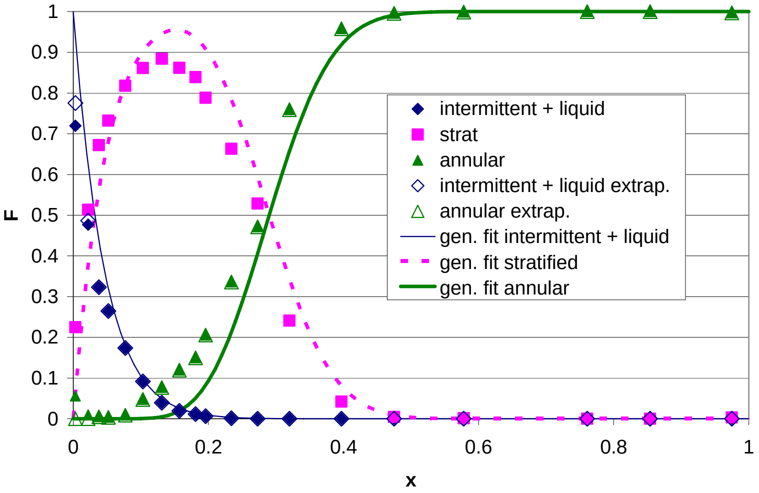

Figure 3.12. Probabilistic flow map with generalized time fraction curve fits for 5.43 mm diameter tube, R134a, 25 ºC, 200 kg/m^2-s

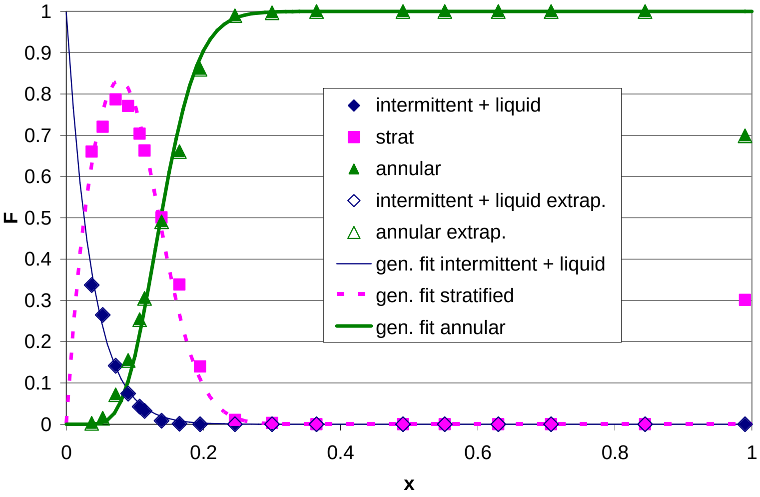

Figure 3.13. Probabilistic flow map with generalized time fraction curve fits for 5.43 mm diameter tube, R134a, 25 ºC, 300 kg/m^2-s

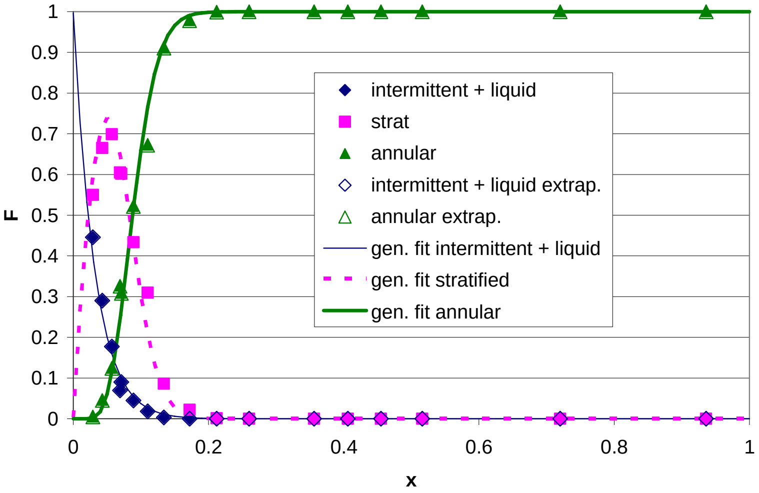

Figure 3.14. Probabilistic flow map with generalized time fraction curve fits for 5.43 mm diameter tube, R134a, 25 ºC, 400 kg/m^2-s

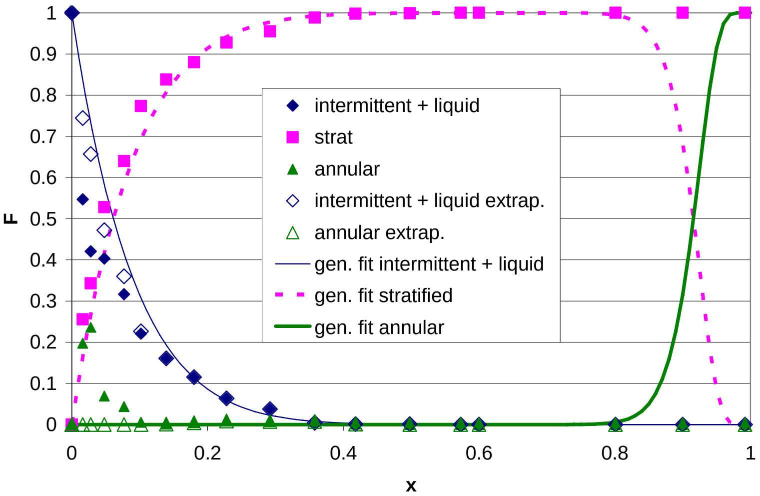

Figure 3.15. Probabilistic flow map with generalized time fraction curve fits for 5.43 mm diameter tube, R410A, 25 ºC, 100 kg/m^2-s

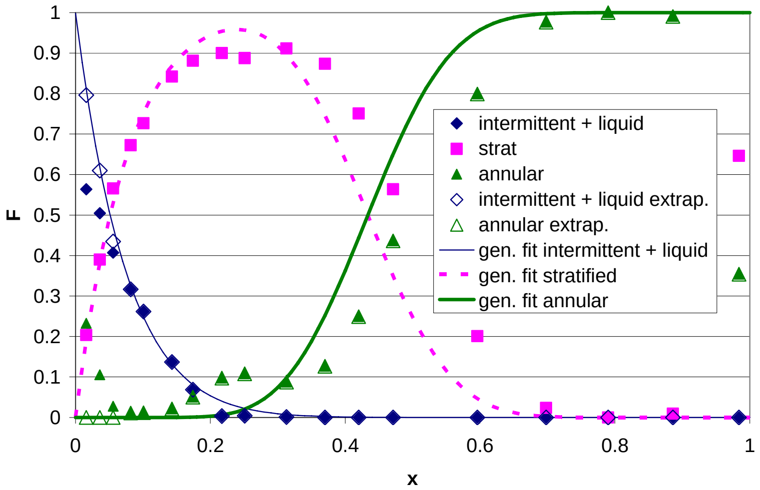

Figure 3.16. Probabilistic flow map with generalized time fraction curve fits for 5.43 mm diameter tube, R410A, 25 ºC, 200 kg/m^2-s

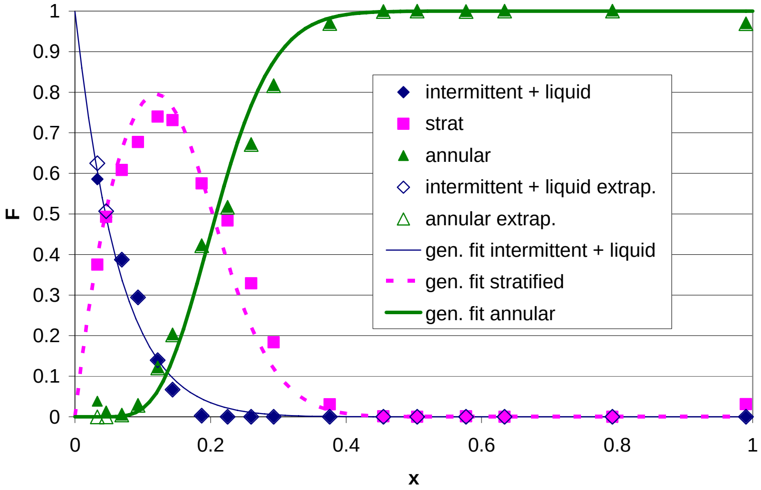

Figure 3.17. Probabilistic flow map with generalized time fraction curve fits for 5.43 mm diameter tube, R410A, 25 ºC, 300 kg/m^2-s

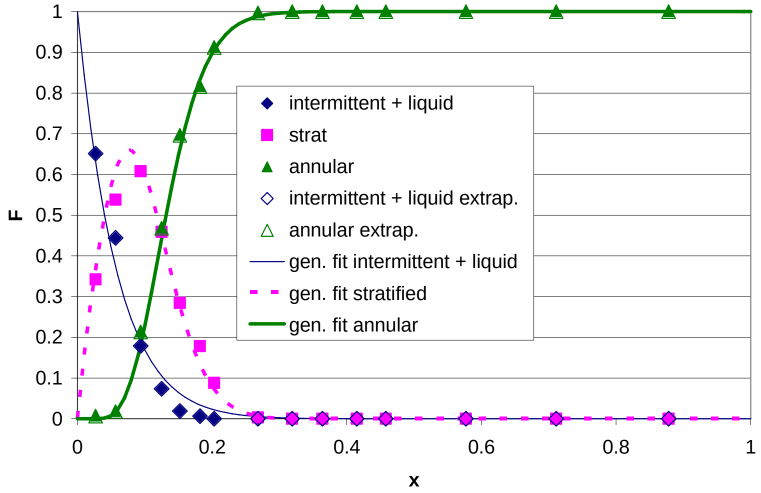

Figure 3.18. Probabilistic flow map with generalized time fraction curve fits for 5.43 mm diameter tube, R410A, 25 ºC, 400 kg/m^2-s

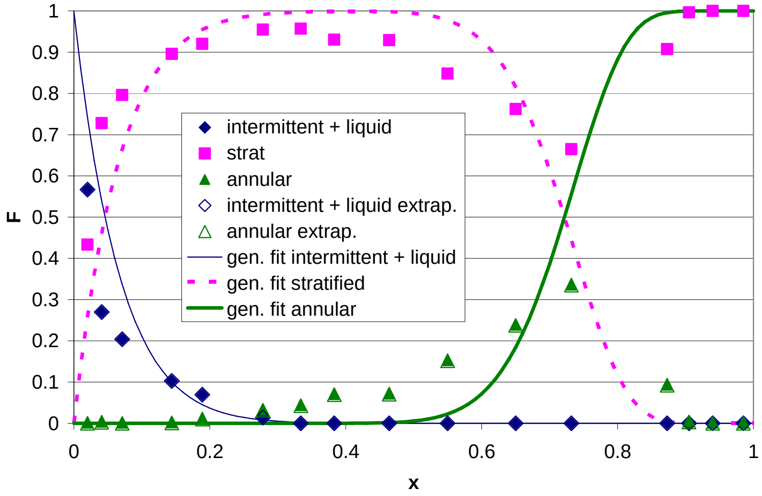

Figure 3.19. Probabilistic flow map with generalized time fraction curve fits for 3.90 mm diameter tube, R134a, 25 ºC, 100 kg/m^2-s

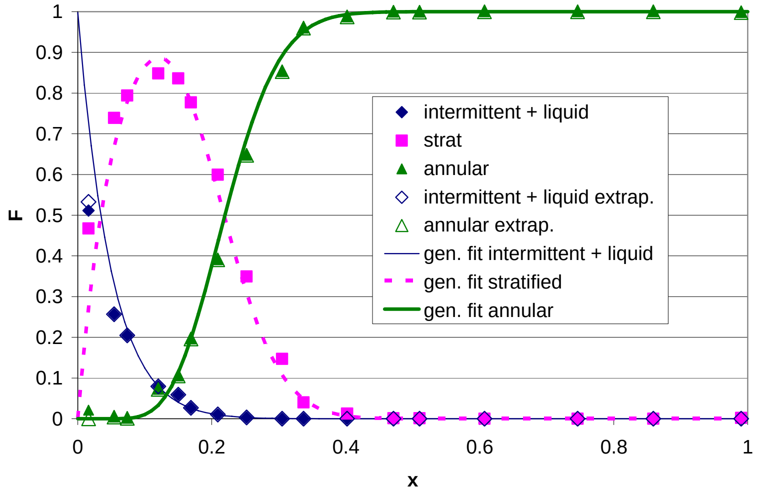

Figure 3.20. Probabilistic flow map with generalized time fraction curve fits for 3.90 mm diameter tube, R134a, 25 ºC, 200 kg/m^2-s

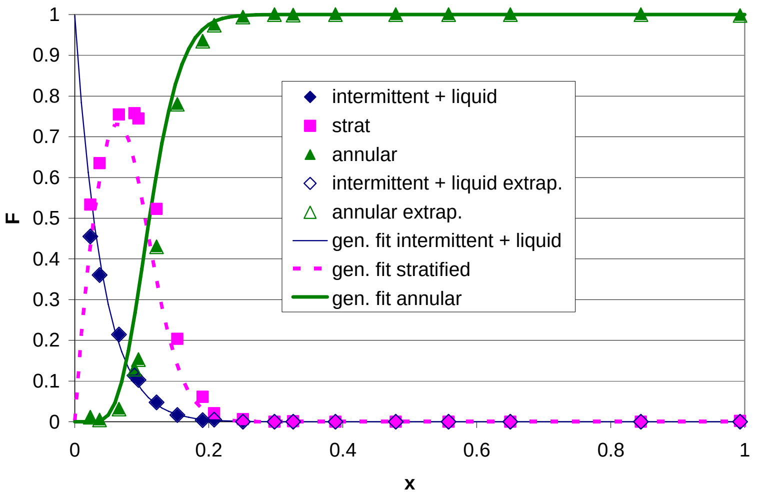

Figure 3.21. Probabilistic flow map with generalized time fraction curve fits for 3.90 mm diameter tube, R134a, 25 ºC, 300 kg/m^2-s

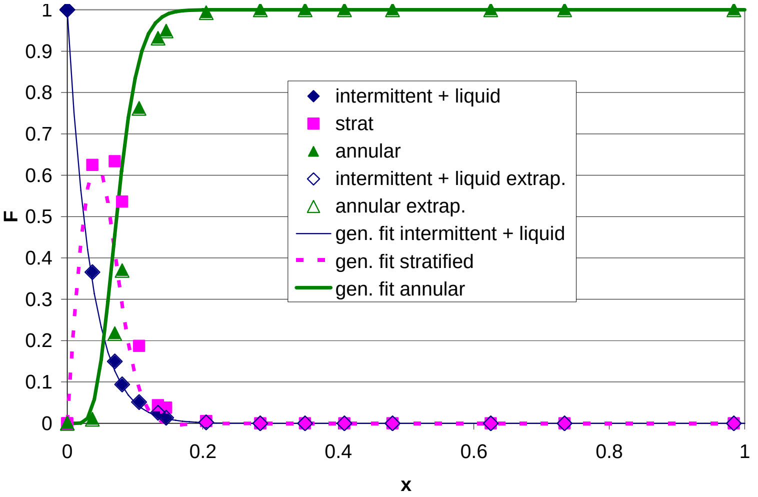

Figure 3.22. Probabilistic flow map with generalized time fraction curve fits for 3.90 mm diameter tube, R134a, 25 ºC, 400 kg/m^2-s

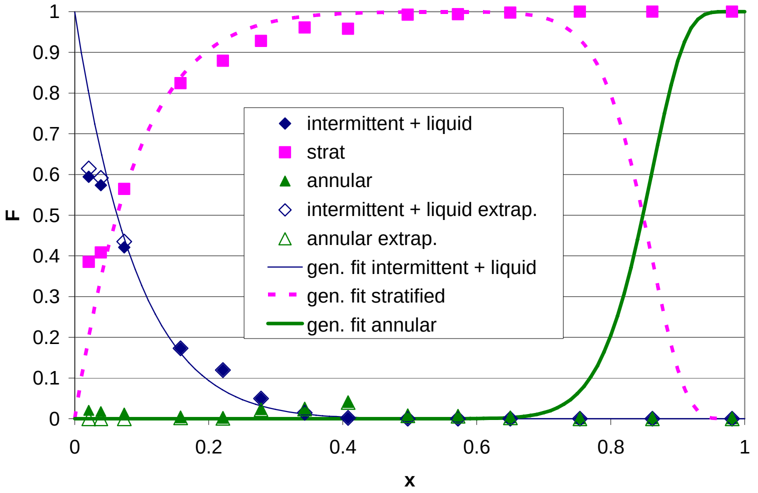

Figure 3.23. Probabilistic flow map with generalized time fraction curve fits for 3.90 mm diameter tube, R410A, 25 ºC, 100 kg/m^2-s

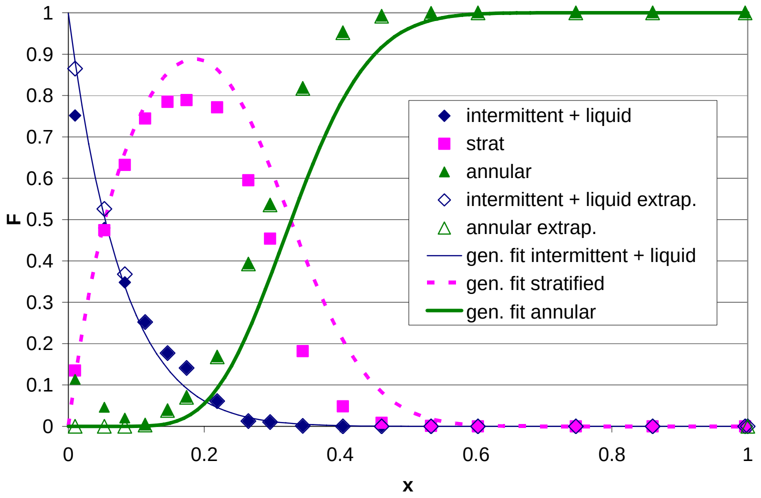

Figure 3.24. Probabilistic flow map with generalized time fraction curve fits for 3.90 mm diameter tube, R410A, 25 ºC, 200 kg/m^2-s

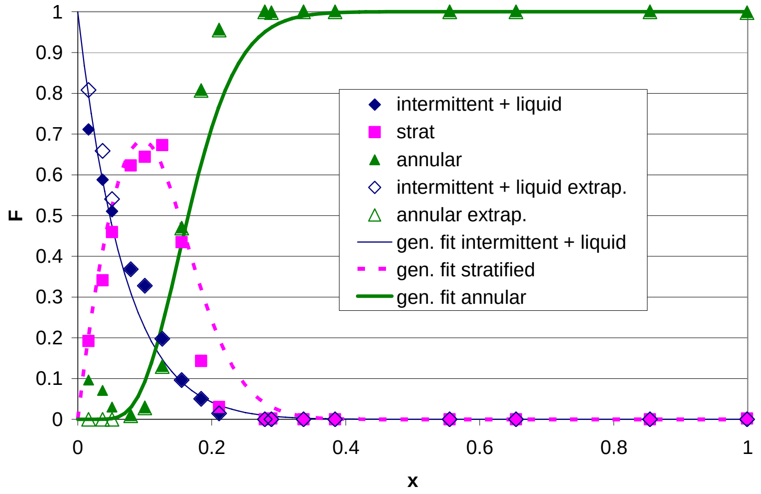

Figure 3.25. Probabilistic flow map with generalized time fraction curve fits for 3.90 mm diameter tube, R410A, 25 ºC, 300 kg/m^2-s

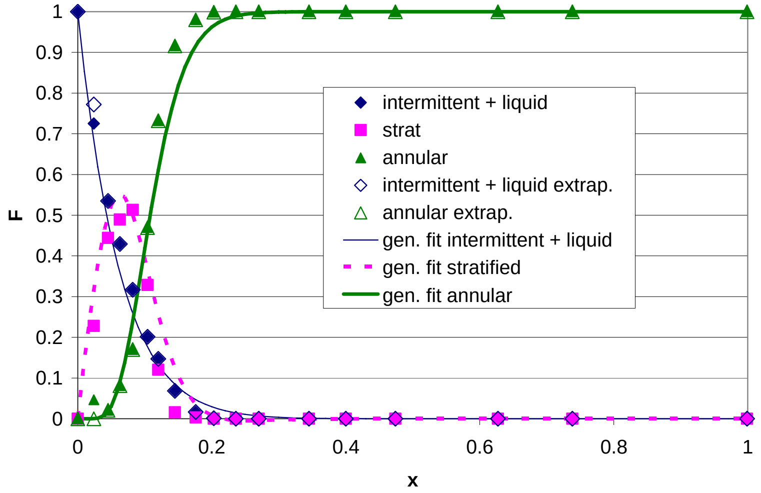

Figure 3.26. Probabilistic flow map with generalized time fraction curve fits for 3.90 mm diameter tube, R410A, 25 ºC, 400 kg/m^2-s

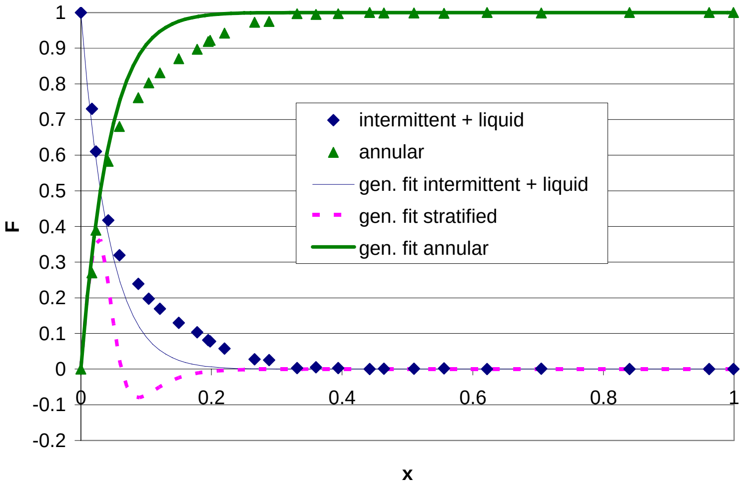

Figure 3.27. Probabilistic flow map with generalized time fraction curve fits for 1.74 mm diameter tube, R134a, 25 ºC, 400 kg/m^2-s

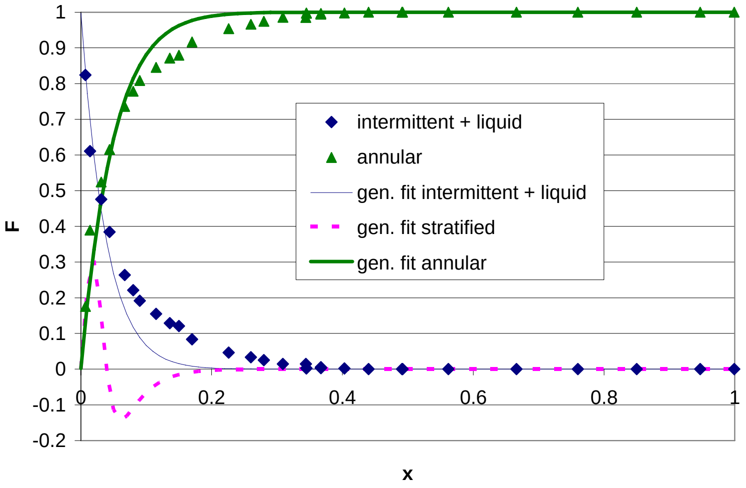

Figure 3.28. Probabilistic flow map with generalized time fraction curve fits for 1.74 mm diameter tube, R134a, 25 ºC, 500 kg/m^2-s

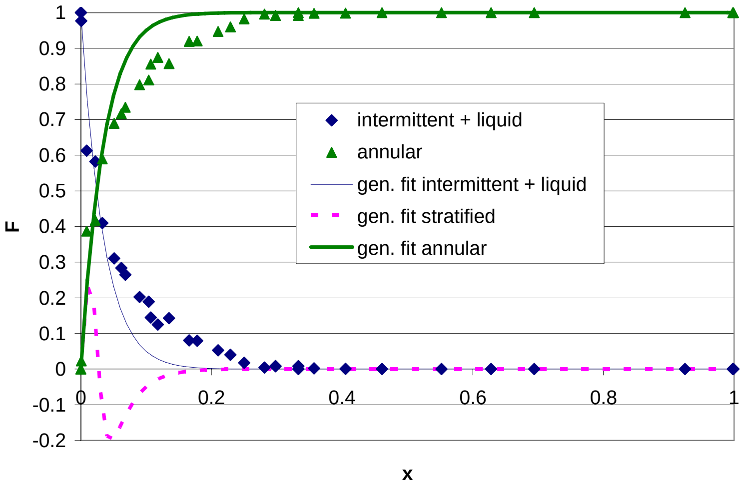

Figure 3.29. Probabilistic flow map with generalized time fraction curve fits for 1.74 mm diameter tube, R134a, 25 ºC, 600 kg/m^2-s

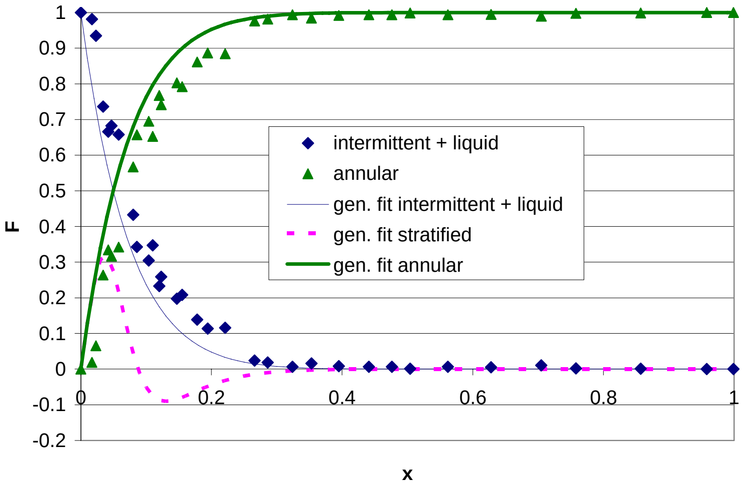

Figure 3.30. Probabilistic flow map with generalized time fraction curve fits for 1.74 mm diameter tube, R410A, 25 ºC, 400 kg/m^2-s

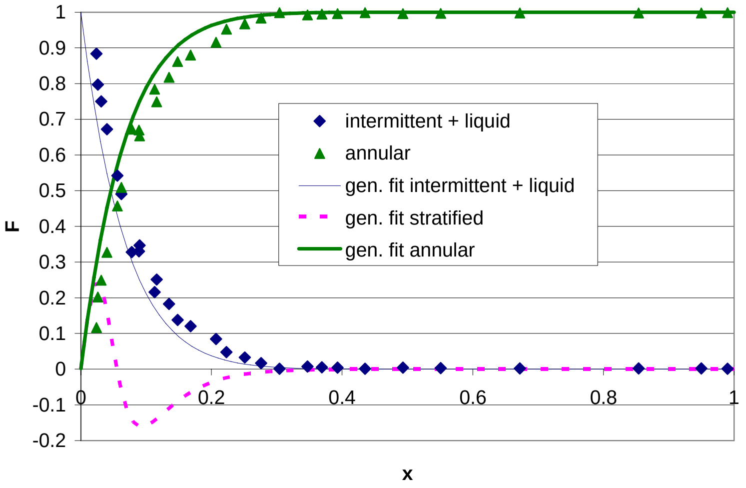

Figure 3.31. Probabilistic flow map with generalized time fraction curve fits for 1.74 mm diameter tube, R410A, 25 ºC, 500 kg/m^2-s

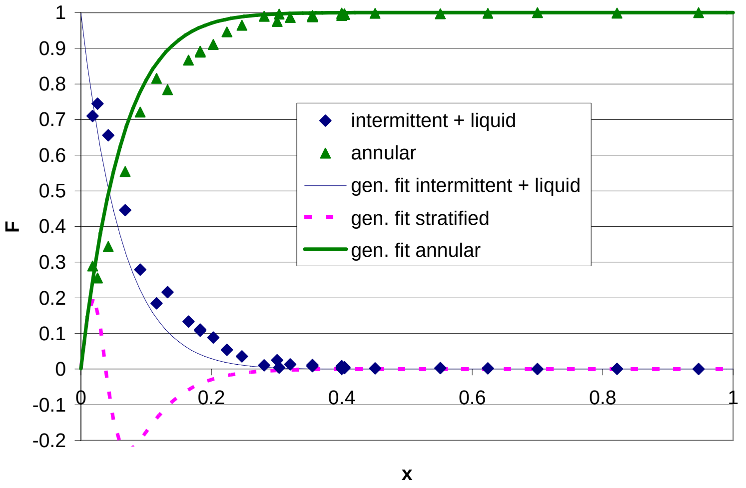

Figure 3.32. Probabilistic flow map with generalized time fraction curve fits for 1.74 mm diameter tube, R410A, 25 ºC, 600 kg/m^2-s

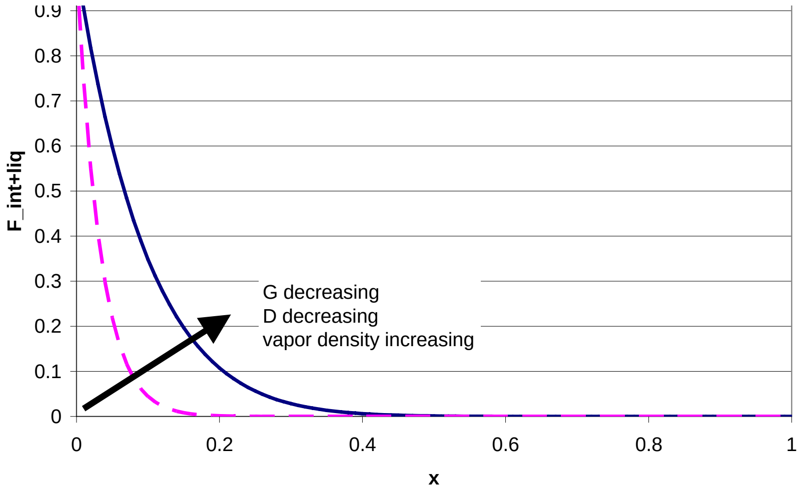

Figure 3.33. Qualitative trend observed as the intermittent/liquid flow regime time fraction curve increases (moves from dashed line to solid line)

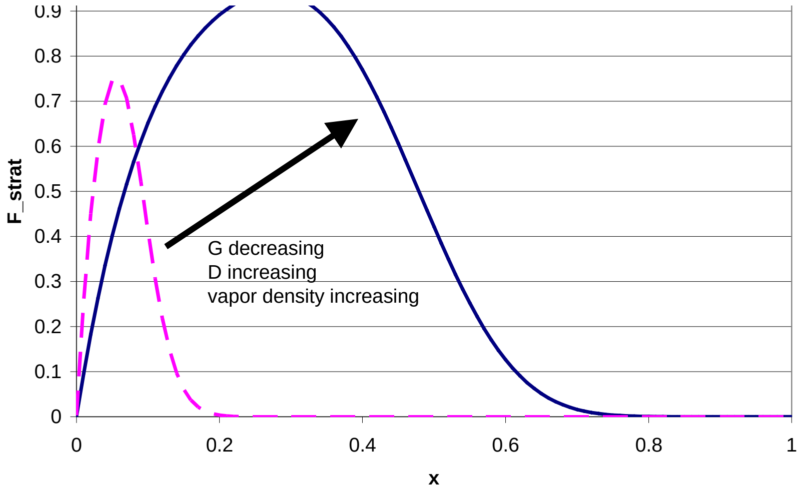

Figure 3.34. Qualitative trend observed as the stratified flow regime time fraction curve increases (moves from dashed line to solid line)

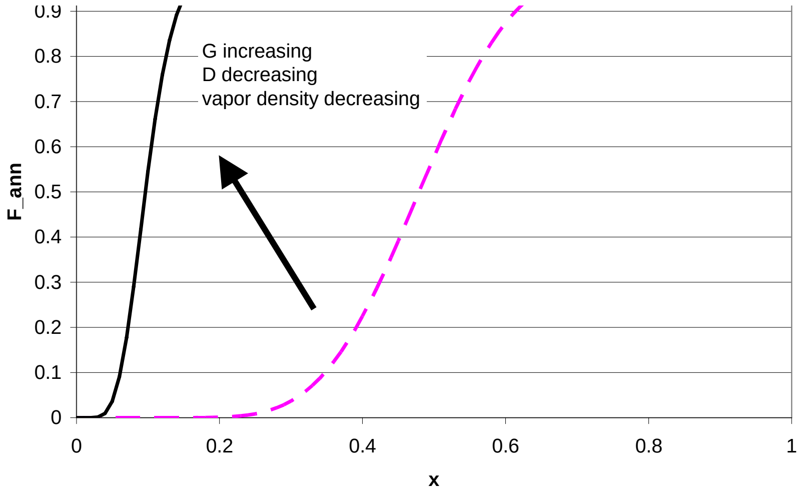

Figure 3.35. Qualitative trend observed as the annular flow regime time fraction curve increases (moves from dashed line to solid line)

3.6 Parametric modeling of time fraction data

A series of modeling functions have been chosen to represent the flow regime characteristics observed in the experimental data. Trends observed in the data caused by parameter variations are accounted for by linking model terms to the observed physical characteristics.

Nonlinear least squares curve fits were made for the intermittent/liquid, stratified, and annular flow regime time fraction data. It was necessary to develop new curve fit functions for single tubes because vapor only flow, observed to be present in multi-port microchannels by Niño (2002), was not observed in single tubes by Jassim et al. (2006a) or anywhere else in the literature except for superheated vapor. Furthermore, the stratified flow regime, absent in microchannels, is present in large tubes. The intermittent/liquid flow regime time fraction function, given in Equation 3.5, is continuous from a quality of 0 to 1 and has the correct physical limits with a time fraction of one at a quality of zero and a time fraction of zero at a quality of one.

$$F_{\mathrm{int}+liq} = (1-x)^i \tag{3.5}$$

The stratified flow regime time fraction function, given in Equation 3.6, is also a continuous function with correct physical limits with a time fraction of zero at a quality of zero and one.

$$F_{strat} = \left(1 - x^{\left(s/\sqrt{x}\right)}\right)^i - (1-x)^i \tag{3.6}$$

In the limit as quality approaches zero the stratified time fraction is equal to zero. However, it is undefined at a quality of zero when using calculators or computers. In order avoid this scenario at a quality of zero, without compromising accuracy, a small number can be added to the quality such as 10^{-10}. The annular flow regime time fraction function, given in Equation 3.7, is simply one minus the time fraction of the other flow regimes.

$$F_{ann} = 1 - F_{\mathrm{int}+liq} - F_{strat} \tag{3.7}$$

These functions represent the time fraction data well as seen in Figure 3.36. for 8.00 mm tube with R134a at 25 ºC and 300 kg/m^2-s and require only 2 curve fit constants which simplifies the generalization of the time fraction functions to physical parameters.

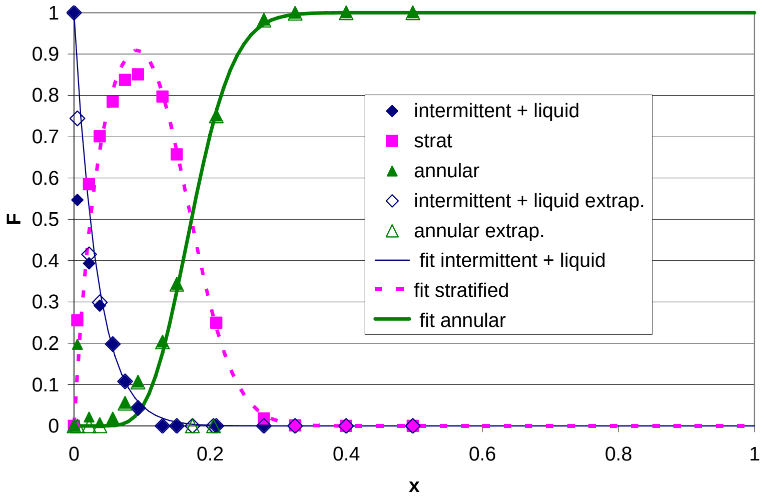

Figure 3.36. Probabilistic flow map with time fraction curve fits for 8.00 mm diameter tube, R134a, 25 ºC, 300 kg/m^2-s

3.7 Generalization of time fraction exponents

The curve fit exponents “i” and “s” of the time fraction curves are linked to physical parameters in order to make the probabilistic two-phase flow regime maps more generally applicable to incremental changes in physical parameters and hence more useful in modeling of two-phase flow. The curve fit exponent “i” is found to have a linear relationship with the dimensionless group *Xi* given in Equation 3.8 and plotted vs. “i” in Figure 3.37.

$$Xi = \left(We_{vo}^{0.4}\right)\left(\frac{\rho_l}{\rho_v}\right) \text{, where} \tag{3.8}$$

Xi contains the vapor only Weber number which is the ratio of the vapor inertial forces to surface tension forces as given in Equation 3.9.

$$We_{vo} = \left(\frac{G^2 D}{\rho_v \sigma}\right) \tag{3.9}$$

The form of *Xi* was determined in order to match the general trends observed in Figure 3.33 for the intermittent/liquid time fraction curves. As the surface tension forces increase in relative value to inertial forces (a result of a decrease in mass flux, or a decrease in pipe diameter, or an increase in vapor density, or an increase in surface tension) and as the liquid to vapor density ratio decreased (vapor density increases) *Xi* decreases (*i* decreases as a result) resulting in the shift of the intermittent/liquid flow regime time fraction from the dashed line to the solid line in Figure 3.33. A least squares linear curve fit, given in Equation 3.10, is made for the *Xi* vs. “*i*” data and shown in Figure 3.37. *Xi* ranges from 105 to 1116 in the present study.

$$i = 0.0243 Xi + 8.07 \tag{3.10}$$

Xi has a linear relationship with the curve fit constant “i” with a linear regression value R^2=0.96. Figure 3.37 does not contain the curve fits of all of the time fraction data obtained by Jassim et al. (2006a). The 1.74 mm data was omitted because it did not seem to fit with the rest of the data. Damianides and Westwater (1988) observed in his air-water flow visualization experiments that the transition from “microchannel” behavior to “large tube” behavior occurs in the 3 mm tube diameter range. They did not observe stratified (“sewer pipe”) flow in tubes smaller than 2 mm in diameter. The 5.43 mm R134a at 49.7 ºC points, 3.90 mm R134a at 35 and 49.7 ºC points also appear to deviate from the relations and were omitted. These deviations may be due to the large temperature difference with the ambient (25 ºC). This could cause some unaccounted error in the quality as a result of refrigerant condensation before it reaches the test section.

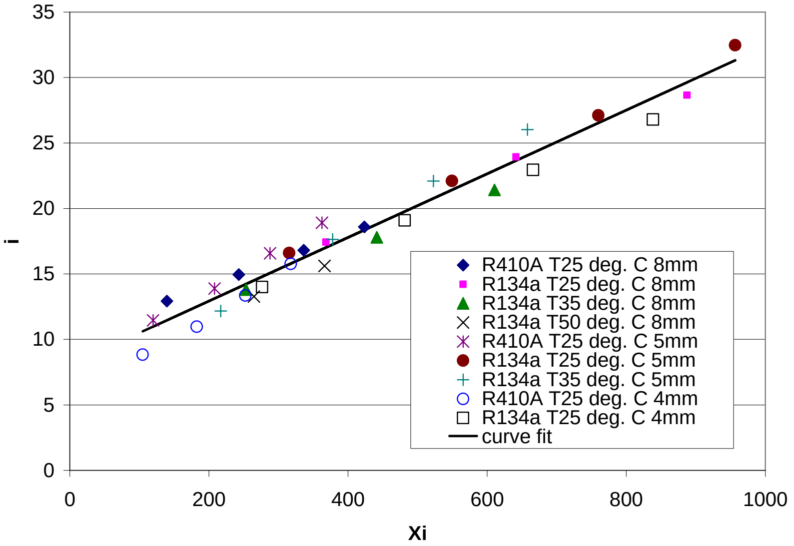

Figure 3.37. The intermittent/liquid time fraction curve fit constants "i" vs. the dimensionless group *Xi*.

The curve fit constant "s" is found to have a strong nonlinear relationship with the dimensionless group *Xs* given in Equation 3.11 and plotted versus "s" in Figure 3.38.

$$Xs = \left(Fr_{vo}^{0.5}\right)\left(\frac{\rho_v}{\rho_l}\right)^{0.65} \tag{3.11}$$

Xs contains the square root of the vapor only Froude number, given in Equation 3.12.

$$Fr_{vo} = \left(\frac{G^2}{\rho_v^2 g_a D}\right) \tag{3.12}$$

The Froude number is a dimensionless term that represents the ratio of inertial to gravitational forces. The form of *Xs* was determined in order to match the general trends observed in Figure 3.34 for the stratified time fraction curves. As the gravitational forces increase in relative value to the inertial forces (as a result of a decrease in mass flux, or an increase in vapor density, or an increase in pipe diameter) *Xs* decreases (*s* increases as a result) resulting in a shift of the stratified flow regime time fraction from the dashed line to the solid line in Figure 3.34. A nonlinear curve fit given in Equation 3.13 is made for the *Xs* vs. "*s*" data and plotted in Figure 3.38

$$s = \frac{1}{0.45Xs} + \frac{1}{0.025Xs^{4.44}} \tag{3.13}$$

In Figure 3.38 the 1.74 mm diameter tubes were omitted since no stratified flow was observed, and the same points were omitted as in Figure 3.37 with the additional omission of the R134a at 49.7 ºC points since there is insufficient high quality data to determine the stratified flow regime constant "*s*", and the points with "*s*" values above 15 because the large slope in this region leads to a high uncertainty.

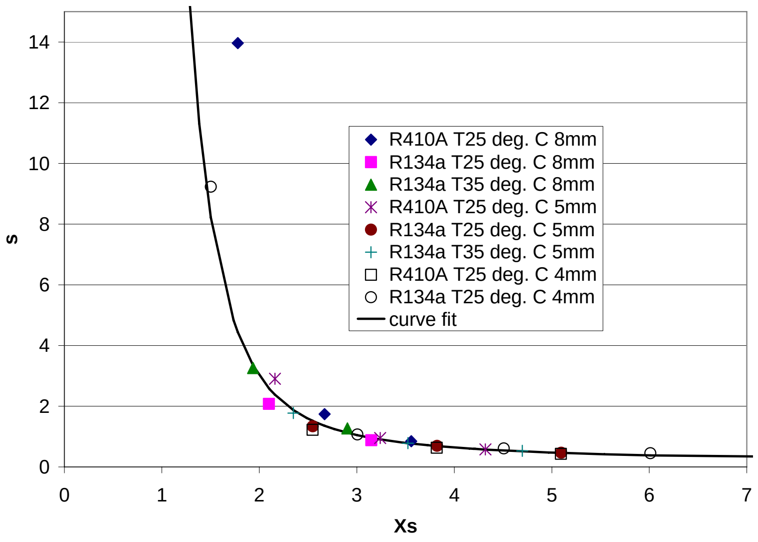

Figure 3.38. The stratified time fraction curve fit constants "s" vs. the dimensionless group *Xs*.

The time fraction functions given in Equations 3.1 through 3.3 for the intermittent/liquid, stratified, and annular flow regimes, respectively are plotted with the time fraction data in Figures 3.4 through 3.26 using the generalized curve fit constant Equations 3.6 and 3.10 for the 3.90 mm diameter and greater data. It can be seen from Figures 3.4 through 3.26 that the generalized time fraction functions reasonably represent the time fraction data. The average error of the generalized time fraction functions with the omission of the time fraction data mentioned above is 0.022, 0.094, and 0.071 for the intermittent/liquid, stratified, and annular flow regimes, respectively. The average error of all of the time fraction data for tubes 3.90 mm and above including the omitted high temperature data is found to be within 0.001 of the above error. The maximum error for all of the predicted intermittent flow regime time fraction is 0.269. The maximum error is found to be 1.0 for the annular and stratified flow regimes with the majority of these points in the high quality ranges where stratified flow exists at mainly 100 kg/m^2-s mass fluxes. The curve fit constant "*s*" approaches infinity as the dimensionless group *Xs* approaches 0. As a result, the slope of the curve fit given in Equation 3.13 is very steep as *Xs* drops below 2. Therefore, it is necessary to obtain additional time fraction data that approaches the fully stratified flow regime, or develop new curve fits in order to obtain a more accurate representation of the time fraction data with *Xs* below 2.

3.8 Evaluation of generalized flow map for 1.74 mm tube

Although the 1.74 mm curve fits for "*i*", the intermittent flow regime curve fit constant, were omitted the generalized curve fit in Equation 3.10 still reasonably represent the intermittent flow regime data as seen in Figures 3.27-3.32. The average and maximum error for the intermittent flow regime in the 1.74 mm tube is 0.044 and 0.22, respectively. The generalized stratified flow regime time fraction, computed using the generalized "s" constant given in Equation 3.14, is relatively insignificant as seen in Figures 3.27-3.32, but is seen to break down at this tube diameter since it yields negative time fraction values which lack a physical basis. Therefore, we have set the stratified flow regime equal to zero at this pipe diameter. Additional data must be obtained in the 3.9 mm to 1.74 mm diameter range to determine where the stratified flow regime can be neglected or to determine new generalized stratified functions which are able to collapse to zero at 1.74 mm diameter. The annular flow regime generalized curves in Figures 3.27-3.32 were obtained by setting the stratified flow regime time fraction to zero, and have an average and maximum error of 0.044 and 0.22, respectively.

3.9 Conclusion

In conclusion, probabilistic two phase flow maps are developed for single, smooth, horizontal, adiabatic tubes. New time fraction functions are developed for single tubes that represent the data well and have physically correct limits. The time fraction function curve fit exponents were determined for R134a at 25 ºC, 35 ºC, and 49.7 ºC, and R410A at 25 ºC with quality ranging from 0 to 1 and mass fluxes varying from 100 to 600 kg/m^2-s in horizontal adiabatic 8.00 mm, 5.43 mm, 3.90 mm, 1.74 mm diameter tubes. Generalized curve fit constants were developed which link the time fraction function curve fit constants to physical parameters. The intermittent flow regime curve fit constant, "*i*", is found to have a linear relationship with a new dimensionless parameter, *Xi*, involving the Webber number and the liquid to vapor density ratio with a linear regression value of 0.96. The stratified flow regime curve fit constant, "*s*", is found to have a strong relationship with the Froude number and the liquid to vapor density ratio. The generalized time fraction functions are found to represent the data well for the 8.00 mm, 5.43 mm, and 3.9 mm diameter tubes with an average error of 0.022, 0.094, and 0.071 for the intermittent/liquid, stratified, and annular flow regimes, respectively. The generalized time fraction functions do not completely extend to the 1.74 mm diameter tube as the stratified flow regime does not collapse to zero. The intermittent flow regime is seen to have an average error of 0.044, and the annular flow regime has the same average error if the stratified flow regime is set to zero. The generalized curve fits allow for probabilistic two phase flow maps to be constructed for flow conditions and tube diameters between those experimentally obtained, which facilitates the incorporation of the time fraction information in two-phase flow models. Caution should be exercised in using the generalized time fraction curve fits for flow conditions and diameters outside the bounds of those tested in the present study and for pipe diameters between 3.9 mm and 1.74 mm. Additional flow visualization experiments are necessary to create or verify that the present generalized time fraction functions are applicable to a wider range of refrigerant properties, tube diameters, and flow conditions.

References

Baker, O., "Simultaneous Flow of Oil and Gas," *Oil and Gas Journal* 53 (1954) 185-195.

Cavallini, A., G. Censi, D. Del Col, L. Doretti, G.A. Longo, and L. Rossetto, "In-Tube Condensation of Halogenated Refrigerants," *ASHRAE Transactions*, 108:1 (2002) 146-161.

Coleman, J.W., S.Garimella, "Two-Phase Flow Regimes in Round, Square and Rectangular Tubes during Condensation of Refrigerant R134a," *International Journal of Refrigeration* 26 (2003) 117-128.

Diamanides, C. and J.W. Westwater, "Two-phase Flow Patterns in a Compact Heat Exchanger and in Small Tubes," *Proceedings of the 2nd. U.K. National Conference on Heat Transfer*, Glasgow, Scotland, (2) (1988) 1257-1268.

Didi, M.B. and N. Kattan, J.R. Thome, "Prediction of Two-Phase Pressure Gradients of Refrigerants in Horizontal Tubes," *International Journal of Refrigeration* 25 (2002) 935-947.

Dobson, M. K. and J.C. Chato, "Condensation in Smooth Horizontal Tubes," *Journal of Heat Transfer* 120 (1998) 245-252.

El Hajal, J., J.R. Thome, and A. Cavalini, "Condensation in Horizontal Tubes, Part 1: Two-Phase Flow Pattern Map," *International Journal of Heat and Mass Transfer* 46 (2003) 3349-3363.

Garimella, S., “Condensation Flow Mechanisms in Microchannels: Basis for Pressure Drop and Heat Transfer Models,” *Heat Transfer Engineering* 25:3 (2004) 104-116.

Garimella, S., J.D. Killion, and J.W. Coleman, “An Experimentally Validated Model for Two-Phase Pressure Drop in the Intermitent Flow Regime for Noncircular Microchannels,” *Journal of Fluids Engineering* 125 (2003) 887-894.

Jassim, E.W. and T. A. Newell. “Prediction of Two-Phase Pressure Drop and Void Fraction in Microchannels using Probabilistic Flow Regime Mapping,” *International Journal of Heat and Mass Transfer* 49 (2006) 2446-2457.

Jassim, E. W., T. A. Newell, and J. C. Chato, “Probabilistic Determination of Two-Phase Flow Regimes Utilizing an Automated Image Recognition Technique,” to be submitted to Experiments In Fluids (2006a)

Mandhane, J.M., G.A. Gregory, and K. Aziz, “A Flow Pattern Map for Gas-Liquid Flow in Horizontal and Inclined Pipes,” *International Journal of Multiphase Flow* 1 (1974) 537-553.

Niño, V.G. “Characterization of Two-phase Flow in Microchannels,” Ph.D. Thesis, University of Illinois, Urbana-Champaign, IL, 2002.

Taitel, Y. and A.E. Dukler, “A Model for Predicting Flow Regime Transitions in Horizontal and Near Horizontal Gas-Liquid Flow,” *American Institute of Chemical Engineering Journal*, 22 (1976) 47-55.

Thome, J.R., J. El Hajal, and A. Cavalini, “Condensation in Horizontal Tubes, Part 2: New Heat Transfer Model Based on Flow Regimes,” *International Journal of Heat and Mass Transfer* 46 (2003) 3365-3387.

Wojtan, L., Ursenbacher, T. and Thome, J.R., 2005, Investigation of Flow Boiling in Horizontal Tubes: Part I – A New Diabatic Two-Phase Flow Pattern Map, *Int. J. Heat Mass Transfer*, Vol. 48: p. 2955-2969.

Wojtan, L., Ursenbacker, T. and Thome, J.R., 2005, Investigation of Flow Boiling in Horizontal Tubes: Part II – Development of a New Heat Transfer Model for Stratified-Wavy, Dryout and Mist Flow Regimes, *Int. J. Heat Mass Transfer*, Vol. 48: p. 2970-2985.

Zurcher, O., D. Farvat, and J.R Thome, “Evaporation of Refrigerants in a Horizontal Tube: And Improved Flow Pattern Dependent Heat Transfer Model Compared to Ammonia Data,” *International Journal of Heat and Mass Transfer* 45 (2002) 303-317.

Zurcher, O., D. Farvat, and J.R. Thome, “Development of a Diabatic Two-Phase Flow Pattern Map for Horizontal Flow Boiling,” *International Journal of Heat and Mass Transfer* 45 (2002) 291-301.

Chapter 4: Prediction of Two-Phase Condensation in Single Tubes Using Probabilistic Flow Regime Maps

4.1 Abstract

A flow regime based condensation model is developed for refrigerants in single, smooth, horizontal tubes utilizing a generalized probabilistic two-phase flow map. The time fraction information from the probabilistic two-phase flow map is used to provide a physically based weighting of heat transfer models developed for different flow regimes. The developed model is compared with other models in the literature and experimentally obtained condensation data of R134a in 8.92 mm diameter tubes and with data found in the literature for 3.14 mm, 7.04 mm, and 9.58 mm tubes with R11, R12, R134a, R22, R410A, and R32/R125 (60/40% by weight) refrigerants and a wide range of mass fluxes and qualities.

4.2 Nomenclature

A_L	cross-sectional area of tube occupied by liquid (m^2)
Cp	specific heat (kJ/kg-K)
D	hydraulic diameter (m)
dP	pressure drop (kPa)
dz	length (m)
e	deviation (-)
e_A	mean absolute deviation (-)
e_R	average deviation (-)
F	observed time fraction (-)
fi	interfacial roughness factor (-)
Fr_{vo}	vapor only Froude number (-)
G	mass flux (kg/m^2-s)
g_a	gravitational acceleration (9.81 m/s^2)
h	heat transfer coefficient (W/m^2-K)
h_{lv}	latent heat of vaporization (kJ/kg)
i	intermittent flow regime curve fit constant (-)
k	thermal conductivity (W/m-K)
N	total number of data points (-)
Pr	Prandtl number (-)
Re_l	superficial liquid Reynolds number (-)
Re_{lt}	Reynolds number of the liquid film (-)
s	stratified flow regime curve fit constant (-)
T	temperature
We_{vo}	vapor only Weber number (-)
x	flow quality (-)
Xi	dimensionless group correlating the intermittent/liquid flow regime (-)
Xs	dimensionless group correlating the stratified flow regime (-)
Xtt	turbulent- turbulent Lockhart - Martinelli parameter (-)

Greek symbols

α	void fraction (-)
α_{ra}	Steiner (1993) version of Rouhani and Axelsson (1970) predicted void fraction given in Equation 4.24 (-)

δ	liquid film thickness of annular ring (m)
μ	dynamic viscosity (kg/m-s)
ρ	density (kg/m^3)
σ	surface tension (N/m)
σ_N	standard deviation
θ	upper angle of the tube not wetted by stratified liquid (radians)

Subscripts

ann	pertaining to the annular flow regime
h	homogeneous
int	pertaining to the intermittent flow regime
int+liq	pertaining to the intermittent and liquid flow regime
l	liquid
liq	pertaining to the liquid flow regime
sat	corresponding to saturation conditions
strat	pertaining to the stratified flow regime
v	vapor
vap	pertaining to the vapor flow regime
wall	at the wall

4.3 Introduction

Numerous two-phase condensation models are available in the literature for specific flow configurations. Recently, flow regime map based models have been developed that span multiple flow regions. The most recent of the flow regime map based models are seen to predict heat transfer for a wide range of tube sizes, fluids, and flow conditions. However, these models are difficult to implement and require interpolation to smoothly transition between flow regimes as a result of the flow regime maps used.

In the present study probabilistic two-phase flow map condensation models, similar to the pressure drop and void fraction models developed by Jassim and Newell (2006), are developed for single, smooth, horizontal tubes in order to predict condensation heat transfer in multiple flow regimes with statistically correlated transitions. An overall condensation heat transfer coefficient is predicted as the sum of the flow regime time fractions multiplied by representative heat transfer models for each flow regime. The time fractions were obtained from a generalized probabilistic two-phase flow regime map for tubes developed by Jassim et al. (2006b). Condensation heat transfer models were identified for the intermittent, stratified, and annular flow regimes. Due to the nature of this model, different condensation models can be implemented. The models developed in the present study predict condensation data of R134a in 8.915 mm diameter smooth tube for a range of qualities and mass fluxes of 100-300 kg/m^2-s experimentally obtained in the present study with an mean absolute deviations of 6%. The present models developed and other flow map based condensation models in the literature are statistically compared to a database of 806 condensation points found in the literature for 3.14 mm, 7.04 mm, and 9.58 mm tubes with R11, R12, R134a, R22, R410A, and 60/40 R32/R125 by weight and a wide range of mass fluxes and qualities. Using this database the present models are found to have errors largely comparable to the models identified in the literature, which makes it a promising new modeling technique for condensation heat transfer and will allow pressure drop and void fraction to be modeled with the same flow regime based time fraction information.

4.4 Literature review

Numerous two-phase flow condensation models can be found in the literature, and most of these models can be categorized as stratified flow models or annular flow models. The Chato (1962) stratified flow model considers film condensation at the top of the tube and neglects the vapor shear driven condensation at the bottom of the tube because the bottom liquid layer is assumed to be thick. Jaster and Kosky (1976) modified the Chato (1962) model by introducing void fraction to account for liquid pool depth variation, but also neglects heat transfer in the liquid pool. This modification is reported by Dobson and Chato (1998) to negatively effect the heat transfer predictions in the stratified flow regime. Rosson and Meyers (1965) developed a model for condensation of acetone and methanol in the stratified and slug plug flow regimes which considered both film condensation and vapor shear driven condensation.

Annular flow heat transfer models can be further divided into two-phase multiplier based, shear based, and boundary layer based models. Two phase multiplier models often resemble a modified Dittus-Boelter (1930) relation such as the condensation models by Akers et al. (1959), Shah (1979), Cavallini and Zecchin (1974), Bivens and Yokozeki (1994), and Tang (1997). Shear based models were originally developed by Carpenter and Colburn (1951) which was subsequently modified by Soliman (1968) who's model was then modified by Chen et al. (1987). Examples of boundary layer correlation based heat transfer models can be found in Traviss et al. (1973), Cavallini and Zecchin (1974) and Hurlburt and Newell (1999). All of the above models tend to predict heat transfer heat transfer most accurately in the flow regime for which they were derived.

Recently, flow regime map based two-phase flow heat transfer models were developed in order to predict condensation heat transfer in multiple flow regimes. Haraguchi et al. (1994) and Dobson and Chato (1998) developed flow regime map based two-phase flow condensation heat transfer models for multiple flow regimes. Dobson and Chato (1998) modeled heat transfer in both the stratified wavy and annular flow regimes. They used a two-phase multiplier approach in developing their annular flow model component. Dobson and Chato's (1998) stratified wavy model component accounted for both forced convective condensation at the bottom of the tube and film condensation at the top of the tube. They used Soliman (1982)'s flow map to determine the transition between stratified wavy and annular flow. Cavallini et al. (2002) then developed a flow regime map based condensation model and validated it with over 2000 data points consisting of 9 different refrigerants in 3.1 to 21.4 mm diameter tubes. Cavallini et al. (2002) accounted for the annular, stratified, and slug flow in their model. They developed an interfacial shear based condensation model for the annular flow regime, a stratified flow model that includes both film and convective condensation, and a slug flow regime model. The transitions between some of the models were determined through an interpolation between the flow regimes. Thome et al. (2003) created a model with less empirical constants and avoids heat transfer jumps across flow regime boundaries that occurs in the Dobson and Chato (1998) and in the slug flow regime transition in the Cavallini et al. (2002) model. Thome et al. (2003) includes models for the intermittent, fully stratified, stratified wavy, annular and mist flow regimes. The annular flow regime model developed is used for intermittent and mist flow regimes. Thome et al (2003) used flow transition criteria from a Steiner (1993) style flow map for condensation conditions which is developed by El Hajal et al. (2003) as a modification of the flow map developed by Kattan et al. (1998) for flow boiling in horizontal tubes. Their model includes the effects of liquid vapor interfacial roughness in their annular flow model and considers both film and convective condensation effects in the stratified wavy and fully stratified flow regimes. An interpolation is used between flow regime boundaries to provide a smooth transition. Thome et al. (2003) compared their flow map based heat transfer model with a larger condensation database of 15 different fluids that includes 1850 refrigerant data points and 2771 hydrocarbon data points. Cavallini et al. (2003) then revised their Cavallini et al. (2002) model to eliminate the discontinuity in the slug flow regime transition.

All of the flow regime map based heat transfer models mentioned utilize traditional Steiner (1993) or Taitel and Dukler (1976) type flow regime maps which indicate a particular flow regime at a given quality and mass flux. The distinct lines seem to lack a physical basis as Coleman and Garimella (2003), El Hajal et al. (2003), and Niño (2002) indicate that more than one flow regime can exist near the boundaries or within a given flow regime on a Steiner (1993) type flow map. Traditional flow maps such as Mandhane (1974), Steiner (1993), and Taitel and Dukler (1976) type flow maps can not be represented as continuous functions for the entire quality range as can be seen from a Steiner (1993) type flow map in Figure 4.1. Consequently, these heat transfer models tend to be complicated with an interpolation scheme to avoid discontinuities at the flow regime boundaries.

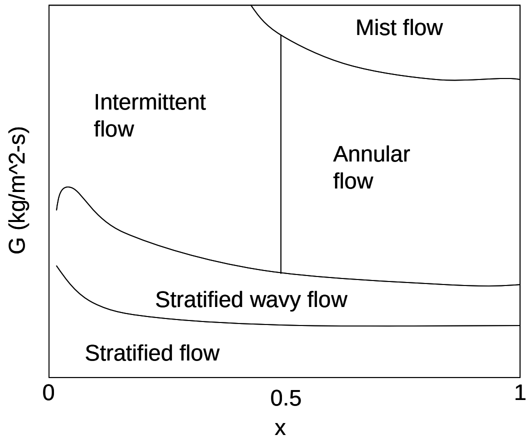

Figure 4.1. Steiner (1993) type flow map depiction

Probabilistic two-phase flow regime maps first developed by Niño (2002) for refrigerant and air-water flow in multi-port microchannels are found by Jassim and Newell (2006) to eliminate the discontinuities created by traditional flow maps. Probabilistic two phase flow regime maps have quality on the horizontal axis and the "fraction of time", *F*, in which a particular flow regime is observed in a series of pictures taken at given flow condition on the ordinate as seen in Figure 4.2. Jassim and Newell (2006) developed curve fit functions to represent the data that are continuous for the entire quality range with correct physical limits for the time fraction data obtained for 6-port microchannels by Niño (2002). Jassim and Newell (2006) then utilized the probabilistic flow regime map time fraction curve fits to predict pressure drop and void fraction as shown in Equations 4.1 and 4.2, respectively.

$$\left(\frac{dP}{dz}\right)_{total} = F_{liq}\left(\frac{dP}{dz}\right)_{liq} + F_{\text{int}}\left(\frac{dP}{dz}\right)_{\text{int}} + F_{vap}\left(\frac{dP}{dz}\right)_{vap} + F_{ann}\left(\frac{dP}{dz}\right)_{ann} \tag{4.1}$$

$$\alpha_{total} = F_{liq}\alpha_{liq} + F_{\text{int}}\alpha_{\text{int}} + F_{vap}\alpha_{vap} + F_{ann}\alpha_{ann} \tag{4.2}$$

Jassim et al. (2006b) then developed probabilistic two-phase flow maps for single tubes with the experimentally obtained time fraction data from Jassim et al. (2006a) who utilized the flow loop depicted in Figure 4.3. Jassim et al. (2006b) developed curve fits for the intermittent/ liquid, stratified and annular flow regime time fraction data. The time fraction functions are given in Equations 4.3 through 4.5 for the intermittent/liquid, stratified, and annular flow regimes, respectively.

$$F_{\mathrm{int}+liq} = (1-x)^{i} \tag{4.3}$$

$$F_{strat} = \left(1 - x^{\left(s/\sqrt{x}\right)}\right)^{i} - (1-x)^{i} \tag{4.4}$$

$$F_{ann} = 1 - F_{\mathrm{int}+liq} - F_{strat} \tag{4.5}$$

The flow maps developed were generalized by linking the time fraction curve fit constants to physical parameters. The intermittent/liquid time fraction curve fit constant "*i*", given in Equation 4.6, has a strong linear relationship with the dimensionless group *Xi*, given in Equation 4.7, which contains the vapor only Webber number, given in Equation 4.8, and the liquid to vapor density ratio.

$$i = 0.0243Xi + 8.07 \tag{4.6}$$

$$Xi = \left(We_{vo}^{0.4}\right)\left(\frac{\rho_l}{\rho_v}\right) \text{, where} \tag{4.7}$$

$$We_{vo} = \left(\frac{G^2 D}{\rho_v \sigma}\right) \tag{4.8}$$

The stratified time fraction curve fit constant "*s*", given in Equation 4.9, has a strong relationship with the dimensionless group *Xs*, given in Equation 4.10, which contains the square root of the vapor only Froude number, given in Equation 4.11, and the vapor to liquid density ratio.

$$s = \frac{1}{0.45Xs} + \frac{1}{0.025Xs^{4.44}} \tag{4.9}$$

$$Xs = \left(Fr_{vo}^{0.5}\right)\left(\frac{\rho_v}{\rho_l}\right)^{0.65} \tag{4.10}$$

$$Fr_{vo} = \left(\frac{G^2}{\rho_v^2 g_a D}\right) \tag{4.11}$$

A sample probabilistic two phase flow regime map with generalized curve fits is depicted in Figure 4.4 for 8.00 mm diameter tube with R134a flowing at 25 ºC and 300 kg/m^2-s. Jassim et al. (2006b) found these generalized curve fit constants to represent the time fraction data with an average absolute error of 0.022, 0.094, and 0.071 for the intermittent/liquid, stratified, and annular flow regimes, respectively, for the 8.00 mm, 5.43 mm, and 3.90 mm diameter tubes. The average absolute error for the 1.74 mm diameter tube in the intermittent flow regime is reported to be 0.044, with the same error for the annular flow regime if the stratified flow regime is neglected, which is not observed for this tube diameter.

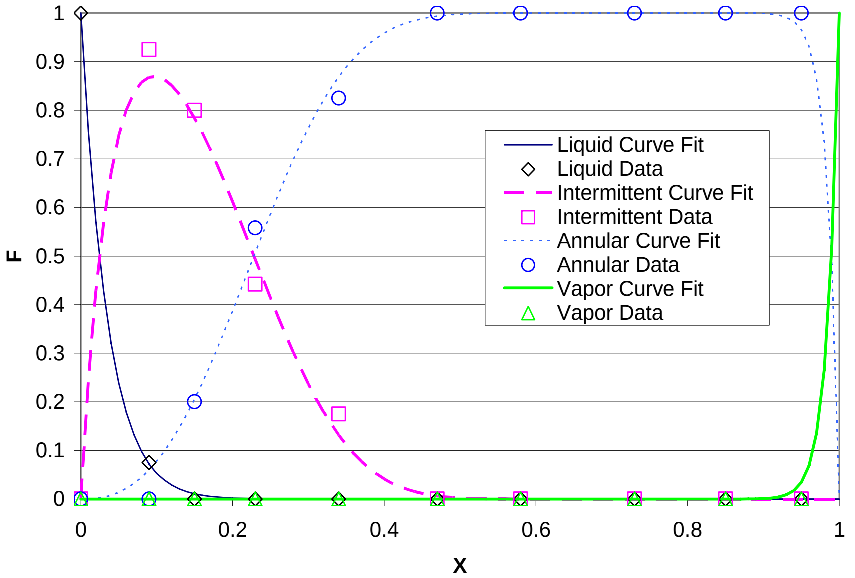

Figure 4.2. Probabilistic flow map with time fraction curve fits for R410A, 10 ºC, 300 kg/m^2-s in a 6-port 1.54 mm hydraulic dia. microchannel taken from Jassim and Newell (2006).

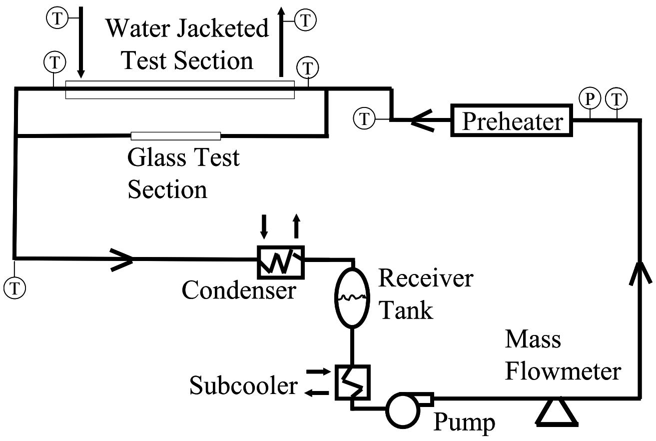

Figure 4.3. Two-phase flow loop schematic

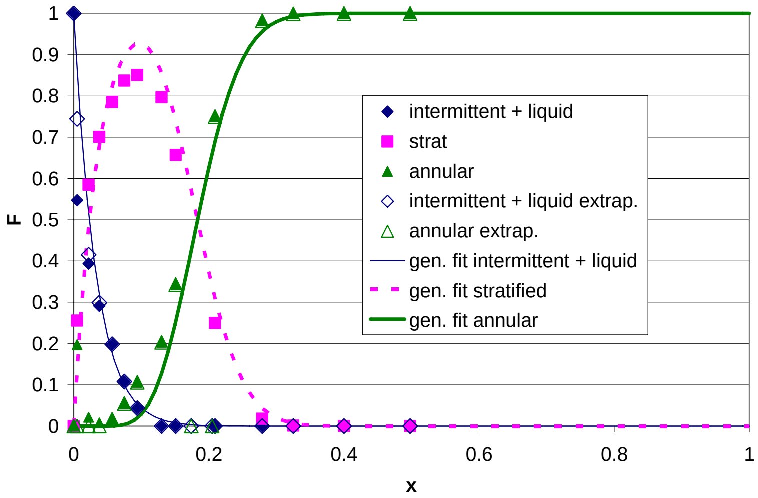

Figure 4.4. Probabilistic flow map with generalized time fraction curve fits for 8.00 mm diameter tube, R134a, 25 ºC, 300 kg/m^2-s.

4.5 Heat transfer data

Heat transfer data was experimentally obtained from the two-phase flow loop facility at the University of Illinois Air Conditioning and Refrigeration Center depicted in Figure 4.3. The liquid refrigerant is pumped with a gear pump that is driven by a variable frequency drive from the bottom of a 2 liter receiver tank through a water cooled shell and tube style subcooler in order to avoid pump cavitation. The liquid refrigerant then travels through a Coriolis style mass flow meter with an uncertainty of ±0.1% followed by a preheater used to reach the desired quality. The preheater consists of a finned tube heat exchanger with opposing electric resistance heater plates bolted on either side of the heat exchanger. The electric heaters are controlled with on/off switches and a variable auto transformer to provide fine adjustment of quality. This preheater design has sufficient thermal mass to avoid "burn-out" at a quality of 100% and has a small enough thermal mass so that steady state conditions can be rapidly attained. The refrigerant is then directed through 90 degree bends to remove effects of heat flux from the preheater such as dryout before it reaches the test section. The refrigerant can be directed either through the flow visualization test section, used by Jassim et al. (2006a), or a heat transfer test section used in the present study. Finally, the refrigerant is condensed in a water cooled brazed plate heat exchanger and is directed back into the receiver tank. The pressure before the inlet of the preheater is measured by a pressure transducer with an uncertainty of ±1.9 kPa. The temperatures before the inlet of the preheater and the test section are measured with type T thermocouples. These pressures and temperatures are used to determine the thermodynamic states necessary to compute the test section inlet quality. An energy balance was performed by heating single phase flow in the preheater and measuring the temperature difference across it along with the flow rate to determine the uncertainty associated with the preheater power input which is ±0.8%.

The test sections consists of an 8.915 mm I.D. copper tube with 4 stations of 4 thermocouples welded on the walls and a clear P.V.C water jacket as seen in Figure 4.5. The wall temperature is determined as the average of the 16 thermocouples welded on the tube wall. Insulation is placed on the outside of the water jacket. The test section is cooled with water supplied from a water conditioner at 15.7 ºC. Thermocouples are placed at the inlet and outlet of the test section in order to determine the average refrigerant temperature. A flow meter is placed in the water jacket loop and thermocouples are placed at the inlet and exit of the test section water jacket in order to determine the heat lost by the copper tube test section. A mixing section consisting of a collapsed plastic net is placed in the water flow stream at the exit of the test section to ensure that the average water temperature is measured. After the test section the refrigerant is condensed in a flat plate heat exchanger with cold water at 5 ºC. The loop temperature is controlled by varying the flow rate of the cold water entering the flat plate condenser. All of the thermocouples in the test section and flow loop are type T and were calibrated with an RTD with an uncertainty of ±0.01 ºC and are determined to have an uncertainty of ±0.1 ºC. Single phase heat transfer tests were conducted to verify that the experimental apparatus is working properly. The single phase heat transfer coefficients for heated sub-cooled liquid R134a in 8.915 mm diameter smooth copper tube at different mass fluxes can be observed in Figure 4.6 along with the Dittus Boelter single phase heat transfer correlations. From this figure it can be seen that the data has good agreement with the Dittus Boelter correlation with all of the predicted points within the experimental uncertainty. There is a set of low heat flux points at the same mass flux as other higher heat flux points indicated in Figure 4.6 which explains the scatter of the data at the low mass flux range. A waterside and refrigerant side energy balance was performed on the single phase tests yielding a maximum error of 5%. All measurements in the present study represent the average of approximately 50 measurements taken at 3 second intervals by a data acquisition system.

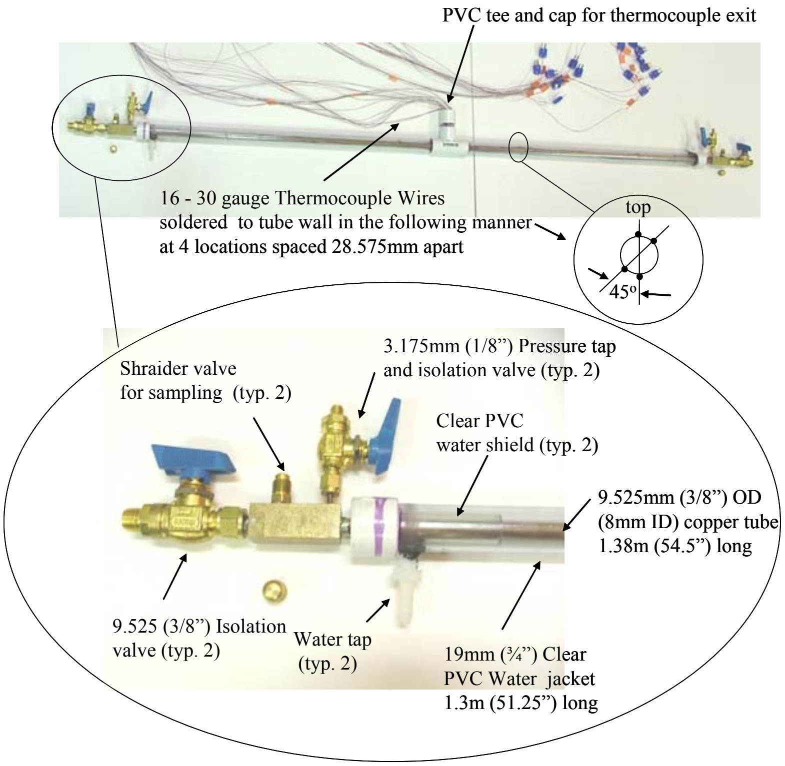

Figure 4.5. Heat transfer test section design

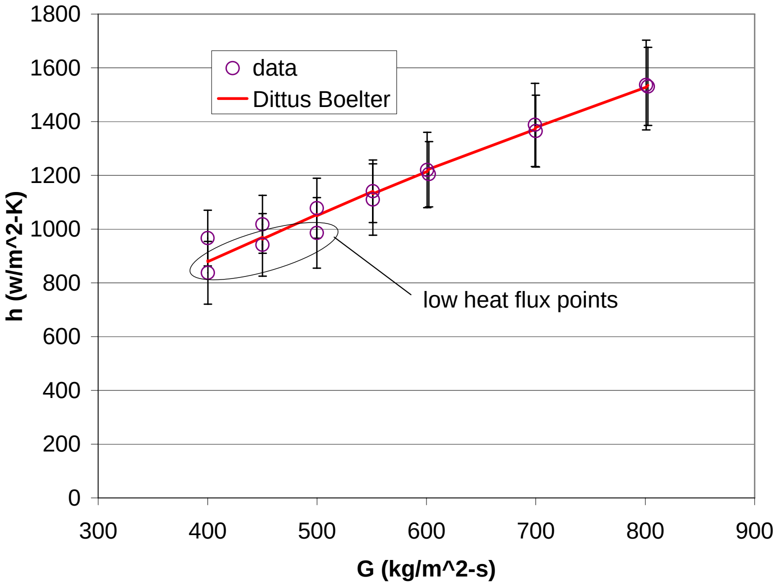

Figure 4.6. Sub-cooled liquid R134a heat transfer in 8.915 mm diameter smooth tube with heat addition varying from 2,600 to 5,600 W/m^2-K

Condensation heat transfer measurements were obtained for R134a at 25 ºC saturation temperature in smooth 8.915 mm diameter copper tube with heat fluxes ranging from 4,600 to 5,600 W/m^2 and mass fluxes of 100, 200, and 300 kg/m^2-s as seen in Figures 4.7 through 4.9, respectively. The uncertainty in average quality is found to be less than ±1% for all the data in Figures 4.7 through 4.9. The average mass flux is found to be within ±1% of the values reported in Figures 4.7 through 4.9. The heat flux varied because the cooling water temperature was held constant. From Figures 4.7 through 4.9 it can be seen that the experimental data agrees well with the models presented by Dobson and Chato (1998), Cavallini (2002), Thome et al. (2003), and the probabilistic flow map based models developed in the present study with different annular flow models used. The models are represented as points, instead of curves, since the heat flux and mass flux varied from point to point.

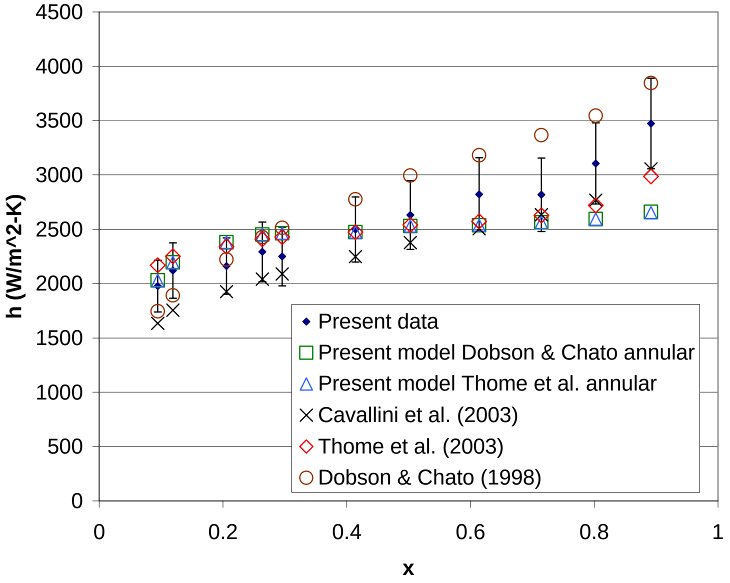

Figure 4.7. Average quality vs. condensation heat transfer coefficients for R134a, 25 ºC, 100 kg/m^2-s, in 8.915 mm I.D. smooth tube, 4600-5400 W/m^2

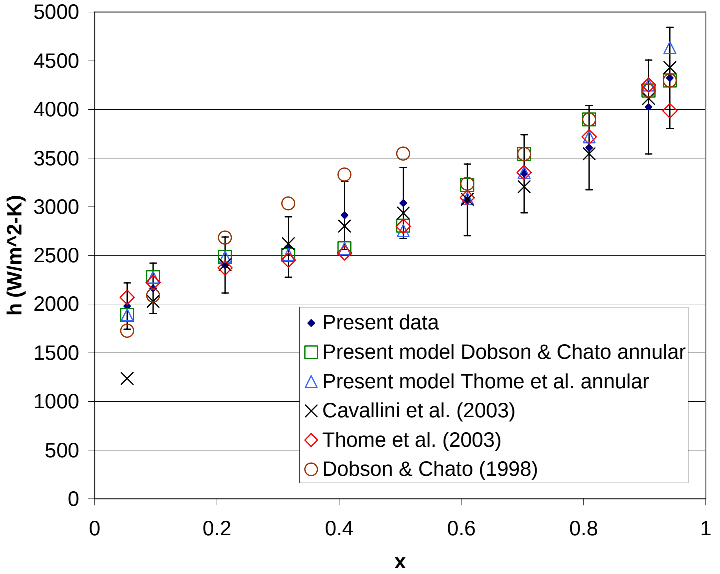

Figure 4.8. Average quality vs. condensation heat transfer coefficients for R134a, 25 ºC, 200 kg/m^2-s, in 8.915 mm I.D. smooth tube, 4700-5600 W/m^2

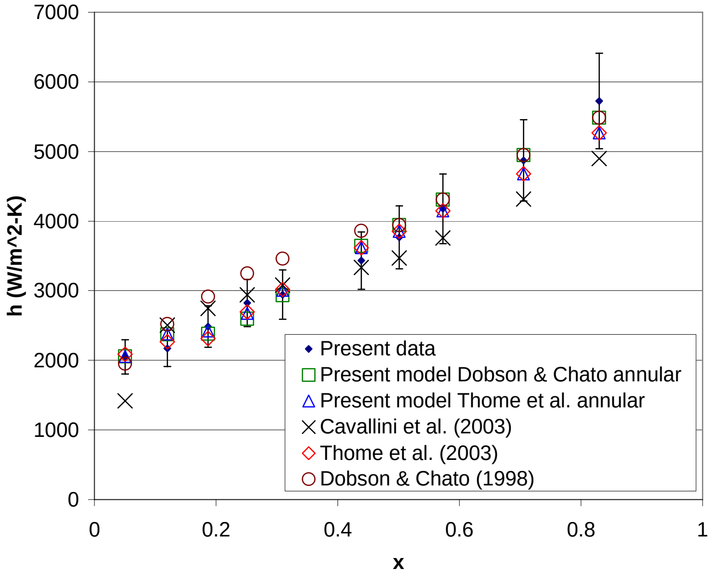

Figure 4.9. Average quality vs. condensation heat transfer coefficients for R134a, 25 ºC, 300 kg/m^2-s, in 8.915 mm I.D. smooth tube, 4700-5500 W/m^2

4.6 Probabilistic two-phase flow map condensation model

A probabilistic two-phase flow map condensation model is formulated for tubes in a similar manner as was formulated for pressure drop and void fraction in microchannels by Jassim and Newell (2006) in Equations 4.1 and 4.2, respectively. The probabilistic two-phase flow map condensation model given in Equation 4.12 is simply the sum of the time fraction for each flow regime multiplied by a model developed for its respective flow regime.

$$h_{total} = F_{\text{int}+liq} h_{\text{int}+liq} + F_{strat} h_{strat} + F_{ann} h_{ann} \tag{4.12}$$

In this way the model applies the appropriate assumptions for a full range of flow conditions. This model is flexible in that different heat transfer models can be chosen for a given flow regime. Furthermore, it allows for pressure drop, void fraction, and heat transfer to be modeled on a consistent flow regime time fraction weighted basis. Simple heat transfer models are developed or identified for each flow regime in the subsequent model description in order to illustrate the effectiveness and flexibility of this modeling technique.

4.6.1 Intermittent/liquid flow regime condensation model

A condensation model based on a modified Dittus Boelter relation is given in Equation 4.13, is developed for the intermittent/liquid flow regime.

$$h_{\text{int}+liq} = 0.023\left(\frac{k_l}{D}\right)\left(\frac{GD}{\mu_l}\right)^{0.8} \Pr_l^{\ 0.3}\text{, where} \tag{4.13}$$

$$\Pr_l = \frac{\mu_l Cp_l}{k_l} \tag{4.14}$$

The Dittus Boelter equation which was developed for turbulent single phase flow is modified by using the two-phase mass flux while using the liquid refrigerant properties. This model assumes that the vapor phase is not contributing to the heat transfer other than the fact that it is a contributor to the total mass flux. As the quality approaches zero, Equation 4.13 approaches the Dittus Boelter equation which is the correct physical limit.

4.6.2 Stratified flow regime condensation model

The Chato (1962) model, given in Equation 4.15, is utilized for the stratified flow regime.

$$h_{strat} = 0.555\left(\frac{k_l}{D}\right)\left(\frac{\rho_l(\rho_l-\rho_v)gh_{lv}D^3}{k_l\mu_l(T_{sat}-T_{wall})}\right)^{0.25} \qquad (4.15)$$

This model was used because it is simple and gives reasonable heat transfer results in the stratified flow regime.

4.6.3 Annular flow regime condensation model

Two different simple annular flow regime models found in the literature were used to represent h_{ann} in the present model for illustration purposes. The Dobson and Chato (1998) two-phase multiplier based heat transfer model for annular flow, given in Equation 4.16, is used to represent h_{ann}.

$$h_{ann} = 0.023\left(\frac{k_l}{D}\right)\mathrm{Re}_l^{0.8}\,\mathrm{Pr}_l^{0.4}\left(1+\frac{2.22}{X_{tt}^{\ 0.889}}\right), \text{ where} \qquad (4.16)$$

$$X_{tt} = \left(\frac{1-x}{x}\right)^{0.9}\left(\frac{\rho_v}{\rho_l}\right)^{0.5}\left(\frac{\mu_l}{\mu_v}\right)^{0.1} \text{, and} \qquad (4.17)$$

$$\mathrm{Re}_l = \frac{GD(1-x)}{\mu_l} \qquad (4.18)$$

The annular portion of the more recently developed Thome et al. (2003) model, which was verified with a wide range of refrigerant and hydrocarbon properties and tube sizes, is also used to represent h_{ann} in the present model. The Thome et al (2003) annular flow, given in Equations 4.19-4.26, is more complicated than that of Dobson and Chato (1998).

$$h_{ann} = 0.003\,\mathrm{Re}_{lt}^{0.74}\,\mathrm{Pr}_l^{0.5}\,\frac{k_l}{\delta}f_i \qquad (4.19)$$

$$f_i = 1+\left(\frac{u_v}{u_l}\right)^{0.5}\left(\frac{(\rho_l-\rho_v)g_a\delta^2}{\sigma}\right)^{0.25} \qquad (4.20)$$

$$\mathrm{Re}_{lt} = \frac{4G(1-x)\delta}{(1-\alpha)\mu_l} \qquad (4.21)$$

$$\delta = 0.5D-0.5\left(D^2-\frac{8A_L}{2\pi-\theta}\right)^{0.5} \text{, where } \theta = 0 \text{ for annular flow} \qquad (4.22)$$

$$A_L = \frac{\pi D^2}{4}(1-\alpha) \qquad (4.23)$$

$$\alpha_{ra} = \frac{x}{\rho_v}\left[\left(1+0.12(1-x)\right)\left(\frac{x}{\rho_v}+\frac{1-x}{\rho_l}\right)+\frac{1.18(1-x)\left[g_a\sigma(\rho_l-\rho_v)\right]^{0.25}}{G\rho_l^{0.5}}\right]^{-1} \qquad (4.24)$$

$$\alpha_h = \left[1+\left(\frac{1-x}{x}\right)\left(\frac{\rho_v}{\rho_l}\right)\right]^{-1} \qquad (4.25)$$

$$\alpha = \frac{\alpha_h - \alpha_{ra}}{\ln\left(\frac{\alpha_h}{\alpha_{ra}}\right)} \tag{4.26}$$

4.7 Probabilistic two-phase flow map condensation model evaluation

The probabilistic two-phase flow map condensation models developed in the present paper are compared with data from multiple sources, summarized in Table 4.1, and with models developed in the literature. The present model using the Thome et al. (2003) annular flow model and using the Dobson and Chato (1998) annular flow model, the Dobson and Chato (1998) model, the Cavallini et al. (2003) model, and the Thome et al. (2003) model predictions are plotted versus the experimental data summarized in Table 4.1 for R11, R12, R134a, R22, R410A, R32/R125 (60/40% by mass) in Figures 4.10 through 4.15, respectively. Figure 4.16 depicts a plot of all of the refrigerant data versus the predictions of the present models along with the models of Dobson and Chato (1998), Cavallini et al. (2003), and Thome et al. (2003). From these figures it can be seen that all five models represent the data well. However, there seems to be a systematic over prediction of the highest pressure R32/R125 (60/40% by weight) refrigerant data by the Dobson and Chato (1998) model which was also noted by Cavallini et al (2003). As a result, the present model using the Dobson and Chato (1998) annular flow model is also seen to over predict the R32/R125 (60/40% by weight) data. A statistical comparison of the present models, the Dobson and Chato (1998) model, the Cavallini et al. (2003) model, and the Thome et al. (2003) model with all of the data detailed in Table 4.1 is summarized in Table 4.2. Table 4.2 contains the mean absolute deviation, e_A, the average deviation, e_R, and the standard deviation, σ_N, given in Equations 4.26 through 4.28, respectively, along with the percentage of predicted points lying with in ±20% error bars.

$$e_A = \frac{1}{N}\sum 100\left|\frac{h_{pred} - h_{data}}{h_{data}}\right| \tag{4.26}$$

$$e_R = \frac{1}{N}\sum 100\left(\frac{h_{pred} - h_{data}}{h_{data}}\right) \tag{4.27}$$

$$\sigma_N = \left[\frac{1}{N-1}\sum (e - e_R)^2\right]^{0.5} \quad \text{where,} \quad e = 100\left(\frac{h_{pred} - h_{data}}{h_{data}}\right) \tag{4.28}$$

It is evident from Table 4.2 that present probabilistic two-phase flow map based condensation models are comparable to the models presented by Dobson and Chato (1998), Cavallini et al. (2003), and Thome et al. (2003) when compared to the present data set. The present condensation model using the Thome et al. (2003) model is seen to have less deviation than the present condensation model using the Dobson and Chato (1998) annular flow model for the high pressure R32/R125 (60/40% by weight) data as observed in Figure 4.15.

Table 4.1. Condensation data pool used to compare the present models with other models in the literature

Source	D (mm)	Refrigerants	G (kg/m^2-s)	T_{sat}(°C)	T_{sat}-Twall(°C)	Data points
Dobson (1994)	3.14, 7.04	R134a, R22, R410A, R32(60%)/R125(40%) by mass	63-773	33.5 - 46.4	1.1 - 8.8	644
Sacks (1975)	9.576	R11, R12, R22	82-902	25 - 32	0.7 - 9.9	130
Present study	8.915	R134a	100 - 300	25	1.0 - 2.4	32

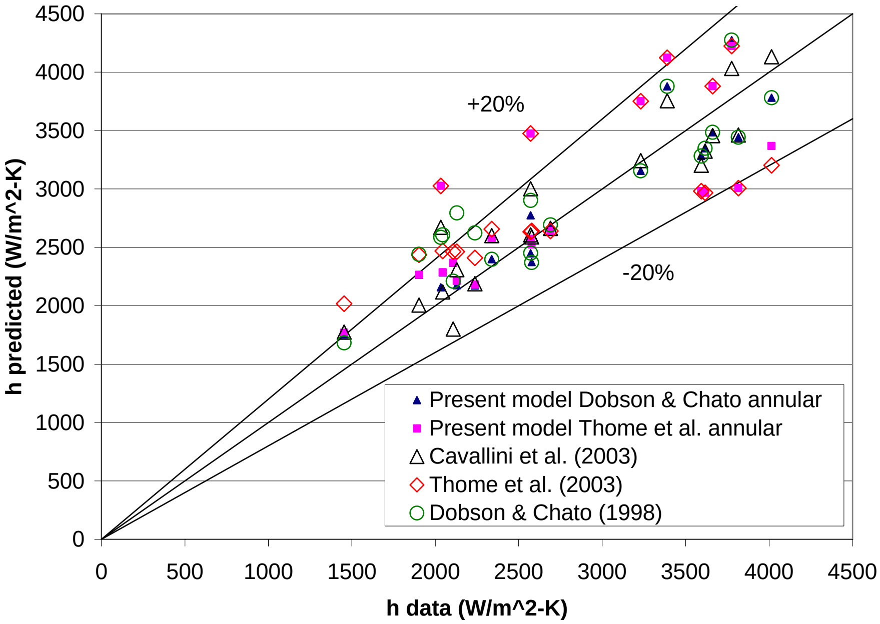

Figure 4.10. Experimental vs. predicted condensation heat transfer for R11 data outlined in Table 4.1

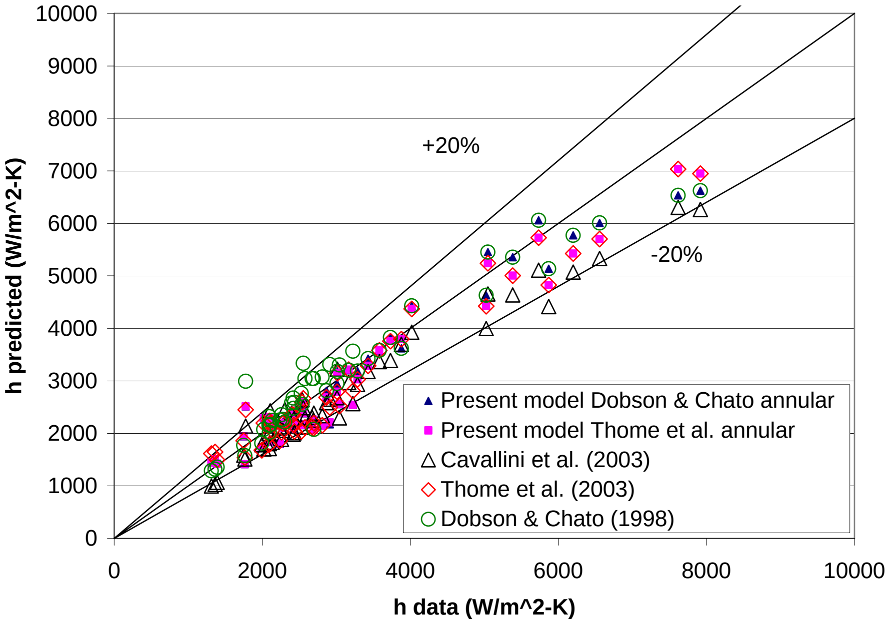

Figure 4.11. Experimental vs. predicted condensation heat transfer for R12 data outlined in Table 4.1

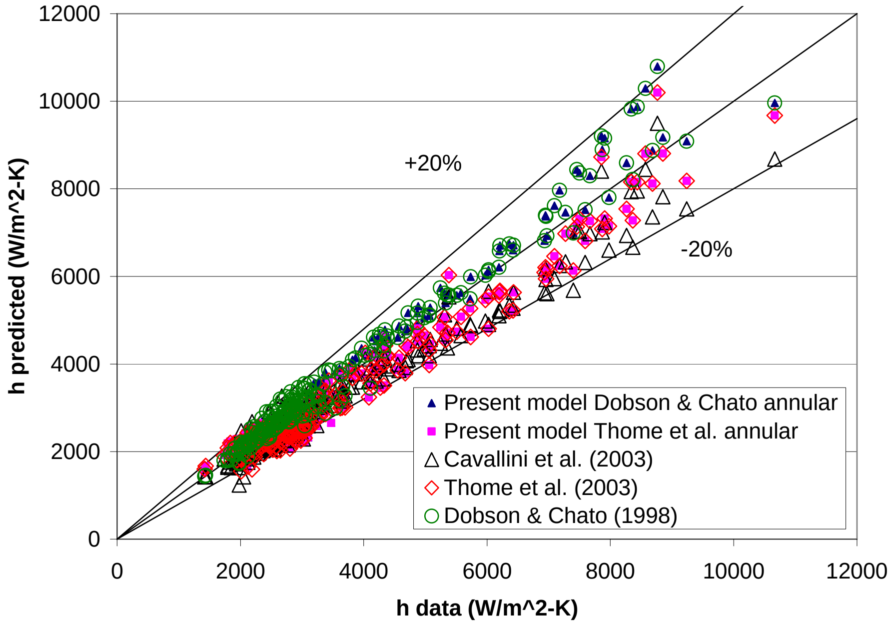

Figure 4.12. Experimental vs. predicted condensation heat transfer for R134a data outlined in Table 4.1

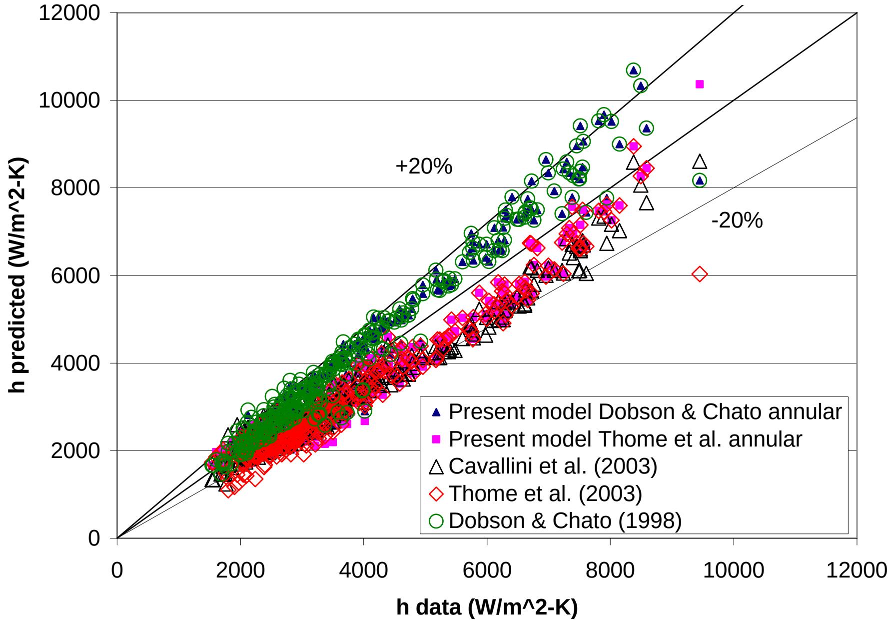

Figure 4.13. Experimental vs. predicted condensation heat transfer for R22 data outlined in Table 4.1

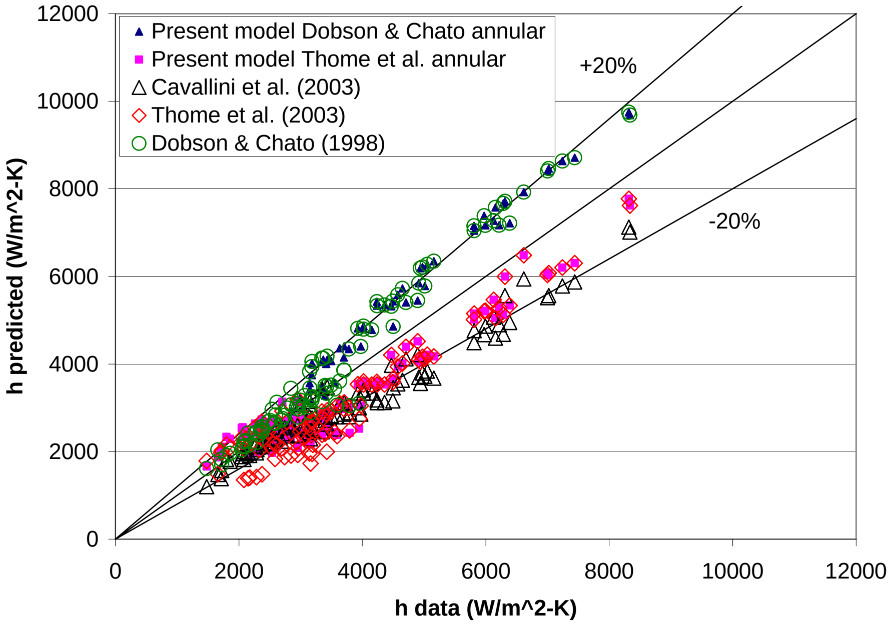

Figure 4.14. Experimental vs. predicted condensation heat transfer for R410A data outlined in Table 4.1

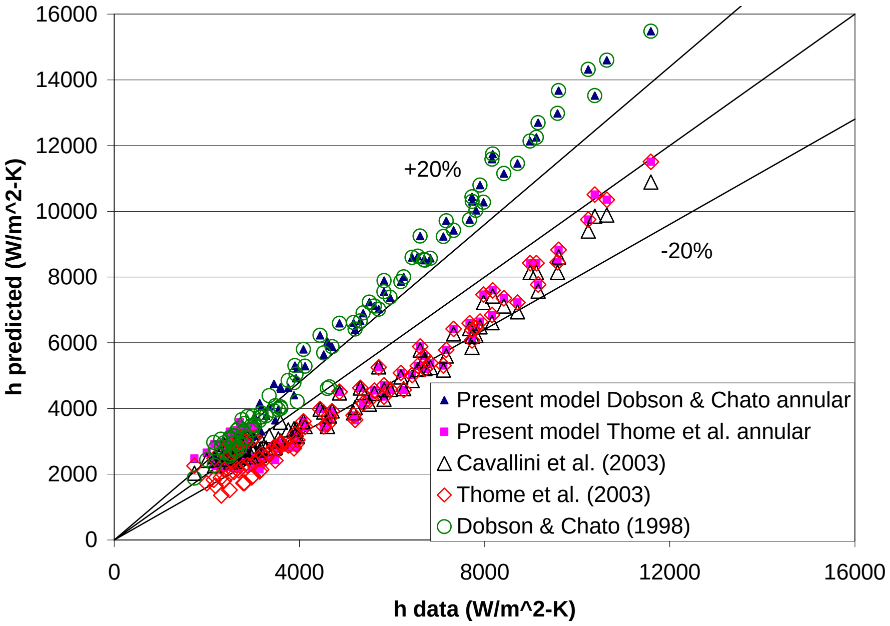

Figure 4.15. Experimental vs. predicted condensation heat transfer for R32/R125 (60/40% by weight) data outlined in Table 4.1

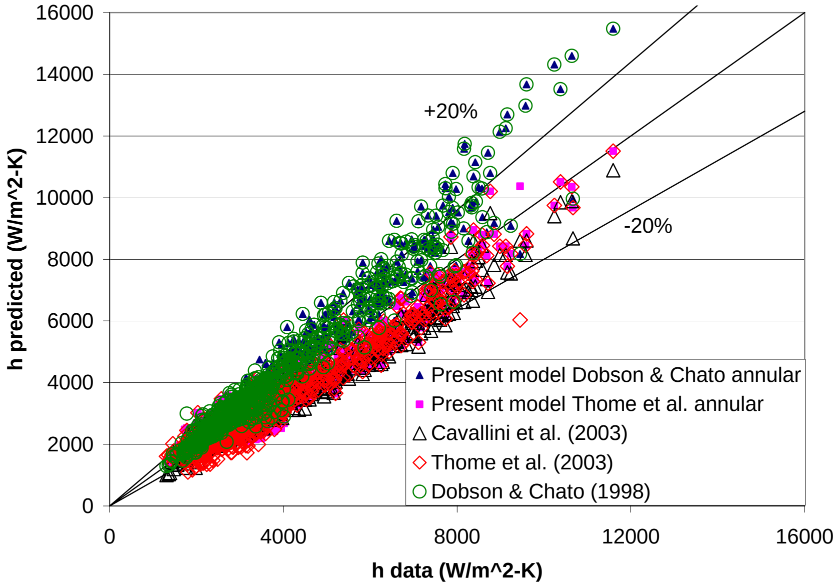

Figure 4.16. Experimental vs. predicted condensation heat transfer for all data outlined in Table 4.1

Table 4.2. Statistical comparison of condensation models with experimental data using different refrigerants (in %)

Refrigerant	Statistical comparison	Present model Thome et al. annular	Present model Dobson & Chato annular	Thome et al. (2003)	Cavallini et al. (2003)	Dobson & Chato (1998)
R11	e_A	14.9	8.2	18.2	8.7	12.3
	e_R	7.0	2.8	10.4	3.5	7.2
	σ_N	18.0	9.8	19.7	11.3	14.0
	within 20%	75.0	95.0	60.0	90.0	80.0
R12	e_A	10.3	9.8	10.5	13.0	8.3
	e_R	-5.4	-4.4	-5.0	-10.9	2.9
	σ_N	12.1	12.2	12.1	9.6	13.2
	within 20%	88.2	90.2	88.2	82.4	94.1
R134a	e_A	10.7	8.3	9.9	10.6	6.4
	e_R	-6.2	1.0	-6.6	-8.2	4.2
	σ_N	10.9	10.1	9.6	9.0	7.1
	within 20%	91.8	94.8	93.9	96.1	98.7
R134a (Present data only)	e_A	6.0	6.2	5.5	9.3	10.1
	e_R	-1.1	-0.6	-1.1	-6.8	7.0
	σ_N	7.9	7.9	6.7	12.5	11.6
	within 20%	96.9	96.9	100.0	93.8	100.0
R22	e_A	13.0	11.8	14.5	13.2	10.3
	e_R	-10.6	5.4	-13.1	-11.2	7.9
	σ_N	10.5	12.3	10.2	9.3	9.5
	within 20%	83.2	89.8	78.9	85.5	90.5
R410A	e_A	15.8	15.3	17.9	16.1	12.3
	e_R	-10.3	9.2	-14.6	-16.0	10.4
	σ_N	14.3	14.4	14.4	7.9	10.7
	within 20%	77.9	67.3	72.1	62.5	72.1
R32/R125 60/40 % by mass	e_A	18.2	26.0	18.1	13.5	24.6
	e_R	-8.6	26.0	-15.5	-10.0	24.6
	σ_N	18.1	10.1	13.1	11.6	10.8
	within 20%	58.3	25.0	59.4	78.1	29.2
all refrigerants	e_A	13.2	12.7	13.9	12.8	11.1
	e_R	-8.3	6.4	-10.6	-10.4	8.8
	σ_N	12.9	14.1	12.5	10.0	11.5
	within 20%	82.1	80.8	80.1	84.6	83.1

4.8 Conclusion

In summary, probabilistic two-phase flow map heat transfer models are developed for single, smooth, horizontal, tubes in a similar manner as pressure drop and void fraction models with a common flow map prediction basis. Previously developed generalized probabilistic two-phase flow regime maps in tubes are utilized in the present condensation models. The probabilistic two-phase flow map heat transfer model weights the importance of the intermittent, stratified, and annular flow regimes based on the time fraction functions which provide smooth physically based transitions. The present model has the flexibility to accept different models developed for each flow regime as more accurate models are identified. Different condensation models were identified in the literature or developed for each flow regime based on their accuracy and simplicity. The present model is compared with condensation data with R134a in 8.915 mm I.D. smooth, adiabatic, horizontal tube experimentally obtained in the present study and with flow map based models found in the literature with good agreement (mean absolute deviation of 6% with the present models). Furthermore, the present probabilistic flow map models developed and flow map based models found in the literature are compared with 806 condensation data points found in the literature with good agreement. The present models using the Thome et al. (2003) and the Dobson and Chato (1998) annular flow components are found to have a mean absolute deviation of 13.2% and 12.7%, respectively, which is comparable to the 13.9% and 12.8% mean absolute deviation of the models by Thome et al. (2003) , and Cavallini et al. (2003), respectively. However, the probabilistic model using the Dobson and Chato (1998) annular flow component is found to over predict high pressure R32/R125 (60/40% by weight) data. Caution must be exercised in using the present models outside of the range of tube diameters, refrigerant properties and flow conditions with which it is presently compared.

References

Ackers, W.W., H.A. Deans, and O.K. Crosser, "Condensation Heat Transfer within Horizontal Tubes," *Chemical Engineering Progress Symposium Series*, 55 (1959)171-176.

Bivens, D.B. and A. Yokozeki, "Heat Transfer Coefficients and Transport Properties for Alternative Refrigerants," *International Refrigerant Conference Proceedings,* Purdue University, July 1994.

Cavallini, A., G. Censi, D. Del Col, L. Doretti, G.A. Longo, and L. Rossetto, "In-Tube Condensation of Halogenated Refrigerants," *ASHRAE Transactions*, 108:1 (2002) 146-161.

Cavallini, A., G. Censi, D. Del Col, L. Doretti, G.A. Longo, L. Rossetto, and C. Zilio, "Condensation Inside and Outside Smooth and Enhanced Tubes - A Review of Recent Research," *International Journal of Refrigeration*, Vol. 26:1, 373-392, 2003.

Cavallini, A. and R. Zecchin, "A Dimensionless Correlation for Heat Transfer in Forced Convective Condensation," *Proceedings of the Fifth International Heat Transfer Conference, Japan Society of Mechanical Engineers*, 3(1974) 309-313.

Carpenter, E.F. and A.P. Colburn, "The Effect of Vapor Velocity on Condensation Inside Tubes," *Proceeding of General Discussion of Heat Transfer,* pp. 20-26, 1951.

Chato, J.C., "Laminar Condensation Inside Horizontal and Inclined Tubes," *ASHRAE Journal,* 4(1962) 52-60.

Chen, S.L., F.M. Gerner, and C.L. Tien, "General Film Condensation Correlations," *Experimental Heat Transfer,* 1(1987) 93-107.

Coleman, J.W., S.Garimella, "Two-Phase Flow Regimes in Round, Square and Rectangular Tubes during Condensation of Refrigerant R134a," *International Journal of Refrigeration* 26 (2003) 117-128.

Dobson, M. K. and J.C. Chato, “Condensation in Smooth Horizontal Tubes,” *Journal of Heat Transfer* 120 (1998) 245-252.

Dittus, F.W. and L.M.K. Boelter, “Heat Transfer in Automobile Radiators of the Tubular Type,” University of California Publications on Engineering, 2(1930) 443-461.

El Hajal, J., J.R. Thome, and A. Cavalini, “Condensation in Horizontal Tubes, Part 1: Two-Phase Flow Pattern Map,” *International Journal of Heat and Mass Transfer* 46 (2003) 3349-3363.

Haraguchi, H., S. Koyama, and T. Fujii, “Condensation of Refrigerants HCFC 22, HFC 134a, and HCFC 123 in a Horizontal Smooth Tube (2nd report, Proposal of Empirical Expressions for Local Heat Transfer Coefficient),” *Trans. JSME* 60(574) (1994) 245-252.

Hurlbert, E.T. and T.A. Newell, “Characteristics of Refrigerant Film Thickness, Pressure Drop, and Condensation Heat Transfer in Annular Flow,” *HVAC&R Research,* 5(3)(1999)229-247.

Jassim, E. W., T. A. Newell, and J. C. Chato, “Probabilistic Determination of Two-Phase Flow Regimes Utilizing an Automated Image Recognition Technique,” to be submitted to Experiments In Fluids (2006a)

Jassim, E.W. and T. A. Newell. “Prediction of Two-Phase Pressure Drop and Void Fraction in Microchannels using Probabilistic Flow Regime Mapping,” *International Journal of Heat and Mass Transfer* 49 (2006) 2446-2457.

Jassim, E. W., T. A. Newell, and J. C. Chato, “Probabilistic Two-Phase Flow Regime Maps in Tubes and Their Generalization to Physical Parameters,” to be submitted to the International Journal of Heat and Mass Transfer (2006b).

Jaster, H. and P.G. Kosky, “Condensation in a Mixed Flow Regime,” *International Journal of Heat and Mass Transfer,* 19(1976) 95-99.

Kattan, N., J.R. Thome, and D. Favrat, “Flow Boiling in Horizontal Tubes: Part 1—Development of a Diabatic Twophase Flow Pattern Map,” *J. Heat Transfer* 120 (1998) 140–147.

Mandhane, J.M., G.A. Gregory, and K. Aziz, “A Flow Pattern Map for Gas-Liquid Flow in Horizontal and Inclined Pipes,” *International Journal of Multiphase Flow* 1 (1974) 537-553.

Niño, V.G. “Characterization of Two-phase Flow in Microchannels,” Ph.D. Thesis, University of Illinois, Urbana-Champaign, IL, 2002.

Rosson, H.F., and J.A. Myers, “Point Values of Condensing Film Coefficients inside a Horizontal Tube,” *Chemical Engineering Progress Symposium Series,* Vol. 61(59), pp.190-199, 1965.

Shah, M.M., “A General Correlation for Heat Transfer during Film Condensation Inside Pipes,” *International Journal of Heat and Mass Transfer,* 22(1979) 547-556.

Soliman, H.M., J.R. Schuster, and P.J. Benson, “A General Heat Transfer Correlation for Annular Flow Condensation,” *Journal of Heat Transfer,* 90(1968) 267-276.

Soliman, H.M., “On the Annular-to-Wavy Flow Pattern Transition during Condensation Inside Horizontal Tubes,” *The Canadian Journal of Chemical Engineering,* 60(1982)475-481.

Steiner, D., “Heat Transfer to Boiling Saturated Liquids,” VDI-Wārmeatlas (VDI Heat Atlas), Verein Deutscher Ingenieure, VDI-Gesellschaft Verfahrenstechnik und Chemieingenieurwesen (GCV), Dū sseldorf, Chapter Hbb (1993).

Taitel, Y. and A.E. Dukler, “A Model for Predicting Flow Regime Transitions in Horizontal and Near Horizontal Gas-Liquid Flow,” *American Institute of Chemical Engineering Journal*, 22 (1976) 47-55.

Tang, L., “Empirical Study of New Refrigerant Flow Condensation Inside Horizontal Smooth Tube and Micro-Fin Tubes,” Ph.D. Thesis, University of Maryland at College Park, 1997.

Thome, J.R., A. Cavallini, and J. El Hajal, “Condensation in Horizontal Tubes Parts 1 and 2,” to appear, ASHRAE Transactions*,* 2003.

Traviss, D.P., W.M. Rohsenow, and A.B. Baron, “Forced Convective Condensation in Tubes: A Heat Transfer Correlation for Condenser Design,” *ASHRAE Transactions,* 79(1)(1973) 157-165.

Chapter 5: Prediction of Refrigerant Void Fraction in Horizontal Tubes Using Probabilistic Flow Regime Maps

5.1 Abstract

A probabilistic two-phase flow map void fraction model is developed for refrigerants under condensation, adiabatic, and evaporation conditions in single, smooth, horizontal, tubes. The time fraction information from a generalized probabilistic two-phase flow map is used to provide a physically based weighting of void fraction models for different flow regimes. The developed model and other void fraction models in the literature are compared to void fraction data from multiple sources that includes R11, R12, R134a, R22, R410A refrigerants, 4.26 to 9.58 mm diameter tubes, mass fluxes from 70 to 900 kg/m^2-s, and a full quality range. The present model is found to have a mean absolute deviation of 3.5%.

5.2 Nomenclature

csf	ratio of maximum to mean velocity in a liquid slug (-)
D	hydraulic diameter (m)
e	deviation (-)
e_A	mean absolute deviation (-)
e_R	average deviation (-)
F	observed time fraction (-)
F_1	Dimensionless parameter defined in Equation 5.17 (-)
F_2	Dimensionless parameter defined in Equation 5.18 (-)
$\mathrm{Fr}_{\mathrm{vo}}$	vapor Froude number (-)
Ft	Froude rate (-)
G	mass flux (kg/m^2-s)
g_a	gravitational acceleration (9.81 m/s^2)
h	heat transfer coefficient (W/m^2-K)
i	intermittent flow regime curve fit constant (-)
K	entrainment ratio (-)
N	total number of data points (-)
n	exponent (-)
$\mathrm{Re}_{\mathrm{lo}}$	liquid only Reynolds number (-)
S	Slip ratio between vapor and liquid (-)
s	stratified flow regime curve fit constant (-)
We_{lo}	liquid only Weber number (-)
We_{vo}	vapor only Weber number (-)
x	flow quality (-)
Xi	dimensionless group correlating the intermittent/liquid flow regime (-)
Xs	dimensionless group correlating the stratified flow regime (-)
X_{tt}	turbulent- turbulent Lockhart - Martinelli parameter (-)
y	Dimensionless parameter defined in Equation 5.19 (-)

Greek symbols

α	void fraction (-)
μ	dynamic viscosity (kg/m-s)
ρ	density (kg/m^3)

σ	surface tension (N/m)
σ_N	standard deviation

Subscripts

ann	pertaining to the annular flow regime
h	homogeneous
int	pertaining to the intermittent flow regime
int+liq	pertaining to the intermittent and liquid flow regime
l	liquid
liq	pertaining to the liquid flow regime
pred	predicted
strat	pertaining to the stratified flow regime
v	vapor
vap	pertaining to the vapor flow regime

5.3 Introduction

Accurate prediction of void fraction is important because it is necessary for refrigerant charge prediction and is commonly used in pressure drop and heat transfer models. Numerous two-phase flow void fraction models are found in the literature that are either empirical or are based on assumptions of the nature of the flow. However, many of the empirical relations or assumptions made in these void fraction models do not apply for a full range of qualities, mass fluxes, tube diameters, and fluid properties.

Flow regime map based heat transfer models have recently been published in the literature by Dobson and Chato (1998), Thome et al. (2003), and Cavallini et al. (2003), and are found to predict heat transfer accurately for a wide range of flow conditions because they incorporate flow regime information. Furthermore, a probabilistic two-phase flow map based void fraction model for multi-port microchannels has recently been developed by Jassim and Newell (2006). However, no flow regime map based void fraction models were found for void fraction in single tubes.

In the present study a probabilistic two-phase flow regime map void fraction model is developed for single, smooth, horizontal tubes. A generalized probabilistic two-phase flow regime map, recently found in the literature by Jassim et al. (2006b) is used in the present model. The void fraction is predicted as the sum of the time fraction of each flow regime multiplied by a model representative of each flow regime. Since the time fraction functions are continuous for the full quality range the void fraction model smoothly transitions between flow regimes without discontinuities. A review of the available void fraction models in the literature is presented and representative models for the intermittent, stratified, and annular flow regimes were identified. The present void fraction model as well as thirteen void fraction models found in the literature are compared to a void fraction database consisting of 427 points from 6 different sources. This database includes void fraction of R11, R12, R134a, R22, R410A refrigerants, 4.26 to 9.58 mm diameter tubes, mass fluxes from 70 to 900 kg/m^2-s, and a full quality range under condensation, adiabatic, and evaporation conditions. The present model is found to have a mean absolute deviation of 3.5%.

5.4 Literature review

Numerous empirical, semi-empirical, and analytical two-phase flow void fraction models can be found in the literature. Most of these models can be classified as Lockhart-Martinelli parameter based, slip ratio based, and mass flux dependent. Furthermore, most of the models assume intermittent or separated flow which can include stratified or annular flow or both.

5.4.1 Lockhart-Martinelli parameter based void fraction models

Lockhart and Martinelli (1949) developed the Lockhart and Martinelli parameter given in Equation 5.1 for the turbulent-turbulent case, and used it in their empirical void fraction model which was presented in tabular form.

$$X_{tt} = \left(\frac{1-x}{x}\right)^{0.9}\left(\frac{\rho_v}{\rho_l}\right)^{0.5}\left(\frac{\mu_l}{\mu_v}\right)^{0.1} \qquad (5.1)$$

Most of the Lockhart-Martinelli parameter based models apply to the annular flow regime where turbulent flow exists in the vapor core and the liquid film. Baroczy (1965) developed an empirical Lockhart-Martinelli parameter based liquid fraction (equals one minus the void fraction) model for vertical upward flow to correlate liquid mercury/nitrogen and air water data and presented it in tabular form. Wallis (1969) used the Lockhart-Martinelli parameter and the air-water void fraction data collected by Lockhart and Martinelli to develop their model given in Equation 5.2. Domanski (1983) then modified the Wallis (1969) correlation by specifying its validity range and added another correlation, given in Equation 5.3, for $10<X_{tt}<189$.

$$\alpha = \left(1 + X_{tt}{}^{0.8}\right)^{-0.378} \qquad X_{tt}<10 \qquad (5.2)$$

$$\alpha = 0.823 - 0.157\ln\left(X_{tt}\right) \qquad 10<X_{tt}<189 \qquad (5.3)$$

5.4.2 Slip ratio based void fraction models

Apart from the homogeneous model, slip ratio based void fraction models are separated flow type models that specify a velocity ratio between the vapor and liquid phases (slip ratio). Most of the slip ratio based void fraction models take the form of Equation 5.4.

$$\alpha = \frac{1}{1+\left(\frac{1-x}{x}\right)\left(\frac{\rho_v}{\rho_l}\right)S} \qquad (5.4)$$

The homogeneous two-phase flow void fraction model, given in Equation 5.5, assumes that the liquid and vapor phases travel at the same velocity and consequently has a slip ratio of one.

$$\alpha_h = \frac{1}{1+\left(\frac{1-x}{x}\right)\left(\frac{\rho_v}{\rho_l}\right)} \qquad (5.5)$$

The homogeneous model tends to over predict void fraction since the vapor is typically traveling at a higher velocity than the liquid. Zivi (1964) analytically derived the slip ratio, given in Equation 5.6, assuming ideal, steady annular flow where the rate of entropy production is minimized, no liquid entrainment is present, and negligible wall friction is assumed. He compared his model to data of Martinelli and Nelson (1948), Larson (1957) and Maurer (1960) and found that his model provides the lower bound of the data while the homogeneous model provides the upper bounds.

$$S=\left(\frac{\rho_l}{\rho_v}\right)^{\frac{1}{3}} \tag{5.6}$$

Smith (1969) developed a semi-empirical relationship for the slip ratio, given in Equation 5.7, which assumes annular flow with a homogeneous mixture of vapor and entrained liquid in the core.

$$S=K+(1-K)\left[\frac{\frac{1}{\frac{\rho_v}{\rho_l}}+K\left(\frac{1-x}{x}\right)}{1+K\left(\frac{1-x}{x}\right)}\right]^{\frac{1}{2}} \tag{5.7}$$

Smith found that an entrainment ratio of K=0.4 (40% liquid entrainment) best correlated his air-water and steam-water data. The Rigot (1973) correlation, perhaps the simplest of the slip ratio based models, assumes a fixed slip ratio equal to two. Ahrens (1983) developed a void fraction correlation, based on the work of Thom (1964). Ahrens's (1983) slip ratio is presented in tabular form as a function of the product of the ratios of the liquid to vapor viscosity and the vapor to liquid density. Levy (1960) assumed equal friction and head losses between the vapor and liquid phases to derive the implicit expression for void fraction given in Equation 5.8.

$$x=\frac{\alpha(1-2\alpha)+\alpha\sqrt{(1-2\alpha)^2+\alpha\left[2\left(\frac{\rho_l}{\rho_v}\right)(1-\alpha)^2+\alpha(1-2\alpha)\right]}}{2\left(\frac{\rho_l}{\rho_v}\right)(1-\alpha)^2+\alpha(1-2\alpha)} \tag{5.8}$$

However, Levy (1960) found that this model only applied to high steam qualities and pressures.

5.4.3 Mass flux based void fraction models

Hughmark (1962) developed an empirical bubbly flow void fraction model for vertical upward flow that assumes that the flow consists of liquid with vapor bubbles suspended in the core that decrease in density as the wall is approached. This model is difficult to use since it is presented in tabular form and requires iterations. Steiner's (1993) version of Rouhani and Axelsson's (1970) drift flux model contains a mass flux term, seen in Equation 5.9, and a surface tension term.

$$\alpha=\frac{x}{\rho_v}\left[(1+0.12(1-x))\left(\frac{x}{\rho_v}+\frac{1-x}{\rho_l}\right)+1.18(1-x)\frac{(g_a\sigma(\rho_l-\rho_v))^{0.25}}{G\rho_l^{0.5}}\right]^{-1} \tag{5.9}$$

El Hajal et al. (2003) developed another mass flux dependent void fraction model, given in Equation 5.10, by computing the log mean of Equation 5.9 and the homogeneous model in order to span a large range of reduced pressures.

$$\alpha = \frac{\alpha_h - \alpha_{ra}}{\ln\left(\frac{\alpha_h}{\alpha_{ra}}\right)} \tag{5.10}$$

The void fraction model presented in Equation 5.10 is used in the prediction of condensation heat transfer by Thome et al. (2003). Taitel and Barnea (1990) developed a semi-empirical void fraction model for fully developed slug flow and is given in Equation 5.11. They assumed that slug flow consists of a stratified region and an entirely liquid region.

$$\alpha = \frac{1}{csf + csf\left(\frac{1-x}{x}\right)\frac{\rho_v}{\rho_l} + 0.35\left(g_a D\right)^{0.5}\frac{\rho_v}{xG}}, \text{ where } csf=1.2 \tag{5.11}$$

Graham (1998) developed an empirical void fraction correlation, given in Equations 5.12 and 5.13, from R134a and R410A data obtained under condensation conditions.

$$\alpha = 1 - \exp\left[-1 - 0.3\ln(Ft) - 0.0328\left(\ln(Ft)\right)^2\right] \qquad Ft>0.01032 \tag{5.12}$$

$$\alpha = 0 \qquad Ft<0.01032 \tag{5.13}$$

This correlation utilizes the Froude rate, given in Equation 5.14, which is the ratio of the vapor kinetic energy to the energy required to lift the liquid to the top of the tube.

$$Ft = \left[\frac{x^3 G^2}{\rho_v{}^2 g_a D(1-x)}\right]^{\frac{1}{2}} \tag{5.14}$$

5.4.4 Other void fraction models

Other separated flow type void fraction models in the literature do not fit into the above classifications or have combinations of the above features. Armand (1946) developed a two-phase flow void fraction model for intermittent flow in horizontal tubes, given in Equation 5.15.

$$\alpha = \frac{(0.833 + 0.167x)x\left(\frac{1}{\rho_v}\right)}{(1-x)\left(\frac{1}{\rho_l}\right) + x\left(\frac{1}{\rho_v}\right)} \tag{5.15}$$

Jassim and Newell (2006) recently found that the Armand (1946) model predicted void fraction in the intermittent flow regime for multi-port microchannels. Premoli (1971) developed an empirical slip ratio type void fraction model, given in Equations 5.16 through 5.21, with a mass flux dependence for vertical, upward, adiabatic, two-phase flow in large tubes.

$$S = 1 + F_1\left(\frac{y}{1+F_2 y} - F_2 y\right)^{\frac{1}{2}} \tag{5.16}$$

$$F_1 = 1.578\,\mathrm{Re}_L{}^{-0.19}\left(\frac{\rho_l}{\rho_v}\right)^{0.22} \tag{5.17}$$

$$F_2 = 0.0273 We_{lo} \mathrm{Re}_{lo}^{-0.51}\left(\frac{\rho_l}{\rho_v}\right)^{-0.08} \tag{5.18}$$

$$y = \frac{\alpha_h}{1-\alpha_h} \tag{5.19}$$

$$We_{lo} = \frac{G^2 D}{\sigma \rho_l} \tag{5.20}$$

$$\mathrm{Re}_{lo} = \frac{GD}{\mu_l} \tag{5.21}$$

Tandon (1985) developed a semi-empirical void fraction model assuming one dimensional, steady, axisymmetric, annular flow, no liquid entrainment, and turbulent vapor and liquid phases with a Von Karman velocity profile. The Tandon (1985) model, given in Equations 5.22 through 5.24, contains both the Lockhart-Martinelli parameter and has a mass flux dependence in the liquid only Reynolds number.

$$\alpha = 1 - 1.928\frac{\mathrm{Re}_{lo}^{-0.315}}{F(X_{tt})} + 0.9293\frac{\mathrm{Re}_{lo}^{-0.63}}{F(X_{tt})^2} \qquad \text{for } 50<\mathrm{Re}_{lo}<1125 \tag{5.22}$$

$$\alpha = 1 - 0.38\frac{\mathrm{Re}_{lo}^{-0.088}}{F(X_{tt})} + 0.0361\frac{\mathrm{Re}_{lo}^{-0.176}}{F(X_{tt})^2} \qquad \text{for } \mathrm{Re}_{lo}>1125 \tag{5.23}$$

where

$$F(X_{tt}) = 0.15\left(\frac{1}{X_{tt}} + \frac{2.85}{X_{tt}^{0.476}}\right) \tag{5.24}$$

Yashar et al. (2001) developed a void fraction model for separated flow that includes the Lockhart-Martinelli parameter and the Froude rate that contains the mass flux. The Yashar et al. (2001) model, given in Equation 5.25, was derived from horizontal smooth and microfinned tube data for refrigerant condensation, adiabatic, and evaporation conditions.

$$\alpha = \left(1 + \frac{1}{Ft} + X_{tt}\right)^{-n}, \tag{5.25}$$

where n=0.375 for microfin condensation and n=0.321 for all other cases.

This model was designed to predict both annular and stratified flow. In the annular flow regime the Lockhart-Martinelli parameter is dominant, but as the quality decreases and the flow becomes stratified the reciprocal of the Froude rate dominates. Harms et al. (2003) developed a mechanistic void fraction model for annular flow in horizontal tubes which is not shown here due to its complexity. Recently, Jassim and Newell (2006) developed a probabilistic two-phase flow map based model for void fraction in multi-port microchannels given in Equation 5.26.

$$\alpha_{total} = F_{liq}\alpha_{liq} + F_{\mathrm{int}}\alpha_{\mathrm{int}} + F_{vap}\alpha_{vap} + F_{ann}\alpha_{ann} \tag{5.26}$$

In Equation 5.26 the total void fraction is predicted as the sum of the product of the fraction of time that each flow regime is observed under a given condition and a representative model of the respective flow regime. Jassim and

Newell (2006) curve fit the time fraction data obtained by Nino (2002) with continuous functions over the entire quality range that have physically correct limits. A probabilistic two-phase flow regime map from Jassim and Newell (2006) with the time fraction data and curve fits can be seen in Figure 5.1. Jassim and Newell (2006) used probabilistic two-phase flow maps because they can easily be represented by continuous functions for the entire quality range which smoothly transition from one flow regime to another. This is not the case with traditionally used flow maps such as the Steiner (1993) type flow map depicted in Figure 5.2, which specifies a particular flow regime at a given flow condition. The void fraction models for each flow regime were identified based on their ability to predict void fraction in multi-port microchannels. The models for the liquid, vapor, and annular flow regimes are given in Equations 5.27 through 5.29, respectively, and the Armand (1946) model given in Equation 5.15 is used for the intermittent flow regime.

$$\alpha_{liq} = 0 \tag{5.27}$$

$$\alpha_{vap} = 1 \tag{5.28}$$

$$\alpha_{ann} = \left[1 + \left(X_{tt} + \frac{1}{We_{vo}^{1.3}}\right)\left(\frac{\rho_l}{\rho_v}\right)^{0.9}\right]^{-0.06} \text{, where} \tag{5.29}$$

$$We_{vo} = \left(\frac{G^2 D}{\rho_v \sigma}\right) \tag{5.30}$$

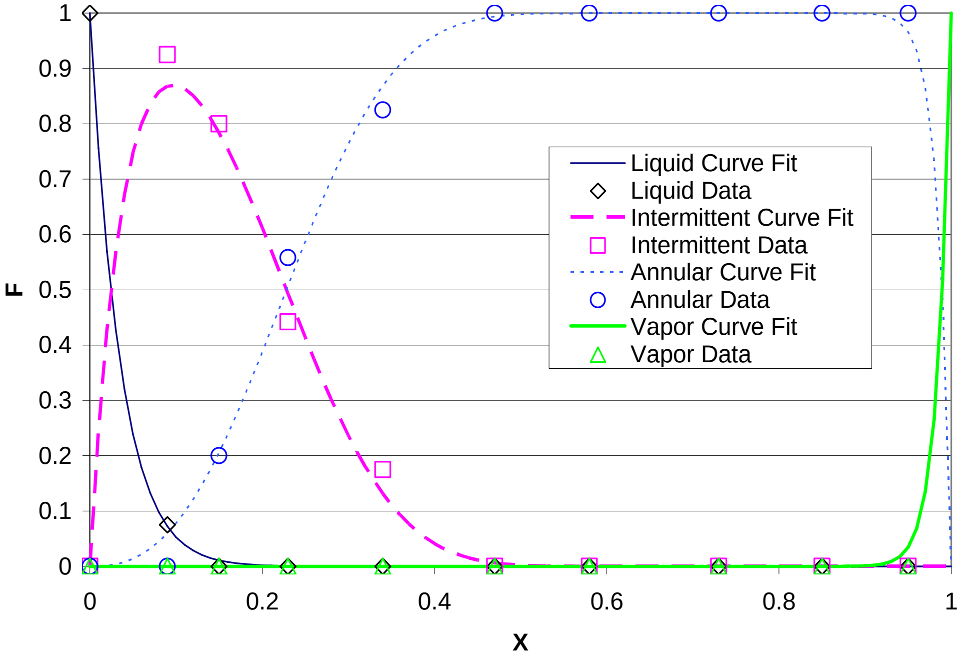

Figure 5.1. Probabilistic flow map with time fraction curve fits for R410A, 10 ºC, 300 kg/m^2-s in a 6-port 1.54 mm hydraulic dia. microchannel taken from Jassim and Newell (2006).

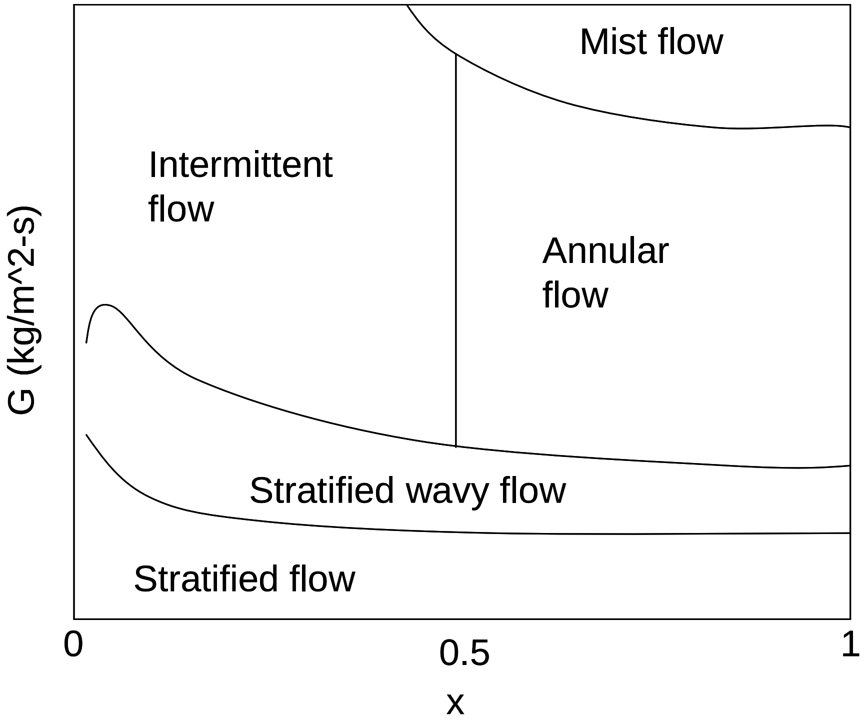

Figure 5.2. Steiner (1993) type flow map depiction

5.5 Present void fraction model development

In the present study a probabilistic two-phase flow regime map void fraction model is developed for single horizontal tubes in a manner similar to that of Jassim and Newell (2006) for multi-port microchannels. The present void fraction model for large tubes is also developed on a consistent time fraction basis as Jassim et al. (2006c) have modeled condensation heat transfer in large tubes.

5.5.1 Generalized two phase flow map

Single tubes of approximately 3 mm in diameter and larger are found to contain a stratified flow regime which is absent in the 1.54 mm hydraulic diameter microchannels of Nino (2002). Damianides and Westwater (1988) support this observation because they indicate that the transition from "microchannel" behavior to "large tube" behavior occurs in the 3 mm tube diameter range. Furthermore, vapor only flow is not present below a quality of 100% in single tubes.

Jassim et al. (2006b) developed probabilistic two-phase flow maps for single tubes with the experimentally obtained time fraction data from Jassim et al. (2006a) who utilized the flow loop depicted in Figure 5.3. Jassim et al. (2006b) developed curve fits for the intermittent/ liquid, stratified, and annular flow regime time fraction data. The time fraction functions are given in Equations 5.31 through 5.33 for the intermittent/liquid, stratified, and annular flow regimes, respectively.

$$F_{\text{int}+liq} = (1-x)^i \tag{5.31}$$

$$F_{strat} = \left(1 - x^{\left(s/\sqrt{x}\right)}\right)^i - \left(1-x\right)^i \tag{5.32}$$

$$F_{ann} = 1 - F_{\text{int}+liq} - F_{strat} \tag{5.33}$$

The flow maps developed were generalized by linking the time fraction curve fit constants to physical parameters. The intermittent/liquid time fraction curve fit constant "*i*", given in Equation 5.34, has a strong linear relationship with the dimensionless group *Xi*, given in Equation 5.35, which contains the vapor only Weber number, given in Equation 5.30, and the liquid to vapor density ratio.

$$i = 0.0243Xi + 8.07 \tag{5.34}$$

$$Xi = \left(We_{vo}^{0.4}\right)\left(\frac{\rho_l}{\rho_v}\right) \tag{5.35}$$

The stratified time fraction curve fit constant "*s*", given in Equation 5.36, has a strong relationship with the dimensionless group *Xs*, given in Equation 5.37, which contains the square root of the liquid only Froude number, given in Equation 5.38, and the vapor to liquid density ratio.

$$s = \frac{1}{0.45Xs} + \frac{1}{0.025Xs^{4.44}} \tag{5.36}$$

$$Xs = \left(Fr_{vo}^{0.5}\right)\left(\frac{\rho_v}{\rho_l}\right)^{0.65} \tag{5.37}$$

$$Fr_{vo} = \left(\frac{G^2}{\rho_v^2 g_a D}\right) \tag{5.38}$$

A sample probabilistic two phase flow regime map with generalized curve fits is depicted in Figure 5.4 for 8.00 mm diameter tube with R134a flowing at 25 ºC and 300 kg/m^2-s. Jassim et al. (2006b) found these generalized curve fit constants to represent the time fraction data with an average absolute error of 0.022, 0.094, and 0.071 for the intermittent/liquid, stratified, and annular flow regimes, respectively, for 8.00 mm, 5.43 mm, and 3.90 mm diameter tubes. The average absolute error for the 1.74 mm diameter tube in the intermittent flow regime is reported to be 0.044, with the same deviation for the annular flow regime if the stratified flow regime is neglected which is not observed for this tube diameter.

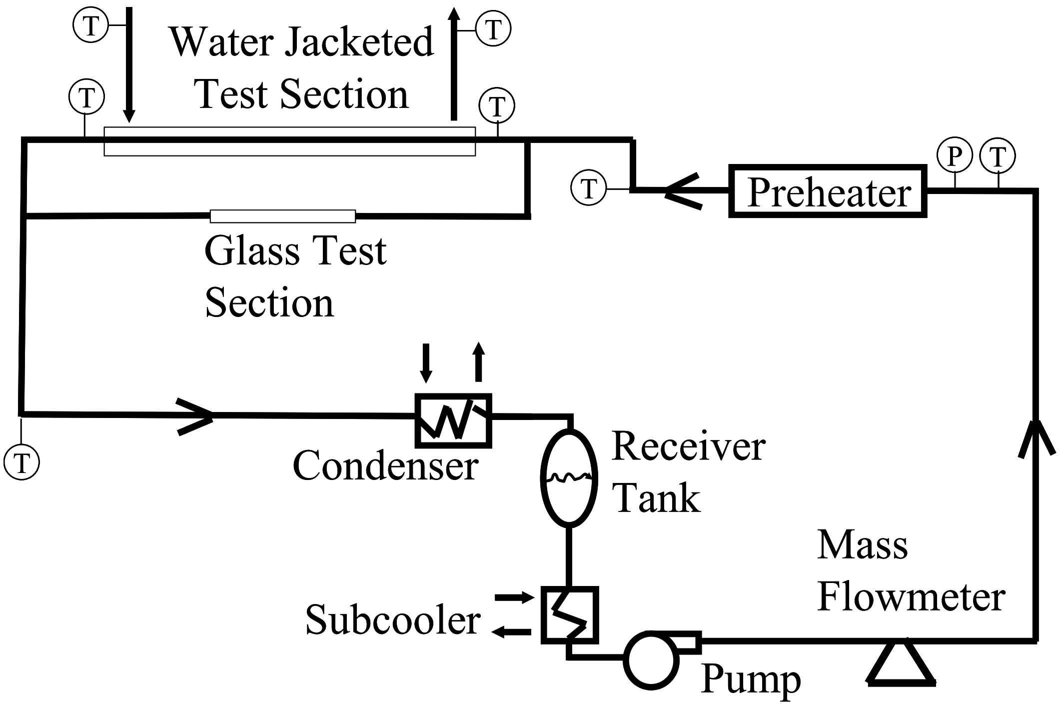

Figure 5.3. Two-phase flow loop schematic

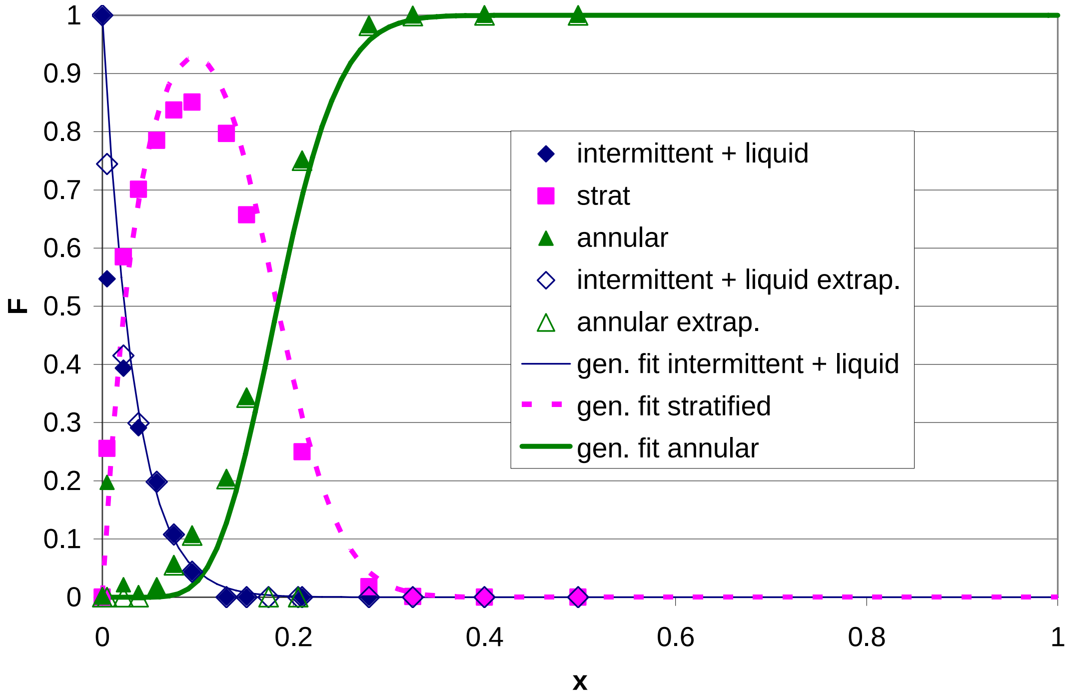

Figure 5.4. Probabilistic flow map with generalized time fraction curve fits for 8.00 mm diameter tube, R134a, 25 ºC, 300 kg/m^2-s.

5.5.2 Probabilistic two-phase flow regime map void fraction model

The present probabilistic two-phase flow regime map void fraction model, given in Equation 5.39, is a modified version of the Jassim and Newell (2006) model for microchannels to reflect the flow regimes present in horizontal single channel tubes.

$$\alpha_{total} = F_{\text{int}+liq}\alpha_{\text{int}+liq} + F_{strat}\alpha_{strat} + F_{ann}\alpha_{ann} \tag{5.39}$$

The total void fraction is simply equal to the time fraction of each flow regime multiplied by a model representative of the respective flow regime. This void fraction model has a consistent time fraction basis as the Jassim et al. (2006c) probabilistic two-phase flow map condensation heat transfer model given in Equation 5.40.

$$h_{total} = F_{\text{int}+liq}h_{\text{int}+liq} + F_{strat}h_{strat} + F_{ann}h_{ann} \tag{5.40}$$

In the present model the Graham (1998) model given in Equation 5.12 is utilized for the intermittent flow regime, the Yashar et al. (1998) model given in Equation 5.25 is utilized for the stratified flow regime, and the Stiener (1993) version of the Rouhani and Axelsson (1970) model given in Equation 5.9 for the annular flow regime. These models were chosen because they were found to best represent the void fraction data summarized in Table 5.1 at predicted time fractions values of 0.7 and above for the respective flow regimes. The present model components can easily be changed as more accurate models are identified for each flow regime.

Table 5.1. Void fraction data used to compare the present models with other models in the literature

Source	D (mm)	Refrigerants	G (kg/m^2-s)	T$_{sat}$(ºC)	Heat transfer	Data points
Yashar (1998)	4.26	R134a, R410A	200-700	5	adiabatic & evaporation	36
Wilson (1998)	6.12	R134a, R410A	75-500	5	adiabatic & evaporation	51
Kopke (1998)	6.04	R134a, R410A	75-300	35	Adiabatic, evaporation, & condensation	24
Graham (1997)	7.04	R134a, R410A	76-467	35	condensation	40
Sacks (1975)	9.576	R11, R12, R22	82-902	25-32	adiabatic & condensation	276

5.5.3 Evaluation of the present void fraction model

The present void fraction model and that of Wallis (1969) and Domanski (1983), Zivi (1964), Smith (1969), Rigot (1973), Stiener (1993) version of Rouhani and Axelsson (1970), El Hajal et al. (2003), Taitel and Barnea (1990), Graham (1998), Armand (1946), Premoli (1971), Tandon (1985), Yashar et al. (2001), and homogeneous are compared to the void fraction database summarized in Table 5.1 in Figures 5.5 through 5.18, respectively. In each of these figures the data is differentiated by refrigerant. The models that are presented in tabular form are not compared, nor are the models of Levy (1960), Harms et al. (2003), and Jassim and Newell (2006). The Levy (1960) model is not defined for many of the points because of the quality and reduced pressure range, the Harms et al. (2003) was not compared due to its complexity, and the Jassim and Newell (2001) model was not compared because it was developed for microchannels. It is evident from these figures that the present model represents the data well. A statistical comparison of all the models in Figures 5.5 through 5.18 with all of the data detailed in Table 5.1 is summarized in Table 5.2. Table 5.2 contains the mean absolute deviation, e_A, the average deviation, e_R, and the standard deviation, σ_N, given in Equations 5.41 through 5.43, respectively along with the percentage of predicted points lying with in $\pm$10% error bars.

$$e_A = \frac{1}{N}\sum 100\left|\frac{h_{pred} - h_{data}}{h_{data}}\right| \tag{5.41}$$

$$e_R = \frac{1}{N}\sum 100\left(\frac{h_{pred} - h_{data}}{h_{data}}\right) \tag{5.42}$$

$$\sigma_N = \left[\frac{1}{N-1}\sum\left(e - e_R\right)^2\right]^{0.5} \quad \text{where, } e = 100\left(\frac{h_{pred} - h_{data}}{h_{data}}\right) \tag{5.43}$$

The models in Table 5.2 are arranged from least to greatest mean absolute deviation. It should be noted that 2 points were removed from the Premoli (1971) model at the high quality range because the void fraction was not defined. If these points are considered to be 100% error the mean absolute deviation, average deviation, standard deviation, and percent of points within 10% error bars is 4.6%, -0.6%, 10.9%, and 88.1%, respectively. From Table 5.2 it can be seen that the present model represents this data well with the lowest mean absolute deviation of 3.5%, the lowest standard deviation, and the highest percent of predicted points within ±10% error bars. Furthermore, it can be seen that it accurately predicts the high pressure R410A with a mean absolute deviation of 4.7%. The only other model with a mean absolute deviation within 2% of the present model for R410A is the Yashar et al. model with a value of 5.3 %.

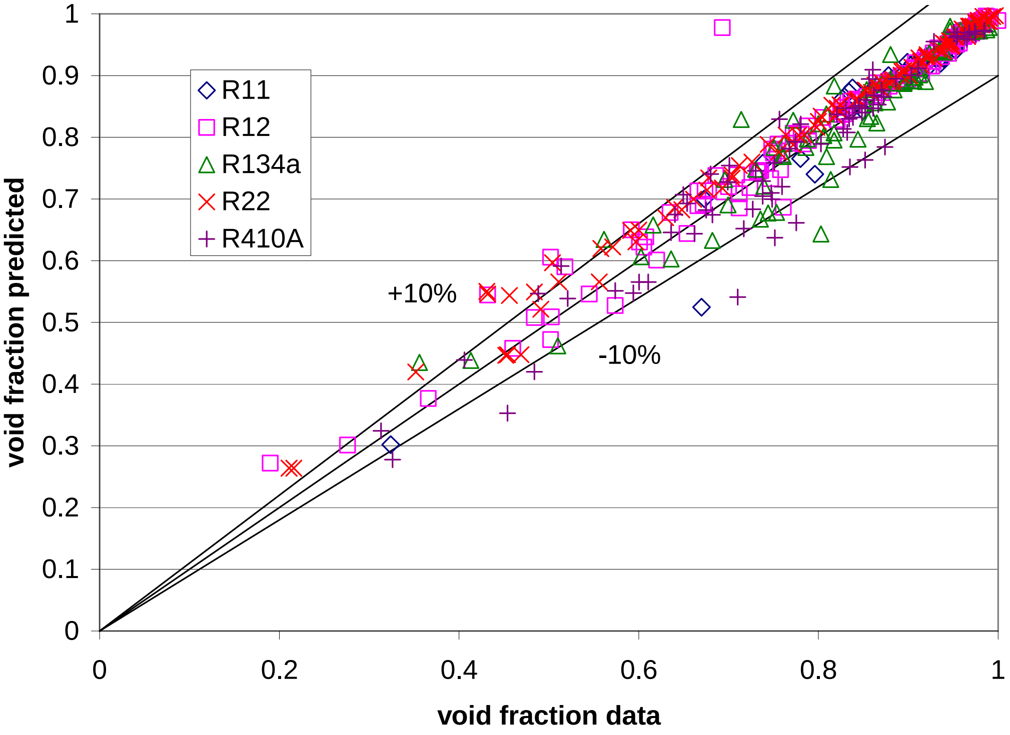

Figure 5.5. Void fraction data summarized in Table 5.1 vs. void fraction predicted by present model and separated by refrigerant

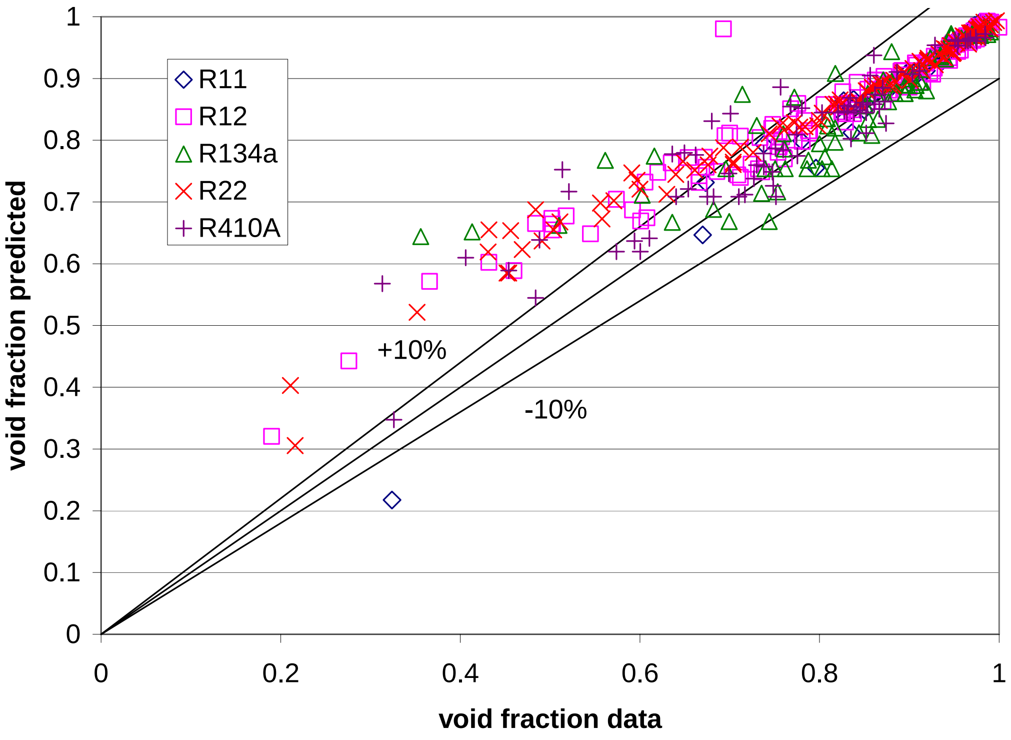

Figure 5.6. Void fraction data summarized in Table 5.1 vs. void fraction predicted by Wallis (1969) and Domanski (1983) and separated by refrigerant

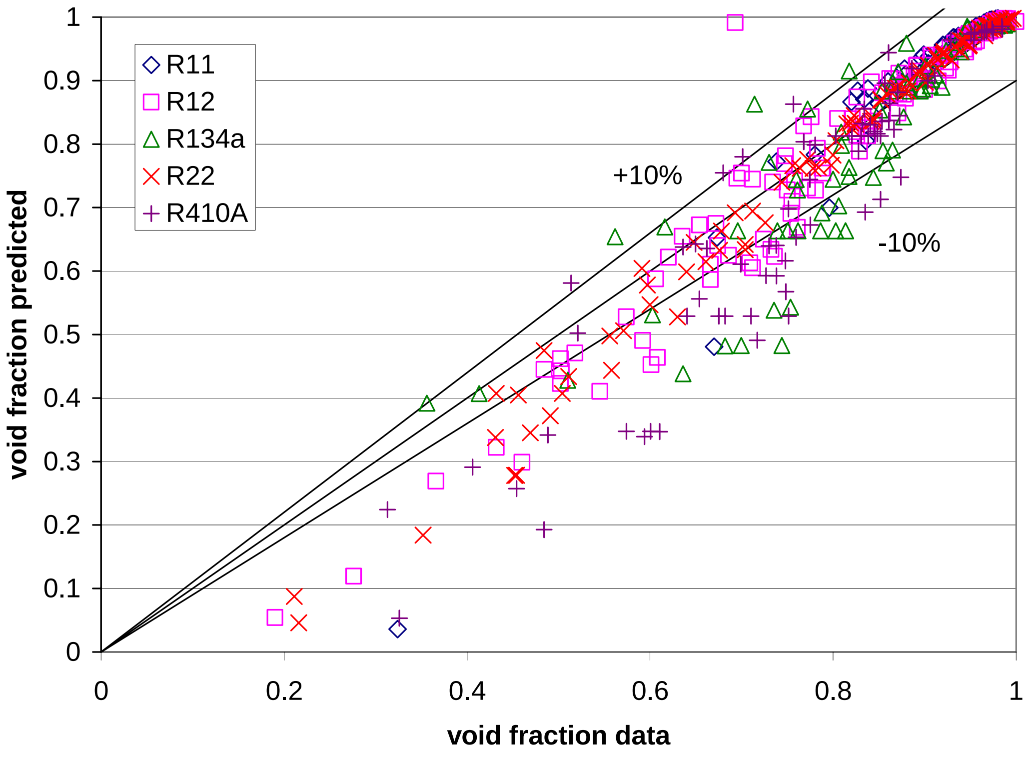

Figure 5.7. Void fraction data summarized in Table 5.1 vs. void fraction predicted by Zivi (1964) and separated by refrigerant

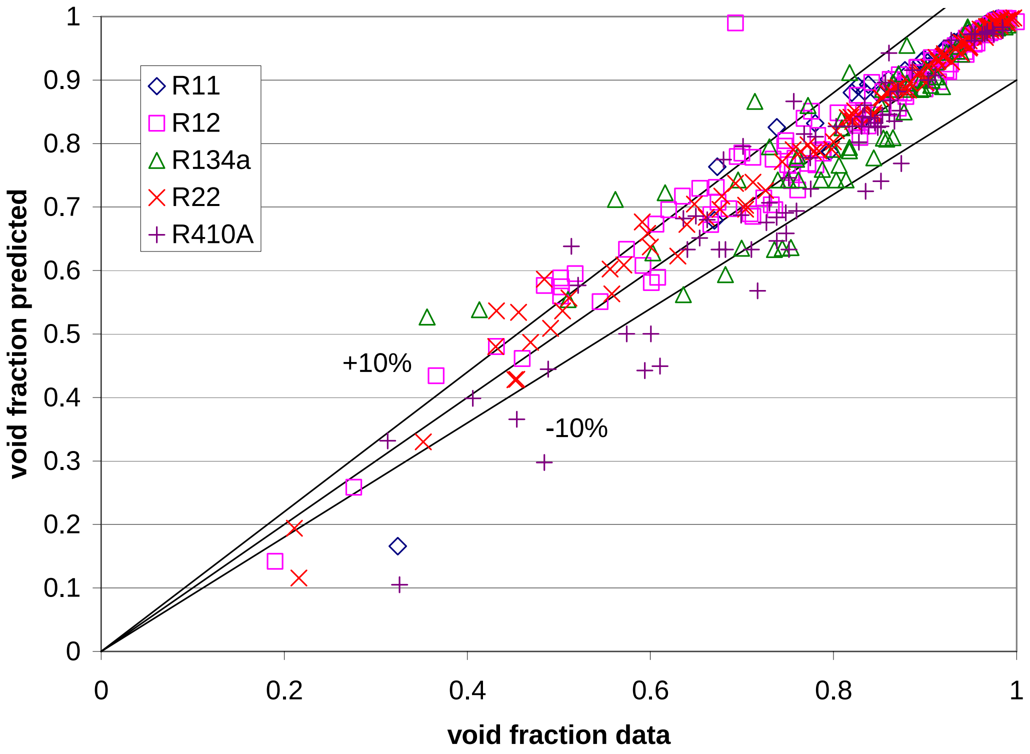

Figure 5.8. Void fraction data summarized in Table 5.1 vs. void fraction predicted by Smith (1969) and separated by refrigerant

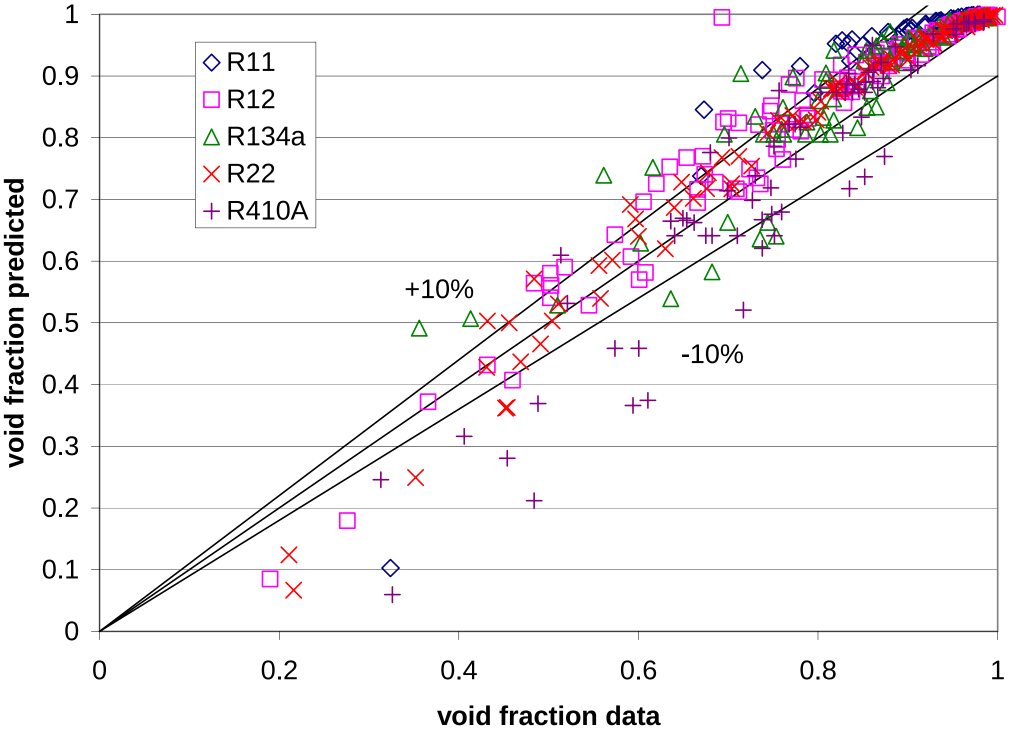

Figure 5.9. Void fraction data summarized in Table 5.1 vs. void fraction predicted by Rigot (1973) and separated by refrigerant

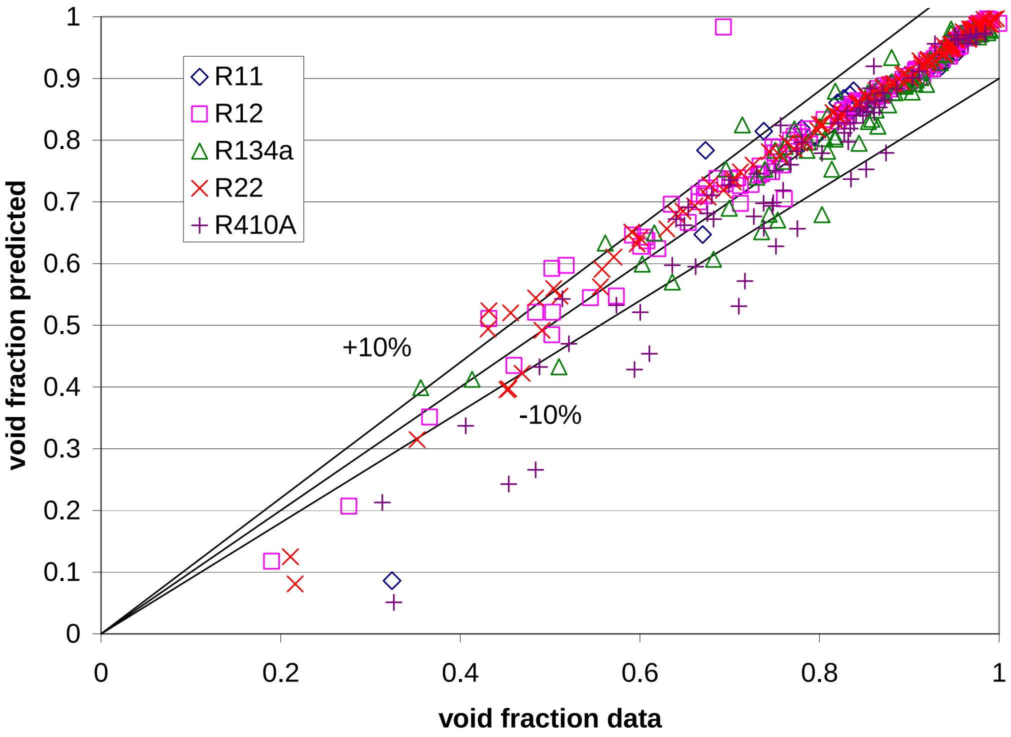

Figure 5.10. Void fraction data summarized in Table 5.1 vs. void fraction predicted by present model Rouhani and Axelsson (1970) and separated by refrigerant

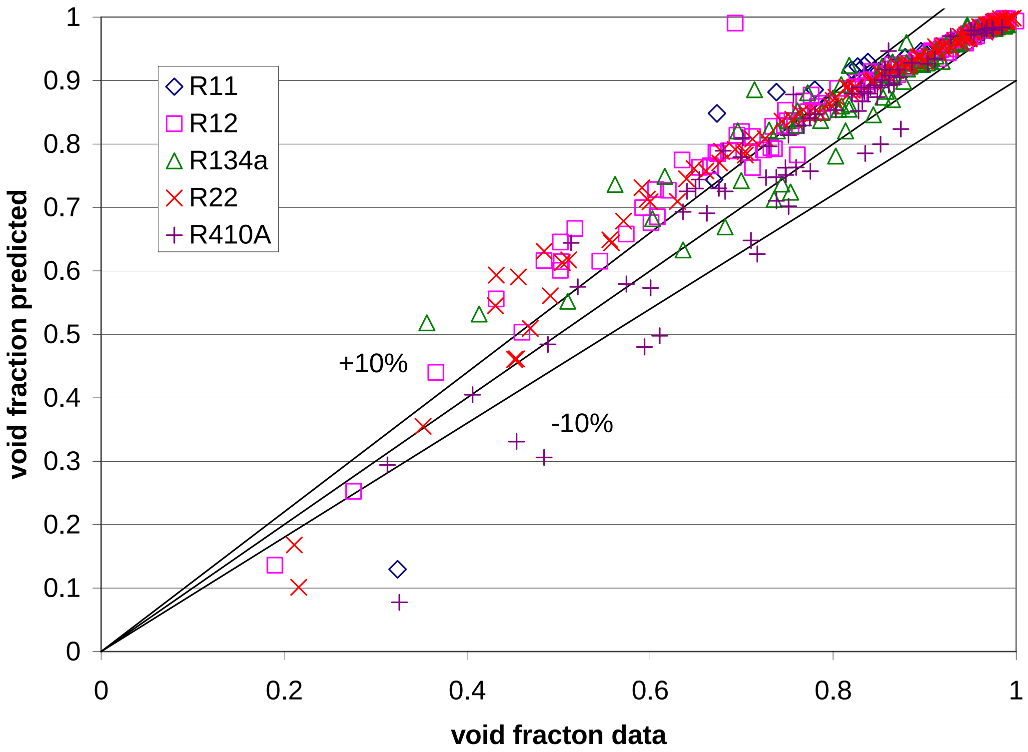

Figure 5.11. Void fraction data summarized in Table 5.1 vs. void fraction predicted by El Hajal et al. (2003) and separated by refrigerant

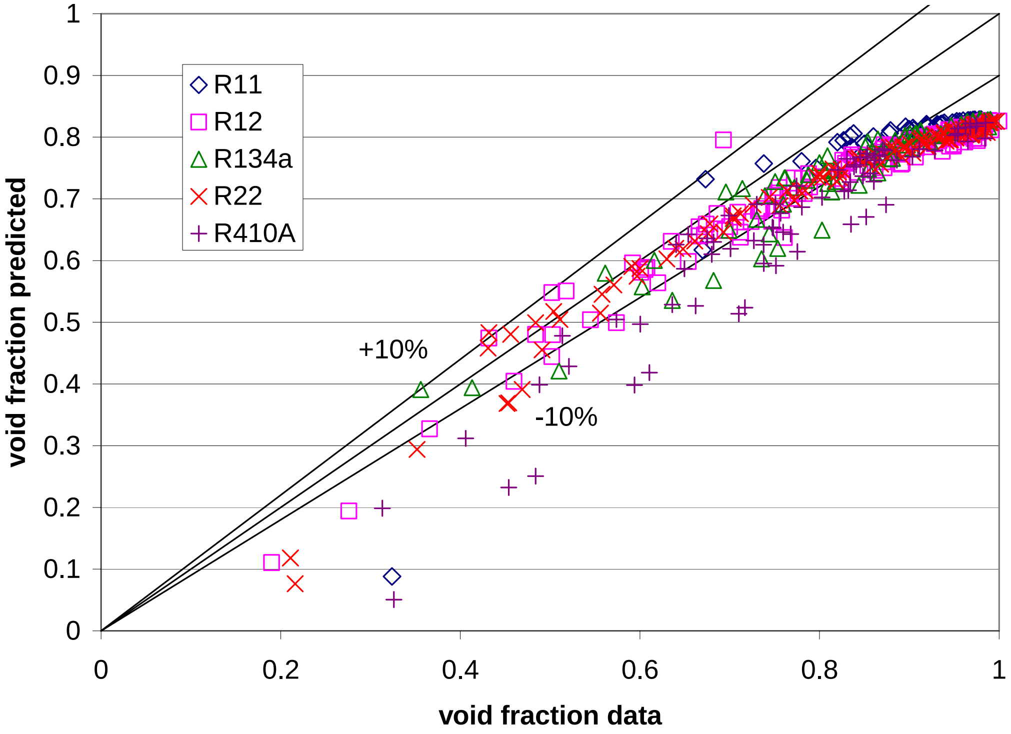

Figure 5.12. Void fraction data summarized in Table 5.1 vs. void fraction predicted by Taitel and Barnea (1990) and separated by refrigerant

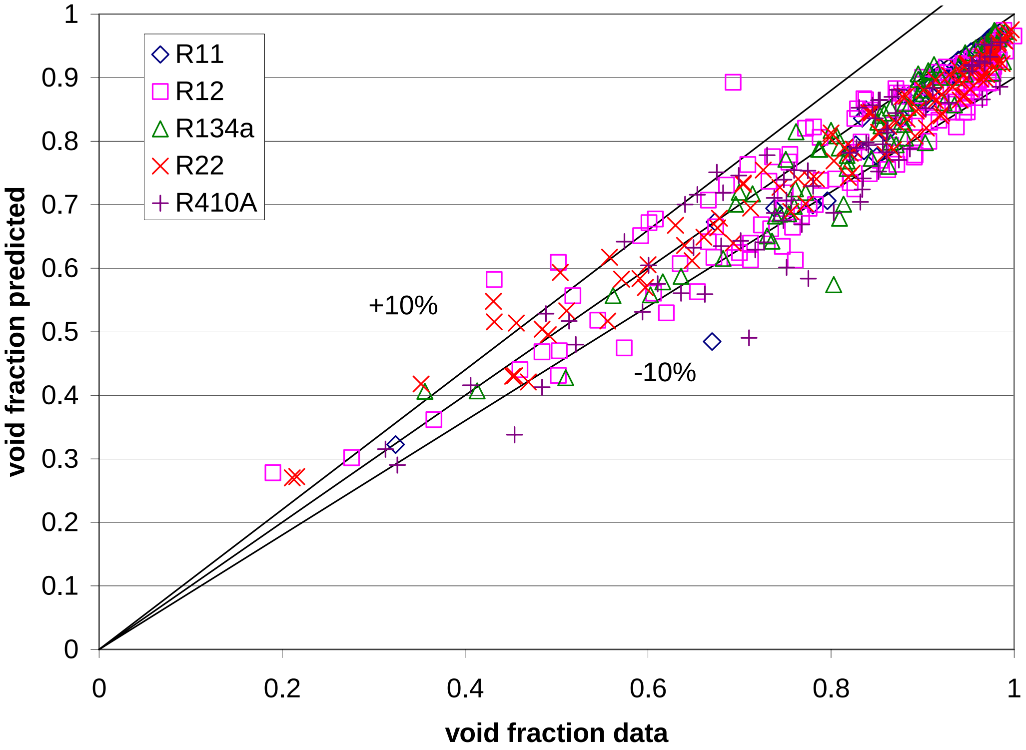

Figure 5.13. Void fraction data summarized in Table 5.1 vs. void fraction predicted by Graham (1998) and separated by refrigerant

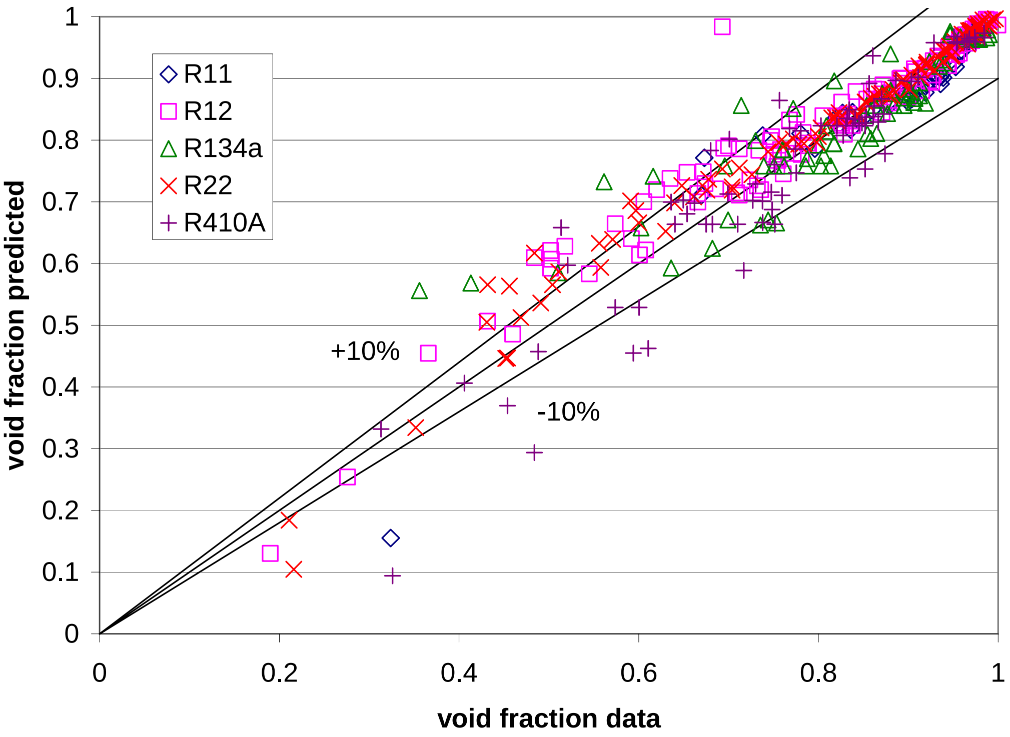

Figure 5.14. Void fraction data summarized in Table 5.1 vs. void fraction predicted by Armand (1946) and separated by refrigerant

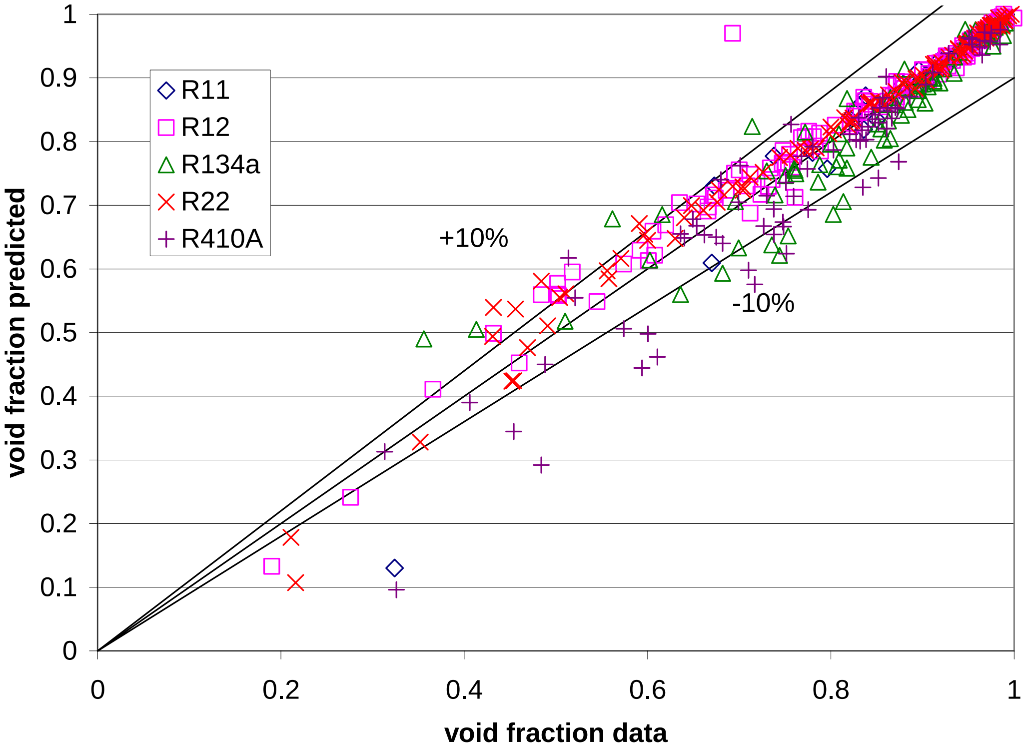

Figure 5.15. Void fraction data summarized in Table 5.1 vs. void fraction predicted by Premoli (1971) and separated by refrigerant

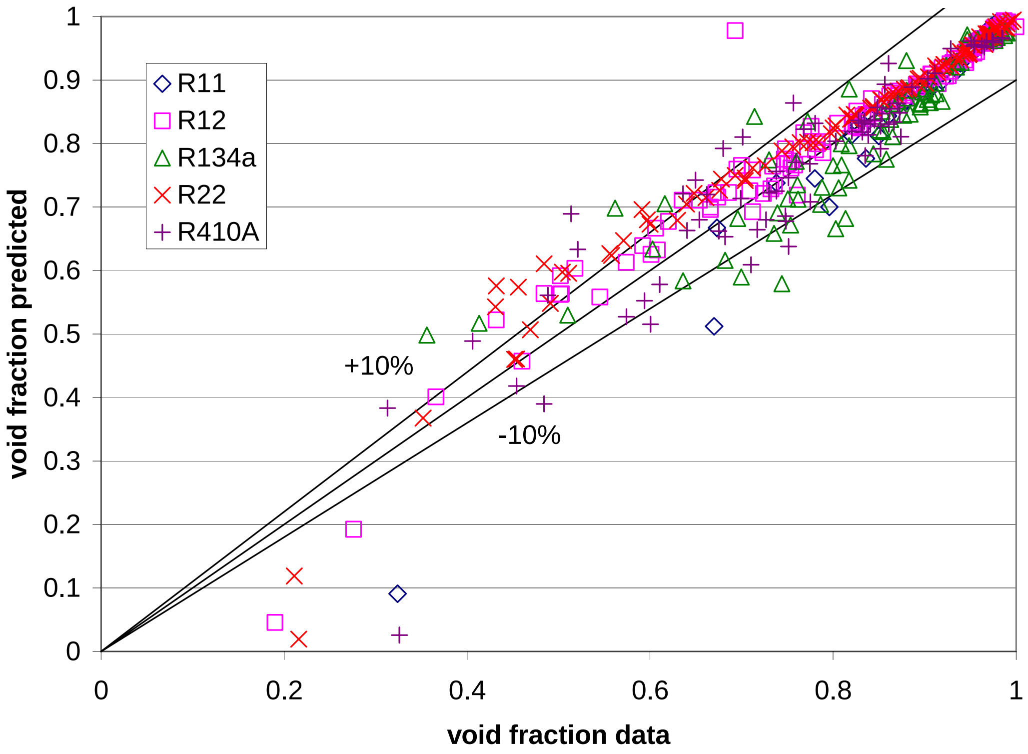

Figure 5.16. Void fraction data summarized in Table 5.1 vs. void fraction predicted by Tandon (1985) and separated by refrigerant

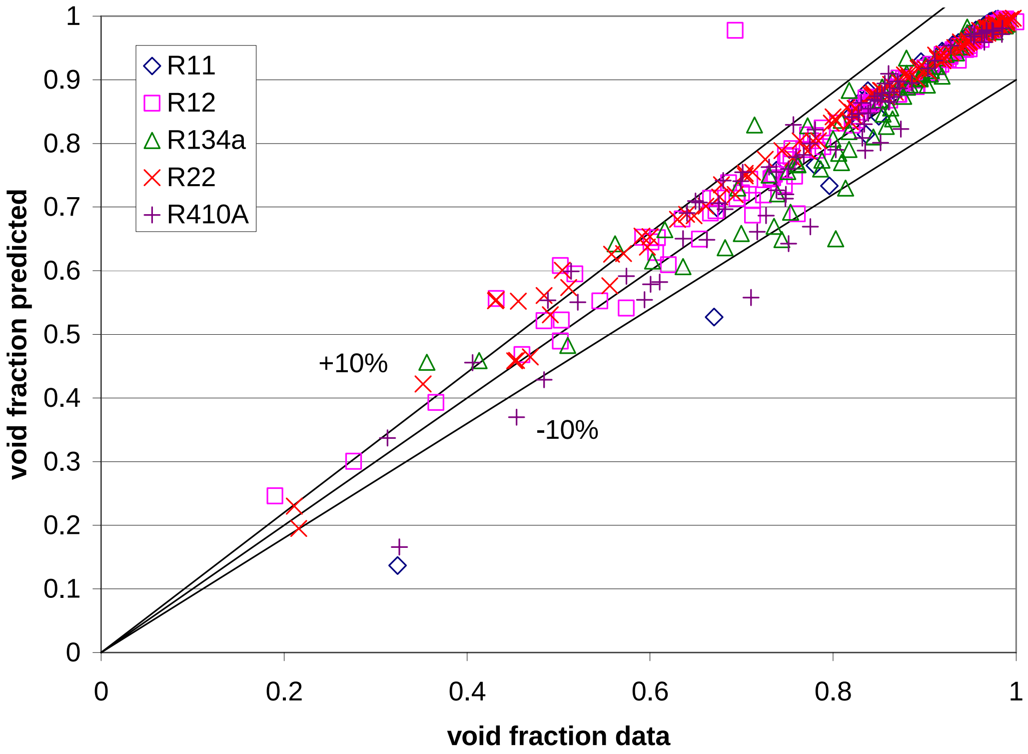

Figure 5.17. Void fraction data summarized in Table 5.1 vs. void fraction predicted by Yashar et al. (2001) and separated by refrigerant

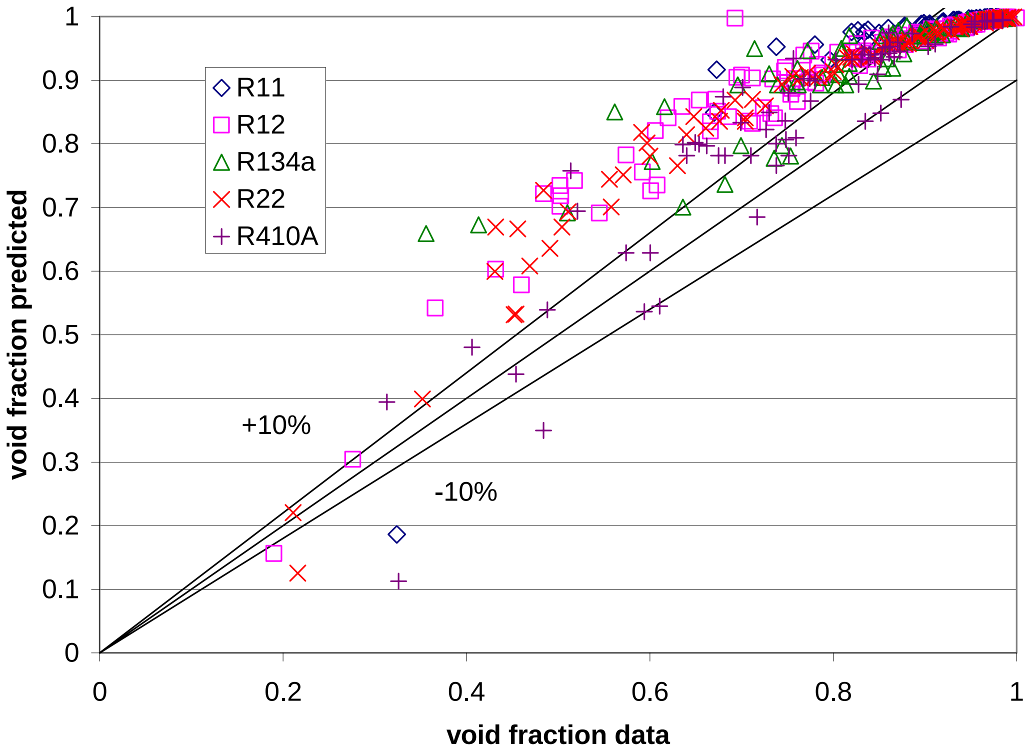

Figure 5.18. Void fraction data summarized in Table 5.1 vs. void fraction predicted by the homogeneous model and separated by refrigerant

Table 5.2. Statistical comparison of void fraction models with experimental data separated by refrigerants (in %)

Refrig.	Statistical comparison	Present model	Yashar et al. (2001)	Premoli (1971)	Rouhani & Axelsson (1970)	Smith (1969)	Armand (1946)	Tandon (1985)	Graham (1998)	Wallis (1969) & Domanski (1983)	Zivi (1964)	Rigot (1973)	El Hajal et al. (2003)	Taitel & Barnea (1990)	Homog.
R11	eA	2.2	4.4	3.0	3.8	4.6	4.1	3.9	3.6	2.5	6.3	9.9	7.2	11.6	11.3
	eR	-0.1	-0.1	-1.1	-0.5	2.2	-2.0	-3.5	-3.5	0.2	-0.4	6.6	4.2	-11.1	9.3
	σN	4.2	10.1	9.8	12.2	8.6	8.9	11.5	4.7	5.8	15.3	13.2	11.5	11.1	11.4
	within 10%	97.6	95.1	97.6	92.7	92.7	95.1	92.7	92.7	97.6	92.7	65.9	78.0	43.9	58.5
R12	eA	3.0	3.2	3.2	3.1	4.0	4.4	3.8	7.5	7.4	6.1	6.7	8.0	11.8	13.8
	eR	2.2	2.8	2.0	1.6	2.8	3.0	1.4	-3.7	7.0	-2.5	4.9	7.4	-11.2	13.6
	σN	6.4	5.8	6.0	6.6	6.4	7.8	9.4	9.1	12.6	11.6	8.9	8.1	6.8	12.3
	within 10%	96.1	95.3	91.3	95.3	87.4	85.8	92.1	73.2	77.2	85.0	80.3	71.7	36.2	48.8
R134a	eA	3.5	3.8	4.7	3.4	5.5	5.6	5.9	5.0	6.1	7.3	7.4	6.5	11.1	13.1
	eR	0.1	0.7	-1.0	-0.3	1.4	1.1	-1.5	-4.2	3.6	-3.4	5.2	6.1	-10.7	13.1
	σN	5.6	6.1	7.9	5.3	9.5	10.3	9.0	5.7	13.5	10.7	8.9	8.0	5.3	13.9
	within 10%	93.4	90.8	84.2	88.2	84.2	89.5	84.2	88.2	85.5	69.7	75.0	80.3	32.9	56.6
R22	eA	3.8	4.2	3.4	3.8	3.4	4.1	5.2	5.7	8.9	5.8	6.1	7.9	12.3	13.1
	eR	3.7	4.0	1.6	1.1	2.0	2.4	2.4	-2.1	8.7	-3.9	2.5	6.5	-11.8	12.3
	σN	5.8	5.5	7.0	8.6	6.4	8.1	12.1	7.3	14.8	12.7	10.1	9.7	8.5	13.0
	within 10%	90.7	91.7	92.6	88.9	93.5	87.0	85.2	91.7	75.0	86.1	89.8	73.1	36.1	50.9
R410A	eA	4.7	5.3	7.0	7.8	7.4	6.9	7.1	7.5	8.1	12.7	10.0	7.8	16.4	12.5
	eR	-1.1	0.1	-4.9	-6.0	-3.5	-2.5	-0.7	-5.4	7.1	-10.1	-4.1	1.3	-16.4	9.2
	σN	6.9	8.6	11.6	14.1	12.2	12.3	14.0	8.0	14.0	17.5	16.3	12.9	11.6	13.7
	within 10%	86.7	88.0	77.3	76.0	73.3	77.3	80.0	69.3	78.7	56.0	70.7	78.7	20.0	45.3
all data	eA	3.5	4.0	4.2	4.2	4.8	4.9	5.1	6.2	7.2	7.4	7.6	7.6	12.6	13.0
	eR	1.4	2.0	-0.1	-0.4	1.2	1.1	0.3	-3.6	6.2	-4.1	2.9	5.6	-12.1	12.0
	σN	6.3	7.0	8.5	9.6	8.7	9.6	11.3	7.6	13.4	13.6	11.7	10.0	8.7	13.0
	within 10%	92.7	92.3	88.5	88.8	86.4	86.2	86.9	81.7	80.3	78.2	78.7	75.4	33.5	51.1

The present model is also compared with the void fraction data summarized in Table 5.1 in Figure 5.19 on a heat transfer basis. No noticeable deviation between adiabatic, evaporation, and condensation conditions can be seen in Figure 5.19.

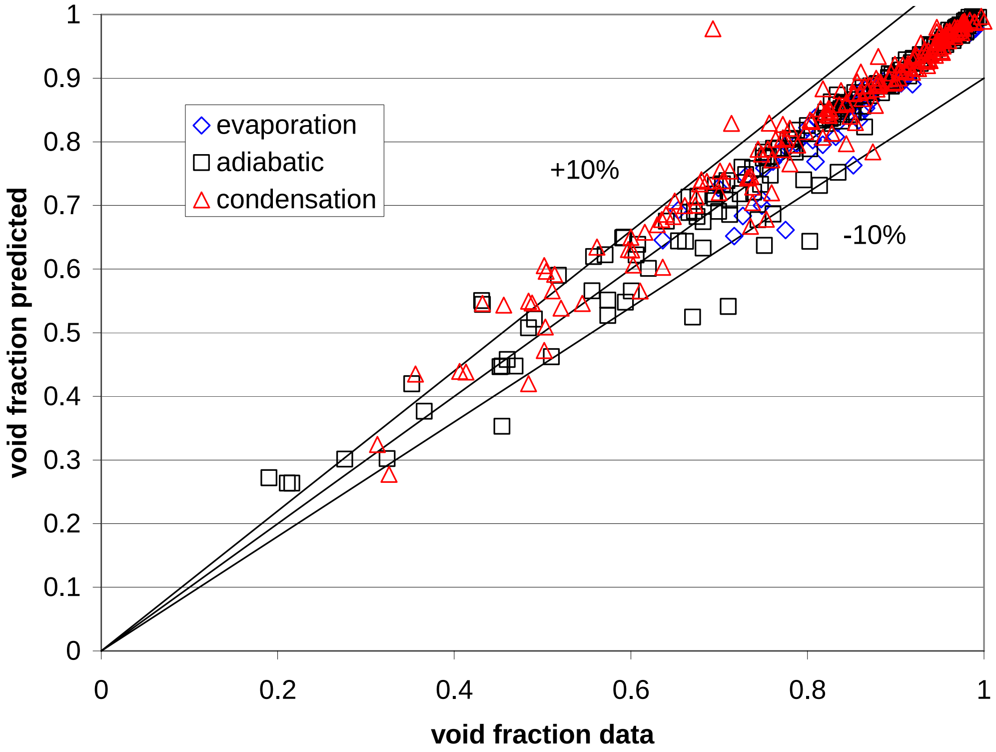

Figure 5.19. Void fraction data summarized in Table 5.1 vs. void fraction predicted by present model and separated by heat transfer type

5.6 Conclusion

In conclusion, probabilistic two-phase flow map modeling of void fraction, previously developed for multi-port microchannels, is developed for single, smooth, horizontal tubes in the present study. The present void fraction model utilizes a generalized probabilistic two phase flow regime map to properly weight models identified to represent the intermittent/liquid, stratified, and annular flow regimes on a time fraction basis. The model is general in that void fraction models for each flow regime can easily be interchanged as more accurate models are identified. The present model exhibits no discontinuities because the time fraction functions are smooth and continuous for the entire quality range. Furthermore, the present void fraction model utilizes a time fraction basis consistent with the probabilistic two-phase flow condensation model found in the literature. The probabilistic model along with 12 other models identified in the literature are compared with a database of 427 data points that include void fraction data of R11, R12, R134a, R22, R410A refrigerants, 4.26 to 9.58 mm diameter tubes, mass fluxes from 70 to 900 kg/m^2-s, and a full quality range under condensation, adiabatic, and evaporation conditions. The probabilistic model is seen to have the lowest mean absolute deviation of 3.5% when compared to the present database. Caution should be exercised in using the present void fraction model outside of the range of tube sizes, flow conditions, and fluid properties with which the model is presently validated. A larger database should be utilized in the future spanning a greater range of tube sizes and refrigerants in order to further validate the present model.

References

Ahrens, F.W., “Heat Pump Modeling, Simulation, and Design.” Heat Pump Fundamentals. Proceedings of the NATO Advanced Study Institute on Heat Pump Fundamentals, Espinho, Spain, 1980. J. Berghmans, ed. The Hague, Netherlands: Martinus Nijhoff Publishers (1983).

Armand, A.A., “The Resistance during the Movement of a Two-Phase System in Horizontal Pipes,” Izv. Vses. Teplotekh. Inst. 1 (1946) 16–23.

Baroczy, C. J., “Correlation of Liquid Fraction in Two-Phase Flow with Application to Liquid Metals.” Chemical Engineering Progress Symposium Series, 61(57) (1965) 179-191.

Diamanides, C. and J.W. Westwater, “Two-phase Flow Patterns in a Compact Heat Exchanger and in Small Tubes,” *Proceedings of the 2nd. U.K. National Conference on Heat Transfer*, Glasgow, Scotland, (2) (1988) 1257-1268.

Domanski, P. and D. Didion, “Computer Modeling of the Vapor Compression Cycle with Constant Flow Area Expansion Device,” NBS-BSS-155, Springfield, VA ,1983, pp. 1-163.

El Hajal, J., J.R. Thome, and A. Cavalini, “Condensation in Horizontal Tubes, Part 1: Two-Phase Flow Pattern Map,” *International Journal of Heat and Mass Transfer* 46 (2003) 3349-3363.

Graham, D.M., “Experimental Investigation of Void Fraction during Refrigerant Condensation,” M.S. Thesis, University of Illinois, Urbana-Champaign, IL, 1998.

Harms, T.M., D. Li, E.A. Groll, and J.E. Braun, “A Void Fraction Model for Annular Flow in Horizontal Tubes,” *International Journal of Heat and Mass Transfer*, 46(21) (2003) 4051-4057.

Hughmark, G.A., “Holdup in Gas-Liquid Flow,” *Chemical Engineering Progress*, 58(4) (1962)62-65.

Jassim, E. W., T. A. Newell, and J. C. Chato, “Probabilistic Two-Phase Flow Regime Maps in Tubes and Their Generalization to Physical Parameters,” to be submitted to the International Journal of Heat and Mass Transfer (2006b).

Jassim, E. W., T. A. Newell, and J. C. Chato, “Prediction of Two-Phase Condensation in Single Tubes using Probabilistic Flow Regime Maps,” to be submitted to the International Journal of Heat and Mass Transfer (2006c).

Jassim, E. W., T. A. Newell, and J. C. Chato, “Probabilistic Determination of Two-Phase Flow Regimes Utilizing an Automated Image Recognition Technique,” to be submitted to Experiments In Fluids (2006a)

Jassim, E.W. and T. A. Newell. “Prediction of Two-Phase Pressure Drop and Void Fraction in Microchannels using Probabilistic Flow Regime Mapping,” *International Journal of Heat and Mass Transfer* 49 (2006) 2446-2457.

Kopke, H.R., “Experimental Investigation of Void Fraction during Refrigerant Condensation in Horizontal Tubes,” M.S. thesis, University of Illinois, Urbana-Champaign, IL 1998.

Larson, H.C., “Void Fractions of Two-Phase Steam Water Mixtures,” M.S.Thesis, University of Minnesota, 1957.

Levy, S., “Steam Slip- Theoretical Prediction from Momentum Model,” *Transactions ASME, Journal of Heat Transfer*, Series C, 82(1960) 113-124.

Lockhart, R.W. and R. C. Martinelli, “Proposed Correlation of Data for Isothermal Two-Phase, Two-Component Flow in Pipes,” *Chemical Engineering Progress*, 45(1) (1949)39-48.

Martinelli, R.C. and D. B. Nelson, “Prediction of Pressure Drop During Forced-Circulation Boiling of Water,” *Transactions ASME*, 70(1948) 695-702.

Maurer, G., “A Method for Predicting Steady-State Boiling Vapor Fractions in Reactor Coolant Channels,” *Bettis Technical Review*, WAPD-BT-19, (1960).

Niño, V.G. “Characterization of Two-phase Flow in Microchannels,” Ph.D. Thesis, University of Illinois, Urbana-Champaign, IL, 2002.

Premoli, A., D. Francesco, and A. Prina. “A Dimensional Correlation for Evaluating Two-Phase Mixture Density,” La Termotecnica, 25(1)(1971)17-26.

Rouhani, Z. and E. Axelsson, “Calculation of Void Volume Fraction in the Subcooled and Quality Boiling Regions,” *Int. J. Heat Mass Transfer*, 13 (1970) 383–393.

Sacks, P.S., “Measured Characteristics of Adiabatic and Condensing Single Component Two-Phase Flow of Refrigerant in a 0.377 in. Diameter Horizontal Tube,” *ASME Winter Annual Meeting*, 75-WA/ HT-24, Houston, Texas (1975)

Smith, S. L., “Void Fractions in Two-Phase Flow: A Correlation Based Upon an Equal Velocity Head Model,” *Proc. Instn. Mech Engrs*., London, 184(36) (1969) 647-664.

Steiner, D., “Heat Transfer to Boiling Saturated Liquids,” VDI-Wārmeatlas (VDI Heat Atlas), Verein Deutscher Ingenieure, VDI-Gesellschaft Verfahrenstechnik und Chemieingenieurwesen (GCV), Dū sseldorf, Chapter Hbb (1993).

Taitel Y. and D. Barnea, “Two-phase slug flow,” *Adv. Heat Transfer,* 20 (1990), pp. 83–132.

Tandon, T. N., H. K. Varma, and C. P. Gupta, “A Void Fraction Model for Annular Two-Phase Flow,” *International Journal of Heat and Mass Transfer*, 28(1) (1985) 191-198.

Thom, J. R. S., “Prediction of Pressure Drop during Forced Circulation Boiling of Water,” *International Journal of Heat and Mass Transfer*, Vol. 7:7 (1964) 709-724.

Thome, J.R., J. El Hajal, and A. Cavalini, “Condensation in Horizontal Tubes, Part 2: New Heat Transfer Model Based on Flow Regimes,” *International Journal of Heat and Mass Transfer* 46 (2003) 3365-3387.

Wallis, G. B., “One-Dimensional Two-Phase Flow,” New York: McGraw-Hill, 1969, pp. 51-54.

Wilson, M.J., “Experimental Investigation of Void Fraction during Horizontal Flow in Larger Diameter Refrigeration Applications,” M.S. thesis, University of Illinois, Urbana-Champaign, IL (1998).

Yashar, D.A., “Experimental Investigation of Void Fraction during Horizontal Flow in Smaller Diameter Refrigeration Applications,” M.S. thesis, University of Illinois, Urbana-Champaign, IL, 1998.

Yashar, D.A., M.J. Wilson, H.R. Kopke, D.M. Graham, J.C. Chato and T.A. Newell, “An Investigation of Refrigerant Void Fraction in Horizontal, Microfin Tubes,” *HVAC&R Research* 7 (2001) 67–82.

Chapter 6. Probabilistic Two-Phase Flow Regime Map Modeling Of Refrigerant Pressure Drop In Horizontal Tubes

6.1 Abstract

A probabilistic two-phase flow regime map pressure drop model is developed for refrigerant flowing through single, smooth, horizontal tubes with and without heat transfer. The time fraction information from a generalized probabilistic two-phase flow map is used to provide a physically based weighting of pressure drop models identified for different flow regimes. The developed model and other pressure drop models in the literature are compared to data from multiple sources that includes R11, R12, R123, R134a, R22, R404A refrigerants, 7.04 to 12.0mm diameter tubes, mass fluxes from 25 to 900 kg/m^2-s, and a full quality range. The present model has a mean absolute deviation of 15.8%.

6.2 Nomenclature

A	cross sectional area of the tube (m^2)
B	parameter defined in Equations 6.30a through 6.30f
C_1	dimensionless parameter defined in Equation 6.21 (-)
C_2	dimensionless parameter defined in Equation 6.22 (-)
D	hydraulic diameter (m)
$\left(\frac{dP}{dz}\right)_{Fr_{lo}}$	pressure drop defined by Equation 6.32 (kPa/m)
e	deviation (-)
e_A	mean absolute deviation (-)
e_R	average deviation (-)
F	observed time fraction (-)
Fr	Froude number (-)
f	friction factor
$f_{Fr_{lo}}$	friction factor defined by Equations 6.33a and 6.33b (-)
G	mass flux (kg/m^2-s)
G_M	dimensionless parameter defined in Equation 6.47 (-)
g_a	gravitational acceleration (9.81 m/s^2)
h	heat transfer coefficient (W/m^2-K)
i	intermittent flow regime curve fit constant (-)
KE_{avg}	average kinetic energy defined in Equation 6.44 (J/m)
L	test section length (m)
M_1	dimensionless parameter defined in Equation 6.14 (-)
M_2	dimensionless parameter defined in Equation 6.15 (-)
N	total number of data points (-)
$N_{conf.}$	confinement number (-)
n	exponent in Equation 6.28 (-)
P_r	reduced pressure (-)
Re	Reynolds number (-)
s	stratified flow regime curve fit constant (-)
We	vapor Weber number (-)
x	flow quality (-)

Xi	dimensionless group correlating the intermittent/liquid flow regime (-)
Xs	dimensionless group correlating the stratified flow regime (-)
X_{tt}	turbulent- turbulent Lockhart - Martinelli parameter (-)
X_{ann}	dimensionless parameter defined by Equation 6.35 (-)
Y	dimensionless parameter defined by Equation 6.29 (-)

Greek symbols

α	void fraction (-)
Γ	dimensionless parameter defined in Equation 6.25 (-)
μ	dynamic viscosity (kg/m-s)
ρ	density (kg/m^3)
σ	surface tension (N/m)
σ_N	standard deviation (-)
θ	tube inclination angle (radians)
Φ^2	two-phase multiplier (-)

Subscripts

acc	due to acceleration
ann	pertaining to the annular flow regime
fr	due to friction
gr	due to gravity
h	homogeneous
int	pertaining to the intermittent flow regime
int+liq	pertaining to the intermittent and liquid flow regime
l	liquid
lo	liquid only
liq	pertaining to the liquid flow regime
pred	predicted
strat	pertaining to the stratified flow regime
v	vapor
vo	vapor only
vap	pertaining to the vapor flow regime
2ϕ	two-phase

6.3 Introduction

Prediction of two-phase pressure drop is important in the design of vapor compression systems. The two-phase pressure drop in these systems affect not only the efficiency of the system but also the size of the compressor required to provide a given capacity. Consequently, there are numerous two-phase flow pressure drop models in the literature. However, the majority of the models in the literature best apply to a particular flow regime, and many of the empirical relations or assumptions made in these pressure drop models do not apply for a full range of qualities, mass fluxes, tube diameters, and fluid properties.

Many sources in the literature describe the importance of using flow regime information in the modeling of two-phase flow such as Garimella (2004), Garimella et al. (2003), Coleman and Garimella (2003), El Hajal et al. (2003), Thome et al. (2003), Didi et al. (2002), Zurcher et al. (2002a&b), Mandhane et al. (1974), and Baker (1954).

Recently, a probabilistic two-phase flow regime map pressure drop model is found in the literature by Jassim and Newell (2006) for multi-port microchannels. However, no flow regime map pressure drop models could be found in the literature for single tubes above 3 mm in diameter.

A probabilistic two-phase flow map pressure drop model is developed and validated for single, smooth, horizontal tubes in the present study. This model utilizes a generalized probabilistic two-phase flow map found in the literature by Jassim et al. (2006b) for smooth, horizontal, adiabatic tubes. The pressure drop is predicted as the sum of the products of the time fraction in which each flow regime is observed and a model representative of the respective flow regime, which is consistent with the probabilistic two-phase flow regime models for heat transfer and void fraction developed by Jassim et al. (2006c), and Jassim et al. (2006d), respectively. Since the time fraction functions are continuous for the full quality range, the pressure drop model smoothly transitions between flow regimes without discontinuities. A review of pressure drop models in the literature is presented and appropriate models for the intermittent, stratified, and annular flow regimes were identified. The present pressure drop model and models identified in the literature are compared to a pressure drop database consisting of 772 points of ammonia, R11, R12, R123, R134a, R22, and R404A pressure drop in 7.04 mm to 12.00 mm diameter smooth tubes at mass fluxes ranging from 25 to 902 kg/m^2-s and a full quality range under evaporation, adiabatic, and condensation conditions. The present model has a mean absolute deviation of 15.8% when compared to the entire database.

6.4 Literature review

The total pressure drop in a tube, given in Equation 6.1, consists of the frictional, accelerational, and gravitational components. The accelerational and gravitational components are given in Equations 6.2 and 6.3, respectively.

$$\frac{dP}{dz} = \left(\frac{dP}{dz}\right)_{fr} + \left(\frac{dP}{dz}\right)_{acc} + \left(\frac{dP}{dz}\right)_{gr} \qquad (6.1)$$

$$\left(\frac{dP}{dz}\right)_{acc} = \frac{G^2}{L}\frac{d}{dz}\left[\frac{1}{A}\left(\frac{x^2}{\rho_v \alpha} + \frac{(1-x)^2}{\rho_l (1-\alpha)}\right)\right] \qquad (6.2)$$

$$\left(\frac{dP}{dz}\right)_{gr} = g_a\left[\sin\theta\left[\alpha\rho_v + (1-\alpha)\rho_l\right]\right] \qquad (6.3)$$

There are numerous two-phase flow pressure drop models found in the literature for the frictional component. The majority of these models tend to predict pressure drop best for a particular flow regime or fluid properties and can be divided into two-phase multiplier models and non two-phase multiplier models.

6.4.1 Two-phase multiplier pressure drop models

Many of the two-phase pressure drop models in the literature are two-phase multiplier based. Martinelli and Nelson (1948) developed two-phase multipliers to relate the two-phase pressure drop to equivalent flow single-phase pressure drop. The liquid only and vapor only two-phase multipliers are given in Equations 6.4 and 6.5, respectively.

$$\Phi_{lo}^2 = \frac{\left(\frac{dP}{dz}\right)_{2\phi}}{\left(\frac{dP}{dz}\right)_{lo}} \tag{6.4}$$

$$\Phi_{vo}^2 = \frac{\left(\frac{dP}{dz}\right)_{2\phi}}{\left(\frac{dP}{dz}\right)_{vo}} \tag{6.5}$$

The liquid only and vapor only pressure drop is calculated assuming the entire flow is either liquid or vapor and are given by Equations 6.6 and 6.7, respectively.

$$\left(\frac{dP}{dz}\right)_{lo} = 2f_{lo}\frac{1}{D}\frac{G^2}{\rho_l} \tag{6.6}$$

$$\left(\frac{dP}{dz}\right)_{vo} = 2f_{vo}\frac{1}{D}\frac{G^2}{\rho_v} \tag{6.7}$$

Most of the two-phase multiplier based models use the Blasius solution friction factor given in Equations 6.8 and 6.9 for liquid and vapor only, respectively.

$$f_{lo} = \frac{0.079}{\mathrm{Re}_{lo}^{0.25}} \tag{6.8}$$

$$f_{vo} = \frac{0.079}{\mathrm{Re}_{vo}^{0.25}} \tag{6.9}$$

The Reynolds number is defined in Equations 6.10 and 6.11 for liquid and vapor only conditions, respectively. In the present document the Blasius friction factors will be assumed unless otherwise indicated.

$$\mathrm{Re}_{lo} = \frac{GD}{\mu_l} \tag{6.10}$$

$$\mathrm{Re}_{vo} = \frac{GD}{\mu_v} \tag{6.11}$$

Martinelli and Nelson (1948) and Lockhart and Martinelli (1949) both developed two-phase multiplier based two-phase flow pressure drop models based on data from mixtures of air and water, kerosene, benzene, and oils. Lockhart and Martinelli (1949) developed the Lockhart-Martinelli parameter, given in Equation 6.12a, to correlate their data. Two different versions of the Lockhart-Martinelli parameter can be found in the literature given in Equations 6.12a and 6.12b. Equation 6.12a is the most commonly used expression for the Lockhart-Martinelli parameter and reflects the original work by Lockhart and Martinelli (1949), consequently this form will be assumed unless indicated otherwise in the present study.

$$X_{tt} = \left(\frac{1-x}{x}\right)^{0.9}\left(\frac{\rho_v}{\rho_l}\right)^{0.5}\left(\frac{\mu_l}{\mu_v}\right)^{0.1} \tag{6.12a}$$

$$X_{tt} = \left(\frac{1-x}{x}\right)^{0.875} \left(\frac{\rho_v}{\rho_l}\right)^{0.5} \left(\frac{\mu_l}{\mu_v}\right)^{0.125} \tag{6.12b}$$

The Lockhart-Martinelli parameter represents the ratio of the liquid to vapor frictional pressure drop assuming that each phase is turbulent and flowing alone at the superficial velocity. Friedel (1979) developed a two-phase liquid only multiplier pressure drop model, given in Equations 6.13 through 6.15, which is based on R12, air-oil, and air-water experiments. The experiments included circular and square test sections with horizontal and vertical upward flow.

$$\Phi_{lo}{}^{2} = M_1 + \frac{3.24 M_2}{Fr_h{}^{0.045} We_h{}^{0.035}} \tag{6.13}$$

$$M_1 = (1-x)^2 + x^2 \left(\frac{\rho_l}{\rho_v}\right)\left(\frac{f_{vo}}{f_{lo}}\right) \tag{6.14}$$

$$M_2 = x^{0.78}(1-x)^{0.224} \left(\frac{\rho_l}{\rho_v}\right)^{0.91} \left(\frac{\mu_v}{\mu_l}\right)^{0.19} \left(1-\frac{\mu_v}{\mu_l}\right)^{0.7} \tag{6.15}$$

The Friedel (1979) model utilizes the homogeneous Froude and Weber numbers given in Equations 6.16 and 6.17, respectively, where the homogeneous density is defined in Equation 6.18.

$$Fr_h = \frac{G^2}{\rho_h{}^{2} g_a D} \tag{6.16}$$

$$We_h = \frac{G^2 D}{\rho_h \sigma} \tag{6.17}$$

$$\rho_h = \frac{\rho_l \rho_v}{x\rho_l + (1-x)\rho_v} \tag{6.18}$$

The liquid only friction factor used in the Friedel model is given in Equation 6.19.

$$f_{lo} = 0.25\left[0.86859 \ln\left(\frac{\mathrm{Re}_{lo}}{1.964\ln(\mathrm{Re}_{lo}) - 3.8215}\right)\right]^{-2} \tag{6.19}$$

Souza et al. (1993) developed the two-phase liquid only multiplier pressure drop model given in Equations 6.20 through 6.22, which is based on R12 and R134a adiabatic, horizontal, 10.9 mm diameter tube data. Their model utilizes the liquid only Froude number, given in Equation 6.23, and the Lockhart-Martinelli parameter of Equation 6.12b to correlate their data.

$$\Phi_{lo}{}^{2} = \left(1.376 + c_1 X_{tt}{}^{-c_2}\right)(1-x)^{1.75} \tag{6.20}$$

$$c_1 = \begin{cases} 4.172 + 5.480 Fr_l - 1.564 Fr_l{}^{2} & (0 < Fr_l \le 0.7) \\ 7.242 & (Fr_l > 0.7) \end{cases} \tag{6.21}$$

$$c_2 = \begin{cases} 1.773 - 0.169 \mathrm{Fr}_l & (0 < \mathrm{Fr}_l \le 0.7) \\ 1.655 & (Fr_l > 0.7) \end{cases} \tag{6.22}$$

$$Fr_{lo} = \frac{G^2}{\rho_l{}^2 g_a D} \tag{6.23}$$

Souza and Pimenta (1995) then developed a different two-phase liquid only multiplier pressure drop model, given in Equation 6.24, from a larger set of data consisting of R12, R22, R134a, MP39, and a R32/125 (60/40% by mass) mixture. Souza and Pimenta (1995) used the Lockhart Martinelli parameter of Equation 6.12b and the dimensionless parameter $\varGamma$, given in Equation 6.25, to correlate their data.

$$\varPhi_{lo}{}^2 = 1 + \left(\varGamma^2 - 1\right)x^{1.75}\left(1 + 0.9524\varGamma X_{tt}{}^{0.4126}\right) \tag{6.24}$$

$$\varGamma = \left(\frac{\rho_l}{\rho_v}\right)^{0.5}\left(\frac{\mu_v}{\mu_l}\right)^{0.125} \tag{6.25}$$

Jung and Radermacher (1989) developed a relatively simple Lockhart-Martinelli parameter based two-phase liquid only multiplier pressure drop model, given in Equation 6.26, which was used to correlate R12, R114, R152a, and R22 pressure drop data under evaporation conditions.

$$\varPhi_{lo}{}^2 = 12.82 X_{tt}{}^{-1.47}(1-x)^{1.8} \tag{6.26}$$

Jung and Radermacher's (1989) model includes acceleration pressure drop since it was found to be small in their experiments. The fiction factor used in this model is defined in Equation 6.27.

$$f_{lo} = \frac{0.046}{\mathrm{Re}_{lo}{}^{0.2}} \tag{6.27}$$

Chisholm (1973) developed the two phase liquid only multiplier pressure drop model given in Equation 6.28. This model utilizes the ratio of vapor only to liquid only pressure drop (Y) given in Equation 6.29 and B given in Equations 6.30a through 6.30f to correlate their data.

$$\varPhi_{lo}{}^2 = 1 + \left(Y^2 - 1\right)\left[Bx^{(2-n)/2}\left(1-x\right)^{(2-n)/2} + x^{2-n}\right] \text{,where n=0.25} \tag{6.28}$$

$$Y^2 = \frac{\left(\dfrac{dP}{dz}\right)_{vo}}{\left(\dfrac{dP}{dz}\right)_{lo}} \tag{6.29}$$

If $0<Y<9.5$ then

$$B = \frac{55}{G^{0.5}} \quad \text{for G} \geq 1900 \text{ kg/m}^2\text{-s} \tag{6.30a}$$

$$B = \frac{2400}{G} \quad \text{for } 500<\text{G}<1900 \text{ kg/m}^2\text{-s} \tag{6.30b}$$

$$B = 4.8 \quad \text{for G} \leq 500 \text{ kg/m}^2\text{-s} \tag{6.30c}$$

If $9.5<Y<28$ then

$$B = \frac{520}{YG^{0.5}} \quad \text{for G} \leq 600 \text{ kg/m}^2\text{-s} \tag{6.30d}$$

$$B = \frac{21}{Y} \quad \text{for G} > 600 \text{ kg/m}^2\text{-s} \tag{6.30e}$$

If Y>28 then

$$B = \frac{15000}{Y^2 G^{0.5}} \tag{6.30f}$$

Grönnerud (1979) developed the two-phase liquid only multiplier pressure drop model given in Equations 6.31, 6.32 and 6.33a&b, which utilizes the liquid only Froude number.

$$\Phi_{lo}{}^2 = 1 + \left(\frac{dP}{dz}\right)_{Fr_{lo}} \left[\frac{\frac{\rho_l}{\rho_v}}{\left(\frac{\mu_l}{\mu_v}\right)^{0.25}} - 1\right] \tag{6.31}$$

$$\left(\frac{dP}{dz}\right)_{Fr_{lo}} = f_{Fr_{lo}} \left[x + 4\left(x^{1.8} - x^{10} f_{Fr_{lo}}^{0.5}\right)\right] \tag{6.32}$$

If $Fr_{lo} \geq 1$

$$f_{Fr_{lo}} = 1 \tag{6.33a}$$

If $Fr_{lo} < 1$

$$f_{Fr_{lo}} = Fr_{lo}{}^{0.3} + 0.0055\left(\ln\frac{1}{Fr_{lo}}\right) \tag{6.33b}$$

Didi et al. (2002) found that the Grönnerud (1979) model represents their database of R134a, R123, R402A, R404A, and R502 pressure drop data well under evaporation conditions in 10.92 mm and 12 mm diameter tubes for the intermittent and stratified wavy flow regimes.

Niño (2002) developed a two-phase vapor only multiplier pressure drop model for R410A, R134a and air-water in multi-port microchannels, given in Equation 6.34, which utilizes the dimensionless group X_{ann}, given in Equation 6.35, that contains the Lockhart-Martinelli parameter of Equation 6.12b and the vapor Webber number given in Equation 6.36.

$$\Phi_{vo}^2 = \exp(-0.046 X_{ann}) + 0.22[\exp(-0.002 X_{ann}) - \exp(-7 X_{ann})] \tag{6.34}$$

$$X_{ann} = \left[\left(X_{tt} + \frac{1}{We_v^{1.3}}\right)\left(\frac{\rho_l}{\rho_v}\right)^{0.9}\right] \tag{6.35}$$

$$We_v = \frac{\left[\frac{(xG)^2}{\rho_v}\right]}{\frac{\sigma}{D}} \tag{6.36}$$

Zhang and Kwon (1999) developed a two-phase liquid only multiplier pressure drop model, given in Equation 6.37, to correlate their pressure drop data of R134a, R22, and R410A in 3.25mm and 6.2mm copper tubes, and 2.13mm 6-port microchannels. This model uses reduced pressure to correlate the data.

$$\Phi_{lo}{}^2 = (1-x)^2 + 2.87 x^2 P_r^{-1} + 1.68 x^{0.8} (1-x)^{0.25} (P_r)^{-1.64} \tag{6.37}$$

Tran et al. (2000) developed a two-phase liquid only multiplier pressure drop model, given in Equation 6.38, to correlate their R134a, R12, and R113 data in 2.46 and 2.92 mm circular microchannel tubes and a 4.06 by 1.7 mm rectangular microchannel.

$$\Phi_{lo}^{\;2} = 1 + \left(4.3\Gamma^2 - 1\right)\left(\mathrm{N}_{conf.}\, x^{0.875}(1-x)^{0.875} + x^{1.75}\right) \tag{6.38}$$

Tran et al. (2000) used the property ratio *Γ*, defined in Equation 6.25, to correlate their data and found that the large tube correlations in the literature under predicted their pressure drop data.

6.4.2 Other pressure drop models

Other two-phase pressure drop models in the literature do not use two-phase multipliers. McAdams (1954) developed a homogeneous pressure drop model given in Equation 6.39, which assumes a homogeneous mixture of the gas and liquid phases with a homogeneous density, viscosity, Reynolds number, and friction factor given in Equations 6.18, 6.40, 6.41, and 6.42, respectively.

$$\left(\frac{dP}{dz}\right)_{fr} = 2 f_h \frac{1}{D}\frac{G^2}{\rho_h} \tag{6.39}$$

$$\mu_h = \left(\frac{x}{\mu_v} + \frac{(1-x)}{\mu_l}\right)^{-1} \tag{6.40}$$

$$\mathrm{Re}_h = \frac{GD}{\mu_h} \tag{6.41}$$

$$f_h = \frac{0.079}{\mathrm{Re}_h^{\;0.25}} \tag{6.42}$$

Asali et al. (1985) developed a two-phase pressure drop model for vertical annular flow which defines a friction factor based on the ratio of film height and pipe diameter. This model requires the knowledge of the mass flow rate of the liquid film traveling along the walls. They compared their model with air-water and air-water/glycerine pressure drop data in 22.9 mm and 42 mm diameter pipes. Niño (2002) developed an average kinetic energy based pressure drop model given in Equation 6.43 where the average kinetic energy is defined in Equation 6.44 with a homogeneous density.

$$\left(\frac{dP}{dz}\right)_{\mathrm{int}} = 0.045\frac{1}{D} KE_{Avg} \tag{6.43}$$

$$KE_{Avg} = \frac{G^2}{2\rho_h} \tag{6.44}$$

Niño (2002), and Niño et al. (2006) found that this model accurately predicts their data for intermitent flow pressure drop in microchannels for air-water, R410A, and R134a in multiport microchannels. Adams (2003) made a slight modification to the model by changing the friction factor constant to 0.035 as seen in Equation 6.45.

$$\left(\frac{dP}{dz}\right)_{fr} = 0.035\frac{1}{D} KE_{Avg} \tag{6.45}$$

Adams (2003) found Equation 6.45 to be valid for R245fa, carbon dioxide, and ammonia in microchannels when compaired to their microchannel data. Müller-Steinhager and Heck (1986) developed the pressure drop model given in Equations 6.46 and 6.47, which is a function of the liquid only and vapor only pressure drop. Didi et al. (2002) found that the Müller-Steinhager and Heck (1986) model represents their database of R134a, R123, R402A, R404A, and R502 pressure drop data well under evaporation conditions in 10.92 mm and 12 mm diameter tubes for the annular and stratified wavy flow regimes.

$$\left(\frac{dP}{dz}\right)_{fr} = G_M (1-x)^{1/3} + \left(\frac{dP}{dz}\right)_{vo} x^3 \tag{6.46}$$

$$G_M = \left(\frac{dP}{dz}\right)_{lo} + 2\left[\left(\frac{dP}{dz}\right)_{vo} - \left(\frac{dP}{dz}\right)_{lo}\right] x \tag{6.47}$$

Garimella (2004), Garimella et al. (2003), and Chung and Kawaji (2004) have developed and presented similar flow regime based pressure drop models of the intermittent two-phase flow regime in microchannels, which attempt to incorporate the physics of the flow into the model. These models require the use of traditional flow regime maps to determine the flow regime that exists and require flow visualization data on the slug rate.

Recently, Jassim and Newell (2006) developed a probabilistic two-phase flow map based model for frictional pressure drop in multi-port microchannels given in Equation 6.48.

$$\left(\frac{dP}{dz}\right)_{total} = F_{liq}\left(\frac{dP}{dz}\right)_{liq} + F_{\text{int}}\left(\frac{dP}{dz}\right)_{\text{int}} + F_{vap}\left(\frac{dP}{dz}\right)_{vap} + F_{ann}\left(\frac{dP}{dz}\right)_{ann} \tag{6.48}$$

In Equation 6.48 the total pressure drop is predicted as the sum of the product of the fraction of time that each flow regime is observed under a given condition and a pressure drop model representative the respective flow regime. Jassim and Newell (2006) curve fit the time fraction data obtained by Nino (2002) with continuous functions over the entire quality range that have physically correct limits. A probabilistic two-phase flow regime map from Jassim and Newell (2006) with the time fraction data and curve fits can be seen in Figure 6.1. Jassim and Newell (2006) used probabilistic two-phase flow maps because they can easily be represented by continuous functions for the entire quality range which smoothly transition from one flow regime to another. This is not the case with traditionally used flow maps such as the Steiner (1993) style flow map depicted in Figure 6.2, which specifies a particular flow regime at a given flow condition. Pressure drop models were chosen for each flow regime based on their ability to predict pressure drop in multi-port microchannels. The models used for the liquid and vapor flow regimes are given by Equations 6.6 and 6.7, respectively. The models given by Equations 6.34 and 6.43 are used for the annular and intermittent flow regimes, respectively.

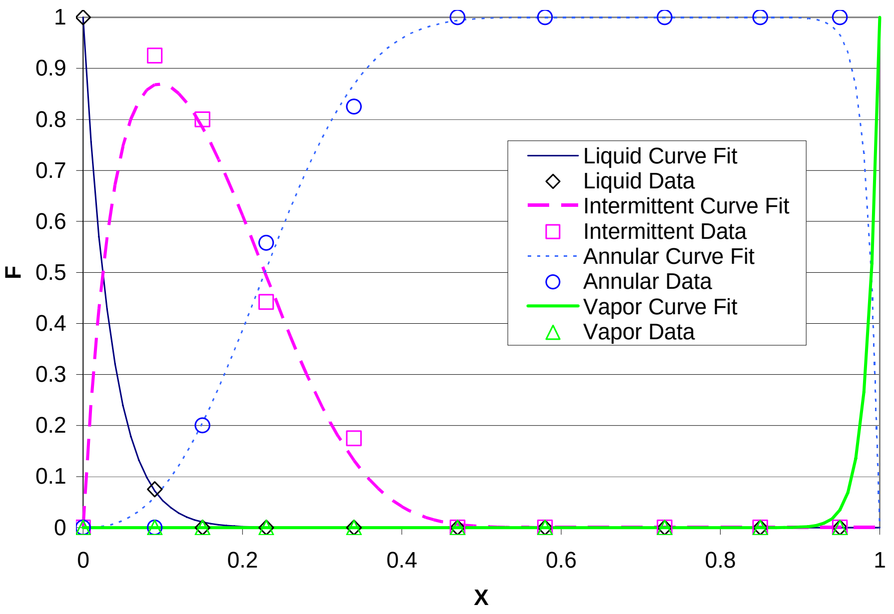

Figure 6.1. Probabilistic flow map with time fraction curve fits for R410A, 10 ºC, 300 kg/m^2-s in a 6-port 1.54 mm hydraulic dia. microchannel taken from Jassim and Newell (2006).

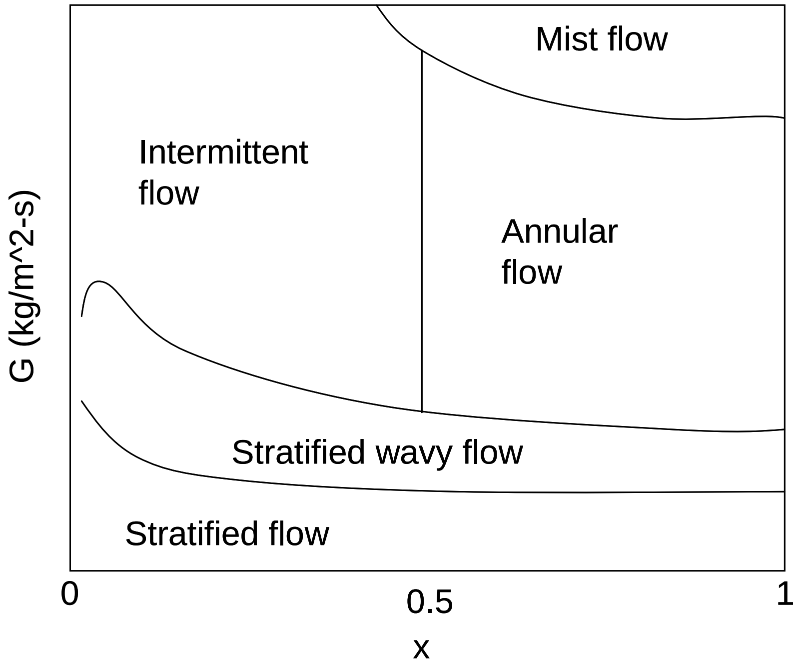

Figure 6.2. Steiner (1993) type flow map depiction

6.5 Present pressure drop model development

A probabilistic two-phase flow regime map pressure drop model is developed for single, horizontal tubes in a manner similar to that of Jassim and Newell (2006) for multi-port microchannels. The present pressure drop model is also developed on a consistent time fraction basis as Jassim et al. (2006c) and Jassim et al. (2006d) have modeled condensation heat transfer and void fraction, respectively, in large tubes.

6.5.1 Generalized two phase flow map

Single tubes of approximately 3mm in diameter and larger are found to contain a stratified flow regime which is absent in the 1.54 mm hydraulic diameter microchannels of Nino (2002). Damianides and Westwater (1988) support this observation in that they indicate that the transition from “microchannel” behavior to “large tube” behavior occurs in the 3 mm tube diameter range. Furthermore, vapor only flow is not present below a quality of 100% in single tubes. Therefore, it is necessary to develop a new set of two-phase flow models for single tubes above 3mm in diameter.

Jassim et al. (2006b) developed probabilistic two-phase flow maps for single tubes with the experimentally obtained time fraction data obtained from Jassim et al. (2006a) who utilized the flow loop depicted in Figure 6.3. Jassim et al. (2006b) developed curve fits for the intermittent/liquid, stratified, and annular flow regime time fraction data. The time fraction functions are given in Equations 6.49 through 6.51 for the intermittent/liquid, stratified, and annular flow regimes, respectively.

$$F_{\text{int}+liq} = (1-x)^{i} \tag{6.49}$$

$$F_{strat} = \left(1 - x^{\left(s/\sqrt{x}\right)}\right)^{i} - (1-x)^{i} \tag{6.50}$$

$$F_{ann} = 1 - F_{\text{int}+liq} - F_{strat} \tag{6.51}$$

The flow maps developed were generalized by linking the time fraction curve fit constants to physical parameters. The intermittent/liquid time fraction curve fit constant “*i*”, given in Equation 6.52, has a linear relationship with the dimensionless group *Xi*, given in Equation 6.53, which contains the vapor only Weber number, given in Equation 6.54, and the liquid to vapor density ratio.

$$i = 0.0243Xi + 8.07 \tag{6.52}$$

$$Xi = \left(We_{vo}^{0.4}\right)\left(\frac{\rho_l}{\rho_v}\right) \text{, where} \tag{6.53}$$

$$We_{vo} = \left(\frac{G^2 D}{\rho_v \sigma}\right) \tag{6.54}$$

The stratified time fraction curve fit constant “*s*”, given in Equation 6.55, has a strong relationship with the dimensionless group *Xs*, given in Equation 6.56, which contains the square root of the vapor only Froude number, given in Equation 6.57, and the vapor to liquid density ratio.

$$s = \frac{1}{0.45Xs} + \frac{1}{0.025Xs^{4.44}} \tag{6.55}$$

$$Xs = \left(Fr_{vo}^{0.5}\right)\left(\frac{\rho_v}{\rho_l}\right)^{0.65} \tag{6.56}$$

$$Fr_{vo} = \left(\frac{G^2}{\rho_v^2 g_a D}\right) \tag{6.57}$$

A sample probabilistic two phase flow regime map with generalized curve fits is depicted in Figure 6.4 for 8.00 mm diameter tube with R134a flowing at 25 ºC and 300 kg/m^2-s. Jassim et al. (2006b) found these generalized curve fit constants to represent the time fraction data with an average absolute error of 0.022, 0.094, and 0.071 for the intermittent/liquid, stratified, and annular flow regimes, respectively, for the 8.00 mm, 5.43 mm, and 3.90 mm diameter tubes. The average absolute error for the 1.74 mm diameter tube in the intermittent flow regime is reported to be 0.044, with the same error for the annular flow regime if the stratified flow regime is neglected which is not observed for this tube diameter.

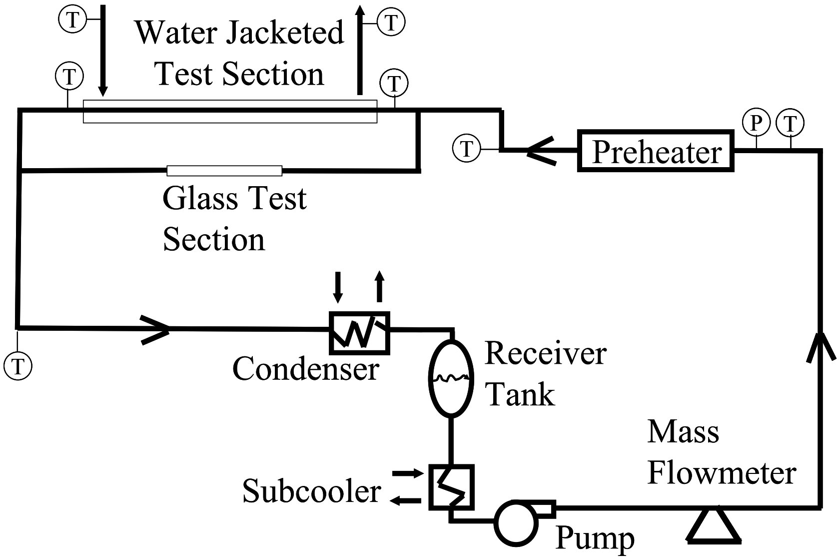

Figure 6.3. Two-phase flow loop schematic from Jassim et al. (2006c)

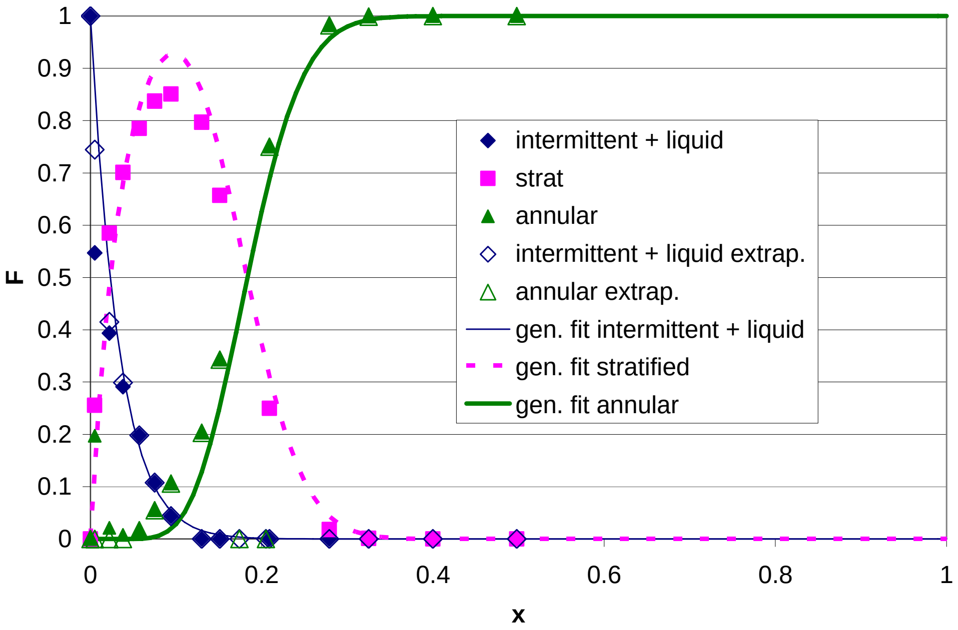

Figure 6.4. Probabilistic flow map with generalized time fraction curve fits for 8.00 mm diameter tube, R134a, 25 °C, 300 kg/m^2-s from Jassim et al. (2006b)

6.5.2 Probabilistic two-phase flow regime map pressure drop model

The present probabilistic two-phase flow regime map pressure drop model, given in Equation 6.58, is a modified version of the Jassim and Newell (2006) model for microchannels to reflect the flow regimes present in horizontal single channel tubes.

$$\left(\frac{dP}{dz}\right)_{total} = F_{\text{int}+liq}\left(\frac{dP}{dz}\right)_{\text{int}+liq} + F_{strat}\left(\frac{dP}{dz}\right)_{strat} + F_{ann}\left(\frac{dP}{dz}\right)_{ann} \tag{6.58}$$

The total pressure drop is simply equal to the time fraction of each flow regime multiplied by a model representative of the respective flow regime. This pressure drop model has a consistent time fraction basis as the Jassim et al. (2006c) condensation heat transfer model, and the Jassim et al. (2006d) void fraction models given in Equations 6.59 and 6.60, respectively.

$$h_{total} = F_{\text{int}+liq} h_{\text{int}+liq} + F_{strat} h_{strat} + F_{ann} h_{ann} \tag{6.59}$$

$$\alpha_{total} = F_{\text{int}+liq} \alpha_{\text{int}+liq} + F_{strat} \alpha_{strat} + F_{ann} \alpha_{ann} \tag{6.60}$$

The present model uses the Grönnerud (1979) model for the intermittent flow regime and the Müller-Steinhager and Heck (1986) model for the stratified flow regime. The Souza et al. (1993) model was modified by using the Lockhart-Martinelli parameter given in Equation 6.12a and is used for the annular flow regime in the present model. These models were chosen because they were found to be good representations of the pressure drop data summarized in Table 6.1 for their respective flow regimes. The present model components can easily be changed as more accurate models are identified for each flow regime.

Table 6.1. Pressure drop data used to compare the present models with other models in the literature

Source	D (mm)	Refrigerants	G (kg/m^2-s)	T_{sat}(ºC)	Heat transfer	Data points
Didi et al. (2002)	10.92, 12.00	R123, R134a, R404A	100 to 318	2 to 30	Evaporation	92
Komandiwirya (2004)	7.721	ammonia	79 to 275	34 to 36	Condensation	21
Sacks (1975)	9.576	R11, R12, R22	86 to 902	25 to 32	Adiabatic & condensation	230
Wattelet (1994)	10.92, 10.21, 7.04	R12, R134a, R22	25 to 543	-20 to 15	evaporation	429

6.5.3 Evaluation of the present pressure drop model

The present pressure drop model and that of Friedel (1979), Souza et al. (1993), modified Souza et al. (1993) using X_{tt} defined in Equation 6.12a, Souza and Pimenta (1995), modified Souza and Pimenta (1995) using X_{tt} defined in Equation 6.12a, Jung and Radermacher (1989), Chisholm (1973), Grönnerud (1979), Niño's (2002) model for annular flow, Zhang and Kwon (1999), Tran et al. (2000), McAdams (1954), Niño's (2002) for intermittent flow, Adams (2003), and Müller-Steinhager and Heck (1986) are compared to the frictional pressure drop data summarized in Table 6.1 in Figures 6.5 through 6.20, respectively. In each of these figures the data is differentiated by refrigerant. The frictional pressure drop was calculated by subtracting the accelerational term given in Equation 6.2. For all of the data under condensation conditions the maximum, minimum, and average accelerational percentage of the fictional pressure drop is 14.2%, 0.01%, and 3.6%, respectively. The largest accelerational pressure drop values are found at the low quality range below 0.4 where void fraction changes significantly with quality. The lowest accelerational pressure drop is found for the ammonia data which has a maximum percentage of 0.1%. This can be attributed to the fact that there was very small quality changes in the ammonia data due to its high heat of vaporization. For all of the data under evaporation conditions the maximum, minimum, and average accelerational percentage of the fictional pressure drop is 15.5%, 1.0%, and 5.18%, respectively. No noticeable trends can be observed in the accelerational pressure drop with respect to quality range or refrigerant type for the evaporation data. The void fraction model given in Equation 6.60 (see Jassim et al. (2006d) for void fraction model components) is used in Equation 6.2 to remove the accelerational component. Furthermore, the pressure drop data in Table 6.1 excludes pressure drop measurements less than 0.1 kPa because pressure drop measurements below this value are inaccurate with experimental uncertainty above 20%. It is evident from these figures that the present model represents the data well as a whole. It is also evident from Figures 6.7 though 6.10 that the modified versions of the Souza et al. (2003) and the Souza and Pimenta (1995) models with the Lockhart-Martinelli parameter given in Equation 6.12b represent the data better as a whole than the with the Lockhart-Martinelli parameter given in Equation 6.12a. A statistical comparison of fourteen of the models detailed in the present study (models with the least average absolute deviation) with the pressure drop data in Table 6.1 is summarized in Table 6.2. The Asali et al. (1985) model is not compared because the mass flow rate of the liquid film flowing on the walls is unknown. Table 6.2 contains the mean absolute deviation, e_A, the average deviation, e_R, and the standard deviation, σ_N, given in Equations 6.61 through 6.63, respectively, along with the percentage of predicted points lying with in ±20% error bars.

$$e_A = \frac{1}{N}\sum 100\left|\frac{\left(\frac{dP}{dz}\right)_{pred} - \left(\frac{dP}{dz}\right)_{data}}{\left(\frac{dP}{dz}\right)_{data}}\right| \tag{6.61}$$

$$e_R = \frac{1}{N}\sum 100\left(\frac{\left(\frac{dP}{dz}\right)_{pred} - \left(\frac{dP}{dz}\right)_{data}}{\left(\frac{dP}{dz}\right)_{data}}\right) \tag{6.62}$$

$$\sigma_N = \left[\frac{1}{N-1}\sum\left(e-e_R\right)^2\right]^{0.5} \text{ where, } e = 100\left(\frac{\left(\frac{dP}{dz}\right)_{pred} - \left(\frac{dP}{dz}\right)_{data}}{\left(\frac{dP}{dz}\right)_{data}}\right) \tag{6.63}$$

The models in Table 6.2 were chosen because they have the least mean absolute deviation from the data in Table 6.1 of the models investigated and are arranged from least to greatest mean absolute deviation. From Table 6.1 it can be seen that the present model has the least mean absolute deviation, least average deviation, and the highest percentage of points within 20% error bars. The Grönnerud (1979) and the original Souza et al. (1993) pressure drop models are seen to have lower standard deviations that the present model, but within 2.5% of the standard deviation of the present model. This means that the Grönnerud (1979) and the original Souza et al. (1993) pressure drop models have a more consistent error magnitude with the Grönnerud (1979) model consistently over predicting pressure drop above 6 kPa and the Souza et al. (1993) model consistently under predicting pressure drop. However, some of the models perform better for particular refrigerants, for example, the Souza et al. (1993) model performs better than the rest for ammonia. Since ammonia was not used in the flow visualization experiments to generate the generalized flow maps used in the present model, the flow regime time fraction information may be inaccurate, or the models used for each flow regime may need to be modified.

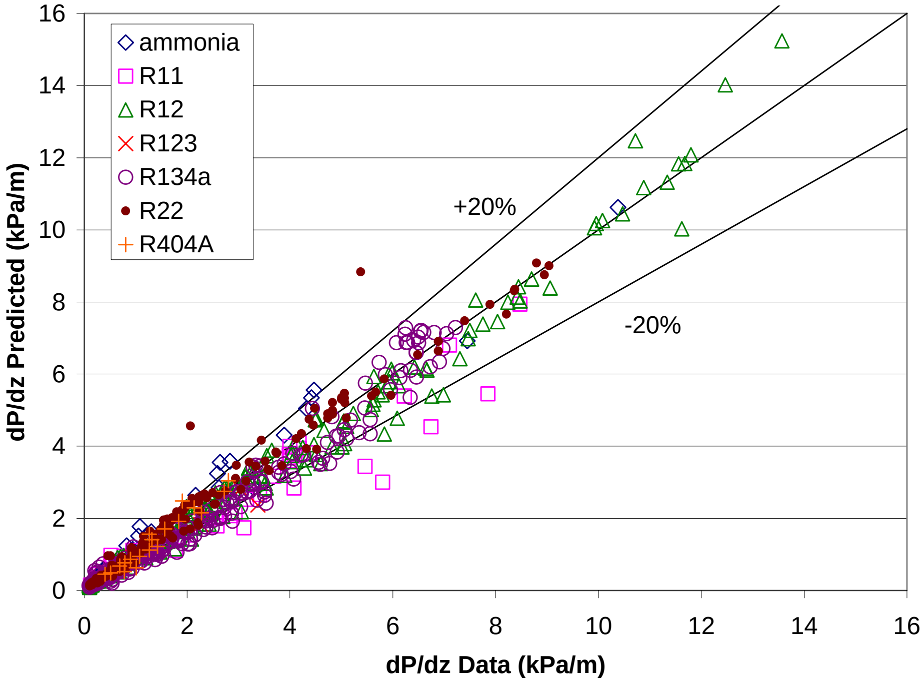

Figure 6.5. Frictional pressure drop data summarized in Table 6.1 vs. pressure drop predicted by present model and separated by refrigerant

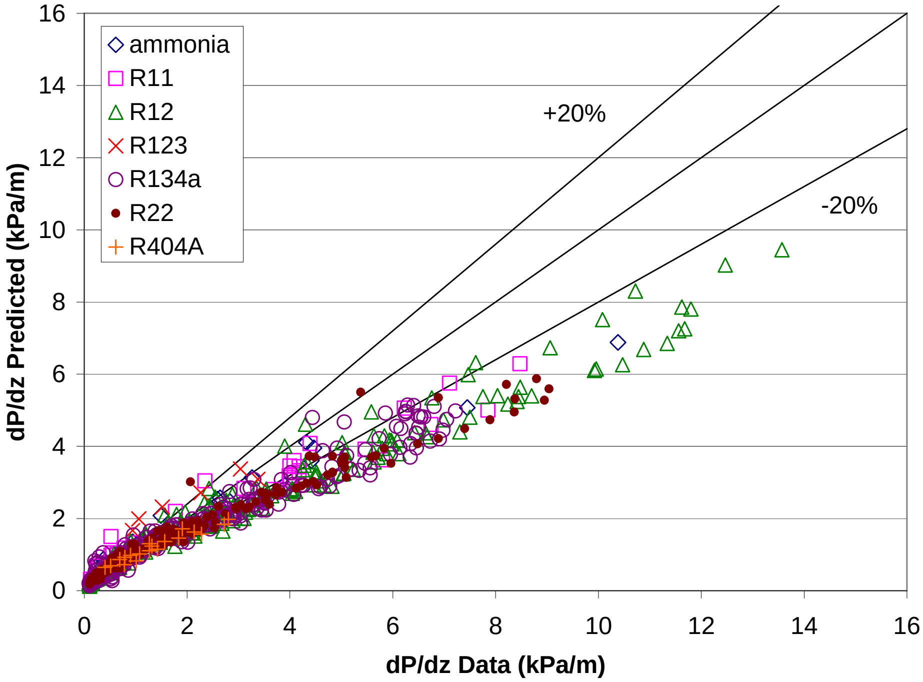

Figure 6.6. Frictional pressure drop data summarized in Table 6.1 vs. pressure drop predicted by Friedel (1979) and separated by refrigerant

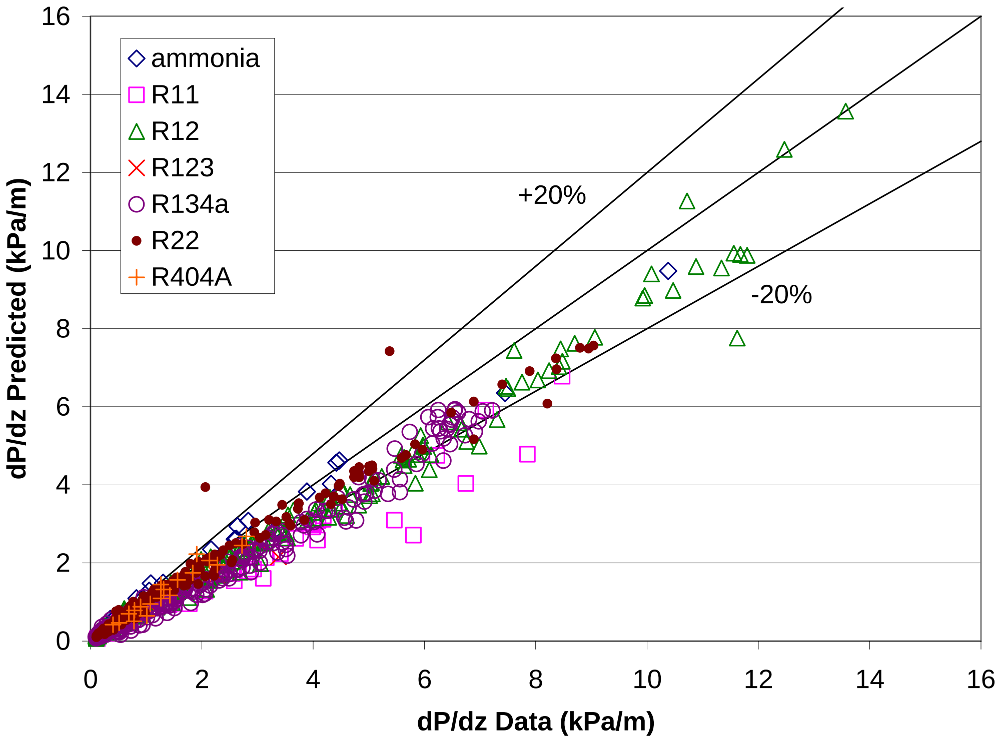

Figure 6.7. Frictional pressure drop data summarized in Table 6.1 vs. pressure drop predicted by Souza et al. (1993) and separated by refrigerant

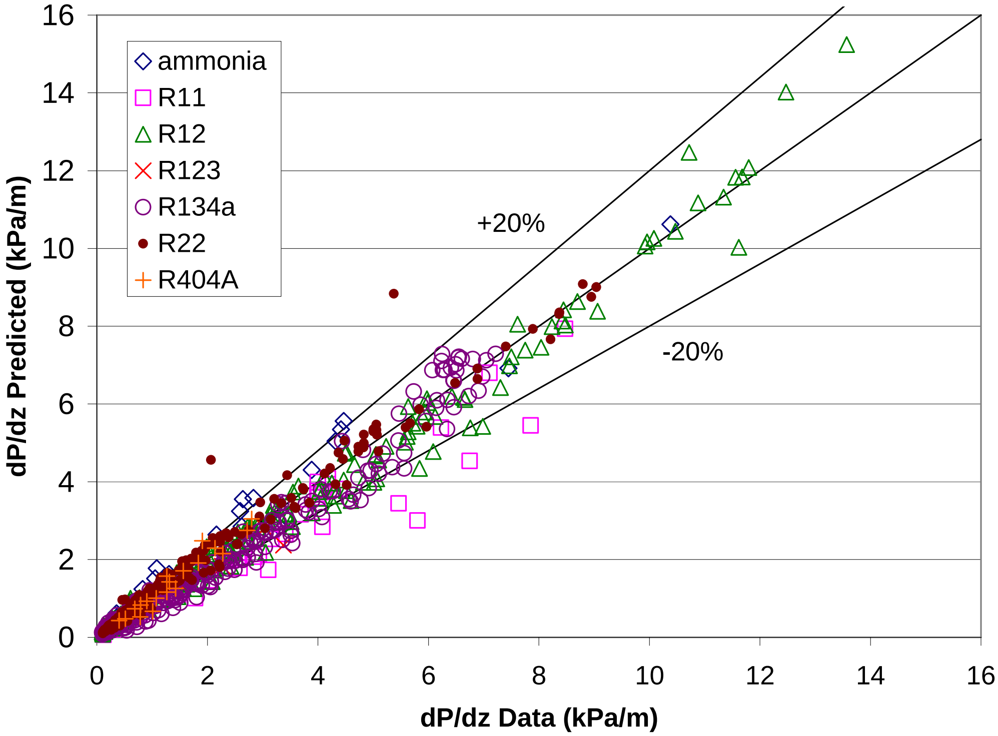

Figure 6.8. Frictional pressure drop data summarized in Table 6.1 vs. pressure drop predicted by modified Souza et al. (1993) and separated by refrigerant

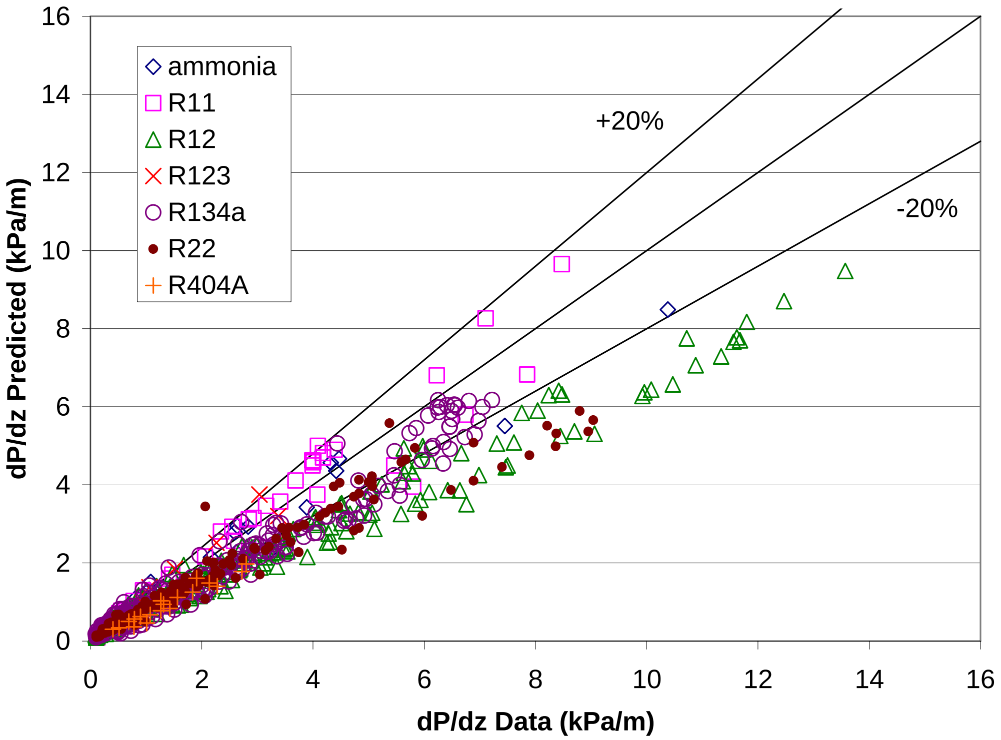

Figure 6.9. Frictional pressure drop data summarized in Table 6.1 vs. pressure drop predicted by Souza and Pimenta (1995) and separated by refrigerant

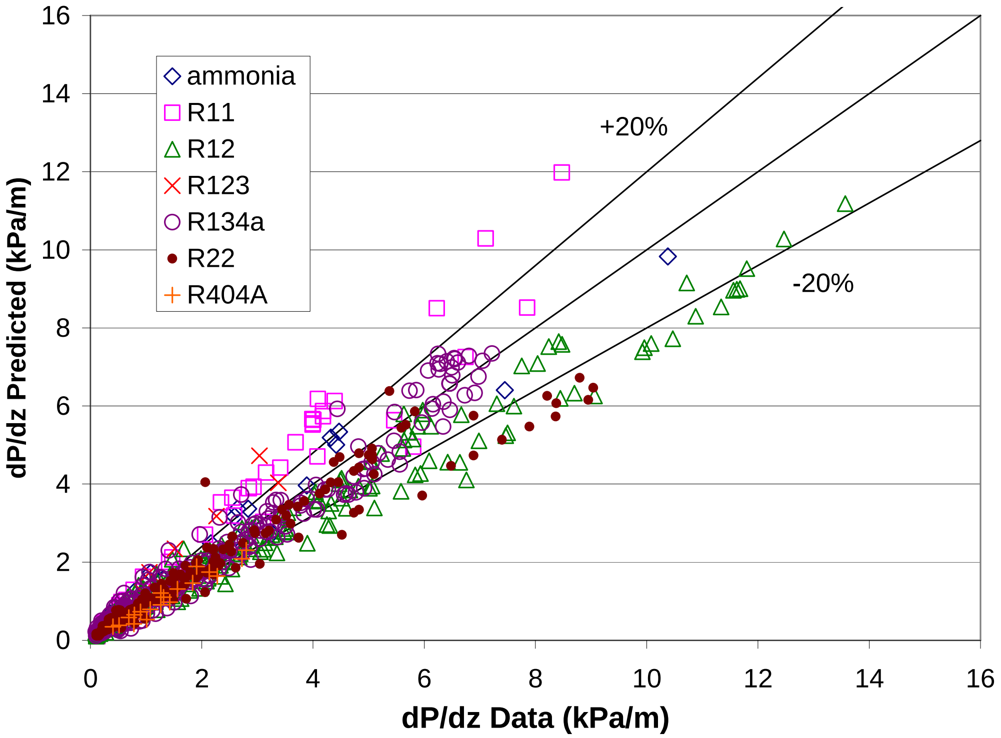

Figure 6.10. Frictional pressure drop data summarized in Table 6.1 vs. pressure drop predicted by modified Souza and Pimenta (1995) and separated by refrigerant

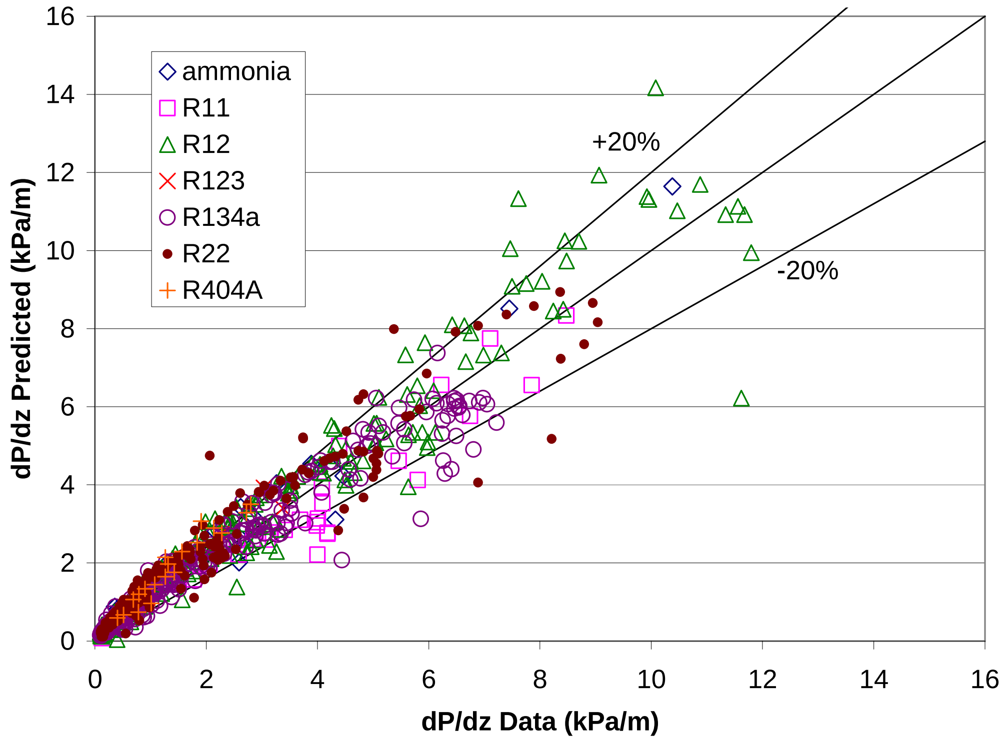

Figure 6.11. Frictional pressure drop data summarized in Table 6.1 vs. pressure drop predicted by Jung and Radermacher (1989) and separated by refrigerant

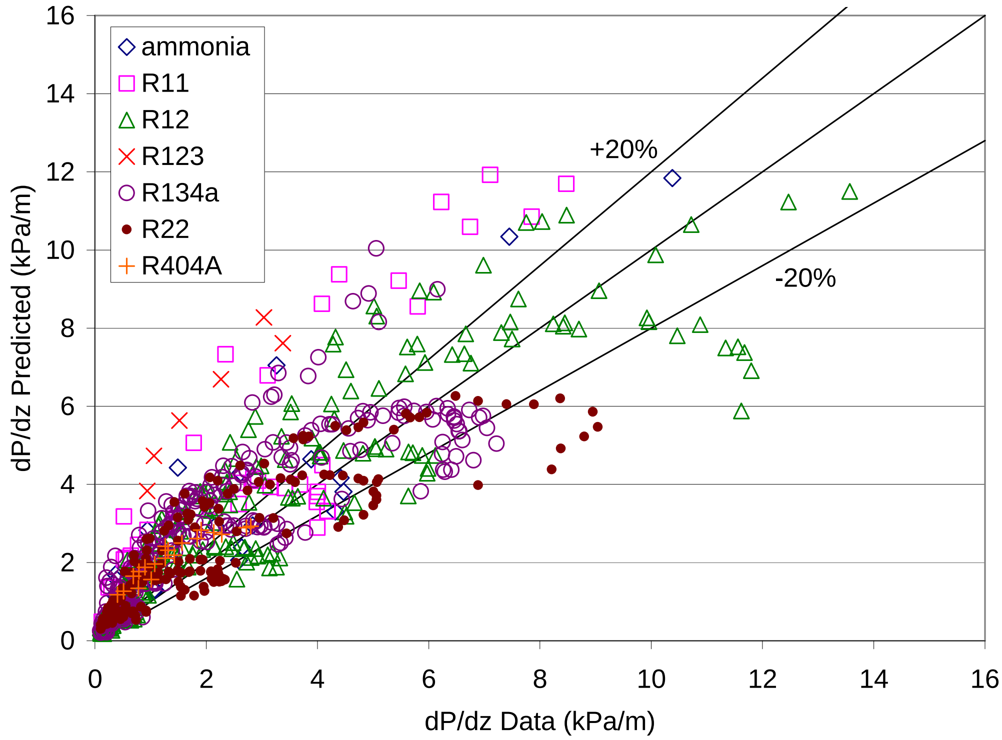

Figure 6.12. Frictional pressure drop data summarized in Table 6.1 vs. pressure drop predicted by Chisholm (1973) and separated by refrigerant

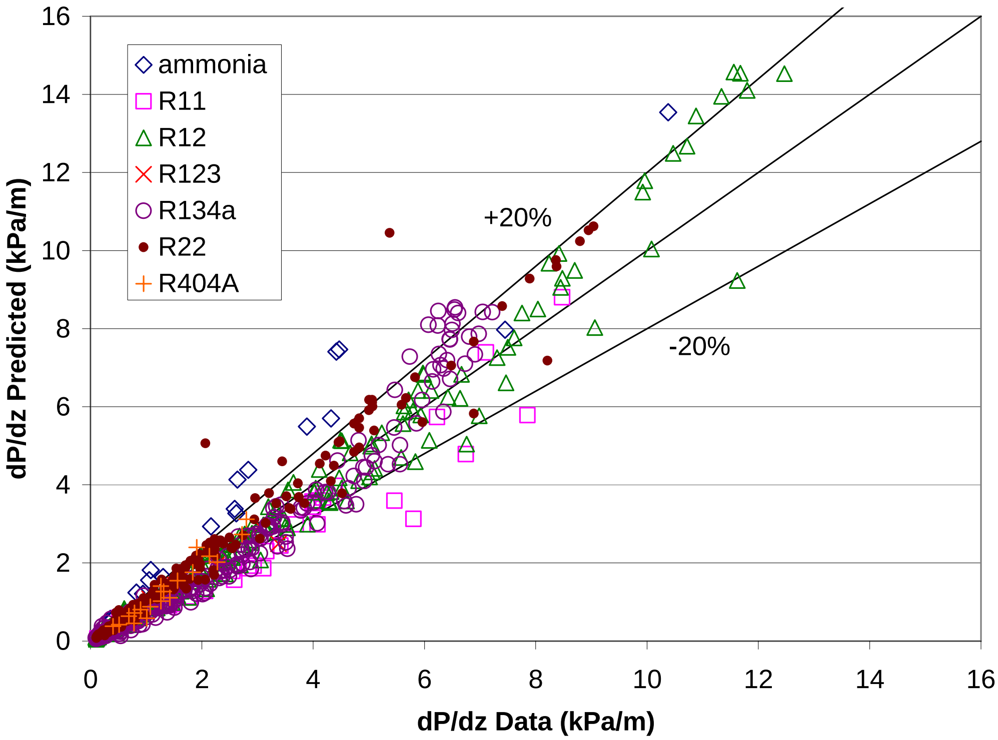

Figure 6.13. Frictional pressure drop data summarized in Table 6.1 vs. pressure drop predicted by Grönnerud (1979) and separated by refrigerant

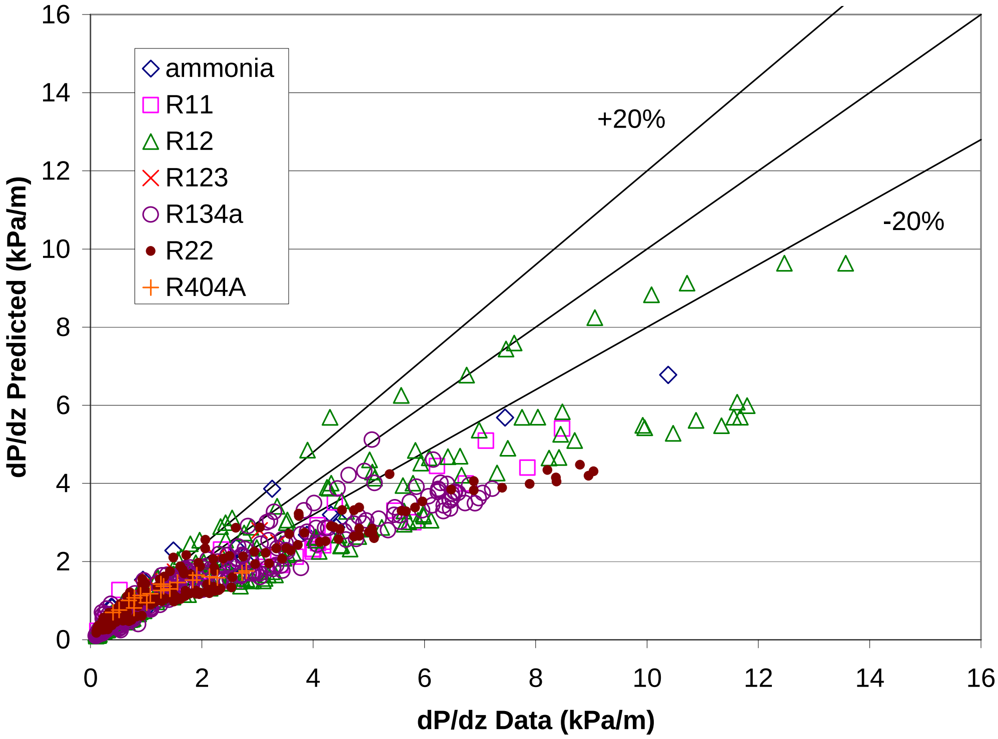

Figure 6.14. Frictional pressure drop data summarized in Table 6.1 vs. pressure drop predicted by Niño's (2002) annular flow model and separated by refrigerant

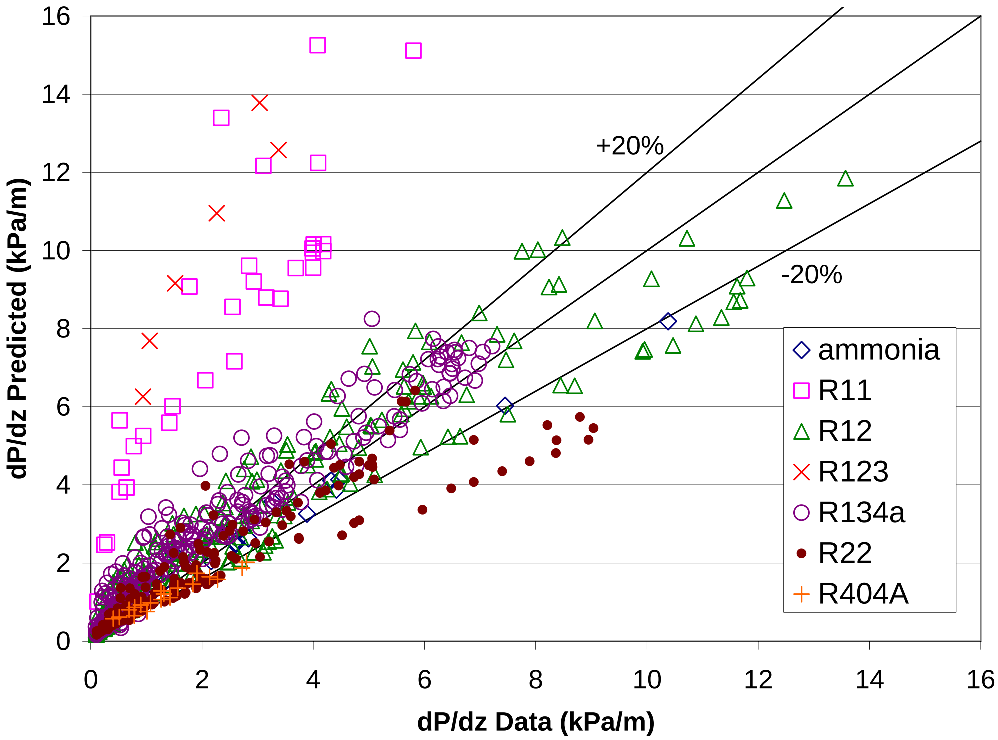

Figure 6.15. Frictional pressure drop data summarized in Table 6.1 vs. pressure drop predicted by Zhang and Kwon (1999) and separated by refrigerant

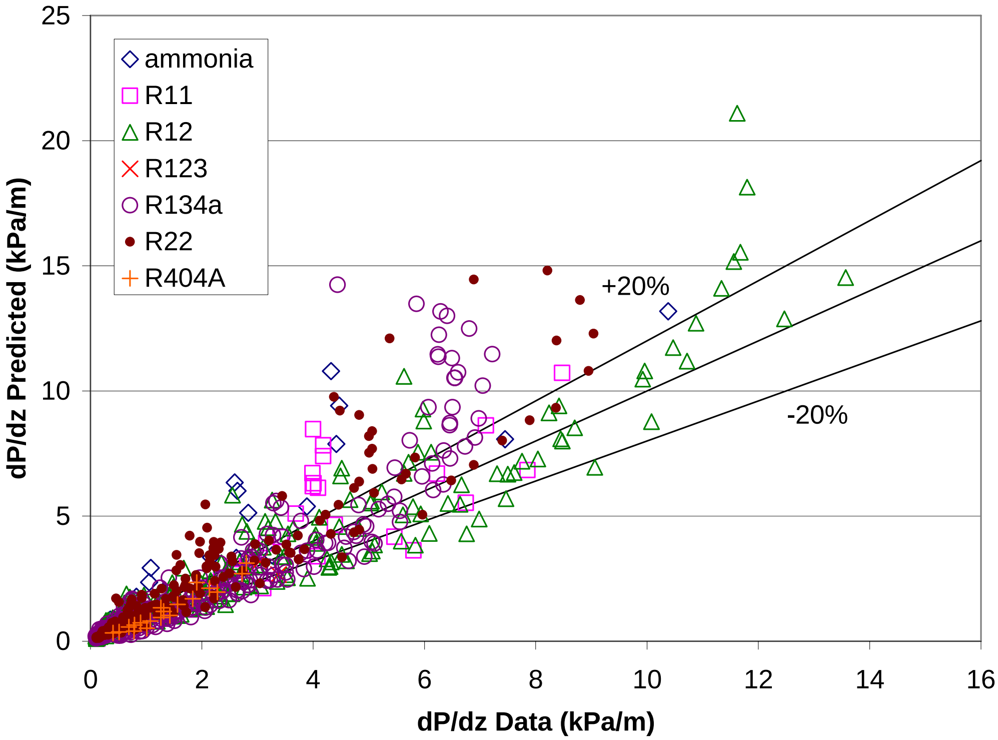

Figure 6.16. Frictional pressure drop data summarized in Table 6.1 vs. pressure drop predicted by Tran et al. (2000) and separated by refrigerant

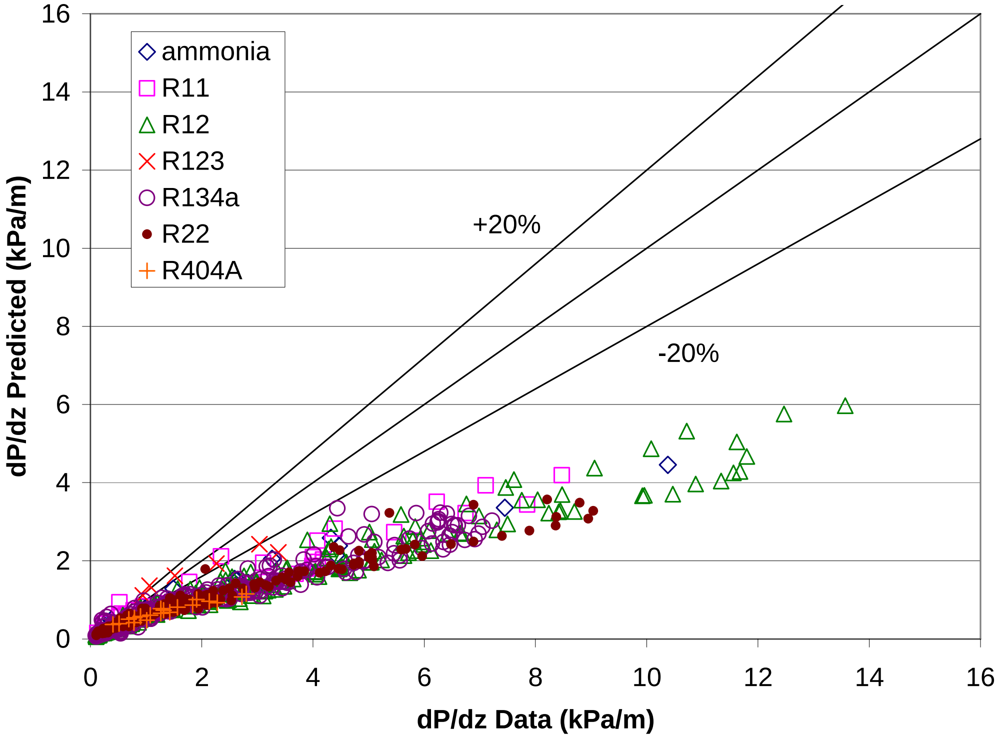

Figure 6.17. Frictional pressure drop data summarized in Table 6.1 vs. pressure drop predicted by McAdams (1954) and separated by refrigerant

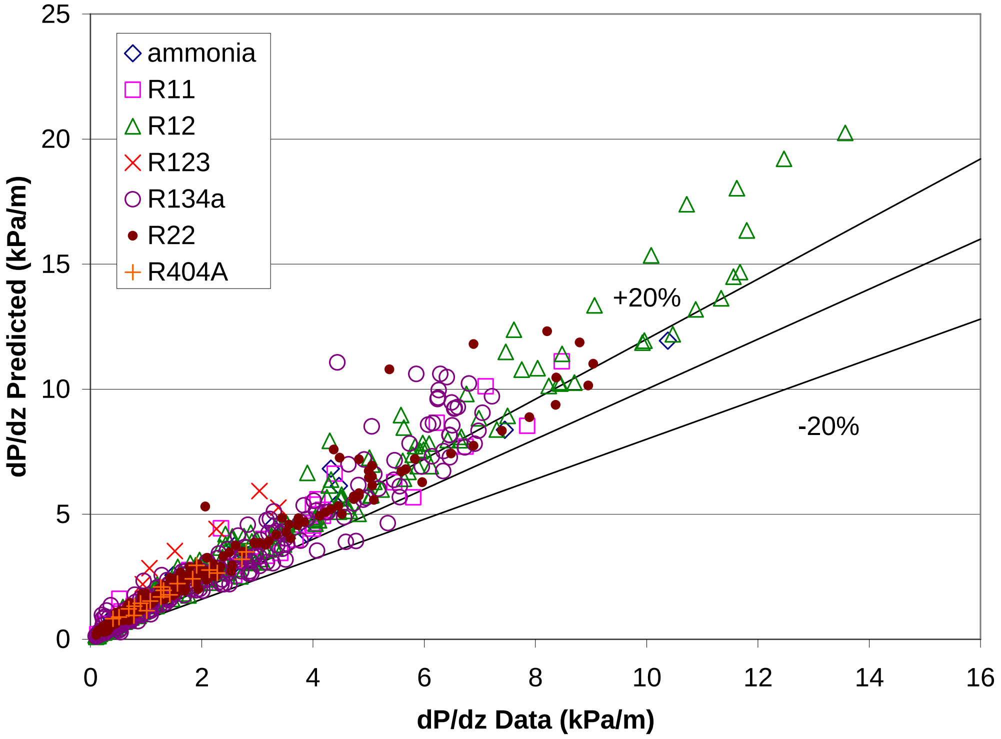

Figure 6.18. Frictional pressure drop data summarized in Table 6.1 vs. pressure drop predicted by Niño's (2002) intermittent flow model and separated by refrigerant

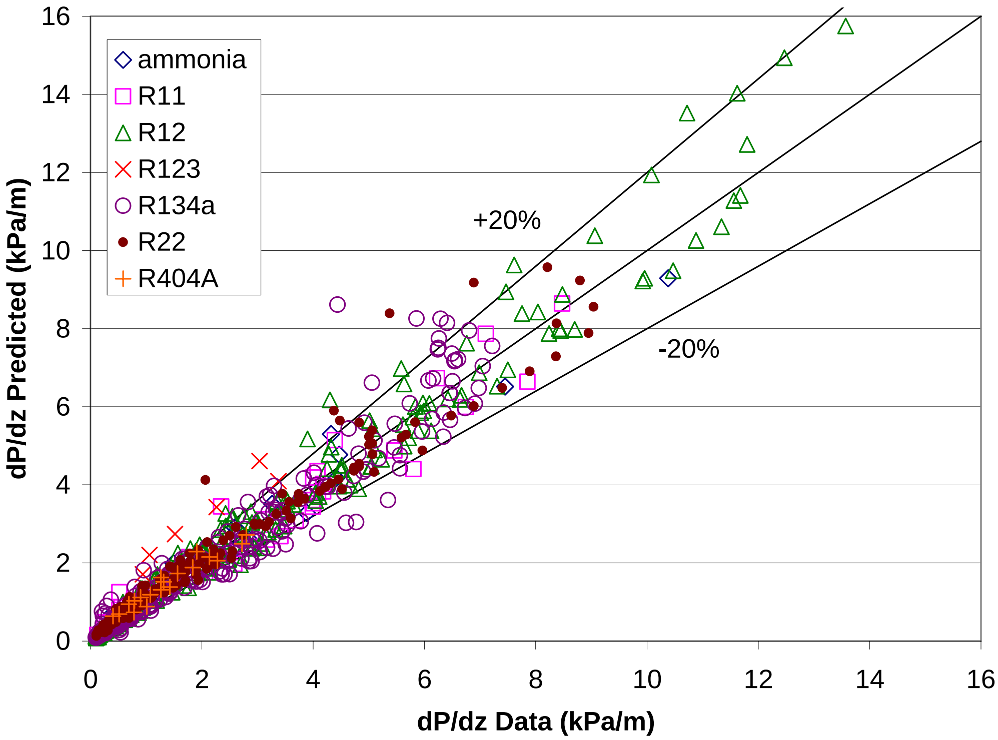

Figure 6.19. Frictional pressure drop data summarized in Table 6.1 vs. pressure drop predicted by Adams (2003) and separated by refrigerant

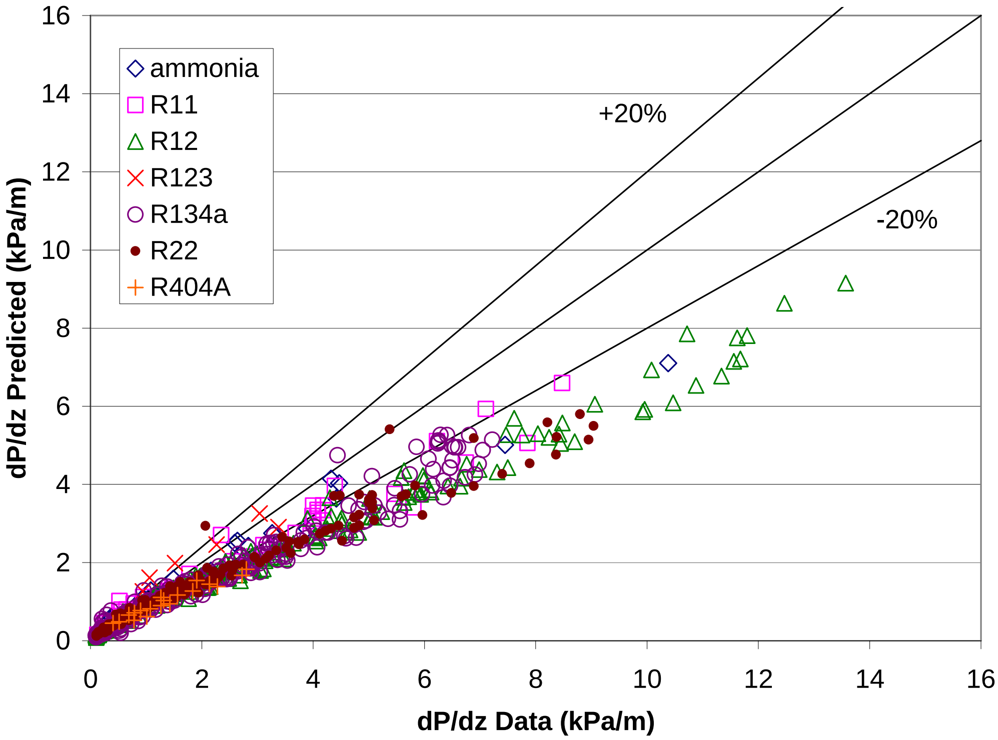

Figure 6.20. Frictional pressure drop data summarized in Table 6.1 vs. pressure drop predicted by Müller-Steinhager and Heck (1986) and separated by refrigerant

Table 6.2. Statistical comparison of pressure drop models with experimental data separated by refrigerants (in %)

Refrigerant	Statistical comparison	Present model	Grönnerud (1979)	mod. Souza et al. (1993)	Souza et al. (1993)	Adams (2003)	Müller-Steinhager & Heck (1986)	Souza and Pimenta (1995)	mod. Souza and Pimenta (1995)	Niño (2002) ann.	Friedel (1979)	Jung and Radermacher (1989)	Tran et al. (2000)	Niño (2002) int.	McAdams (1954)
ammonia	e_A	27.8	38.9	27.3	16.5	19.2	20.5	17.3	26.1	37.3	30.7	38.0	79.3	44.4	37.5
	e_R	24.9	37.8	24.4	10.7	12.3	1.1	5.1	21.2	6.4	14.2	32.6	79.3	44.4	-32.4
	σ_N	22.2	21.7	22.5	19.9	25.1	27.3	23.4	26.9	50.0	44.7	41.5	51.2	32.3	24.4
	within 20%	33.3	14.3	33.3	71.4	71.4	66.7	61.9	57.1	28.6	52.4	33.3	14.3	28.6	19.0
R11	e_A	25.0	24.1	21.5	31.3	23.5	27.1	18.2	38.7	37.0	41.4	21.1	27.7	41.6	42.1
	e_R	-4.7	-23.0	-21.5	-31.3	9.9	-5.2	9.8	36.9	-15.6	13.1	-1.7	17.5	41.3	-29.9
	σ_N	31.6	14.1	13.1	9.9	34.6	32.2	18.7	23.7	42.3	61.2	25.3	33.0	44.5	34.7
	within 20%	42.1	39.5	42.1	5.3	63.2	28.9	71.1	21.1	15.8	28.9	55.3	47.4	44.7	18.4
R12	e_A	13.1	13.3	18.4	16.7	16.2	23.5	27.8	30.8	28.5	35.3	41.2	49.1	40.2	40.5
	e_R	3.3	-4.7	9.1	-3.9	8.9	-9.5	-5.2	12.6	-4.9	11.3	36.7	37.6	40.0	-39.0
	σ_N	19.3	16.1	25.5	20.8	20.7	26.8	32.4	39.4	35.8	44.5	42.9	57.3	26.6	20.0
	within 20%	79.7	77.7	66.1	74.1	72.1	44.6	32.3	41.8	40.6	27.5	35.9	32.7	25.5	12.0
R123	e_A	12.6	11.1	17.5	23.5	65.7	24.3	15.9	43.9	23.0	42.8	24.8	9.6	113.0	20.5
	e_R	-12.6	-10.4	-17.5	-23.5	65.7	19.7	14.1	43.9	9.2	39.9	24.8	-6.9	113.0	-2.7
	σ_N	10.6	10.3	9.5	8.8	30.5	23.5	13.3	16.8	27.9	38.5	15.7	10.7	39.2	24.4
	within 20%	83.3	83.3	66.7	50.0	0.0	50.0	50.0	16.7	50.0	50.0	33.3	83.3	0.0	50.0
R134a	e_A	18.3	21.9	18.4	22.6	20.4	25.3	25.3	25.1	28.1	31.1	24.9	37.6	37.7	44.0
	e_R	-6.0	-15.5	-8.5	-18.9	5.4	-13.9	-10.0	8.7	-10.0	5.7	16.4	16.0	35.5	-39.4
	σ_N	25.5	21.0	21.6	18.0	36.3	28.5	28.6	35.0	38.5	47.7	31.7	47.9	46.6	25.7
	within 20%	67.5	49.4	61.4	45.4	69.9	41.4	41.4	58.2	42.6	39.8	56.6	34.5	39.4	7.6
R22	e_A	13.5	13.2	16.5	13.2	18.8	22.5	20.5	15.0	37.7	30.3	42.9	37.7	45.8	41.6
	e_R	8.3	4.1	11.8	0.0	13.4	-12.7	-16.3	-3.0	0.1	6.2	37.1	31.1	45.8	-39.9
	σ_N	19.1	19.2	19.9	17.4	23.8	22.3	17.5	20.9	46.6	40.2	39.9	44.1	30.6	20.9
	within 20%	80.3	84.6	67.0	82.4	69.7	42.6	51.1	76.6	25.0	38.3	34.0	41.0	19.1	15.4
R404A	e_A	12.2	14.1	11.5	10.7	16.7	24.2	33.2	21.9	23.1	19.9	36.5	18.9	44.3	43.8
	e_R	-1.5	-8.8	0.3	-6.8	12.2	-23.0	-33.2	-21.9	4.0	-4.4	35.4	-14.8	44.3	-43.8
	σ_N	16.6	16.7	15.8	13.6	19.2	14.0	9.8	11.6	30.3	24.2	19.7	18.4	24.7	13.7
	within 20%	78.9	78.9	78.9	89.5	63.2	36.8	10.5	52.6	52.6	57.9	10.5	63.2	15.8	5.3
all data	e_A	15.8	17.3	18.2	18.4	19.1	24.0	24.5	25.2	31.1	32.6	35.0	41.3	41.6	41.8
	e_R	1.5	-5.9	2.6	-9.0	9.5	-11.3	-9.0	8.4	-5.2	8.2	28.1	27.6	40.8	-38.6
	σ_N	23.2	21.6	24.6	20.8	28.7	26.7	27.8	34.2	40.3	45.2	39.1	51.1	36.8	23.3
	within 20%	72.8	66.7	63.1	63.6	69.6	42.7	42.1	55.1	36.3	35.8	42.4	36.7	29.0	12.0

The present model is also compared with the pressure drop data summarized in Table 6.1 in Figure 6.21 on a heat transfer basis. No noticeable deviation between adiabatic, evaporation, and condensation conditions can be seen in Figure 6.21. Similarly no deviation can be observed with respect to tube size for the pressure drop data in Table 6.1.

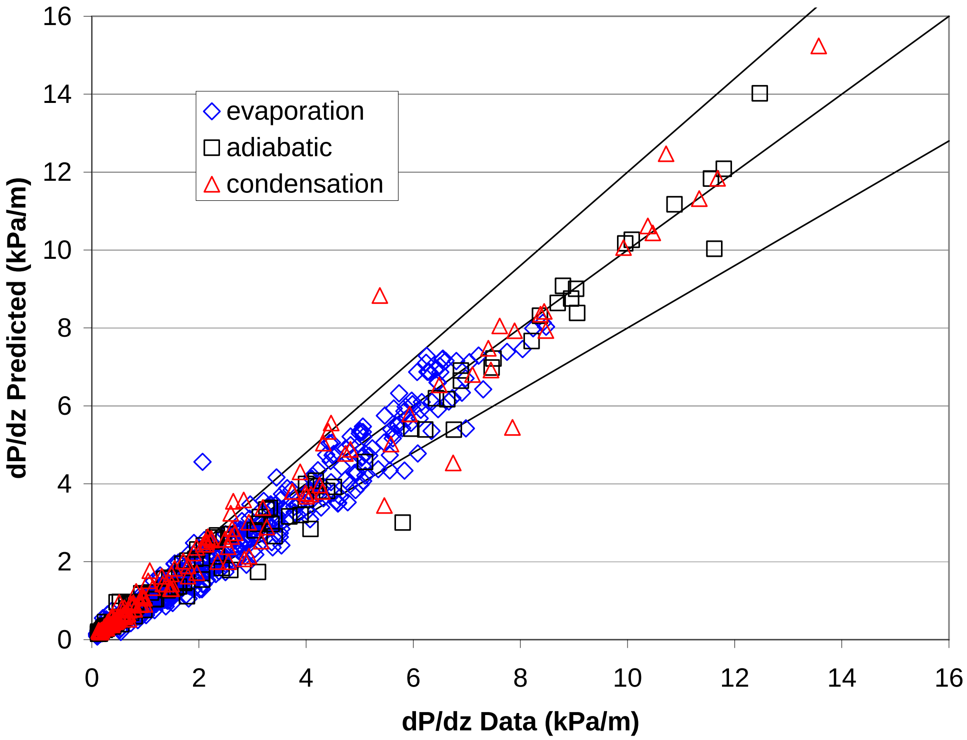

Figure 6.21. Frictional pressure drop data summarized in Table 6.1 vs. pressure drop predicted by present model and separated by heat transfer conditions

6.6 Conclusion

In conclusion, a probabilistic two-phase flow map pressure drop model is developed for single, smooth, horizontal tubes in a similar manner as previously developed for multi-port microchannels. The present pressure drop model utilizes a generalized probabilistic two phase flow regime map to properly weight models identified to represent the intermittent/liquid, stratified, and annular flow regimes on a time fraction basis. Consequently, the present model is developed on a consistent time fraction basis as probabilistic two-phase flow map condensation heat transfer and void fraction models found in the literature. The model is general in that pressure drop models for each flow regime can easily be interchanged as more accurate models are identified. The present pressure drop model exhibits no discontinuities because the time fraction functions are smooth and continuous for the entire quality range. The present pressure drop model and 15 other pressure drop models identified in the literature or modified from the literature are compared to a pressure drop database consisting of 772 points of ammonia, R11, R12, R123, R134a, R22, and R404A in 7.04 mm to 12.00 mm diameter smooth tubes at mass fluxes ranging from 25 to 902 kg/m^2-s and a full quality range under evaporation, adiabatic and condensation conditions. The present model has a mean absolute deviation of 15.8% when compared to the database. Caution should be exercised in using the present pressure drop model outside of the range of tube sizes, flow conditions, and fluid properties with which the model is presently validated.

References

Adams, D., “Pressure Drop and Void Fraction in Microchannels using Carbon Dioxide, Ammonia and R245FA as Refrigerants,” M.S. Thesis, University of Illinois, Urbana-Champaign, IL, 2003.

Asali, J.C., T.J. Hanratty, and P. Andreussi, “Interfacial Drag and Film Height for Vertical Annular Flow,” *AIChE Journal* 31(6) (1985) 895-902.

Baker, O., “Simultaneous Flow of Oil and Gas,” *Oil and Gas Journal* 53 (1954) 185-195.

Chisholm, D., “Pressure Gradients Due to Friction during the Flow of Evaporating Two-Phase Mixtures in Smooth Tubes and Channels,” *International Journal of Heat and Mass Transfer*, (16) (1973) 347–358.

Chung, P.M.-Y. and M. Kawaji, “The Effect of Channel Diameter on Adiabatic Two-Phase Flow Characteristics in Microchannels,” *International Journal of Multiphase Flow* 30 (2004) 735-761.

Coleman, J.W., and S.Garimella, “Two-Phase Flow Regimes in Round, Square and Rectangular Tubes during Condensation of Refrigerant R134a,” *International Journal of Refrigeration,* 26 (2003) 117-128.

Diamanides, C. and J.W. Westwater, “Two-phase Flow Patterns in a Compact Heat Exchanger and in Small Tubes,” *Proceedings of the 2nd. U.K. National Conference on Heat Transfer*, Glasgow, Scotland, (2) (1988) 1257-1268.

Didi, M.B. and N. Kattan, J.R. Thome, “Prediction of Two-Phase Pressure Gradients of Refrigerants in Horizontal Tubes,” *International Journal of Refrigeration* 25 (2002) 935-947.

El Hajal, J., J.R. Thome, and A. Cavalini, “Condensation in Horizontal Tubes, Part 1: Two-Phase Flow Pattern Map,” *International Journal of Heat and Mass Transfer* 46 (2003) 3349-3363.

Friedel, L., “Improved Friction Pressure Drop Correlations for Horizontal and Vertical Two Phase Pipe Flow,” European Two-Phase Flow Group Meeting, Ispra, Italy, 1979, Paper E2.

Garimella, S., “Condensation Flow Mechanisms in Microchannels: Basis for Pressure Drop and Heat Transfer Models,” *Heat Transfer Engineering* 25:3 (2004) 104-116.

Garimella, S., J.D. Killion, and J.W. Coleman, “An Experimentally Validated Model for Two-Phase Pressure Drop in the Intermitent Flow Regime for Noncircular Microchannels,” *Journal of Fluids Engineering* 125 (2003) 887-894.

Grönnerud, R., “Investigation of Liquid Hold-Up, Flow-Resistance and Heat Transfer in Circulation Type Evaporators, Part IV: Two-Phase Flow Resistance in Boiling Refrigerants,” Annexe 1972-1, Bull. de l’Inst. du Froid, (1979).

Jassim, E. W., T. A. Newell, and J. C. Chato, “Probabilistic Two-Phase Flow Regime Maps in Tubes and Their Generalization to Physical Parameters,” to be submitted to the International Journal of Heat and Mass Transfer (2006b).

Jassim, E. W., T. A. Newell, and J. C. Chato, “Prediction of Refrigerant Void Fraction in Horizontal Tubes using Probabilistic Flow Regime Maps,” to be submitted to the International Journal of Heat and Mass Transfer (2006d).

Jassim, E. W., T. A. Newell, and J. C. Chato, “Prediction of Two-Phase Condensation in Single Tubes using Probabilistic Flow Regime Maps,” to be submitted to the International Journal of Heat and Mass Transfer (2006c).

Jassim, E. W., T. A. Newell, and J. C. Chato, “Probabilistic Determination of Two-Phase Flow Regimes Utilizing an Automated Image Recognition Technique,” to be submitted to Experiments In Fluids (2006a)

Jassim, E.W. and T. A. Newell. “Prediction of Two-Phase Pressure Drop and Void Fraction in Microchannels using Probabilistic Flow Regime Mapping,” *International Journal of Heat and Mass Transfer* 49 (2006) 2446-2457.

Jung, D.S. and R. Radermacher, “Prediction of Pressure Drop During Horizontal Annular Flow Boiling of Pure and Mixed Refrigerants,” *International Journal of Heat and Mass Transfer* 32 (12) (1989) 2435-2446.

Komandiwirya, H.B., P.S. Hrnjak, and T.A. Newell, “An Experimental Investigation of Pressure Drop and Heat Transfer in an In-Tube Condensation System of Ammonia with and Without Miscible Oil in Smooth and Enhanced Tubes,” *M.S. Thesis*, University of Illinois at Urbana-Champaign, 2004.

Lockhart, R.W. and R. C. Martinelli, “Proposed Correlation of Data for Isothermal Two-Phase, Two-Component Flow in Pipes,” *Chemical Engineering Progress*, 45(1) (1949)39-48.

Mandhane, J.M., G.A. Gregory, and K. Aziz, “A Flow Pattern Map for Gas-Liquid Flow in Horizontal and Inclined Pipes,” *International Journal of Multiphase Flow* 1 (1974) 537-553.

Martinelli, R.C. and D. B. Nelson, “Prediction of Pressure Drop During Forced-Circulation Boiling of Water,” *Transactions ASME*, 70(1948) 695-702.

McAdams, W. H., Heat Transmission, 3rd Edition, McGraw Hill, New York, 1954.

Müller-Steinhagen, H. and K. Heck, “A Simple Friction Pressure Drop Correlation for Two-Phase Flow in Pipes,” *Chemical Engineering Process* (20)(1986) 297–308.

Niño, V.G. “Characterization of Two-phase Flow in Microchannels,” Ph.D. Thesis, University of Illinois, Urbana-Champaign, IL, 2002.

Niño, V.G., E.W. Jassim, P. S. Hrnjak, and T.A. Newell, “Flow-Regime-Based Model for Pressure Drop Predictions in Microchannels,” *HVAC&R Research* 12 (1) (2006) 17-34.

Sacks, P.S., “Measured Characteristics of Adiabatic and Condensing Single Component Two-Phase Flow of Refrigerant in a 0.377 in. Diameter Horizontal Tube,” *ASME Winter Annual Meeting*, 75-WA/ HT-24, Houston, Texas (1975)

Souza, A.L. and M.M. Pimenta, “Prediction of Pressure Drop during Horizontal Two-Phase Flow of Pure and Mixed Refrigerants,” *ASME Conference on Cavitation and Multiphase Floe*, ASME, New York, (210) (1995) 161-171.

Souza, A.L., J.C. Chato, J.P. Wattelet, and B.R. Christoffersen, “Pressure Drop During Two-Phase Flow of Pure Refrigerants and Refrigerant-oil Mixtures in Horizontal Smooth Tubes,” *Heat Transfer with Alternate Refrigerants (ASME)* HTD 243 (1993), 35-41.

Steiner, D., “Heat Transfer to Boiling Saturated Liquids,” VDI-Wārmeatlas (VDI Heat Atlas), Verein Deutscher Ingenieure, VDI-Gesellschaft Verfahrenstechnik und Chemieingenieurwesen (GCV), Dū sseldorf, Chapter Hbb (1993).

Thome, J.R., J. El Hajal, and A. Cavalini, “Condensation in Horizontal Tubes, Part 2: New Heat Transfer Model Based on Flow Regimes,” *International Journal of Heat and Mass Transfer* 46 (2003) 3365-3387.

Tran, T. N., M. C. Chyu, M. W. Wambsganss, and D.M. France, “Two-Phase Pressure Drop of Refrigerants during Flow Boiling in Small Channels: An Experimental Investigation and Correlation Development,” *International Journal of Multiphase Flow*, (26) (2000) 1739-1754.

Wattelet, J.P., “Heat Transfer Flow Regimes of Refrigerants in a Horizontal-Tube Evaporator,” *Ph.D. Thesis*, University of Illinois, Urbana-Champaign, IL, 1994.

Zhang, M. and S.L. Kwon, “Two-Phase Frictional Pressure Drop for Refrigerants in Small Diameter Tubes,” in R.K. Shah (Eds.), Compact Heat Exchangers and Enhancement Technology for the Process Industries, Begell House, New York, 1999.

Zurcher, O., D. Farvat, and J.R Thome, “Evaporation of Refrigerants in a Horizontal Tube: And Improved Flow Pattern Dependent Heat Transfer Model Compared to Ammonia Data,” *International Journal of Heat and Mass Transfer* 45 (2002) 303-317.

Zurcher, O., D. Farvat, and J.R. Thome, “Development of a Diabatic Two-Phase Flow Pattern Map for Horizontal Flow Boiling,” *International Journal of Heat and Mass Transfer* 45 (2002) 291-301.

Chapter 7: Concluding Remarks

7.1 Nomenclature

D	hydraulic diameter (m)
dP	pressure drop (kPa)
dz	unit length (m)
F	observed time fraction (-)
Fr_{vo}	vapor only Froude number (-)
G	mass flux (kg/m^2-s)
g_a	gravitational acceleration (9.81 m/s^2)
h	heat transfer coefficient (W/m^2-K)
i	intermittent flow regime curve fit constant (-)
s	stratified flow regime curve fit constant (-)
We_{vo}	vapor only Weber number (-)
Xi	dimensionless group correlating the intermittent/liquid flow regime (-)
Xs	dimensionless group correlating the stratified flow regime (-)

Greek symbols

α	void fraction (-)
ρ	density (kg/m^3)
σ	surface tension (N/m)

Subscripts

l	liquid
liq	pertaining to the liquid flow regime
int	pertaining to the intermittent flow regime
v	vapor
vap	pertaining to the vapor flow regime
ann	pertaining to the annular flow regime

7.2 Conclusion

Probabilistic two-phase heat transfer, void fraction, and pressure drop models are developed on a consistent time fraction basis for single, smooth, horizontal tubes in order to provide accurate and easy to use tools to aid engineers in the design and optimization of two-phase flow systems such as air conditioning, refrigeration, power generation, and chemical processing systems. Ultimately this research can lead to the design of smaller heat exchangers that use less material, and systems with a lower charge inventory and energy usage.

The experimental development of probabilistic two-phase flow regime maps in tubes is described in Chapter 2. Flow visualization images were obtained for R134a at 25, 35 and 49.7 ºC and R410A at 25 ºC with a wide range of mass fluxes and qualities in glass tubes ranging from 1.74 mm to 8.00 mm in diameter with an illuminated striped diffuse background. The stripes in the background are found to enhance the images and aid in the image recognition process. Image recognition software is developed to automatically classify the flow regimes present in approximately 1 million images and compute time fractions for each flow condition.

A generalized probabilistic two-phase flow regime map, given in Equations 7.1 through 7.9, is developed as functions of physical parameters in Chapter 3 from the time fraction data collected in Chapter 2.

$$F_{\mathrm{int}+liq} = (1-x)^i \tag{7.1}$$

$$F_{strat} = \left(1 - x^{\left(s/\sqrt{x}\right)}\right)^i - (1-x)^i \tag{7.2}$$

$$F_{ann} = 1 - F_{\mathrm{int}+liq} - F_{strat} \tag{7.3}$$

$$i = 0.0243Xi + 8.07 \tag{7.4}$$

$$Xi = \left(We_{vo}^{0.4}\right)\left(\frac{\rho_l}{\rho_v}\right) \text{, where} \tag{7.5}$$

$$We_{vo} = \left(\frac{G^2 D}{\rho_v \sigma}\right) \tag{7.6}$$

$$s = \frac{1}{0.45Xs} + \frac{1}{0.025Xs^{4.44}} \tag{7.7}$$

$$Xs = \left(Fr_{vo}^{0.5}\right)\left(\frac{\rho_v}{\rho_l}\right)^{0.65} \tag{7.8}$$

$$Fr_{vo} = \left(\frac{G^2}{\rho_v^2 g_a D}\right) \tag{7.9}$$

The generalized flow map presented in Chapter 3 is used to predict condensation heat transfer, void fraction, and pressure drop on a consistent basis in Chapters 4, 5 and 6, respectively. The condensation heat transfer, void fraction, and pressure drop models developed are given in Equations 7.10 through 7.12, respectively.

$$h_{total} = F_{\mathrm{int}+liq} h_{\mathrm{int}+liq} + F_{strat} h_{strat} + F_{ann} h_{ann} \tag{7.10}$$

$$\alpha_{total} = F_{\mathrm{int}+liq} \alpha_{\mathrm{int}+liq} + F_{strat} \alpha_{strat} + F_{ann} \alpha_{ann} \tag{7.11}$$

$$\left(\frac{dP}{dz}\right)_{total} = F_{\mathrm{int}+liq}\left(\frac{dP}{dz}\right)_{\mathrm{int}+liq} + F_{strat}\left(\frac{dP}{dz}\right)_{strat} + F_{ann}\left(\frac{dP}{dz}\right)_{ann} \tag{7.12}$$

The developed heat transfer model given in Equation 7.10 is used with a modified Dittus Boelter relation, with the Chato (1962) model, and with the Thome et al (2003) or Dobson and Chato (1998) model components for the intermittent/liquid, stratified, and annular flow regimes, respectively. The present model is compared to traditional flow regime map based models found in the literature. The models were compared with data experimentally obtained in the present study for R134a in 8.915 mm diameter smooth copper tube, and with a database for condensation in 3.14 mm, 7.04 mm, and 9.58 mm tubes with R11, R12, R134a, R22, R410A, and R32/R125 (60/40% by weight) refrigerants and a wide range of mass fluxes and qualities obtained from multiple sources. The present model using the Thome et al. (2003) and the Dobson and Chato (1998) annular flow components are found to have a mean absolute deviation of 13.2% and 12.7%, respectively, which is comparable to the 13.9% and 12.8% mean absolute deviation of the models of Thome et al. (2003) , and Cavallini et al. (2003), respectively. However, the probabilistic model using the Dobson and Chato (1998) annular flow component is found to over predict high pressure R32/R125 (60/40% by weight) data.

The present void fraction model given in Equation 7.11 is recommended to be used with the Graham (1998), Yashar et al. (2001), and the Steiner (1993) version of the Rouhani and Axelsson (1970) models for the intermittent/liquid, stratified, and annular flow regimes, respectively. The present model and twelve other models found in the literature are compared to a database consisting of 427 data points that include void fraction data of R11, R12, R134a, R22, R410A refrigerants, 4.26 to 9.58 mm diameter tubes, mass fluxes from 70 to 902 kg/m^2-s, and a full quality range under condensation, adiabatic, and evaporation conditions. The probabilistic model is seen to represent this data well with a mean absolute deviation of 3.5% which is 0.5% less than the next most accurate model given by Yashar et al. (2001). The majority of the improvement is at the lower quality range which is most important for charge determination.

The present pressure drop model given in Equation 12 using the Grönnerud (1979), Müller-Steinhager and Heck (1986), and modified Souza et al. (1993) models for the intermittent/liquid, stratified, and annular flow regimes, respectively, and sixteen other models found or modified from the literature are compared to a pressure drop database of 772 points that includes ammonia, R11, R12, R123, R134a, R22, and R404A in 7.04 mm to 12.00 mm diameter smooth tubes at mass fluxes ranging from 25 to 902 kg/m^2-s and a full quality range under evaporation, adiabatic and condensation conditions. The present model has a mean absolute deviation of 15.8% which is 1.5% less than the Grönnerud (1979) model, the next most accurate model when compared to the database. Furthermore, 72.8% of the predicted points of the present model lie within 20% error bars which is 6.1% greater than the Grönnerud (1979) model.

7.3 Future work

There are several ways in which improved accuracy and applicability of the present models can be obtained. In the present study the transition from large tube behavior, with a stratified flow regime present, observed at 3.90 mm and microchannel behavior, with the stratified flow regime absent, observed at 1.74 mm was not fully explained. While the intermittent/liquid flow regime is reasonably predicted by the generalized probabilistic two-phase flow regime map for the 1.74 mm diameter microchannel, the stratified flow regime prediction still remains. Additional flow visualization experiments and analysis similar to that presented in chapter 2 should be conducted with the 1.74 mm microchannels at lower mass fluxes in the 50 to 400 kg/m^2-s range where the present loop is not capable of attaining with the minimum obtainable flow rate by the gear pump being 400 kg/m^2-s. Furthermore, additional pipe diameters should be investigated between the 1.74 mm and 3.90 mm diameter test sections to fully capture the transition. Additional flow regimes can be considered, such as, stratified wavy and mist flow. The mass flux range and tube sizes investigated should both be expanded in order to further expand the flow map. Furthermore, a wider range of fluid properties should be investigated with the present flow visualization techniques such as ammonia, hydrocarbons, and refrigerant/oil mixtures. Efforts should be made to understand how tube enhancements affect the flow maps developed since enhancements are often used. In addition, the generalized two-phase flow maps should be extended to account for future observations in vertical and inclined tubes. Flow visualization experiments could be conducted in the future with a high speed camera in order to investigate transient effects such as transition time between flow regimes and instability. Neural networks could be utilized in the generalization of the expanded flow regime map to physical parameters. Reduced pressures may play an important role in the developed time fraction functions as a greater range of fluid properties are investigated (the reduced pressures in the present study ranged from 0.164 for R134a at 25 ºC to 0.3346 for R410A at ºC).

In addition to obtaining more accurate and universally applicable probabilistic two-phase flow regime maps, it is necessary to develop more accurate flow regime model components applicable to a wider range of flow conditions, fluid properties, and tube geometries. Additional condensation heat transfer, void fraction, and pressure drop data must similarly be obtained for a wider range of flow conditions, fluid properties, and tube geometries in order to develop and verify the new models. This modeling technique should be extended to evaporation heat transfer as it was applied to condensation heat transfer in the present study. Finally, a linear time fraction waiting of models for each flow regime is used in the present study, but in the future other possible weightings should be considered.

References

Cavallini, A., G. Censi, D. Del Col, L. Doretti, G.A. Longo, L. Rossetto, and C. Zilio, "Condensation Inside and Outside Smooth and Enhanced Tubes - A Review of Recent Research," *International Journal of Refrigeration*, Vol. 26:1, 373-392, 2003.

Chato, J.C., "Laminar Condensation Inside Horizontal and Inclined Tubes," *ASHRAE Journal,* 4(1962) 52-60.

Dobson, M. K. and J.C. Chato, "Condensation in Smooth Horizontal Tubes," *Journal of Heat Transfer* 120 (1998) 245-252.

Graham, D.M., "Experimental Investigation of Void Fraction during Refrigerant Condensation," M.S. Thesis, University of Illinois, Urbana-Champaign, IL, 1998.

Grönnerud, R., "Investigation of Liquid Hold-Up, Flow-Resistance and Heat Transfer in Circulation Type Evaporators, Part IV: Two-Phase Flow Resistance in Boiling Refrigerants," Annexe 1972-1, Bull. de l'Inst. du Froid, (1979).

Müller-Steinhagen, H. and K. Heck, "A Simple Friction Pressure Drop Correlation for Two-Phase Flow in Pipes," *Chemical Engineering Process* (20)(1986) 297–308.

Rouhani, Z. and E. Axelsson, "Calculation of Void Volume Fraction in the Subcooled and Quality Boiling Regions," *Int. J. Heat Mass Transfer*, 13 (1970) 383–393.

Souza, A.L., J.C. Chato, J.P. Wattelet, and B.R. Christoffersen, "Pressure Drop During Two-Phase Flow of Pure Refrigerants and Refrigerant-oil Mixtures in Horizontal Smooth Tubes," *Heat Transfer with Alternate Refrigerants (ASME)* HTD 243 (1993), 35-41.

Steiner, D., "Heat Transfer to Boiling Saturated Liquids," VDI-Wārmeatlas (VDI Heat Atlas), Verein Deutscher Ingenieure, VDI-Gesellschaft Verfahrenstechnik und Chemieingenieurwesen (GCV), Dū sseldorf, Chapter Hbb (1993).

Thome, J.R., J. El Hajal, and A. Cavalini, "Condensation in Horizontal Tubes, Part 2: New Heat Transfer Model Based on Flow Regimes," *International Journal of Heat and Mass Transfer* 46 (2003) 3365-3387.

Yashar, D.A., M.J. Wilson, H.R. Kopke, D.M. Graham, J.C. Chato and T.A. Newell, "An Investigation of Refrigerant Void Fraction in Horizontal, Microfin Tubes," *HVAC&R Research* 7 (2001) 67–82.

Appendix A: Additional Probabilistic Two-Phase Flow Maps

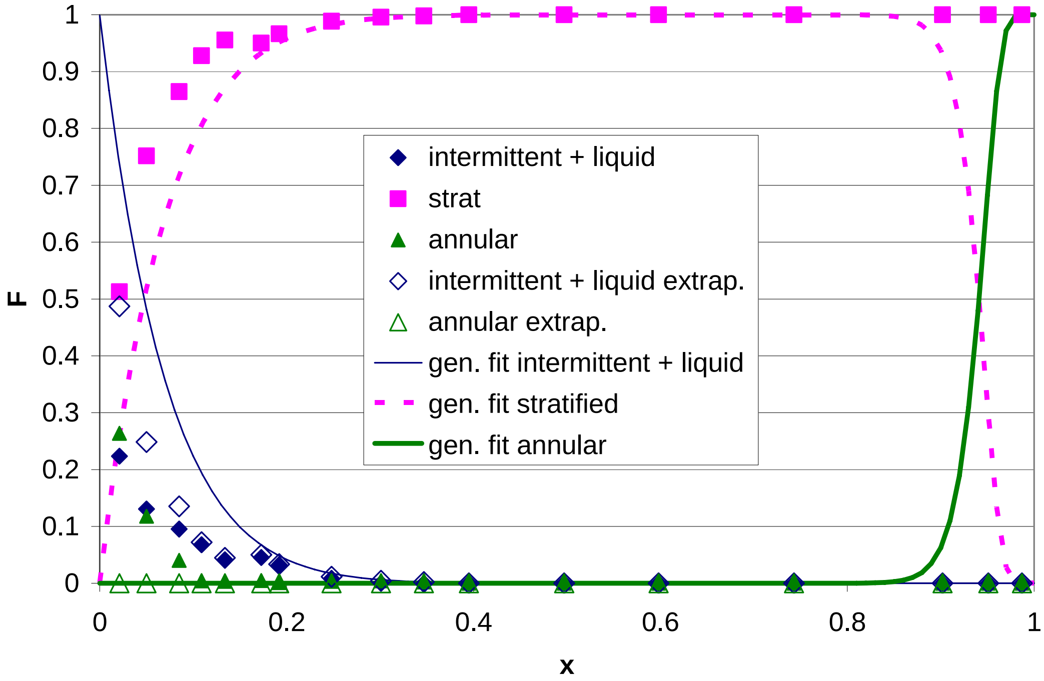

Figure A.1. Probabilistic flow map with generalized time fraction curve fits for 8.00 mm diameter tube, R134a, 35 ºC, 100 kg/m^2-s

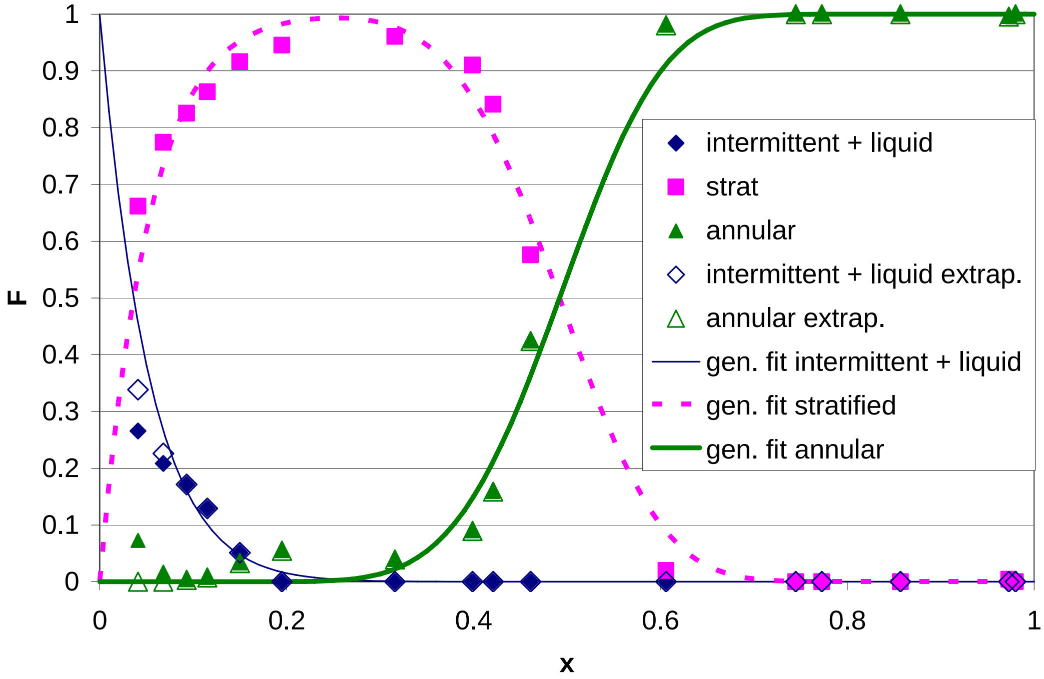

Figure A.2. Probabilistic flow map with generalized time fraction curve fits for 8.00 mm diameter tube, R134a, 35 ºC, 200 kg/m^2-s

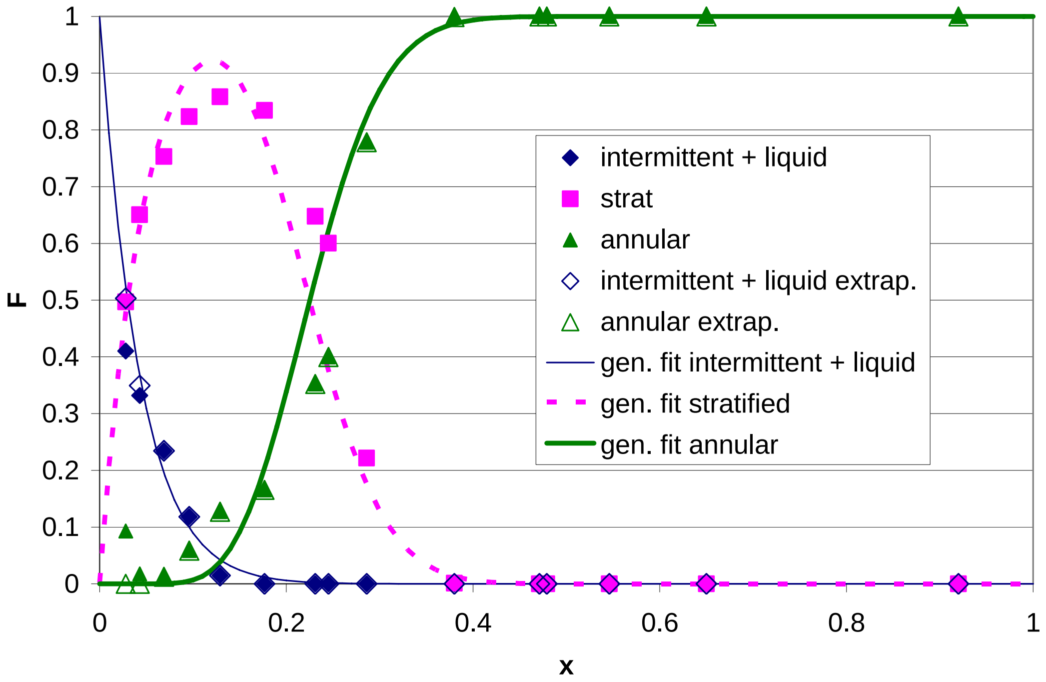

Figure A.3. Probabilistic flow map with generalized time fraction curve fits for 8.00 mm diameter tube, R134a, 35 ºC, 300 kg/m^2-s

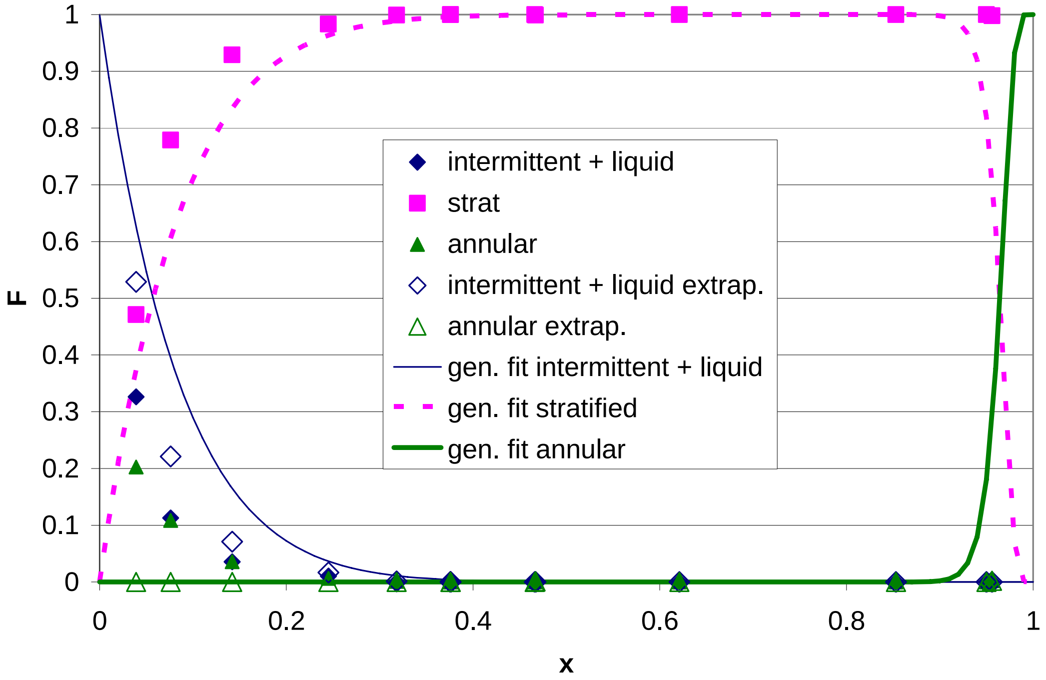

Figure A.4. Probabilistic flow map with generalized time fraction curve fits for 8.00 mm diameter tube, R134a, 49.7 ºC, 100 kg/m^2-s

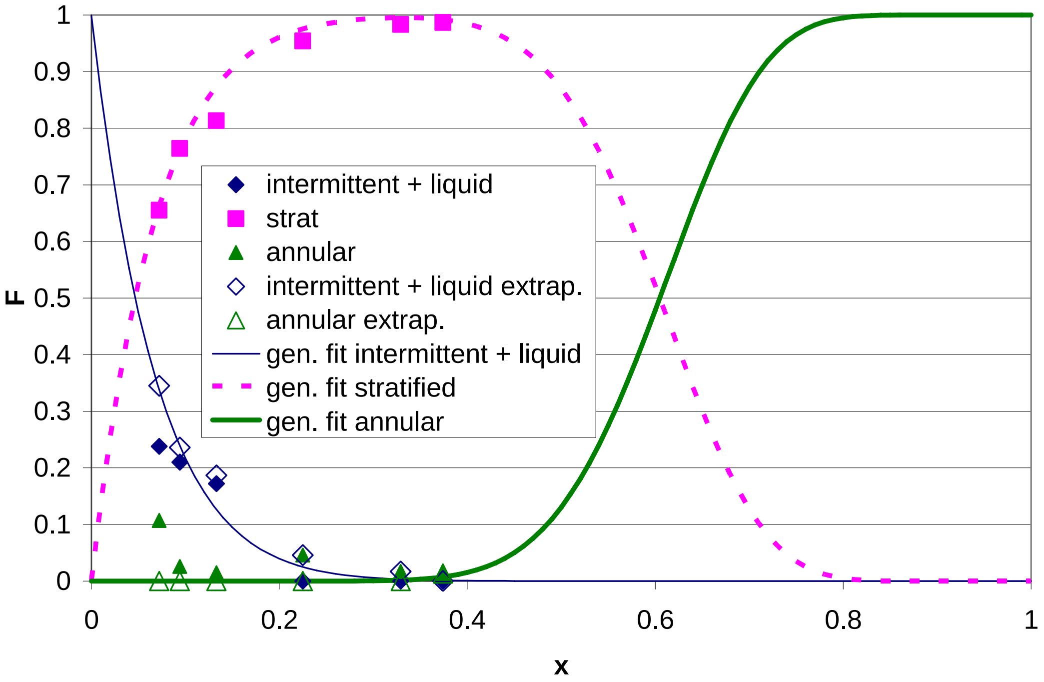

Figure A.5. Probabilistic flow map with generalized time fraction curve fits for 8.00 mm diameter tube, R134a, 49.7 ºC, 200 kg/m^2-s

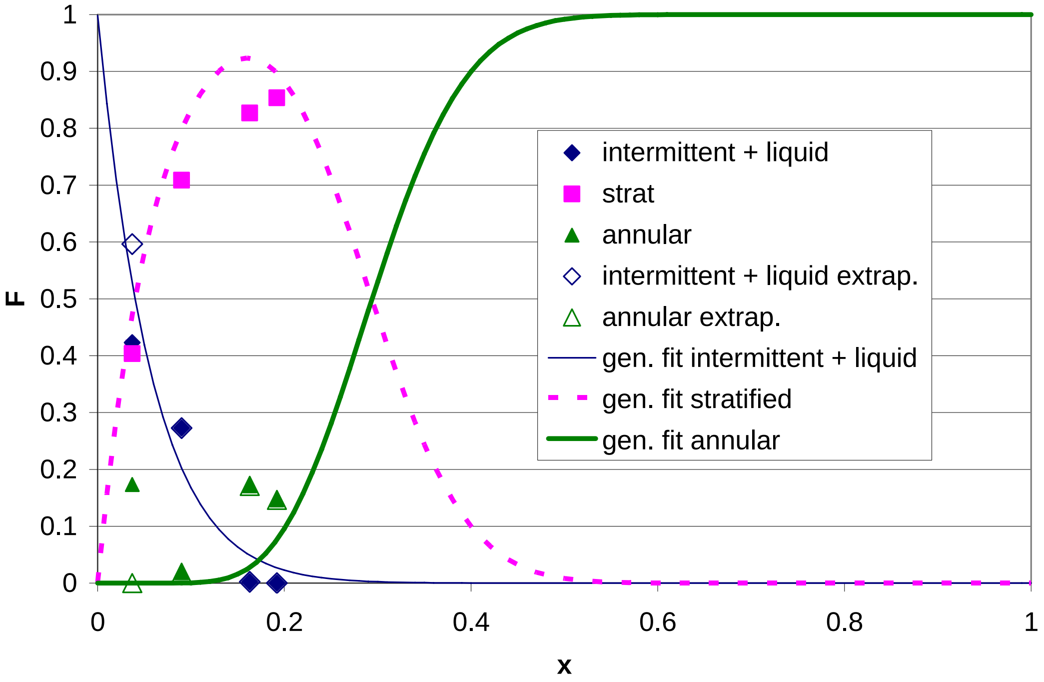

Figure A.6. Probabilistic flow map with generalized time fraction curve fits for 8.00 mm diameter tube, R134a, 49.7 ºC, 300 kg/m^2-s

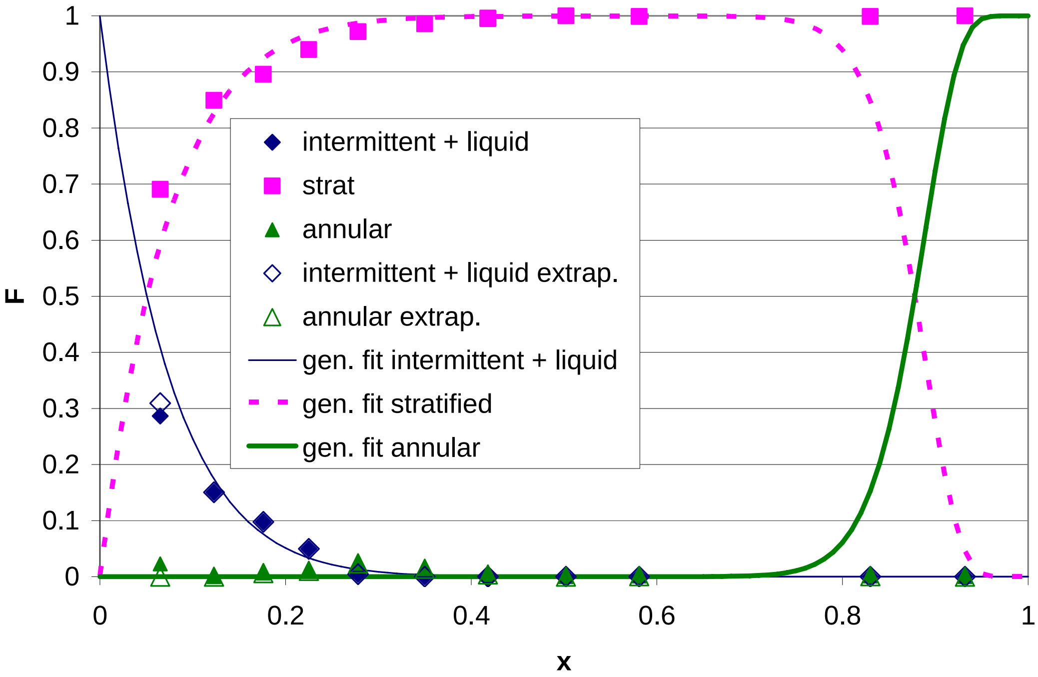

Figure A.7. Probabilistic flow map with generalized time fraction curve fits for 5.43 mm diameter tube, R134a, 35 ºC, 100 kg/m^2-s

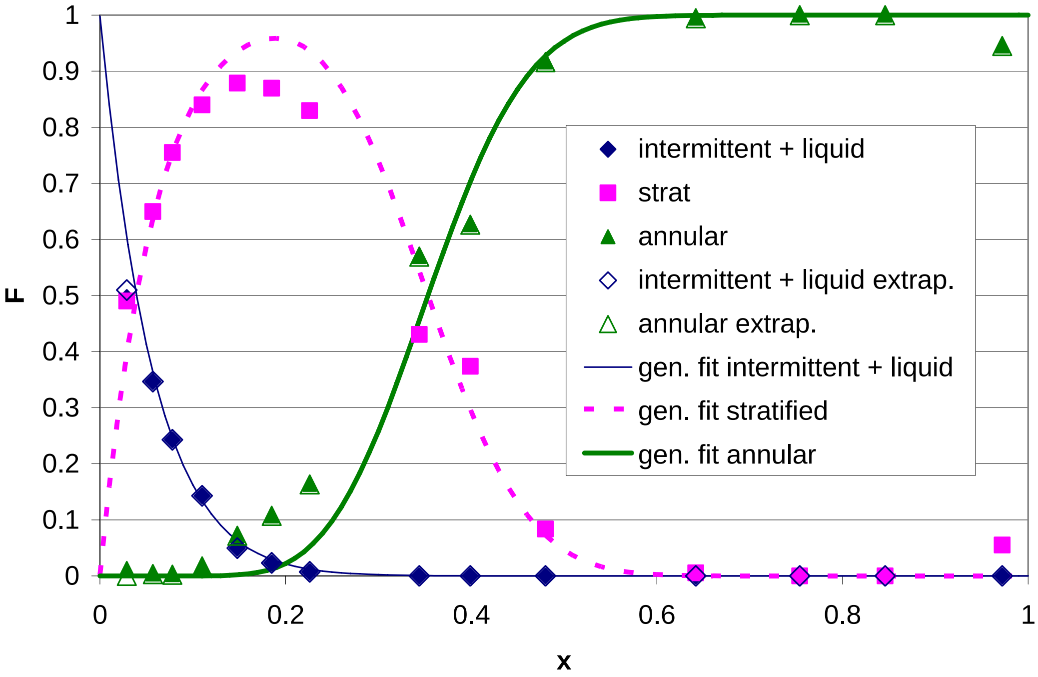

Figure A.8. Probabilistic flow map with generalized time fraction curve fits for 5.43 mm diameter tube, R134a, 35 ºC, 200 kg/m^2-s

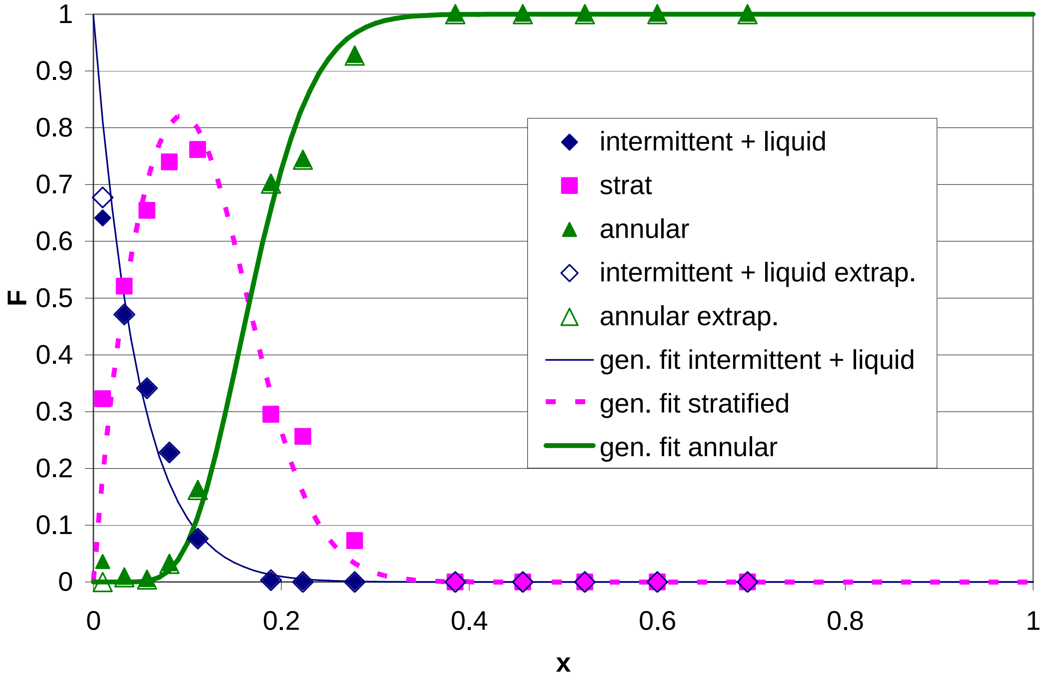

Figure A.9. Probabilistic flow map with generalized time fraction curve fits for 5.43 mm diameter tube, R134a, 35 ºC, 300 kg/m^2-s

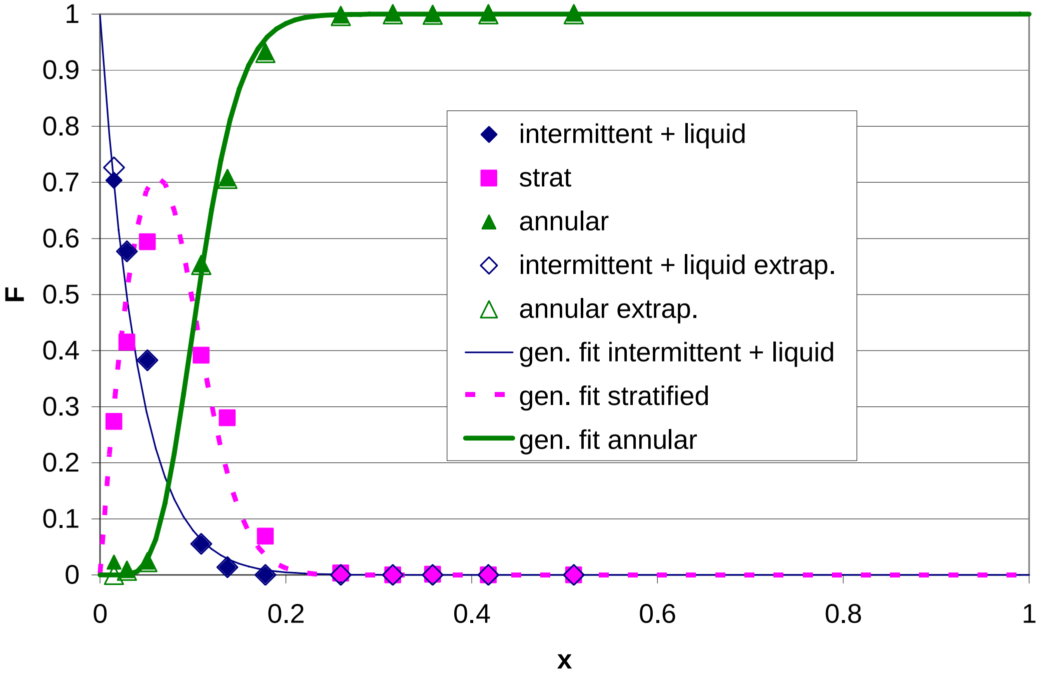

Figure A.10. Probabilistic flow map with generalized time fraction curve fits for 5.43 mm diameter tube, R134a, 35 ºC, 400 kg/m^2-s

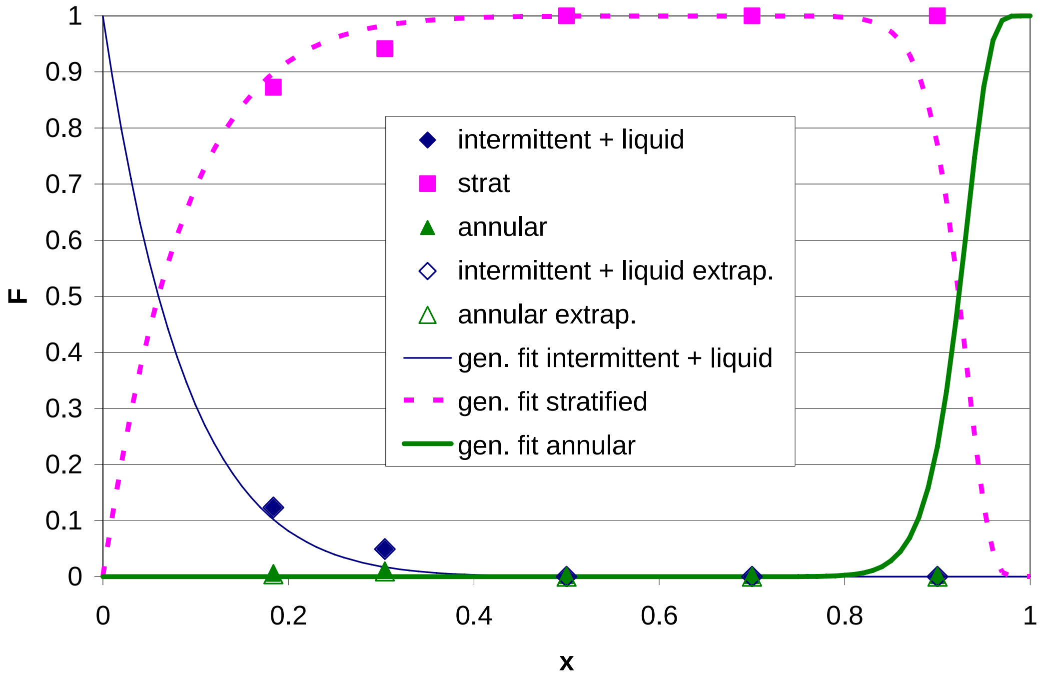

Figure A.11. Probabilistic flow map with generalized time fraction curve fits for 5.43 mm diameter tube, R134a, 49.7 ºC, 100 kg/m^2-s

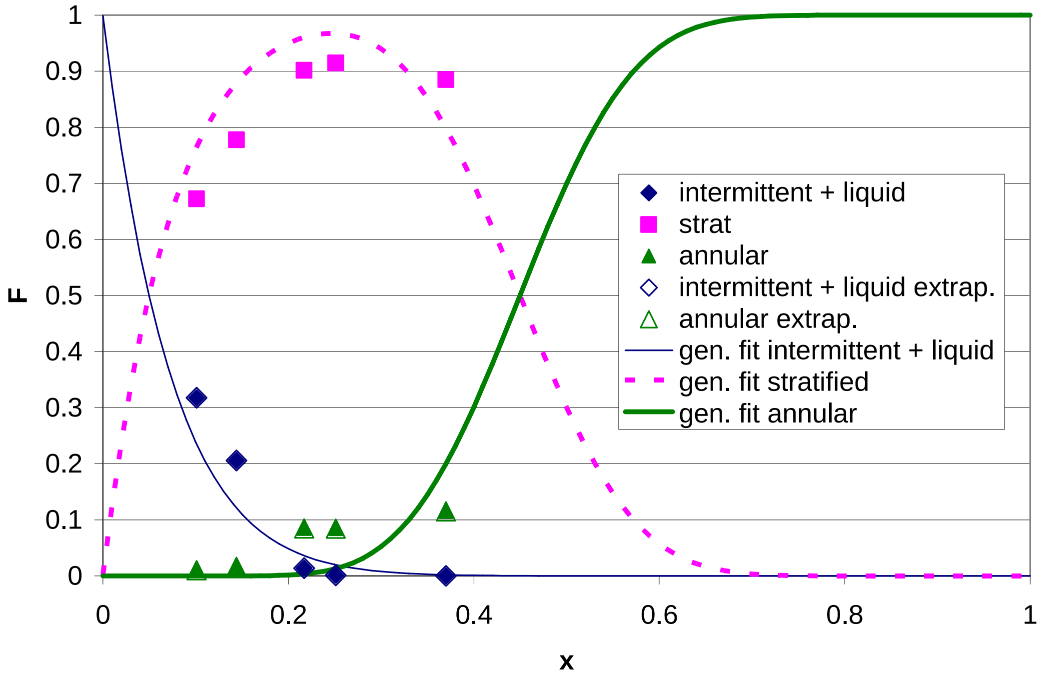

Figure A.12. Probabilistic flow map with generalized time fraction curve fits for 5.43 mm diameter tube, R134a, 49.7 ºC, 200 kg/m^2-s

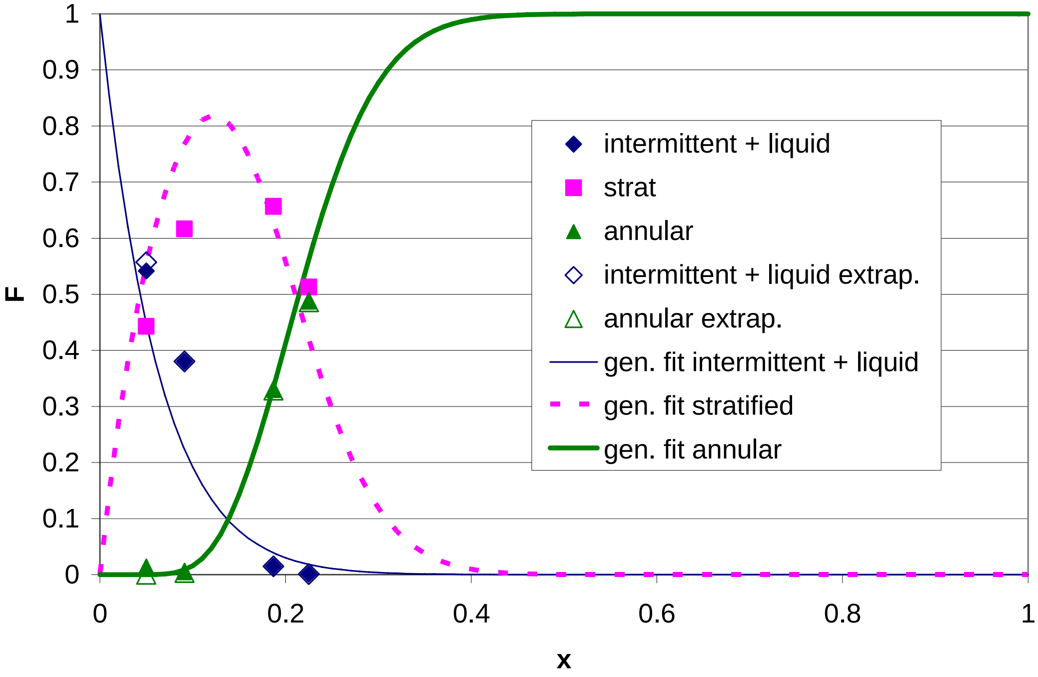

Figure A.13. Probabilistic flow map with generalized time fraction curve fits for 5.43 mm diameter tube, R134a, 49.7 ºC, 300 kg/m^2-s

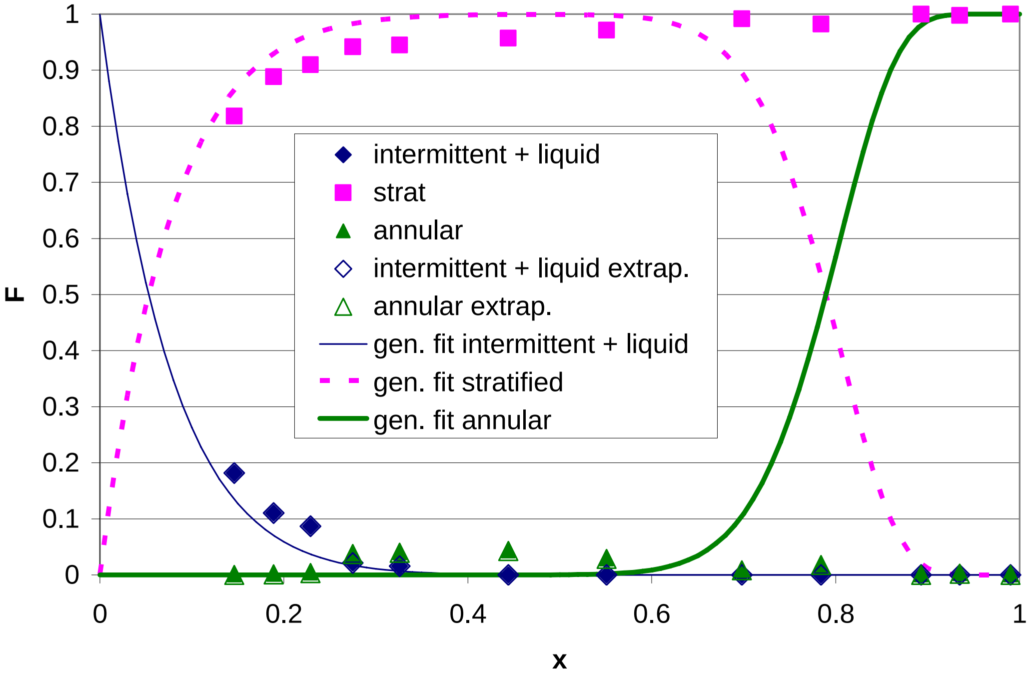

Figure A.14. Probabilistic flow map with generalized time fraction curve fits for 3.90 mm diameter tube, R134a, 35 ºC, 100 kg/m^2-s

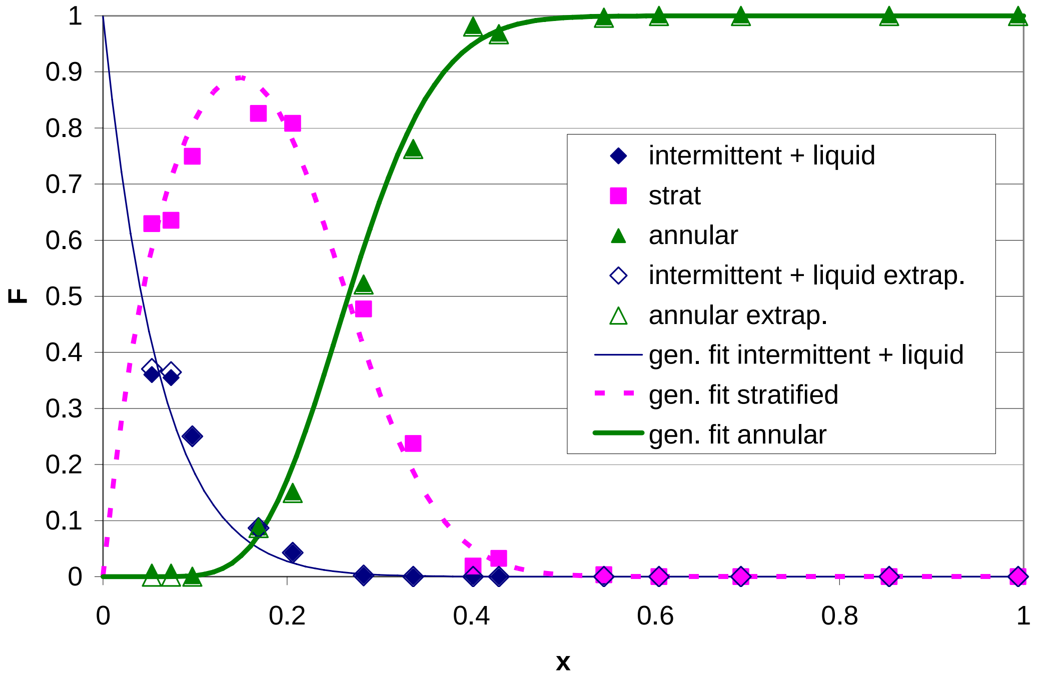

Figure A.15. Probabilistic flow map with generalized time fraction curve fits for 3.90 mm diameter tube, R134a, 35 ºC, 200 kg/m^2-s

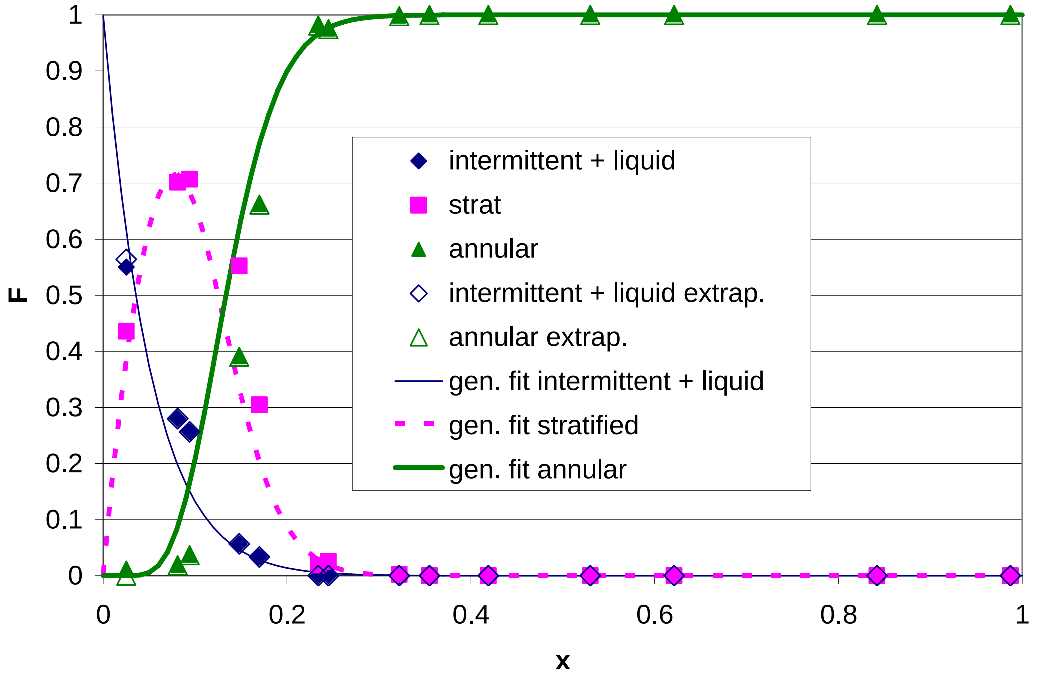

Figure A.16. Probabilistic flow map with generalized time fraction curve fits for 3.90 mm diameter tube, R134a, 35 ºC, 300 kg/m^2-s

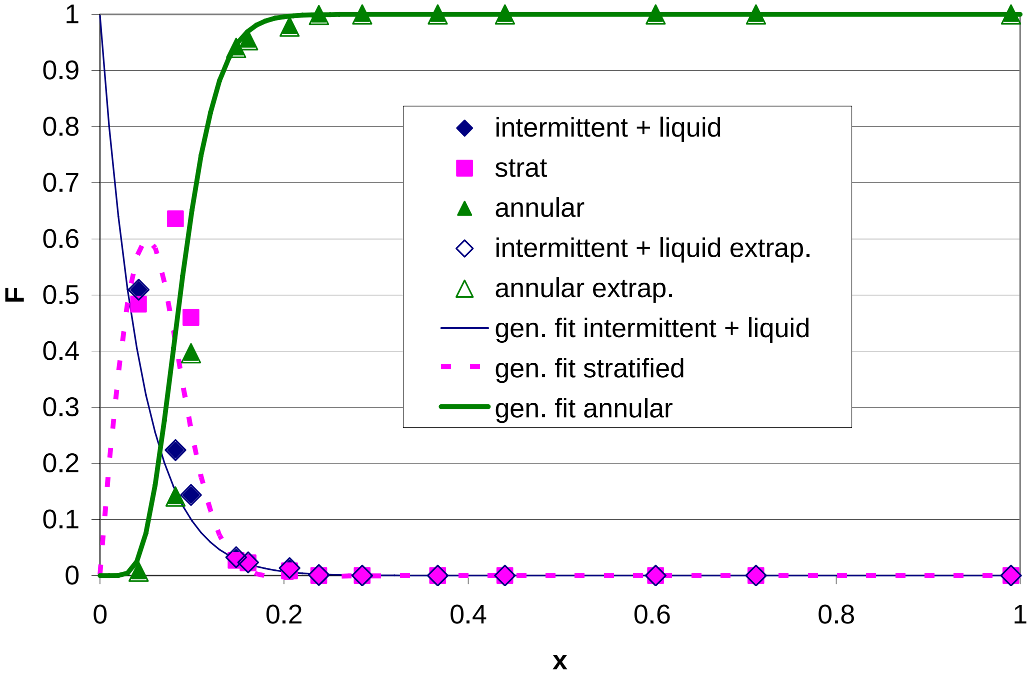

Figure A.17. Probabilistic flow map with generalized time fraction curve fits for 3.90 mm diameter tube, R134a, 35 ºC, 400 kg/m^2-s

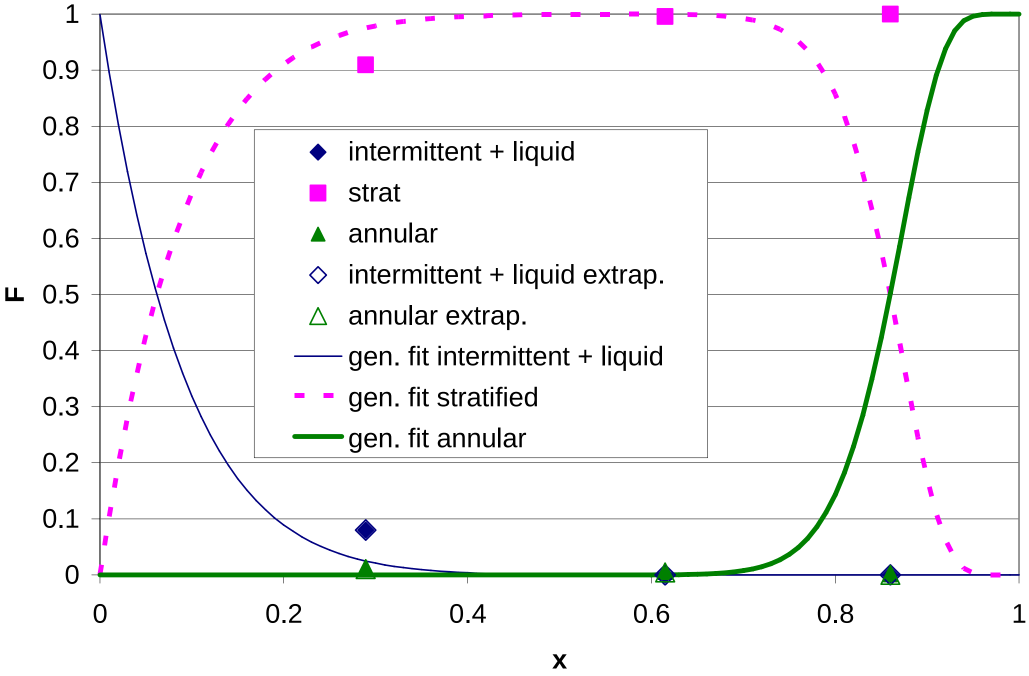

Figure A.18. Probabilistic flow map with generalized time fraction curve fits for 3.90 mm diameter tube, R134a, 49.7 ºC, 100 kg/m^2-s

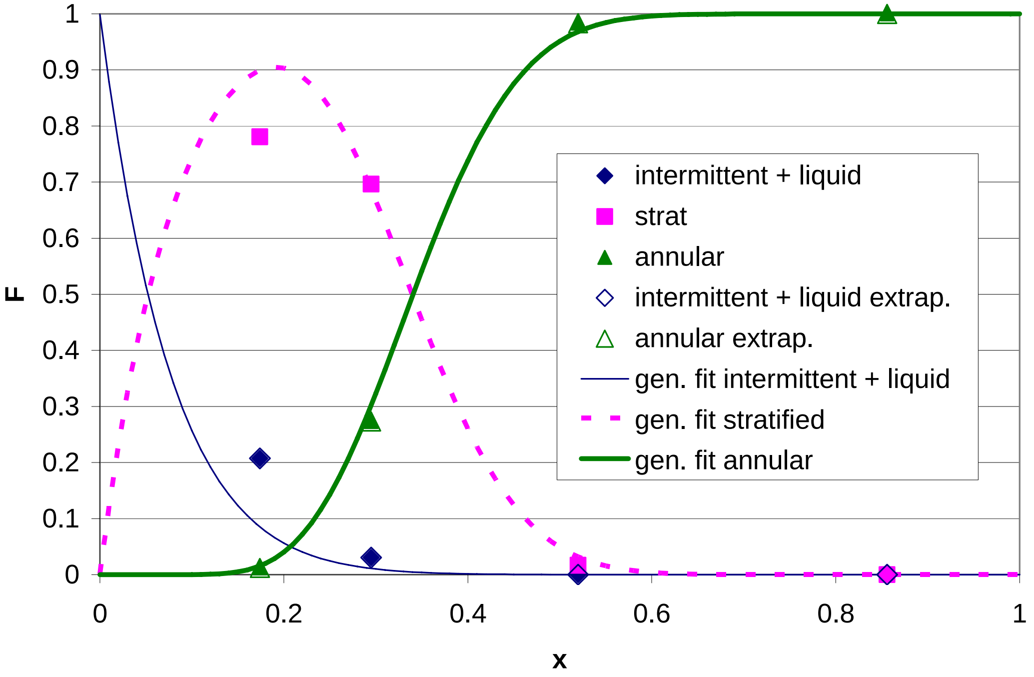

Figure A.19. Probabilistic flow map with generalized time fraction curve fits for 3.90 mm diameter tube, R134a, 49.7 ºC, 200 kg/m^2-s

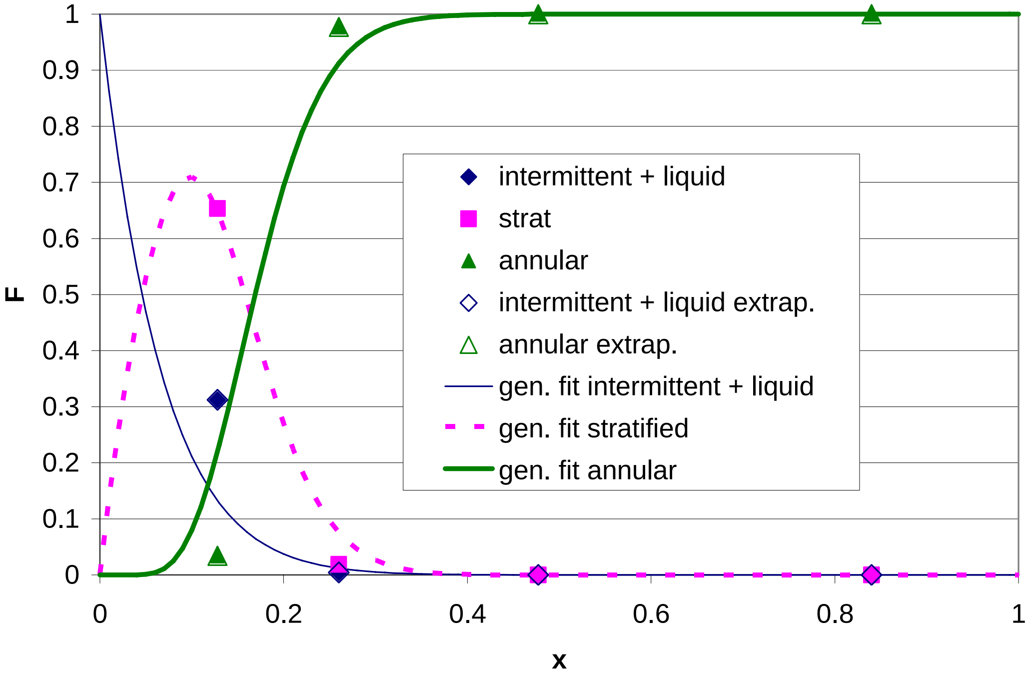

Figure A.20. Probabilistic flow map with generalized time fraction curve fits for 3.90 mm diameter tube, R134a, 49.7 ºC, 300 kg/m^2-s

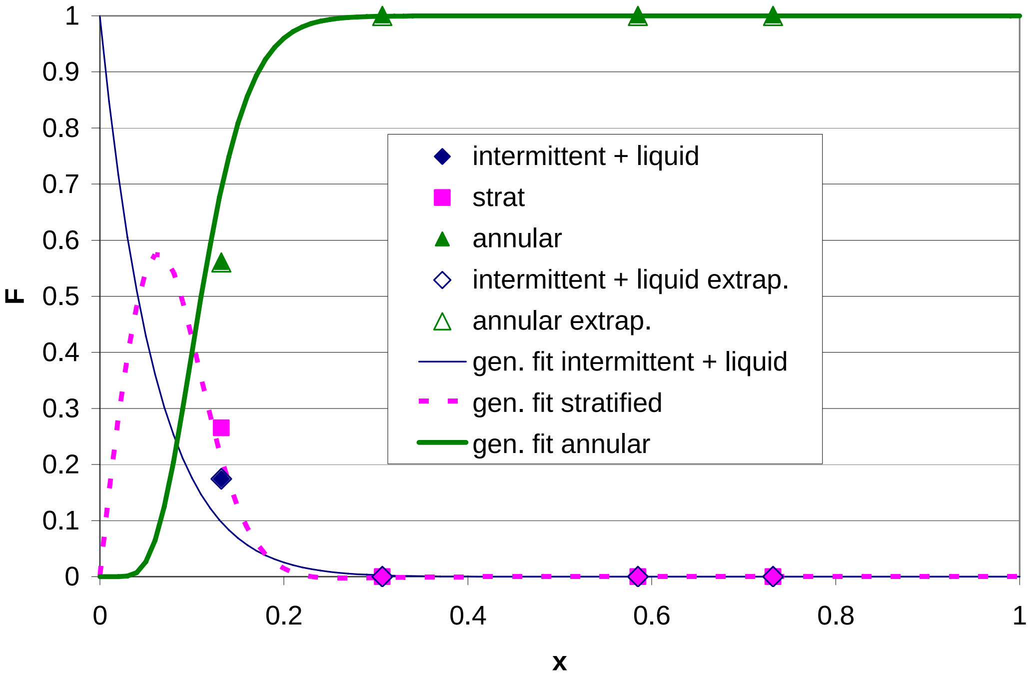

Figure A.21. Probabilistic flow map with generalized time fraction curve fits for 3.90 mm diameter tube, R134a, 49.7 ºC, 400 kg/m^2-s

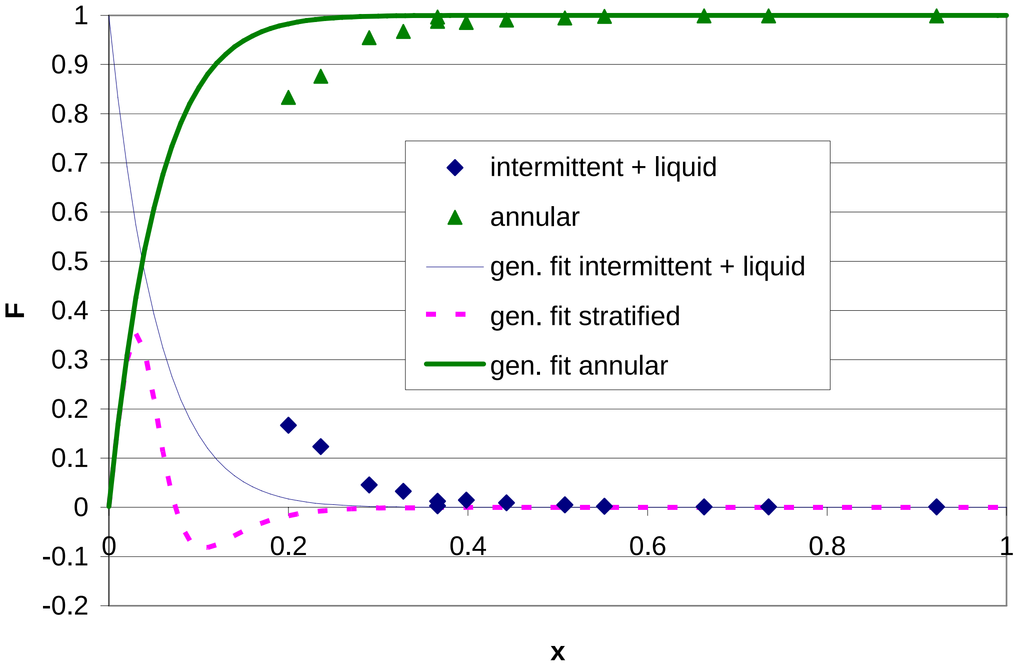

Figure A.22. Probabilistic flow map with generalized time fraction curve fits for 1.74 mm diameter tube, R134a, 35 ºC, 400 kg/m^2-s

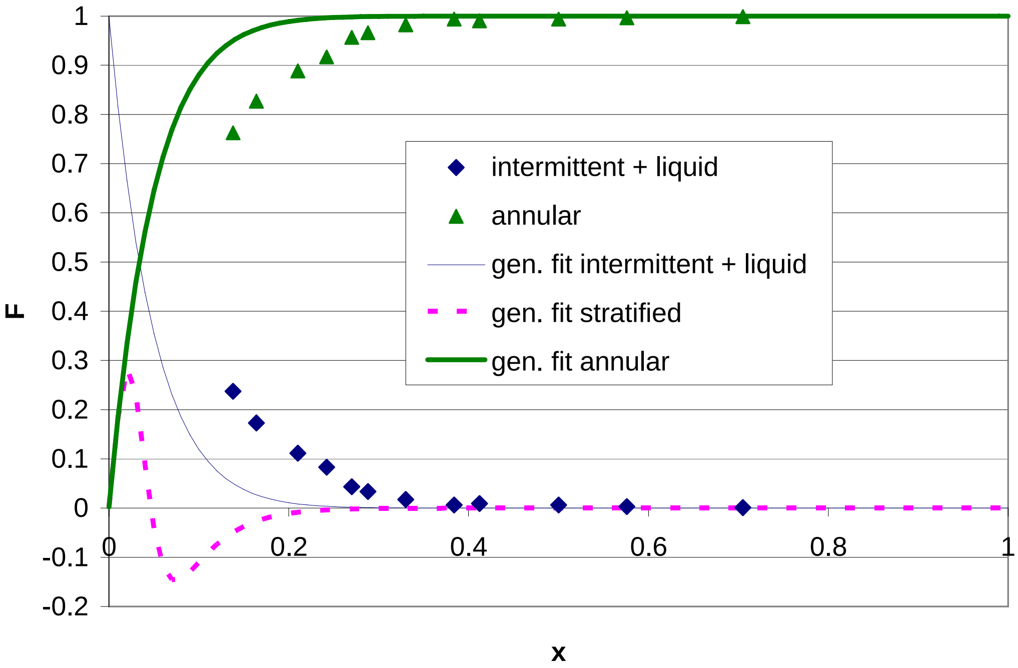

Figure A.23. Probabilistic flow map with generalized time fraction curve fits for 1.74 mm diameter tube, R134a, 35 ºC, 500 kg/m^2-s

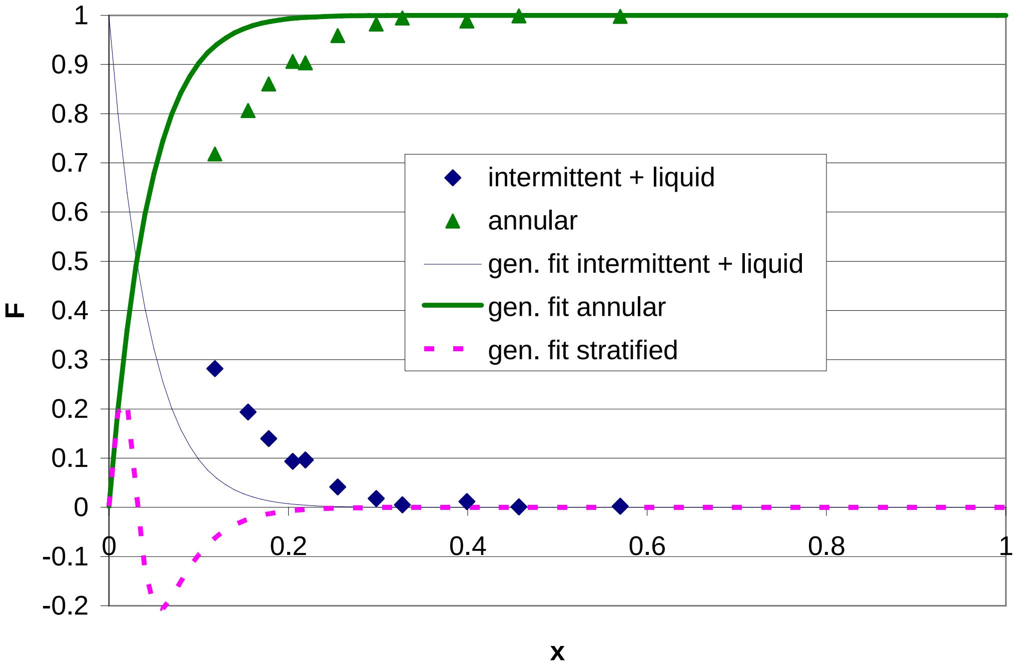

Figure A.24. Probabilistic flow map with generalized time fraction curve fits for 1.74 mm diameter tube, R134a, 35 ºC, 600 kg/m^2-s